Hydrogen Bond Rearrangements and the Motion of Charge Defects in Water Viewed using Multidimensional Ultrafast Infrared Spectroscopy

by

Sean T. Roberts

B.S. Chemistry
University of California, Los Angeles, 2003

MASSACHUSETTS INSTITUTE OF TECHNOLOGY
FEB 26 2010
LIBRARIES

ARCHIVES

Submitted to the Department of Chemistry
in partial fulfillment of the requirements for the degree of

Doctor of Philosophy

at the

Massachusetts Institute of Technology

December 2009
[February 2010]

© 2010 Massachusetts Institute of Technology. All rights reserved.

Signature of Author: _____
Sean T. Roberts
December 7, 2009

Certified by: _____
Andrei Tokmakoff
Associate Professor of Chemistry
Thesis Supervisor

Accepted by: _____
Robert W. Field
Professor of Chemistry
Chairman, Departmental Committee on Graduate Studies

This doctoral thesis has been examined by a committee of the Department of Chemistry that included:

Professor Keith A. Nelson _____
Chair

Associate Professor Troy Van Voorhis___

Professor Andrei Tokmakoff _____
Thesis Supervisor

Hydrogen Bond Rearrangements and the Motion of Charge Defects in Water Viewed using Multidimensional Ultrafast Infrared Spectroscopy

by

Sean T. Roberts

Submitted to the Department of Chemistry on December 13, 2009
in partial fulfillment of the requirements for the degree of
Doctor of Philosophy

Abstract

Compared with other molecular liquids, water is highly structured due to its ability to form up to four hydrogen bonds to its nearest neighbors, resulting in a tetrahedral network of molecules. However, this network is highly dynamic, exhibiting fluctuations and rearrangements that take place on femtosecond to picosecond time scales. The transport of excess protons and proton holes in water makes exclusive use of water's hydrogen bonding network. Compared to ions of similar size and charge density, both hydronium and hydroxide ions exhibit anomalously high diffusion rates due to the fact that water molecules that neighbor these ions can undergo a proton transfer reaction with the ion. This allows the structural diffusion of the ion to occur apart from the displacement of individual water molecules.

In this thesis we adopt a joint experimental and theoretical approach to characterize the fluctuations of water's hydrogen bonding network and how these fluctuations act to drive the structural diffusion of the aqueous hydroxide ion. The experimental data that we present consists of a series of ultrafast nonlinear infrared spectroscopies, in particular two-dimensional infrared spectroscopy (2D IR), applied to the O-H stretching transition of a dilute solution of HOD in NaOD/D_2O. The frequency of the O-H stretch, ω_{OH}, is highly sensitive to the configuration of its hydrogen bonding partner. 2D IR spectroscopy allows us to measure rapid shifts in ω_{OH} that reveal time scales for changes in the local environment of the HOD molecule. The calculation of 2D IR spectra from molecular dynamics simulations then allows us to make a direct connection between the results of our experiments and the underlying dynamics of the system that drive both hydrogen bond exchange and the structural diffusion of the hydroxide ion.

2D IR spectra recorded for dilute HOD in D_2O show a strong asymmetry, preferentially broadening in the frequency region indicative of strained or broken hydrogen bonds, indicating that these configurations are unstable and quickly return to a hydrogen bond. The time scale over which the 2D spectra broaden, ~60 fs, is similar to

the librational period of water and suggests that molecules exchange hydrogen bonding partners though rapid, large amplitude rotations. Molecular dynamics simulations find that the transition state for hydrogen bond exchange resembles a bifurcated hydrogen bond. In roughly half of the examined exchange events, a second solvation shell water molecule inserts across the breaking hydrogen bond. This suggests that hydrogen bond rearrangements are tied to the restructuring of a water molecule's solvation shell.

Upon the addition of NaOD to HOD/D_2O solution, a large absorption continuum appears to the low frequency side of the O-H stretch due to the formation of strong hydrogen bonds between HOD molecules and OD^- ions. At early waiting times, 2D IR spectra show large, offdiagonal intensity in this frequency range that rapidly relaxes within ~110 fs. Modeling using an empirical valence bond simulation (MS-EVB) model of aqueous NaOH suggests that as the O-H stretching potential symmetrizes during proton transfer events, overtone transitions of the shared proton contribute strongly to 2D spectra. The rapid loss of offdiagonal intensity results from the spectral sweeping of these vibrational overtones as the solvent modulates the motion of the shared proton. The collective electric field of the solvent is found to be an appropriate reaction coordinate for the formation and modulation of shared proton states.

Over picosecond waiting times, spectral features appear in the 2D IR spectra that are indicative of the exchange of population between OH^- ions and HOD molecules due to proton transfer. The construction of a spectral fitting model gives a lower bound of 3 ps for this exchange. Calculations of structural parameters following proton exchange using the MS-EVB simulation model suggest that the observed exchange process corresponds to the formation and breakage of hydrogen bonds donated by the HOD/OD^- pair formed as a result of the proton transfer. A full description of the structural diffusion of the hydroxide ion requires both a description of the local hydrogen bonding structure of the ion as well as the dielectric fluctuations of the surrounding solvent.

Thesis Supervisor: Andrei Tokmakoff
Title: Professor of Chemistry

To Giselle,

For helping me see this work through from beginning to end.

Acknowledgements

Anyone who knows me well can tell you that I am horrible at remembering things, and given the enormous number of people that I have been lucky enough to work with during my time at MIT, I wish to apologize in advance to anyone who I may accidentally leave out of these acknowledgements.

Living in Boston and working at MIT over the past 6+ years has been a tremendous pleasure. As with all things, at times I have had a bit of a love/hate relationship with graduate school, but overall the good times have overwhelmingly outweighed the bad. Graduate school was a time of great self discovery in my life. It has shown me that I am capable of achieving goals that I would not have thought otherwise possible. It has also shown me my limits, and helped me to realize that truly good work only comes about when you are able to work with friends, colleagues, and advisors that are both highly gifted and that you respect and admire.

I am greatly indebted to my advisor Andrei Tokmakoff for all of the guidance and support that he has given me throughout my stay at MIT. Andrei is a tremendous scientist whom always seems to find insightful ways of breaking down difficult questions into bits we can address in lab. Andrei is not one to shy away from tough problems, and has continually encouraged me to study hard problems because, more often than not, they prove to be the interesting ones. Working in the fiery furnace of the Tokmakoff group has made me into a much better scientist than I would have otherwise become, and I am grateful for the opportunity to do research under Andrei's guidance.

When I first started research at MIT, I was lucky enough to work with an incredibly talented pair of graduate students. Joel Eaves introduced me to both the art of

molecular dynamics and the humor that can be found in the force of nature that is the Boston Brogue. Much of the experimental work that I present in this thesis was recorded in 2-041, aptly referred to by the Tokmakoff group as the "Water Lab" (this nickname refers to the fact that our experimental sample was most often water, although the periodic floods our lab suffered may suggest a different origin for this name). Here, Joe Loparo served as my experimental tutor, showing me the difficulties that lie in the measurement of non-linear signals, and how to surmount them (at least on days when the laser agreed to cooperate). Joe was a very gifted and patient teacher, and a good friend.

As time passed, I gradually moved into the role of a senior student and received help from a set of excellent graduate students and post-docs. Over the past three years, my research project has greatly benefited from the work of both Krupa Ramasesha and Poul Petersen. Krupa is one of the nicest people that I have met during my time at MIT. I am sure that the Water Lab will prosper under her guidance. Poul was a perpetually happy person who served as a sounding board for many of the crazy ideas I came up with to explain my data. I wish him the best as he starts a research program of his own at Cornell.

Although we only had the opportunity to work in lab together a few times, Becky Nicodemus has been a fantastic member of the "Water Project," and has often helped me examine some of the quantitative details of my data which I have a tendency to overlook at times. Aritra Mandal is the newest member of the group to work on the "Water Project," and I am thankful for his help in measurement and calculation of some of the spectra that appear in Chapters 6 and 7.

I also wish to thank our collaborators Ivan Ufimtsev and Todd Martinez at Stanford University for the donation of trajectories of an empirical valence bond simulation model of aqueous hydroxide. The analysis of these trajectories forms the basis of Chapter 7 and has allowed me to make mechanistic connections to experimental results that I would not have been able to make otherwise. The U.S. Department of Energy also deserves special recognition for providing the funding for my research project. Without their financial support, the document that you are now reading would not exist.

Often, the people that you work with become good friends and the Tokmakoff group is no exception. I am happy to have met and worked with Hoi Sung Chung, Lauren DeFlores, Adam Smith, Ziad Ganim, Kevin Jones, Josh Lessing, Harold Hwang, Jongjin Kim, and most recently Sam Peng and Andrew Horning. Hoi Sung, Lauren and Adam were each terrific role models who showed me what it meant to be a member of the Tokmakoff group. Ziad entered graduate school at the same time that I did, and I am glad that he chose to join the Tokmakoff group since there have been many times that his advice has helped me to overcome many of the problems that I have encountered in the course of my research work. I have a great deal of respect for Ziad, and I am sure that he will go far in his career.

I lost count long ago of the numerous times that Kevin has made me stop and laugh. From his self-published Kevin calendar to his unhealthy obsession with peanut butter, Kevin has always kept the mood light in the group while still proving that he is capable of accomplishing difficult experiments. Over the past few years, I have become good friends with both Josh and Harold. Josh has given me a crash course of sorts into

why peptide synthesis can prove to be extremely interesting. Together with Harold, Josh also taught me both a good appreciation of Scotch and that sometimes the best thing you can do to help your research is to take a break and grab a few beers. Sam and Andrew are some of the newest members of the Tokmakoff group, and they have already demonstrated that the group will be in good hands after I depart. While I am excited to move on to a new set of research problems in a new setting, it also saddens me that I will not be able to talk to each of these terrific individuals on a daily basis.

I also want to thank my parents for the many sacrifices that they have made to allow me to become the person that I am today. My mother has always stressed education above all things and my father has served as my role model for a person who bears the burden of hard work for the benefit of his family. This thesis is just as much a product of their efforts as my own.

Finally, I would like to dedicate this thesis to Giselle Cuadros, my amazing fiancé. Giselle and I first met while we were both starting college in Southern California and without her love and support, I probably would not have been strong enough to undertake the series of trials that form the core of the graduate school experience. Giselle has stood by me during both the all too rare highs and the deep, deep lows that are part of graduate school, and for that she deserves more thanks that I can put into words.

Table of Contents

List of Figures **15**

List of Tables **20**

1. Introduction **21**

1.1. Water is a Peculiar Liquid 21

1.2. Water's Fluctuations make it Difficult to Characterize 24

1.3. Understanding Water Requires Understanding its Dynamics 25

1.4. Experimental Probes of Water's Time Dependent Structure 28

1.5. Thesis Outline 31

References 33

2. An Introduction to Nonlinear Vibrational Spectroscopy and the Calculation of Third Order Signals **39**

2.1. Introduction 39

2.2. The Third Order Polarization 41

2.3. A Pictorial Representation of the Third Order Response 46

2.4. Useful Approximations for the Calculation of Spectroscopic Observables 49

2.4.1. Energy Gap Fluctuation Description of the Third Order Response 50

2.4.2. Second Cumulant Approximation....54
2.4.3. Linear Absorption Lineshapes....56
2.4.4. Treatment of Population Relaxation and Reorientation....58
2.5. Vibrational Echo Spectroscopy and Other Probes of Vibrational Dynamics....59
2.5.1. Two-Dimensional Infrared Spectroscopy....65
2.5.2. Vibrational Echo Peak Shift Spectroscopy....68
2.5.3. Pump-Probe and Transient Grating Spectroscopy....69
References....71

3. Characterization of Spectral Diffusion from 2D Lineshapes....77
3.1. Introduction....77
3.2. Response Function Formalism....80
3.3. Analysis of Lineshapes....82
3.4. Model Calculations & Discussion....88
Acknowledgements....96
References....96
3.A. Appendix: Analysis of Lineshapes for a Three Level System....100

4. Generation of Sub-50 fs Mid-Infrared Pulses and the Measurement of Nonlinear Infrared Signals....103
4.1. Introduction....103
4.2. Generation of Mid-Infrared Pulses....106
4.3. Acquisition of Vibrational Echo Signals....111
4.3.1. Calibration of Stages for Interferometric Measurements....114

4.3.2. Photon Echo Peak Shift Experiments....117

4.3.3. Two-Dimensional Infrared Spectroscopy....119

Acknowledgements....131

References....132

5. Structural Rearrangements in Water Viewed Through Two-Dimensional Infrared Spectroscopy....135

5.1. Introduction....135

5.2. Experimental and Theoretical Methods....140

5.3. Frequency-Structure Correlations....142

5.4. Scenarios for Hydrogen Bond Exchange....143

5.5. Two-Dimensional Infrared Spectroscopy of HOD in D_2O....145

5.6. 1D and 2D Lineshapes Calculated from Classical MD Simulations....149

5.7. Energetics of Water's Hydrogen Bonding Network....158

5.8. Reorientation During Hydrogen Bond Exchange....160

5.9. The Connection Between Reorientation and Frequency Shifts....163

5.10. Switching Through Water Insertion....169

5.11. Conclusions....171

Acknowledgements....172

References....172

5.A. Appendix: The Role of Motional Narrowing in 2D Lineshapes....179

6. Different Stages of Proton Transfer in Aqueous Hydroxide Solutions Visualized using Ultrafast Infrared Spectroscopy.....183

6.1. Introduction.....183

6.2. Experimental Methods.....190

6.3. Infrared Spectroscopy of Isotopically Dilute Hydroxide Solutions.....193

6.4. Observation of Proton Transfer Dynamics using 2D IR Spectroscopy.....201

6.5. Spectral Signatures of Chemical Exchange Processes in 2D IR Spectra.....208

6.6. Treatment of Chemical Exchange in 2D IR Lineshapes.....214

6.7. Model of Chemical Exchange in Isotopically Dilute Deuteroxide Solution.....220

6.7.1. Treatment of Diagonal and Exchange Cross Peaks.....223

6.7.2. Treatment of Thermal Effects.....229

6.7.3. Constraints for Fitting Parameters.....232

6.8. Comparison Between Model Calculations and Experiment.....234

6.8.1. FT-IR and Magic Angle Pump-Probe Experiments.....234

6.8.2. Photon Echo Peak Shift.....237

6.8.3. Determining an Exchange Timescale from 2D IR Measurements.....243

6.8.4. Implications of the Exchange Time Scale.....248

6.9. Conclusions.....249

Acknowledgements.....251

References.....251

6.A. Appendix: Calculation of Linear Absorption Spectra.....259

6.B. Appendix: Fit Parameters used for the Spectral Model.....259

7. An Examination of Reaction Coordinates for Proton Transfer in Liquid Water using an Empirical Valence Bond Model of Aqueous NaOH.....262

7.1. Introduction.....262

7.2. MS-EVB Simulation Model of Aqueous Sodium Hydroxide.....268

7.3. Methodology for the Calculation of Vibrational Frequencies.....271

7.4. Correlations Between Frequency and Structure.....279

7.5. Signatures of Proton Transport in 1D Lineshapes.....281

7.6. Calculation of the Third Order Response Including Forbidden Transitions.....292

7.7. 2D IR Spectra of Proton Transfer Events.....297

7.8. Linear and Nonlinear Spectra of the Free OH^- Ion Stretch.....302

7.9. Reaction Coordinates for the Structural Diffusion of the OH^- Ion.....307

7.10. Solvation of the $DOD\cdot\cdot OH^-$ Ion Following Proton Transfer.....315

7.11. Summary and Conclusions.....319

Acknowledgements.....320

References.....320

7.A. Appendix: Calculation of Frequencies and Transition Dipole Moments.....328

Curriculum Vitae.....334

List of Figures

1-1. A Potential Realization of Grotthuss Proton Transfer.....23

1-2. Infrared Absorption Spectrum of Dilute HOD in D_2O and the Connection Between the O-H Frequency and Water Structure.....29

1-3. Infrared Spectra of Concentrated Acid and Base.....31

2-1. Pulse Sequence for Third Order Nonlinear Spectroscopy.....45

2-2. Feynman Interaction Pathways for a General Multilevel System.....48

2-3. Feynman Diagrams for a Two Level System.....60

2-4. Schematic Illustration of the Generation of a Vibrational Echo Signal.....62

2-5. Feynman Diagrams for a Three Level Vibrational System.....63

2-6. Pulse Sequence, Geometries, and Phase Matching Conditions for 2D IR Spectroscopy and other Third Order Experiments.....66

2-7. Schematic Illustration of the Information Content of 2D IR Spectra.....67

3-1. Illustration of 2D Spectra in both the Inhomogeneous and Homogeneous Dephasing Limits.....83

3-2. Comparison Between Correlation Metrics Derived from Model 2D Spectra and the Frequency-Frequency Correlation Function used to Generate the Spectra.....90

3-3. Evaluation of Inversion Relationships that Allow the Calculation of the Frequency-Frequency Correlation Function of a Measured Transition on the Basis of its 2D Spectrum.....91

3-4. Evaluation of Metrics that allow the Determination of Excited State Lifetimes on the Basis of the 2D Spectrum of the Probed Transition.....93

3-5. Comparison of Metrics that Characterize Spectral Diffusion in 2D IR Lineshapes of a Model Three Level System that Account for the Finite Duration of the Excitation Pulses used in a 2D IR Experiment.....95

4-1. Schematic of the Experimental Setup used for Nonlinear Vibrational Spectroscopy Experiments....107
4-2. Characterization of the Amplified Ti:Sapphire Laser Used to Generate Mid-Infrared Pulses....108
4-3. Characterization of the 3μm Mid-Infrared Pulses Generated by a Home Built BBO/$KNbO_3$ OPA....110
4-4. Illustration of the Mach-Zehnder Interferometer Used for Nonlinear Experiments as well as the Experimental Pulse Sequence and Sample Geometry....112
4-5. Procedure for the Calibration of Mechanical Delay Stages....117
4-6. Illustration of Two Pulse Vibrational Echo Signals Used to Correct Pulse Timing Errors....119
4-7. Comparison Between the Projection of a 2D IR Spectrum onto its ω_3 Axis and a Dispersed Pump-Probe Spectrum....121
4-8. Experimental Layouts for the Measurement of 2D IR Spectra....122
4-9. Demonstration of Balanced Signal Detection....124
4-10. Example 2D IR Spectrum Measured using Time/Frequency Scanning....126
4-11. Procedure for the Determination of the τ_3 Time Axis for a Rapidly Scanned Time Domain 2D IR Spectrum....129
4-12. Example 2D IR Spectrum Acquired the Time Domain using Rapid Scanning...131
5-1. The distribution of O-H Stretching Frequencies of Dilute HOD in D_2O and their Correlation to Dielectric Fluctuations of the Solvent....143
5-2. Cartoon Free Energy Surfaces that Represent Concerted and Stepwise Scenarios for Hydrogen Bond Exchange in Liquid Water....144
5-3. Experimental 2D IR Spectra of 1% HOD in D_2O....146
5-4. Metrics Tracking the Loss of Frequency Correlation of the O-H Stretch of HOD in D_2O....147
5-5. The First Moment of Slices Taken along the ω_3 Axis of the 2D IR Spectra of HOD in D_2O....148
5-6. IR and Raman Spectra of HOD in D_2O and the Empirical Transition Dipole Moment Extracted from their Comparison....151
5-7. The Influence of Non-Condon Effects on 1D and 2D Lineshapes....153

5-8. 2D IR Spectra Calculated from a Molecular Dynamics (MD) Simulation of Dilute HOD in D_2O.....155
5-9. The First Moment of ω_3 Slices of 2D IR Lineshapes and Frequency-Frequency Correlation Functions Calculated from MD Simulation.....156
5-10. Energetics of Hydrogen Bond Rearrangements on the basis of MD Simulation.....159
5-11. How the Frequency of the HOD Molecule Changes During Hydrogen Bond Exchange Events.....161
5-12. Free Energy Surface for Hydrogen Bond Exchange Calculated from MD Simulation.....162
5-13. Joint Probabilities for Angular Rotation of the HOD Molecule.....164
5-14. Simulated 2D Anisotropy Spectra of HOD in D_2O.....166
5-15. Comparison Between Experimental and Simulated 2D Anisotropy Spectra.....168
5-16. Snapshots from MD Simulation showing the Insertion of a Water Molecule Across a Hydrogen Bond.....170
5-A1. Simulated Joint Probability Distributions of the O-H Stretching Frequency of HOD in D_2O.....181
6-1. FT-IR spectra of ~1% HOD in Varying Concentrations of NaOD/D_2O.....194
6-2. Pump-Probe Decay Traces of Dilute HOD in NaOD/D_2O.....196
6-3. Transient Grating Data of HOD in NaOD/D_2O and KOD/D_2O.....197
6-4. Photon Echo Peak Shift Measurements of HOD in NaOD/D_2O for Waiting Times up to 1 ps.....198
6-5. Behavior of the Photon Echo Peak Shift for Waiting Times Between 1 ps and 10 ps.....200
6-6. 2D IR Spectra of Dilute HOD in NaOD/D_2O as a Function of NaOD Concentration.....202
6-7. Integrated Offdiagonal Intensity of the 2D IR Spectra.....204
6-8. Cartoon Illustrating how Vibrational Overtones of the O-H Stretching Potential may Contribute to 2D IR Measurements During Proton Transfer Events.....207
6-9. 2D IR Spectra of HOD in NaOD/D_2O Measured for Waiting Times Between 1 ps and 6 ps.....210

6-10. 2D Difference Spectra Highlighting the Growth of Intensity in the Offdiagonal Regions of the 2D IR Spectra with Increasing Waiting Time.....213
6-11. Illustration of the Growth of Cross Peaks in 2D IR Spectra due to Chemical Exchange.....215
6-12. Feynman Excitation Pathways that Describe Chemical Exchange.....219
6-13. Different Types of Exchange Processes in Aqueous Hydroxide Solutions.....222
6-14. Comparison Between Experimental FT-IR and Pump-Probe Data and Fits from our Spectral Model.....235
6-15. Comparison Between the Photon Echo Peak Shift Calculated using our Spectral Model and that Measured Experimentally.....238
6-16. Intensity of the Static Contribution to the Frequency-Frequency Correlation Function Determined from the Spectral Model.....240
6-17. Comparison Between Experimental and Calculated 2D IR Spectra.....244
6-18. Comparison of Spectra Calculated for Different Values of the Hydroxide Ion/Water Exchange Time Constant.....246
7-1. Empirical Charged Ring Model of the OH^- Ion.....270
7-2. Methodology used to Calculate Vibrational Frequencies from an Empirical Valence Bond Molecular Dynamics Simulation of Aqueous NaOH.....274
7-3. Comparison Between the Collective Electric Field and the Frequency of the v = 1←0 Vibrational Transition.....275
7-4. Solvent Coordinate Map used for the Calculation of the Frequency of the v = 1←0 Vibrational Transition.....277
7-5. Correlation Between Frequency and Structural Parameters in Aqueous NaOH Solution.....280
7-6. 1D Lineshapes Calculated from a Multistate Empirical Valence Bond Simulation (MS-EVB) of Aqueous NaOH.....282
7-7. Variation of the O-H Transition Dipole with Frequency and the Behavior of Vibrational Transitions of the O-H Stretch During Proton Transfer Events.....284
7-8. A Comparison Between Spectra Calculated from MS-EVB Simulation Extrapolated to High NaOD Concentration and Experimental NIR Spectra.....289
7-9. Feynman Diagrams For Dipole Forbidden Transitions.....293

7-10. Comparison of 2D IR Spectra Calculated for HOD/D_2O and for HOD Molecules Engaging in Proton Transfer....298
7-11. Integrated Offdiagonal Intensity of the Calculated 2D Spectra....299
7-12. Static Frequency Distribution and Absorption Spectra of the OH^- Ion....303
7-13. Calculated 2D IR Spectra Demonstrating Exchange between the OH^- and HOD Stretching Transitions Upon Proton Transfer....304
7-14. Growth of the Cross Peak Showing Exchange Between the OH^- and HOD Stretches....306
7-15. Average Number of Hydrogen Bonds Donated to the OH^- Ion During Proton Transfer Events....308
7-16. Average Frequencies and Transition Dipoles of the O-H Stretch During Proton Transfer....310
7-17. Time Scales for the Return of Vibrational Frequencies to their Equilibrium Values following Proton Transfer....311
7-18. Behavior of the Collective Electric Field During Proton Transfer....314
7-19. Solvation of the D_2O/OH^- Pair Following Proton Transfer....316
7-A1. Solvation Coordinate/Frequency Maps for ω_{20}, ω_{30}, and ω_{40}....329
7-A2. Comparison Between the Collective Electric Field Magnitude of the Derivative of the Electric Dipole Moment....330
7-A3. Empirical Maps for Transition Dipoles of the O-H Stretching Potential....332

List of Tables

6-1. Constraints for Spectral Fitting Parameters.....233

6-2. Relative Populations of Different Species in Aqueous NaOH.....236

6-B1. Best Fit Parameters that do not Vary as a Function of NaOD Concentration Obtained from our Spectral Model.....261

6-B2. Best Fit Parameters that do Vary as a Function of NaOD Concentration.....261

6-B3. Time Scales of Components and Initial Values of each of the Frequency-Frequency Correlation Functions used to Model Nonlinear Spectra of HOD in $NaOD/D_2O$.....261

6-B4. Amplitudes of Each of the Frequency-Frequency Correlation Function Components.....261

7-A1. Empirical Relationship Between ΔE_{DFT} and ΔE_{EVB}.....333

7-A2. Fitting Parameters Linking ΔE_{DFT} and each of the Vibrational Frequencies of the O-H Stretching Potential.....333

7-A3. Empirical Relationships Between the Transition Dipoles of the Fundamental and First Overtone Transitions of the O-H Stretching Potential and their Respective Frequencies.....333

7-A4. Empirical Mapping Parameters Allowing the Calculation of Various Transition Dipoles of the O-H Potential from μ_{10}.....333

Chapter 1

Introduction

1.1. Water is a Peculiar Liquid

While studying chemistry for the first time in high school, I remember being surprised to learn that water is considered a strange liquid. After all, among the large number of room temperature liquids, water is the one that everyone interacts with on a daily basis. For many, their day begins and ends with water, from a hot shower in the morning to brushing their teeth before bed, water is a part of everyone's daily routine. However, despite the omnipresence of water in the world around us, it possesses a number of anomalous properties that make it unique among liquids. Water expands when it freezes which causes ice cubes to float, becomes less viscous when compressed at room temperature, and possesses extremely high melting and boiling points for a molecule that consists of only three atoms. In addition to these well known thermodynamic peculiarities, water acts as an excellent solvent for many key chemical and biological processes, such as the folding of proteins into their native structures and electron transfer reactions that form a crucial part of cellular respiration.[1-3]

The reason that such a simple liquid can display such complex behavior arises from water's unique ability to accept and donate two hydrogen bonds. A hydrogen bond

is a weak electrostatic interaction formed between an electropositive hydrogen atom and an electronegative atom.[4] Although ~100 times weaker than a covalent bond, a hydrogen bond is ~10 stronger than other types of non-covalent interactions.[3] Whereas the structures of most liquids are shaped by repulsive forces that cause liquid molecules to organize in a manner resembling close packed spheres, the structure of water represents a fine balance between these repulsive forces and attractive hydrogen bonding interactions. The directionality of hydrogen bonds enables water to form an extended tetrahedral network of molecules,[5] the presence of which allows us to rationalize many of water's odd properties. Ice floats because in the solid phase the average spacing between molecules increases relative to the liquid to accommodate the formation of four hydrogen bonds. Water's high melting and boiling points are the result of the extra attractive hydrogen bonding interactions not present in other liquids that must be overcome to trigger a phase transition.

Water's hydrogen bonding network also enables chemical reactions to occur that are uniquely exclusive to water. The transport of excess protons and proton holes are arguably the most important members of this class of reactions, forming the heart of biological redox chemistry and energy conversion processes such as photosynthesis and cellular respiration.[6] It is well known that both the excess proton and the hydroxide ion display anomalously high diffusion rates compared to ions of similar size and charge density.[7] The explanation for the rapid structural diffusion of these ions is that they can utilize hydrogen bonds to accept or donate a proton, thereby leading to the translocation of the ion. This process is illustrated schematically in Fig. 1-1 and is often referred to as the Grotthuss mechanism in honor of Theodor Christian

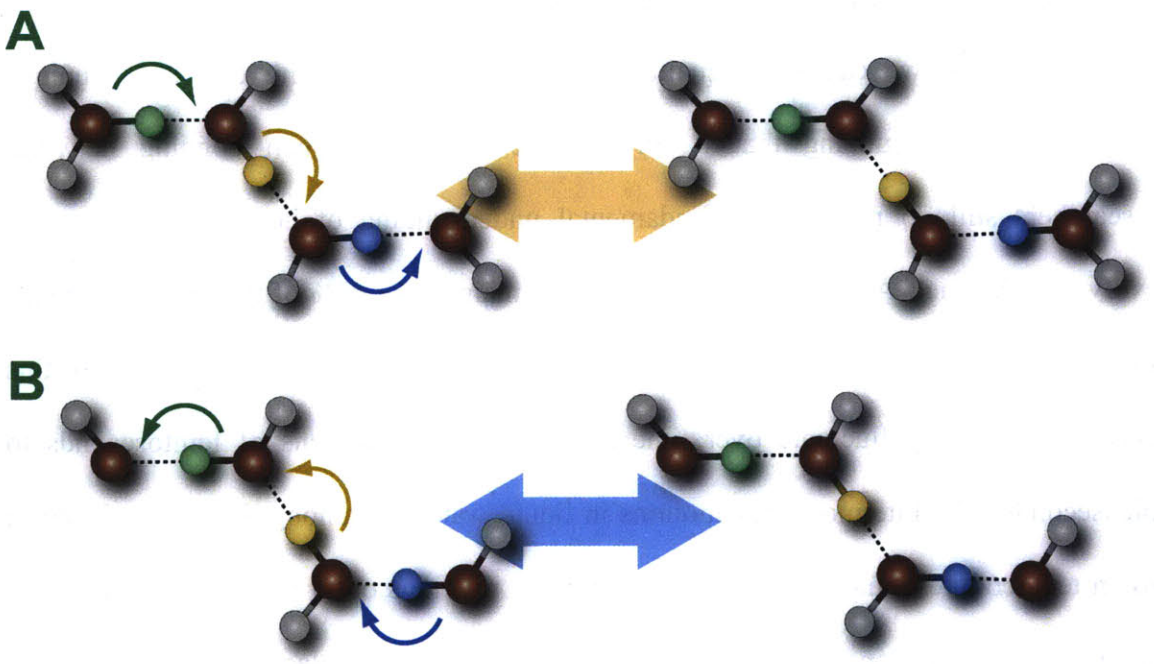


Figure 1-1: Simplified representations of Grotthuss proton hopping in the case of (A) the excess proton and (B) the hydroxide ion.

Johann Dietrich von Grotthuss who proposed that charge could be conducted through water without the displacement of individual water molecules as an explanation for the electrolysis of water in Volta's Galvanic cell.[8,9] This mechanism has often been invoked when describing proton transfer within protein molecules. Excess protons can transfer between amino acid residues or through trans-membrane protein channels by making use of "water wires", chains of hydrogen bonded water molecules that can serve as scaffolding for the motion of an excess proton.[6,10] On the basis of proton mobility data, an activation barrier of 2-3 kcal/mol has been estimated for the structural diffusion of the excess proton.[11] Given estimates of the strength of a hydrogen bond in water (5-6 kcal/mol),[12] this is suggestive that hydrogen bond rearrangements play a role in guiding the proton's motion.[13]

1.2. Water's Fluctuations make it Difficult to Characterize

Although we can build qualitative explanations for many of water's unique properties by recognizing that it forms an extended hydrogen bonding network, researchers still do not have a fundamental understanding of how water's structure evolves with time. At room temperature, water maintains ~90% of the hydrogen bonds formed in ice,[2,14] yet the weak nature of hydrogen bonds allows the connectivity of this network to rapidly fluctuate over time scales ranging from tens of femtoseconds to picoseconds.[15-17] Intermolecular motions in liquid water are among the fastest found in room temperature liquids. Librations or hindered rotations occur on a ~50 fs time scale whereas hydrogen bond stretching and O··O··O bending take place on 180 and 550 fs time scales respectively.[15] The pliability of water's hydrogen bonding network forms the heart of aqueous reactivity, permitting water to rapidly respond to changes in the charge distribution of solutes during the course of chemical reactions.[18] However, these rapid motions also make it difficult to build a model that can fully describe the time dependent evolution of the liquid. The mechanism by which a given water molecule breaks a hydrogen bond to form one with a new partner remains an open question.

Even less understood than the mechanism that guides water's hydrogen bond rearrangements is how the fluctuations of water's hydrogen bonding network act to guide the motion of a proton from one water molecule to another. Although simplistic pictures such as Fig. 1-1 allow us to rationalize the enhanced structural diffusion of protons and proton holes in water, it is unclear from the figure what serves as the driving force for the motion of the proton. Water is a polar liquid, and one might hypothesize that the same type of dielectric fluctuations invoked by Marcus theory[19,20] to describe electron transfer

will also play a major role in guiding the motion of excess protons and proton holes. However, a full description of the transport mechanism must also account for the fact that both hydronium and hydroxide ions represent charged defects in water's hydrogen bonding network. Neutron scattering measurements[21,22] and molecular dynamics (MD) simulations[23,24] have shown that both the hydronium and hydroxide ions possess asymmetric solvation shells that are distinct from that of a water molecule. Hence, the transport of a proton to or from each of these ions must also involve a rearrangement of waters around the molecule that is to accept or donate a proton to the ion as well as a reincorporation of the nascent molecule formed by the reaction back into water's hydrogen bonding network. Such processes require the concerted motion of multiple water molecules in the solvation shells of these ions, making the determination of an appropriate reaction coordinate that can describe proton transfer difficult indeed.

1.3. Understanding Water Requires Understanding its Dynamics

Numerous structural descriptions of liquid water have been posited based on decades of experiments and theoretical investigations. Broadly speaking, many of these proposals can be labeled as either continuum models, which assume that liquid water is comprised of a continuous distribution of hydrogen bonded configurations, or mixture models, which instead suggest that two or more distinct hydrogen bonding species are present in liquid water.[2] However, a strict description of water within the context of either of these two types of models is misleading since both are largely defined in static terms. By neglecting dynamics, these models neglect that only small barriers separate different hydrogen bonding configurations in the liquid and that thermal fluctuations at

room temperature have sufficient energy to drive large, rapid changes in the liquid's structure.

Since water cannot be well characterized by instantaneous snapshots of the liquid, this raises the question of what constitutes an appropriate criterion for the definition of a hydrogen bond. Hydrogen bonds are often identified in MD simulations on the basis of instantaneous geometric or energetic criteria,[25-27] such as the distance between the oxygen atoms of two neighboring water molecules and an angle describing their mutual orientation. However a hydrogen bond definition based solely on instantaneous parameters cannot differentiate between the breakage of a hydrogen bond and a large amplitude but ultimately transient excursion about a stable hydrogen bonded state. The same questions are equally applicable to proton transfer reactions. If the barriers for proton transfer are sufficiently small, do isolated hydronium and hydroxide ions exist in acidic or basic solution? Is it more accurate to describe these ions as being spread over multiple water molecules, as $H_5O_2^+$ or $H_3O_2^-$, or possibly even larger ions?

Instead of focusing on a static description of the liquid, an adequate picture of water needs to include a description of both the liquid's stable configurations and the characteristic time dependent fluctuations within these configurations.[28] Building such a description is a substantial challenge because the motion of an individual water molecule is coupled to the behavior of its neighbors. MD simulations provide evidence that suggests that the breakage of a hydrogen bond is not a localized event, but requires the correlated motion of many water molecules. Calculation of inherent structures of water,[28] configurations that correspond to minima of the potential energy surface of the liquid, have shown that large collective motions involving the displacement of many molecules

are necessary to move from one inherent structure to the next.[16,29] Recently, Laage and Hynes[30-32] have shown that in SPC/E water, a commonly used water simulation model, hydrogen bond exchange events are correlated with a number of changes in the solvation shell of the exchanging molecule. Leading up to the exchange, the new hydrogen bond acceptor becomes under-coordinated as the original hydrogen bond acceptor becomes over-coordinated, suggesting that density fluctuations may play a role in hydrogen bond rearrangements.

The transport of protons and proton holes in water are also guided by collective motions of the liquid. Zundel[33,34] hypothesized that fluctuations of the solvent polarization in the vicinity of excess protons can serve as a means of guiding their structural diffusion. More recently, Lapid et al. [23] showed that the transport of the excess proton in water can be affected by the formation and breakage of hydrogen bonds as far away as the second solvation shell of the excess proton. Petersen, Hatt, and Voth[35] found that in an empirical valence bond model that describes transport of the hydronium ion (H_3O^+) the time scale for the ion to donate a proton to a neighboring water molecule matches that for the breakage of a hydrogen bond. In the case of the hydroxide ion, it has been suggested that changes in the solvation shell size of the ion plays a crucial role in regulating its ability to accept a proton from a hydrogen bonded partner.[24,36]

It is clear from these observations that instead of asking questions regarding water's structure, a better characterization of the liquid can be gained by asking what is an appropriate interaction length for water. In other words, over what distance do the motions of two water molecules remain correlated and what is the mechanism that generates this correlation? The same questions can be asked with regards to proton

diffusion in liquid water. To what extent is the motion of the excess proton or proton hole dependent on the motions of individual water molecules near the charge defect? How do the fluctuations of the surrounding liquid guide the motion of the charge defect through the liquid? Clearly, hydrogen bonding will play a strong role in answering each of these questions.

1.4. Experimental Probes of Water's Time Dependent Structure

Much of the scientific discussion regarding water's structure has focused on static descriptions of the liquid because very few of the experimental probes exist that can directly measure its dynamics. X-ray and neutron scattering measure the average arrangement of molecules on molecular length scales, but are only slightly sensitive to time dependent changes in the liquids structure.[14,37] Dielectric relaxation and nuclear magnetic resonance dipolar relaxation experiments can be modeled to provide an average reorientation time scale for water molecules, but they are not structurally sensitive and do not directly observe these motions.[38] Typical ultrafast techniques, such as electronic solvation dynamics experiments[18,39] and optical Kerr effect measurements[15,40,41] possess femtosecond time resolution, but lack sensitivity to water's hydrogen bonding structure.

Time resolved ultrafast infrared spectroscopy can surmount many of these experimental shortcomings since water's O-H stretching frequency is highly sensitive to its local environment. To avoid complications due to the inter- and intramolecular coupling of nearly degenerate oscillators, many experimentalists have chosen to investigate dilute solutions of HOD dissolved in D_2O (Fig. 1-2A). The O-H stretching transition of such a solution is broad (~260 cm^{-1} FWHM) due to the large distribution of hydrogen bonding geometries present in the liquid. Given an accurate map between

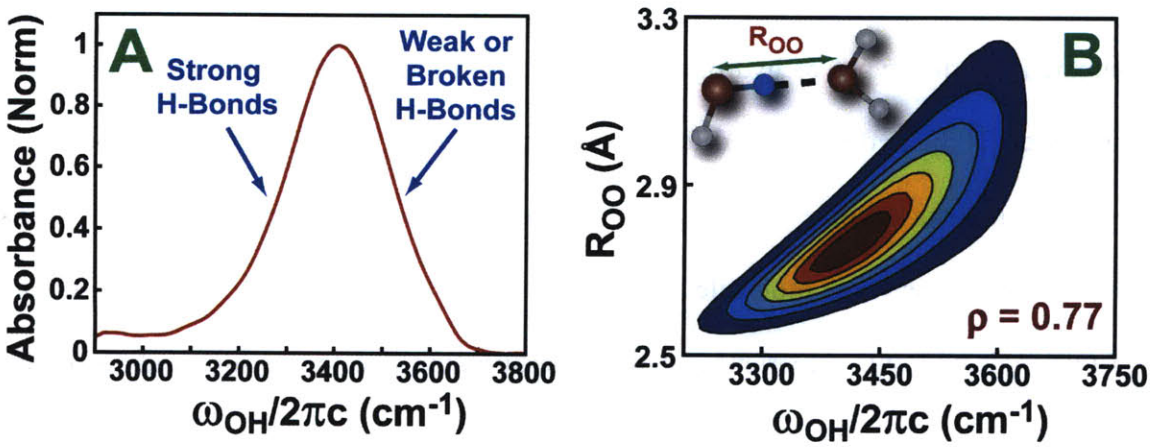


Figure 1-2: (A) Infrared absorption spectrum of ~1% HOD in D_2O. (B) Joint probability distribution between ω_{OH} and ROO calculated from MD simulation. From Ref. 42.

structure and O-H frequency, we can monitor time-dependent changes in water's hydrogen bonding structure by exciting the HOD molecules' O-H stretching transition with a series of temporally short infrared pulses and then watching how the frequencies of excited molecules evolve with time.

Measurements of infrared spectra of hydrogen bonding crystals have established that a correlation exists between the frequency of an O-H stretching transition, ω_{OH}, and R_{OO}, the distance separating the two oxygen atoms of the hydrogen bond donor and acceptor.[43-45] The correlation between ω_{OH} and the strength of a hydrogen bond can be understood by recognizing that the formation of a hydrogen bond adds an attractive force that pulls on the O-H stretching potential, causing it to broaden and thereby decreasing ω_{OH}. MD simulations using mixed quantum-classical approaches[17,42,46,47] have established that the correlation between ω_{OH} and R_{OO} is preserved in liquid water (Fig. 1-2B).

While a hydrogen bond formed between two water molecules is very weak compared to other types of hydrogen bonds present in other systems such as carboxylic acid dimers,[48] the hydrogen bond formed between a water molecule and a hydronium or hydroxide ion can become so strong that the hydrogen bonding proton becomes equally shared between the water molecule and the ion. Whereas the O-H stretching potential for a HOD molecule only experiences a weak perturbation due to the surrounding solvent that results in a decrease of ω_{OH} by ~300 cm^{-1} relative to its gas phase value (3707 cm^{-1}),[49] the O-H stretching potential of a proton that participates in a hydrogen bond with either a hydronium or hydroxide ion can be highly altered. In the extreme case of an equally shared proton, the O-H stretching potential resembles a double well with a low or even non-existent barrier[50] and ω_{OH} can reach values as low as 600-700 cm^{-1}![51] In the liquid phase, a large distribution of different shared proton states are present, causing concentrated acids[33,34,52] and bases[53] to have a very characteristic absorption continua that ranges from low frequency up to the edge of the water O-H stretching transition (Fig. 1-3). Zundel suggested that the absorption continua could be explained by the modulation of the shared proton stretching potentials of $H_5O_2^+$ and $H_3O_2^-$ ions by polarization fluctuations of the surrounding solvent, and used the existence of this spectral feature to argue that $H_5O_2^+$ and $H_3O_2^-$ are the dominant species present in concentrated acids and bases.[33,34] Simulations of model $A\cdot\cdot H^+\cdot\cdot A$ systems[54,55] support this conclusion, and show that electric field fluctuations can lead to absorption bands covering a broad spectral range. Since water's dielectric fluctuations are intimately tied to the collective motions of water molecules, the large breath of this absorption feature may be related to water's rapid intermolecular dynamics. This absorption continua is also present in solutions of

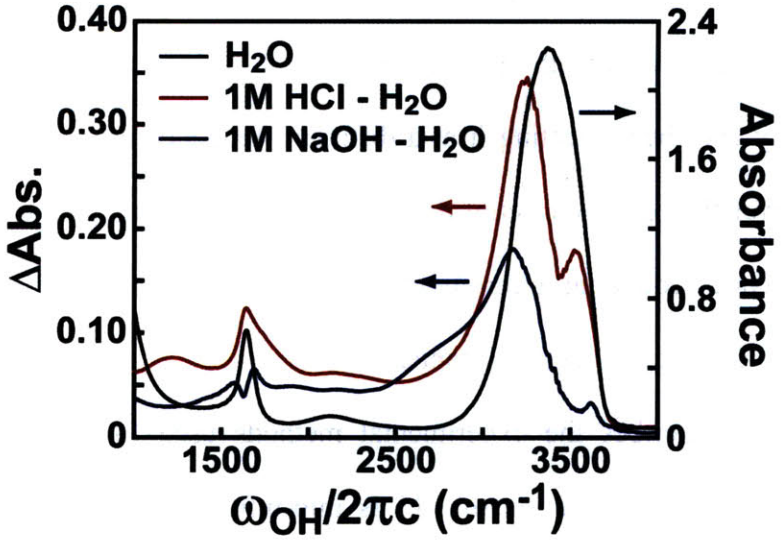


Figure 1-3: Infrared absorption spectrum of H_2O and absorption spectra of 1M HCl and NaOH solutions with the H_2O background removed in order to highlight changes to the water spectrum upon the addition of acid or base.

dilute HOD dissolved in DCl/D_2O or $NaOD/D_2O$.[56-59] Just as in the case of dilute HOD in D_2O, we can use femtosecond infrared pulses to track the changes in ω_{OH} across this broad spectral range to infer how fluctuations in the hydrogen bonding environment around shared protons allow them to form a stable covalent bond.

1.5. Thesis Outline

In this thesis I present the results of several ultrafast spectroscopic investigations of water and aqueous hydroxide solutions that provide insight into how water's hydrogen bonding network rearranges on femtosecond time scales and how these rearrangements let the aqueous hydroxide ion accept a proton from one of its hydrogen bonding partners. Chapter 2 serves as a brief introduction to nonlinear spectroscopy. In this chapter I use perturbation theory to derive expressions for the calculation of nonlinear signals within a number of different useful approximations. In particular, this chapter provides a

description of two-dimensional infrared spectroscopy (2D IR), a correlation technique whose observable is related to the joint probability of exciting a molecule with a given initial frequency and then detecting it at a different frequency after a set waiting time. The loss of correlation due to spectral diffusion, frequency shifts due to changes in the local environment surrounding a chromophore, can be quantified through a number of simple metrics that are developed in Chapter 3.

Chapter 4 describes the experimental methods used for the measurement of nonlinear signals. The generation of ~45 fs mid-infrared pulses using a home-built optical parametric amplifier[60] is described as well as the creation of variable delays between these pulses using a five beam Mach-Zehnder interferometer. Collection schemes for pump-probe, three pulse photon echo peak shift, transient grating, and 2D IR experiments are described. This chapter concludes with a description of a novel collection scheme that enables the rapid collection of 2D spectra entirely in the time domain that uses a HeNe reference to determine one of the two time axes that comprise a 2D spectrum.

The results of experiments and MD simulations that describe how water's intermolecular dynamics lead to rearrangements of the liquid's structure appear in Chapter 5. Experimental 2D IR spectra display a pronounced asymmetry with increasing waiting time. This asymmetric broadening shows that broken hydrogen bonded states do not comprise a stable minimum on water's free energy surface. The time scale over which this asymmetric broadening occurs suggests that hydrogen bond rearrangements are primarily driven by librations. MD simulations find that the transition state for hydrogen bond exchange in liquid water resembles a bifurcated hydrogen bond. The total

exchange process resembles the insertion of a water molecule across a hydrogen bond and can involve the correlated motion of waters as far away as the second solvation shell of the exchanging molecule.

Chapters 6 and 7 describe experiments and simulations that examine the dynamics of aqueous hydroxide solutions. Pump-probe and 2D IR measurements show the presence of a broad spectral feature that decays with a 110 fs time scale. The calculation of spectra from a multistate empirical valence bond simulation model (MS-EVB) of aqueous sodium hydroxide shows that this feature is a spectral signature characteristic of a proton that is equally shared within a transiently formed $DO\cdot\cdot H\cdot\cdot OD^-$ ion that represents the transition state for proton transfer. Calculations based on the MS-EVB model argue that the collective electric field due to the surrounding solvent projected along the proton transfer direction is an appropriate coordinate to describe the creation and relaxation of these shared proton states. Although the motion of the proton appears to be directed by dielectric fluctuations of the solvent in the vicinity of the shared proton, the proton transfer reaction is not complete until the newly formed water molecule and hydroxide ion are fully solvated by the surrounding water bath. This process is found to occur on a time scale of ~7.5 ps on the basis of the MS-EVB simulation, and involves the formation of an asymmetric solvation shell around the newly formed hydroxide ion. This solvation process may serve as a microscopic explanation for the large rise in solution viscosity[61] that occurs with increasing hydroxide ion concentration.

References

(1) *Water - A Comprehensive Treatise* edited by F. Franks, (Plenum, New York, 1972-1982).

(2) D. Eisenberg and W. Kauzmann, *The Structure and Properties of Water*, (Clarendon Press, Oxford, 1969).

(3) P. Ball, *Life's Matrix: A Biography of Water*, (University of California Press, Berkeley, CA, 2001).

(4) L. Pauling, "The Structure of water," in *Hydrogen Bonding: Papers Presented at the Symposium on Hydrogen Bonding (1957; Slovenia)*, edited by D. Hadzi, (Pergamon Press, New York, 1959).

(5) F. H. Stillinger, "Water revisited," Science 209, 451 (1980).

(6) P. Ball, "Water as an active constituent in cell biology," Chem. Rev. 108, 74 (2008).

(7) P. Atkins, *Physical Chemistry*, 6th, (Oxford University Press, Oxford, U.K., 1997).

(8) C. J. T. d. Grotthuss, "Sur la décomposition de l'eau et des corps qu'elle tient en dissolution à l'aide de l'électricité galvanique," Ann. Chim. LVIII, 54 (1806).

(9) C. J. T. d. Grotthuss, "Memoir on the decomposition of water and of the bodies that it holds in solution by means of galvanic electricity," Biochim. Biophys. Acta 1757, 871 (2006).

(10) R. Pomes and B. Roux, "Molecular mechanism of H^+ conduction in the single-file water chain of the gramicidin channel," Biophys. J 82, 2304 (2002).

(11) R. A. Robinson and R. H. Stokes, *Electrolyte Solutions*, 2nd Revised Ed., (Dover, Mineola, N.Y., 1959).

(12) S. J. Suresh and V. M. Naik, "Hydrogen bond thermodynamic properties of water from dielectric constant data," J. Chem. Phys. 113, 9727 (2000).

(13) N. Agmon, "The Grotthuss mechanism," Chem. Phys. Lett. 244, 456 (1995).

(14) T. Head-Gordon and G. Hura, "Water structure from scattering experiments and simulation," Chem. Rev. 102, 2651 (2002).

(15) E. W. Castner, Jr., Y. J. Chang, Y. C. Chu and G. E. Walrafen, "The intermolecular dynamics of liquid water," J. Chem. Phys. 102, 653 (1995).

(16) I. Ohmine, "Liquid water dynamics: Collective motions, fluctuation, and relaxation," J. Phys. Chem. 99, 6767 (1995).

(17) C. J. Fecko, J. D. Eaves, J. J. Loparo, A. Tokmakoff and P. L. Geissler, "Ultrafast hydrogen bond dynamics in the infrared spectroscopy of water," Science 301, 1698 (2003).

(18) R. Jimenez, G. R. Fleming, P. V. Kumar and M. Maroncelli, "Femtosecond solvation dynamics of water," Nature 369, 471 (1994).

(19) R. A. Marcus, "On the theory of oxidation-reduction reactions involving electron transfer. I," J. Chem. Phys. 24, 966 (1956).

(20) R. A. Marcus and N. Sutin, "Electron transfers in chemistry and biology," Biochim. Biophys. Acta 811, 265 (1985).

(21) A. Botti, F. Bruni, S. Imberti, M. A. Ricci and A. K. Soper, "Ions in water: The microscopic structure of a concentrated HCl solution," J. Chem. Phys. 121, 7840 (2004).

(22) A. Botti, F. Bruni, S. Imberti, M. A. Ricci and A. K. Soper, "Ions in water: The microscopic structure of concentrated NaOH solutions," J. Chem. Phys. 120, 10154 (2004).

(23) H. Lapid, N. Agmon, M. K. Petersen and G. A. Voth, "A bond-order analysis of the mechanism for hydrated proton mobility in liquid water," J. Chem. Phys. 122, 014506 (2005).

(24) M. E. Tuckerman, A. Chandra and D. Marx, "Structure and dynamics of OH^- (aq)," Acc. Chem. Res. 39, 151 (2006).

(25) A. Rahman and F. H. Stillinger, "Molecular dynamics study of liquid water," J. Chem. Phys. 55, 3336 (1971).

(26) A. Luzar and D. Chandler, "Effect of environment on hydrogen bond dynamics in liquid water," Phys. Rev. Lett. 76, 928 (1996).

(27) R. Kumar, J. R. Schmidt and J.L.Skinner, "Hydrogen bonding definitions and dynamics in liquid water," J. Chem. Phys. 126, 204107 (2007).

(28) F. H. Stillinger and T. A. Weber, "Inherent structure in water," J. Phys. Chem. 87, 2833 (1983).

(29) I. Ohmine and S. Saito, "Water dynamics: fluctuation, relaxation, and chemical reactions in hydrogen bond network rearrangement," Acc. Chem. Res. 32, 741 (1999).

(30) D. Laage and J. T. Hynes, "A molecular jump mechanism of water reorientation," Science 311, 833 (2006).

(31) D. Laage and J. T. Hynes, "Do more strongly hydrogen-bonded water molecules reorient more slowly?," Chem. Phys. Lett. 433, 80 (2006).

(32) D. Laage and J. T. Hynes, "On the molecular mechanism of water reorientation," J. Phys. Chem. B 112, 14230 (2008).

(33) G. Zundel, "Hydrogen bonds with large proton polarizability and proton transfer processes in electrochemistry and biology," Adv. Chem. Phys. 111, 1 (2000).

(34) G. Zundel, in *The Hydrogen Bond: Recent Developments in Theory and Experiment, Vol. II*, edited by P. Schuster, G. Zundel and C. Sandorfy, (North Holland, Amsterdam, 1976).

(35) M. K. Petersen, A. J. Hatt and G. A. Voth, "Orientational dynamics of water in the nafion polymer electrolyte membrane and its relationship to proton transport," J. Phys. Chem. B 112, 7754 (2008).

(36) A. Chandra, M. E. Tuckerman and D. Marx, "Connecting solvation shell structure to proton transport kinetics in hydrogen-bonded networks via population correlation functions," Phys. Rev. Lett. 99, 145901 (2007).

(37) A. K. Soper, "The radial distribution functions of water and ice from 220 to 673 K and at pressures up to 400 MPa," Chem. Phys. 258, 121 (2000).

(38) D. W. G. Smith and J. G. Powles, "Proton spin-lattice relaxation in liquid water and liquid ammonia," Mol. Phys. 10, 451 (1966).

(39) W. Jarzeba, G. C. Walker, A. E. Johnson, M. A. Kahlow and P. F. Barbara, "Femtosecond microscopic solvation dynamics of aqueous solutions," J. Phys. Chem. 92, 7039 (1988).

(40) S. Palese, L. Schilling, R. J. D. Miller, P. R. Staver and W. T. Lotshaw, "Femtosecond optical Kerr effect studies of water," J. Phys. Chem. 98, 6308 (1994).

(41) C. J. Fecko, J. D. Eaves and A. Tokmakoff, "Isotropic and anisotropic Raman scattering from molecular liquids measured by spatially masked optical Kerr effect spectroscopy," J. Chem. Phys. 117, 1139 (2002).

(42) J. D. Eaves, A. Tokmakoff and P. Geissler, "Electric field fluctuations drive vibrational dephasing in water," J. Phys. Chem. A 109, 9424 (2005).

(43) R. M. Badger, "The relation between the internuclear distances and force constants of molecules and its application to polyatomic molecules," J. Chem. Phys. 3, 710 (1935).

(44) R. M. Badger, "The relation between the energy of a hydrogen bond and the frequencies of the O-H bands," J. Chem. Phys. 8, 288 (1940).

(45) A. Novak, "Hydrogen bonding in solids. Correlation of spectroscopic and crystallographic data," in *Structure and Bonding*, edited by J. D. Dunitz et al., (Springer-Verlag, New York, 1974).

(46) R. Rey, K. B. Møller and J. T. Hynes, "Hydrogen bond dynamics in water and ultrafast infrared spectroscopy," J. Phys. Chem. A 106, 11993 (2002).

(47) C. P. Lawrence and J. L. Skinner, "Vibrational spectroscopy of HOD in D_2O. III. Spectral diffusion, and hydrogen-bonding and rotational dynamics," J. Chem. Phys. 118, 264 (2003).

(48) E. T. J. Nibbering and T. Elsaesser, "Ultrafast vibrational dynamics of hydrogen bonds in the condensed phase," Chem. Rev. 104, 1887 (2004).

(49) L. S. Rothman, C. P. Rinsland, A. Goldman, S. T. Massie, D. P. Edwards, J.-M. Flaud, A. Perrin, C. Camy-peyret, V. Dana, J.-Y. Mandin, J. Schroeder, A. McCann, R. R. Gamache, R. B. Wattson, K. Yoshino, K. V. Chance, K. W. Jucks, L. R. Brown, V. Nemtchinov and P. Varanasi, "The HITRAN molecular spectroscopic database and hawks (HITRAN atmospheric workstation): 1996 edition," J. Quant. Spectrosc. Radiat. Transfer 60, 665 (1998).

(50) C. C. M. Samson and W. Klopper, "*Ab initio* claculation of proton barrier and binding energy of the $(H_2O)OH^-$ complex," J. Mol. Struct. THEOCHEM 586, 201 (2002).

(51) E. G. Diken, J. M. Headrick, J. R. Roscioli, J. C. Bopp, M. A. Johnson and A. B. McCoy, "Fundamental excitations of the shared proton in the $H_3O_2^-$ and $H_5O_2^+$ complexes," J. Phys. Chem. A 109, 1487 (2005).

(52) J. Kim, U. Schmitt, J. Greutzmacher, G. A. Voth and N. E. Scherer, "The vibrational spectrum of the hydrated proton: Comparison of experiment, simulation, and normal mode analysis," J. Chem. Phys. 116, 737 (2002).

(53) D. Schiöberg and G. Zundel, "Very polarizable hydrogen bonds in solutions of bases having infra-red absorption continua," J. Chem. Soc., Faraday Trans. 2 69, 771 (1973).

(54) D. Borgis, G. Tarjus and H. Azzouz, "An adiabatic dynamical simulation study of the Zundel polarization of H-bonded complexes in solution," J. Chem. Phys. 97, 1390 (1992).

(55) G. Hanna and E. Geva, "Computational study of the one and two dimensional infrared spectra of a vibrational mode strongly coupled to its environment: Beyond the Cumulant and Condon approximations," J. Phys. Chem. B 114, 12991 (2008).

(56) H.-K. Nienhuys, A. J. Lock, R. A. v. Santen and H. J. Bakker, "Dynamics of water molecules in an alkaline environment," J. Chem. Phys. 117, 8021 (2002).

(57) M. Śmiechowski and J. Stangret, "Proton hydration in aqueous solution: Fourier transfrom infrared studies of HDO spectra," J. Chem. Phys. 125, 204508 (2006).

(58) M. Śmiechowski and J. Stangret, "Hydroxide ion hydration in aqueous solutions," J. Phys. Chem. A 111, 2889 (2007).

(59) S. T. Roberts, P. B. Petersen, K. Ramasesha, A. Tokmakoff, I. S. Ufimtsev and T. J. Martinez, "Observation of a Zundel-like transition state during proton transfer in aqueous hydroxide solutions," Proc. Natl. Acad. Sci. U.S.A. 106, 15154 (2009).

(60) C. J. Fecko, J. J. Loparo and A. Tokmakoff, "Generation of 45 femtosecond pulses at 3 μm with a $KNbO_3$ optical parametric amplifier," Opt. Commun. 241, 521 (2004).

(61) "Concentrative properties of aqueous solutions: Density, refractive index, freezing point depression, and viscosity," in *CRC Handbook of Chemistry and Physics*, edited by D. R. Lide, 89th, (CRC Press/Taylor and Francis, Boca Raton, FL, 2009).

Chapter 2

An Introduction to Nonlinear Vibrational Spectroscopy and the Calculation of Third-Order Signals

2.1. Introduction

Nonlinear vibrational spectroscopy is a powerful tool that can be used to characterize fluctuations in complex liquid systems. Linear spectroscopies, such as absorption or reflection, are primarily sensitive to the distribution of vibrational eigenstates of a system. By introducing short time delays between subsequent field-matter interactions, nonlinear spectroscopy can be used to excite and track time dependent changes in the set of frequencies associated with the vibrational transitions of the system. Measurement of these time dependent shifts, or spectral diffusion, can be used to infer the dynamic changes in the surrounding liquid that give rise to these frequency shifts.[1,2] Additionally, kinetic processes such as the transfer of vibrational energy between oscillators[3] or the exchange of molecules from one liquid environment to another[4] can be observed using nonlinear spectroscopy. Unfortunately, the relationship between the spectroscopic observables that are measured in a nonlinear experiment and the underlying dynamics of the system is not simple. A methodology is required to relate

these quantities and to allow the extraction of meaningful parameters from experiment that can be used to describe the time evolution of the system under study.

The experiments described in this thesis fall under the general heading of four-wave mixing spectroscopies. In a four-wave mixing experiment, three separate light fields interact with a sample, creating a nonlinear polarization that then radiates a signal field. Characterization of the emitted field can be used to infer different properties of the system, including how long molecules remain vibrationally excited, how long it takes them to reorient, and how long before they exchange liquid environments. Various types of four-wave mixing experiments have different sensitivities to each of these properties. Pump-probe and transient grating measurements primarily report on vibrational population dynamics and the orientational relaxation of excited molecules, whereas photon echo peak shift experiments can be used to track the spectral diffusion of excited oscillators.[1] Arguably the most powerful among these techniques is two dimensional infrared spectroscopy (2D IR), which provides a full characterization of the amplitude and phase of the emitted signal field.[5-8] The frequency domain representation of a 2D IR spectrum is related to the joint probability of exciting a particular vibration at a given initial frequency, ω_1, and then detecting it at a frequency, ω_3, after a fixed waiting period, τ_2. 2D IR spectra detected as a function of τ_2 can be used to separate different subpopulations that reside under a congested 1D lineshape based on how their dynamics vary as a function of time. If these subpopulations have different spectral signatures, 2D IR can also be used to observe their exchange through the appearance of cross peaks in the 2D spectrum.[4,9]

The goal of this chapter is to provide a brief introduction to third-order nonlinear spectroscopy within the confines of time-dependent perturbation theory. Equations that can be used to calculate third-order signals based on experimentally measurable input parameters or from the results of molecular dynamics (MD) simulations will be described as well as the key approximations in their derivation. In particular, the development of methods for the calculation of nonlinear signals on the basis of classical MD simulations[7,8] is a powerful approach to the interpretation of nonlinear experiments since it allows us to build a direct connection between the experimental signals that we measure and the microscopic system dynamics responsible for their generation. These equations will be used in Chapters 5-7 to calculate third-order signals for the O-H stretching transition of the HOD molecule in both D_2O and NaOD solution. This chapter will conclude by providing a brief introduction to different experimental third-order techniques. While a full description of the measurement of nonlinear signals will be reserved for Chapter 4, the sensitivity of each technique to liquid dynamics is discussed.

2.2. The Third-order Polarization

In a nonlinear spectroscopy experiment, a series of input electric fields act to create a macroscopic polarization within a sample that then radiates a signal field. To describe the process by which this signal field is generated, we define a Hamiltonian for the total system:

$$H_{total}(t) = H_{liquid} + H_{light} + H_{int}(t). \tag{2-1}$$

H_{liquid} describes the behavior of the liquid in the absence of an external electric field and includes the internal degrees of freedom of each individual molecule as well as their intermolecular interactions. H_{light} is the Hamiltonian for each laser pulse external to the

liquid, while H_{int} describes the interaction between each electromagnetic field and the liquid. When describing the liquid, we make a separation between the degrees of freedom that interact with the light field, the system, and those that do not, the bath. This allows us to write H_{liquid} as:

$$H_{liquid} = H_S(\mathbf{P},\mathbf{Q}) + H_B(\mathbf{p},\mathbf{q}) + H_{SB}(\mathbf{P},\mathbf{Q},\mathbf{p},\mathbf{q}) \tag{2-2}$$

where **Q** and **P** denote the positions and momenta of the set of system coordinates, while **q** and **p** refer to those of the bath.*

Since we are primarily concerned with the dynamics of the liquid and spontaneous emission does not contribute to the signal fields that are measured in coherent third-order experiments, we can neglect H_{field} in Eq. 2-1. In water, the characteristic field-matter interaction length scales are on the order of Angströms, which is much smaller than the wavelengths of the infrared probing light (microns). This allows us to make the electric dipole approximation, which allows us to treat each molecule as a point dipole in a time dependent electric field.[10] Thus, we can write H_{int} simply as:

$$H_{int}(t) = -\boldsymbol{\mu}(\mathbf{Q},\mathbf{q},t)\bullet\mathbf{E}(\mathbf{r},t) \tag{2-3}$$

where $\boldsymbol{\mu}(\mathbf{Q},\mathbf{q},t)$ is the dipole moment operator that depends on the both the microscopic degrees of freedom of the system and the bath and:

$$\mathbf{E}(\mathbf{r},t) = \varepsilon(\mathbf{r})\exp\left[i\left(\mathbf{k}\bullet\mathbf{r} - \omega(t-t_o)\right)\right] + c.c. \tag{2-4}$$

is the external field strength at position **r** and time t.

The macroscopic polarization generated by the interaction of each of the input external fields and the system serves as a source term for the nonlinear signal field that is

* Throughout this chapter and in the remainder of this thesis, vector quantities will be represented using bold type.

measured during a four-wave mixing experiment. The total polarization of the sample is given by the expectation value of the dipole operator:

$$\mathbf{P}(\mathbf{r},t) = Tr\left[\boldsymbol{\mu}(\mathbf{Q},\mathbf{q},t)\rho(t)\right], \tag{2-5}$$

where $\rho(t)$ denotes the density matrix of the system. The time dependence of the density matrix is given by the Liouville-von Neumann equation:

$$i\hbar\frac{\partial\rho(t)}{\partial t} = \left[H_{total}(t),\rho(t)\right]. \tag{2-6}$$

We can simplify Eq. 2-6 by making the substitution $\rho_I(t) = e^{-iH_{liquid}t}\rho(t)e^{iH_{liquid}t}$. Upon making this substitution and inserting Eq. 2-1 into Eq. 2-6, we obtain:

$$i\hbar\frac{\partial\rho_I(t)}{\partial t} = \left[H_{int}(t),\rho_I(t)\right]. \tag{2-7}$$

We can obtain a solution for $\rho_I(t)$ by integrating both sides of Eq. 2-7 with respect to time:

$$i\hbar\rho_I(t) = \int_{-\infty}^{t} dt'\left[H_{int}(t'),\rho_I(t')\right] \tag{2-8}$$

By inserting the right side of Eq. 2-8 back into Eq. 2-7 and integrating iteratively, we can develop a perturbative series for the density matrix:

$$\rho_I(t) = \sum_{n=0}^{\infty}\rho_I^{(n)}(t), \tag{2-9}$$

where each term is given by:

$$\rho_I^{(n)}(t) = \left(\frac{1}{i\hbar}\right)^n \int_{-\infty}^{t} dt'_n \int_{-\infty}^{t'_n} dt'_{n-1} \ldots \int_{-\infty}^{t'_1} dt'_1\left[H_{int}(t'_n),\left[H_{int}(t'_{n-1}),\ldots\left[H_{int}(t'_o),\rho_I(-\infty)\right]\right]\right]. \tag{2-10}$$

In Eq. 2-10, each time point, t'_n, represents a time-ordered point of interaction with an external electromagnetic field. Substitution of this solution for the density matrix into Eq.

2-5 yields a similar pertrubative solution for the polarization where each subsequent term in the expansion describes an increasing number of field-matter interactions:

$$\mathbf{P}(\mathbf{r},t) = \sum_{n=1}^{\infty} \mathbf{P}^{(n)}(\mathbf{r},t). \tag{2-11}$$

The first order term describes the linear optical properties of the sample that can be determined using absorption or reflection experiments. For isotropic media, each of the even order terms in the expansion vanish due to symmetry.[11] The lowest order nonlinear term corresponds to the third-order polarization, $\mathbf{P}^{(3)}$, which can be measured using four-wave mixing spectroscopies.

The most general way to describe the generation of the third-order polarization is by defining a time dependent quantity, the third-order response function, $\mathbf{R}^{(3)}$, that describes the how the system behaves in response to three seperate field-matter interactions. The third-order polarization can be represented as the convolution of this quantity with each of the input electromagnetic fields, $\mathbf{E}(t)$:[12]

$$\mathbf{P}^{(3)}(t) = \int_0^{\infty} dt_3 \int_0^{\infty} dt_2 \int_0^{\infty} dt_1 \mathbf{R}^{(3)}(t_3,t_2,t_1)\mathbf{E}_{\alpha}(t-\tau_3)\mathbf{E}_{\beta}(t-\tau_3-\tau_2)\mathbf{E}_{\gamma}(t-\tau_3-\tau_2-\tau_1). \tag{2-12}$$

In Eq. 2-12, t_1 and t_2 refer to the time periods separating the three field-matter interactions and t_3 refers to the time between the third interaction and the detection of the signal field (Fig. 2-1), while the indices α, β, and γ denote the $\mathbf{k}$ vector of each excitation field, $\mathbf{k}_{\alpha}$, $\mathbf{k}_{\beta}$, and $\mathbf{k}_{\gamma}$ respectively. In practice, each of these three field-matter interactions need not occur at the peak of each pulse, but can occur at any time within the pulse envelope. We use a separate set of variables, τ_1, τ_2, and τ_3 to denote time delays between the peak of each excitation pulse and the detection of the signal field. According to

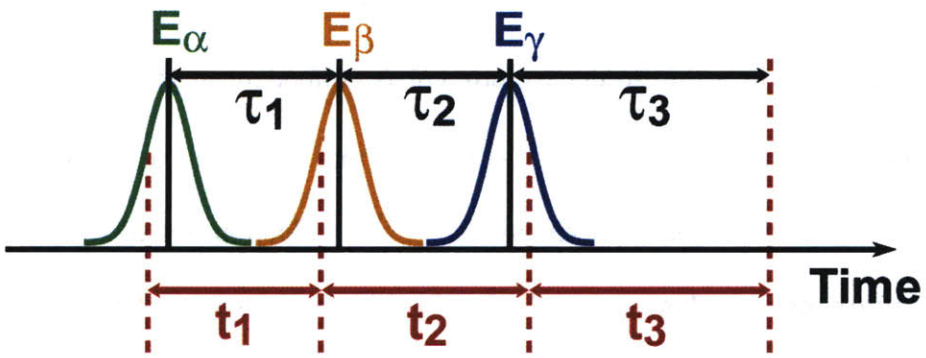


Figure 2-1: Pulse sequence for third-order nonlinear spectroscopy. The labels τ_1 and τ_2 refer to the time delays between the peaks of each excitation pulse and τ_3 denotes the time separating the peak of the third pulse and the detection of the signal field. In general, the interaction of each field with the material system can occur at any time within the envelope of each excitation pulse. The time periods t_1, t_2, and t_3 are analogous to τ_1, τ_2, and τ_3, but instead define the time periods between each field-matter interaction and the detection of the signal field. In the impulsive limit where each excitation pulse is infinitely short in time, these two sets of time delays are equal to one another.

Maxwell's equations, the signal field, $\mathbf{E}_{sig}(t)$, recorded in a third-order experiment corresponds to the time derivative of Eq. 2-12:[13]

$$\mathbf{E}_{sig}(t) \propto \frac{\partial \mathbf{P}^{(3)}}{\partial t}. \tag{2-13}$$

Comparison of Eq. 2-10 and 2-12 shows that the third-order response function, $\mathbf{R}^{(3)}$, consists of a triply nested commutator of the system's transition dipole operator evaluated at the time of each field-matter interaction and the time of the signal field detection:

$$\mathbf{R}^{(3)}(t_3,t_2,t_1) = \left(\frac{i}{\hbar}\right)^3 \theta(t_1)\theta(t_2)\theta(t_3)\left\langle\left[\left[\left[\boldsymbol{\mu}(t_3+t_2+t_1),\boldsymbol{\mu}(t_2+t_1)\right],\boldsymbol{\mu}(t_1)\right],\boldsymbol{\mu}(0)\right]\right\rangle. \tag{2-14}$$

The Heaviside step functions, $\theta(t)$, are included as part of the response to enforce causality and the angular brackets indicate an equilibrium ensemble average over the liquid degrees of freedom.

In the limit of delta function excitation pulses, the integrals in Eq. 2-12 vanish and the measured signal in a third-order experiment is equivalent to $\mathbf{R}^{(3)}$. In recent years, many different methodologies have been developed that allow for the calculation of $\mathbf{R}^{(3)}$ within a variety of different approximations.[7-9,12,14-17] Section 2.4 of this chapter will describe approximations that are used later in this thesis to calculate the third-order response of the O-H stretching transition of a dilute amount of HOD dissolved in either D_2O or $NaOD/D_2O$ solution. However, before these approximations can be described in detail, the following section will first introduce a useful notation that enables us to represent each of the terms that comprise the nested commutator of Eq. 2-14 pictorially.

2.3. A Pictorial Representation of the Third-order Response

We begin by expanding the commutator of Eq. 2-14. Doing so yields eight separate terms, but only four unique terms are found since half of the terms represent the complex conjugate of one of the other terms. By inserting the complete set of system eigenstates, $1 = \sum_n |n\rangle\langle n|$, between the dipole matrix operators in each term, we can rewrite Eq. 2-13 in terms of the system eigenstates:[14]

$$\mathbf{R}^{(3)}(t_3,t_2,t_1) = \left(\frac{i}{\hbar}\right)^3 \sum_{n=1}^{4} \mathbf{R}_n(t_3,t_2,t_1) - \mathbf{R}_n^*(t_3,t_2,t_1) \tag{2-15}$$

where the four terms, $\mathbf{R}_n$, are given by:

$$\begin{aligned}
\mathbf{R}_1 &= \sum_{abcd} P_a \langle \boldsymbol{\mu}_{ab}(t_3+t_2+t_1)\boldsymbol{\mu}_{bc}(t_2+t_1)\boldsymbol{\mu}_{cd}(t_1)\boldsymbol{\mu}_{da}(0)\rangle \\
\mathbf{R}_2 &= \sum_{abcd} P_a \langle \boldsymbol{\mu}_{ab}(t_1)\boldsymbol{\mu}_{bc}(t_2+t_1)\boldsymbol{\mu}_{cd}(t_3+t_2+t_1)\boldsymbol{\mu}_{da}(0)\rangle \\
\mathbf{R}_3 &= \sum_{abcd} P_a \langle \boldsymbol{\mu}_{dc}(t_1)\boldsymbol{\mu}_{cb}(t_3+t_2+t_1)\boldsymbol{\mu}_{ba}(t_2+t_1)\boldsymbol{\mu}_{ad}(0)\rangle \\
\mathbf{R}_4 &= \sum_{abcd} P_a \langle \boldsymbol{\mu}_{dc}(t_2+t_1)\boldsymbol{\mu}_{cb}(t_3+t_2+t_1)\boldsymbol{\mu}_{ba}(t_1)\boldsymbol{\mu}_{ad}(0)\rangle.
\end{aligned} \tag{2-16}$$

Here, the set of indices {a, b, c, d} run over the eigenstates of the system, $\boldsymbol{\mu}_{ij}$ represents the matrix elements of the transition dipole operator, $\boldsymbol{\mu}_{ij} = \langle i|\boldsymbol{\mu}|j\rangle$, and P_a denotes the probability that that population resides in eigenstate "a" at the time of the first field-matter interaction. Assuming that the system is initially at equilibrium, $P_a = \exp[-E_a/k_bT]/\sum_n \exp[-E_n/k_bT]$.

The advantage that we gain by rewriting Eq. 2-16 in terms of the system eigenstates is that each term in the equation can now be interpreted in terms of a set of time-ordered field-matter interactions that link specific eigenstates of the system. For example, if we look at the first term, $\mathbf{R}_1$, at t = 0 the first field-matter interaction creates a coherent superposition between the "d" and "a" system eigenstates. The next interaction at $t = t_1$ changes this coherence into a superposition of the "c" and "a" eigenstates and the final interaction creates a "ba" coherence. The signal is emitted at $t = t_1 + t_2 + t_3$ and involves radiating a photon with energy equivalent to the energy splitting between the "a" and "b" eigenstates.[†]

We can describe this series of interactions by making use of double-sided Feynman diagrams,[12] a convenient tool that lets us represent each of the terms in Eq. 2-16 pictorially. Fig. 2-2 displays the four diagrams that represent each of the four terms in Eq. 2-16. Time runs from the bottom of each diagram forward and the left and right hand sides of the diagram represent the bra and ket of the density matrix respectively. Arrows

[†] It should also be noted that each of these four indices may refer to the same eigenstate. Thus in the example outlined above, if "a" and "c" both refer to the ground state of a system and "b" and "d" correspond to the system's first excited state, then the first interaction prepares a coherence between the ground and excited state, and the second interaction converts this coherence to a ground state population where no phase oscillation occurs. The third pulse generates a new ground-excited state coherence and the signal is emitted with a frequency determined by the difference in energy between the ground and excited states. As we shall see in Section 2.5, the formation of a population during the second waiting period allows us to monitor spectral diffusion.

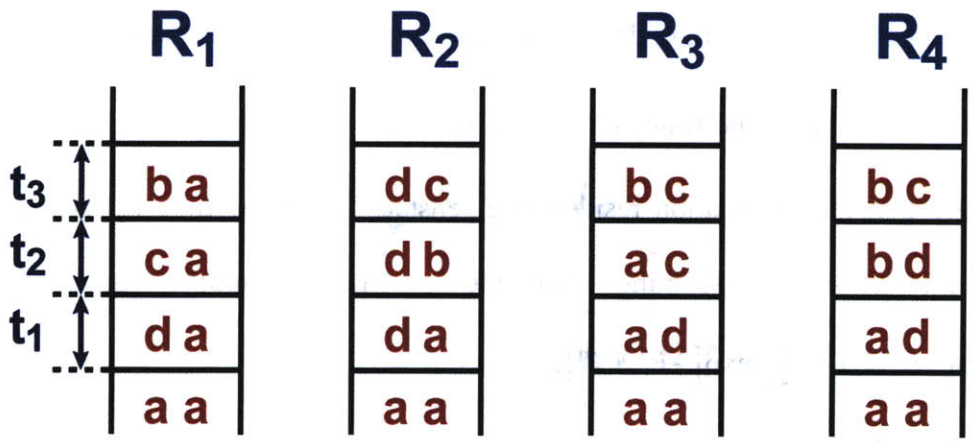


Figure 2-2: Feynman diagrams for each of the four terms that comprise Eq. 2-16. Time runs forward from the bottom to the top of the diagram. The set of indices {a,b,c,d} denote the eigenstates of the system and the horizontal lines represent field-matter interactions. The two indices listed for each time period denote the state of the system. Mixed sets of indices represent a coherent superposition of two eigenstates whereas pairs of identical indices denote the formation of a population in the listed eigenstate.

pointing toward a diagram represent the absorption of a photon while those pointing away denote stimulated emission.[‡] The side upon which an arrow is drawn denotes what side of the density matrix the transition dipole operator is acting on and also denotes the phase of the interaction, $+\mathbf{k}$ or $-\mathbf{k}$ which are represented by left or right pointing arrows respectively. Keeping track of the phase of each interaction is important because the conservation of energy dictates that both the wave vector and frequency of the signal field be equal to the sum of the wave vectors and frequencies of the excitation fields:

$$\begin{aligned} \mathbf{k}_{sig} &= \pm\mathbf{k}_{\alpha} \pm \mathbf{k}_{\beta} \pm \mathbf{k}_{\gamma} \\ \omega_{sig} &= \pm\omega_{\alpha} \pm \omega_{\beta} \pm \omega_{\gamma}. \end{aligned} \tag{2-17}$$

Here, as in Eq. 2-12, the subscripts α, β, and γ denote the three excitation pulses employed during the experiment.

[‡] Since the Feynman diagrams in Fig. 2-2 represent an arbitrary level structure, it is not appropriate to draw arrows on either side of the diagrams since the relative energies of the four eigenstates are not specified. Fig. 2-3 in Section 2.5 presents the set of Feynman pathways for a two-level system and includes arrows denoting absorption and emission.

The description of the third-order response that we have outlined in this section was originally developed for the treatment of a system containing only a ground and excited state.[18-20] However, the equations that we have used are general for any multilevel system,[14,21] which allows us to model the vibrational systems that we describe in the following chapters. To determine the specific set of excitation pathways for a given system, we need to evaluate the sums in Eq. 2-16 with respect to the system eigenstates, and the number of possible excitation pathways can rapidly escalate as the system size increases. Many of these terms involve transitions between states of the system that are not resonant with the excitation pulses used in the experiment and can be ignored. This assumption is known as the rotating wave approximation[12] and holds well for most vibrational systems. The phase matching conditions that appear in Eq. 2-17 allow us to further select against different excitation pathways. In any nonlinear experiment, we are free to exhibit control over the wave vectors of the excitation fields. For experiments performed using identical pulses in the boxcar geometry, such as those described in the following chapters of this thesis, only signals emitted in the $\mathbf{k}_{sig} = -\mathbf{k}_{\alpha} + \mathbf{k}_{\beta} + \mathbf{k}_{\gamma}$ phase matching direction need to be considered (See Section 2.5).

2.4. Useful Approximations for the Calculation of Spectroscopic Observables

Up to this point in the derivation of $\mathbf{R}^{(3)}$, we have only assumed that the excitation fields can be described classically and that the form of the interaction between the material system and the light fields is dipolar, which holds well for weak excitation fields. While Eq. 2-16 is useful for building an interpretation of how each field-matter interaction can act to drive transitions between different quantum states of the system, it

is not easy to use it to directly calculate the third-order response. Calculation of the time dependent quantum mechanical dipole operator is often only feasible for quantum calculations carried out on small systems. To calculate experimental observables from either MD simulations or from fitting models, we must first make further simplifications to Eq. 2-16. The following subsections derive expressions that are used throughout the following chapters of this thesis to calculate both linear and nonlinear signals.

2.4.1. Energy Gap Fluctuation Description of the Third-order Response

We can simplify the set of $\mathbf{R}_n$ described by Eq. 2-16 by rewriting the dipole matrix elements as: $\boldsymbol{\mu}_{ab}(t) = \exp[iH_a t/\hbar]\boldsymbol{\mu}_{ab}\exp[-iH_b t/\hbar]$. Making this substitution we obtain:

$$\begin{aligned}
\mathbf{R}_1 &= \sum_{abcd} P_a \left\langle e^{iH_a(t_3+t_2+t_1)/\hbar}\boldsymbol{\mu}_{ab}e^{-iH_b t_3/\hbar}\boldsymbol{\mu}_{bc}e^{-iH_c t_2/\hbar}\boldsymbol{\mu}_{cd}e^{-iH_d t_1/\hbar}\boldsymbol{\mu}_{da}\right\rangle \\
\mathbf{R}_2 &= \sum_{abcd} P_a \left\langle e^{iH_a t_1/\hbar}\boldsymbol{\mu}_{ab}e^{iH_b t_2/\hbar}\boldsymbol{\mu}_{bc}e^{iH_c t_3/\hbar}\boldsymbol{\mu}_{cd}e^{-iH_d(t_3+t_2+t_1)/\hbar}\boldsymbol{\mu}_{da}\right\rangle \\
\mathbf{R}_3 &= \sum_{abcd} P_a \left\langle e^{iH_d t_1/\hbar}\boldsymbol{\mu}_{dc}e^{iH_c(t_3+t_2)/\hbar}\boldsymbol{\mu}_{cb}e^{-iH_b t_3/\hbar}\boldsymbol{\mu}_{ba}e^{-iH_a(t_2+t_1)/\hbar}\boldsymbol{\mu}_{ad}\right\rangle \\
\mathbf{R}_4 &= \sum_{abcd} P_a \left\langle e^{iH_d(t_2+t_1)/\hbar}\boldsymbol{\mu}_{dc}e^{iH_c t_3/\hbar}\boldsymbol{\mu}_{cb}e^{-iH_b(t_3+t_2)/\hbar}\boldsymbol{\mu}_{ba}e^{-iH_a t_1/\hbar}\boldsymbol{\mu}_{ad}\right\rangle.
\end{aligned} \tag{2-18}$$

For many vibrational systems, it is valid to make the Condon approximation, which neglects the dependence of the dipole matrix elements on the fluctuations of the bath.[12,22] Since the angled brackets in Eq. 2-18 denote an equilibrium average over the bath degrees of freedom, this approximation allows us to move each of the dipole matrix elements, $\boldsymbol{\mu}_{ij}$, outside of the average. However, for the case of hydrogen bonding systems, it is well known that O-H bonds that participate in strong hydrogen bonds display highly increased infrared absorption cross sections.[23,24] In the case of dilute HOD dissolved in D_2O, electronic structure calculations[17,25-27] have predicted that the HOD

molecule's transition dipole increases strongly as the frequency of the O-H stretch decreases. Based on these observations, we will refrain from making the Condon approximation until we cannot proceed further without doing so.

At this point, it becomes useful to rewrite Eq. 2-18 in terms of the energy gap fluctuations between the eigenstates of the system and a reference state. For our reference, we will choose the ground state of the system, denoted by the index "a". Although this choice is arbitrary, it will not affect the results we outline below. To implement this substitution, we make use of the identity:[12]

$$e^{-iH_a t/\hbar} e^{iH_b t/\hbar} = \exp_+\left[-\frac{i}{\hbar}\int_0^t d\tau H_{ab}(\tau)\right] \tag{2-19}$$

where $H_{ab} = H_a - H_b$ and $\exp_+$ denotes a time-ordered exponential series:

$$\exp_+\left[\int_0^t d\tau A(\tau)\right] = 1 + \sum_{n=1}^{\infty}\int_0^t d\tau_n \int_0^{\tau_n} d\tau_{n-1}\ldots\int_0^{\tau_2} d\tau_1 A(\tau_n)A(\tau_{n-1})\ldots A(\tau_1). \tag{2-20}$$

Judicious usage of Eq. 2-19 as well as the insertion of the identity $1 = e^{-iH_a t/\hbar} e^{iH_a t/\hbar}$ allows us to rewrite Eq. 2-18 as:

$$\begin{aligned}\mathbf{R}_1 = \sum_{abcd} P_a \Big\langle & \boldsymbol{\mu}_{ab}(t_3+t_2+t_1)\exp_+\left[-\frac{i}{\hbar}\int_0^{t_1+t_2+t_3} H_{ba}(\tau)d\tau\right]\exp_+\left[\frac{i}{\hbar}\int_0^{t_1+t_2} H_{ba}(\tau)d\tau\right] \\ & \times \boldsymbol{\mu}_{bc}(t_2+t_1)\exp_+\left[-\frac{i}{\hbar}\int_0^{t_1+t_2} H_{ca}(\tau)d\tau\right]\exp_+\left[\frac{i}{\hbar}\int_0^{t_1} H_{ca}(\tau)d\tau\right] \\ & \times \boldsymbol{\mu}_{cd}(t_1)\exp_+\left[-\frac{i}{\hbar}\int_0^{t_1} H_{da}(\tau)d\tau\right]\boldsymbol{\mu}_{da}(0)\Big\rangle\end{aligned} \tag{2-21a}$$

$$\begin{aligned}\mathbf{R}_2 = \sum_{abcd} P_a \Big\langle & \boldsymbol{\mu}_{ab}(t_1)\exp_+\left[-\frac{i}{\hbar}\int_0^{t_1} H_{ba}(\tau)d\tau\right]\exp_+\left[\frac{i}{\hbar}\int_0^{t_1+t_2} H_{ba}(\tau)d\tau\right] \\ & \times \boldsymbol{\mu}_{bc}(t_2+t_1)\exp_+\left[-\frac{i}{\hbar}\int_0^{t_1+t_2} H_{ca}(\tau)d\tau\right]\exp_+\left[\frac{i}{\hbar}\int_0^{t_1+t_2+t_3} H_{ca}(\tau)d\tau\right] \\ & \times \boldsymbol{\mu}_{cd}(t_3+t_2+t_1)\exp_+\left[-\frac{i}{\hbar}\int_0^{t_1+t_2+t_3} H_{da}(\tau)d\tau\right]\boldsymbol{\mu}_{da}(0)\Big\rangle\end{aligned} \tag{2-21b}$$

$$\mathbf{R}_3 = \sum_{abcd} P_a \left\langle \boldsymbol{\mu}_{dc}(t_1)\exp_+\left[-\frac{i}{\hbar}\int_0^{t_1} H_{ca}(\tau)d\tau\right]\exp_+\left[\frac{i}{\hbar}\int_0^{t_1+t_2+t_3} H_{ca}(\tau)d\tau\right]\right.$$
$$\times \boldsymbol{\mu}_{cb}(t_3+t_2+t_1)\exp_+\left[-\frac{i}{\hbar}\int_0^{t_1+t_2+t_3} H_{ba}(\tau)d\tau\right]\exp_+\left[\frac{i}{\hbar}\int_0^{t_1+t_2} H_{ba}(\tau)d\tau\right] \quad (2\text{-}21c)$$
$$\left.\times \boldsymbol{\mu}_{ba}(t_2+t_1)\boldsymbol{\mu}_{ad}(0)\exp_+\left[\frac{i}{\hbar}\int_0^{t_1} H_{da}(\tau)d\tau\right]\right\rangle$$

$$\mathbf{R}_4 = \sum_{abcd} P_a \left\langle \boldsymbol{\mu}_{dc}(t_2+t_1)\exp_+\left[-\frac{i}{\hbar}\int_0^{t_1+t_2} H_{ca}(\tau)d\tau\right]\exp_+\left[\frac{i}{\hbar}\int_0^{t_1+t_2+t_3} H_{ca}(\tau)d\tau\right]\right.$$
$$\times \boldsymbol{\mu}_{cb}(t_3+t_2+t_1)\exp_+\left[-\frac{i}{\hbar}\int_0^{t_1+t_2+t_3} H_{ba}(\tau)d\tau\right]\exp_+\left[\frac{i}{\hbar}\int_0^{t_1} H_{ba}(\tau)d\tau\right] \quad (2\text{-}21d)$$
$$\left.\times \boldsymbol{\mu}_{ba}(t_1)\boldsymbol{\mu}_{ad}(0)\exp_+\left[\frac{i}{\hbar}\int_0^{t_1+t_2} H_{da}(\tau)d\tau\right]\right\rangle.$$

In Eq. 2-21, the time dependence of each dipole matrix element now occurs with respect to our chosen reference state, $\boldsymbol{\mu}_{ij}(t) = \exp[iH_a t/\hbar]\boldsymbol{\mu}_{ij}\exp[-iH_a t/\hbar]$.

The expressions given above are exact in the limit of weak excitation fields where the dipole approximation for field-matter interactions holds. Unfortunately, to evaluate each term we need to have exact knowledge of the quantum dynamics of the system, a daunting task for any liquid system. As a key simplifying approximation, we will make a semiclassical approximation and assume that each term in Eq. 2-21 can be replaced by its classical analogue.[12,15,28,29] This allows us to exchange each time ordered exponential in Eq. 2-21 with an ordinary exponential function, giving the final result:

$$\begin{aligned}
\mathbf{R}_1 &= \sum_{abcd} P_a \left\langle \boldsymbol{\mu}_{ab}(t_3+t_2+t_1)\boldsymbol{\mu}_{bc}(t_2+t_1)\boldsymbol{\mu}_{cd}(t_1)\boldsymbol{\mu}_{da}(0)\phi^{(1)}_{abcd}\right\rangle \\
\mathbf{R}_2 &= \sum_{abcd} P_a \left\langle \boldsymbol{\mu}_{ab}(t_1)\boldsymbol{\mu}_{bc}(t_2+t_1)\boldsymbol{\mu}_{cd}(t_3+t_2+t_1)\boldsymbol{\mu}_{da}(0)\phi^{(2)}_{abcd}\right\rangle \\
\mathbf{R}_3 &= \sum_{abcd} P_a \left\langle \boldsymbol{\mu}_{da}(0)\boldsymbol{\mu}_{ab}(t_2+t_1)\boldsymbol{\mu}_{bc}(t_3+t_2+t_1)\boldsymbol{\mu}_{cd}(t_1)\phi^{(3)}_{abcd}\right\rangle \\
\mathbf{R}_4 &= \sum_{abcd} P_a \left\langle \boldsymbol{\mu}_{da}(0)\boldsymbol{\mu}_{ab}(t_1)\boldsymbol{\mu}_{bc}(t_3+t_2+t_1)\boldsymbol{\mu}_{cd}(t_2+t_1)\phi^{(4)}_{abcd}\right\rangle,
\end{aligned} \quad (2\text{-}22)$$

where the set of dephasing functions, $\phi^{(n)}_{abcd}$, are defined as:

$$\begin{aligned}
\phi^{(1)}_{abcd} &= \exp\left[-i\int_{t_1+t_2}^{t_1+t_2+t_3}\omega_{ba}(\tau)d\tau - i\int_{t_1}^{t_1+t_2}\omega_{ca}(\tau)d\tau - i\int_{0}^{t_1}\omega_{da}(\tau)d\tau\right] \\
\phi^{(2)}_{abcd} &= \exp\left[-i\int_{t_1+t_2}^{t_1+t_2+t_3}\omega_{dc}(\tau)d\tau - i\int_{t_1}^{t_1+t_2}\omega_{db}(\tau)d\tau - i\int_{0}^{t_1}\omega_{da}(\tau)d\tau\right] \\
\phi^{(3)}_{abcd} &= \exp\left[-i\int_{t_1+t_2}^{t_1+t_2+t_3}\omega_{bc}(\tau)d\tau + i\int_{t_1}^{t_1+t_2}\omega_{ca}(\tau)d\tau + i\int_{0}^{t_1}\omega_{da}(\tau)d\tau\right] \\
\phi^{(4)}_{abcd} &= \exp\left[-i\int_{t_1+t_2}^{t_1+t_2+t_3}\omega_{bc}(\tau)d\tau + i\int_{t_1}^{t_1+t_2}\omega_{db}(\tau)d\tau + i\int_{0}^{t_1}\omega_{da}(\tau)d\tau\right]
\end{aligned} \tag{2-23}$$

and $\omega_{ij}(t) = H_{ij}(t)/\hbar$.

Examining Eq. 2-22, we find that in each time period the system oscillates in a coherent state and each field-matter interaction acts to change the two states that comprise the coherence. Eq. 2-22 is a powerful result because it enables us to calculate the third-order response directly from classical MD simulations. Over the course of the past decade, numerous mixed quantum-classical techniques have been developed that allow for the calculation of vibrational frequencies from a MD simulation. Many of these techniques calculate quantum vibrational degrees of freedom by using either perturbation theory[30-32] or frequency maps derived from high level density functional theory[25,27] or *ab initio*[33] calculations. The input to these calculations is generally the instantaneous configuration of the simulated system, which allows for the calculation of a set of trajectories of the energy of each system eigenstate, as well as the transition dipoles linking these states. With a set of trajectories in hand, $\mathbf{R}^{(3)}$ can be calculated using the approximate result shown in Eq. 2-22. Chapters 5 and 7 present results where this approach is used to calculate 2D IR spectra for the O-H stretching transition of HOD dissolved in D_2O and NaOD solution.

2.4.2. Second Cumulant Approximation

The expressions derived in the previous section allow for the straightforward calculation of nonlinear signals from fluctuating trajectories of the vibrational frequencies and transition dipoles of a system. However, in the absence of a means of generating such trajectories, further approximations need to be made to derive an expression for the response that can be calculated from experimentally constrained fitting parameters. Simplification of Eq. 2-20 can be made by rewriting it in terms of a series of energy gap time correlation functions:

$$C_{nm}(t-t_o) = \left\langle \delta\omega_{na}(t)\,\delta\omega_{ma}(t_o) \right\rangle \tag{2-24}$$

where $\omega_{na} = (E_n - E_a)/\hbar$ is the difference in energy between the eigenstate "n" and our chosen reference eigenstate "a", and $\delta\omega_{na}(t) = \omega_{na}(t) - \langle\omega_{na}\rangle$. The advantage gained by making this transformation is that the set of time correlation functions, $C_{nm}(t)$, can serve as parameters that can be adjusted to fit experimental results. Once a sufficient fit is found, these time correlation functions provide an average measure of the time scale over which fluctuations of the bath cause the system to undergo spectral diffusion.

We begin our simplification of Eq. 2-21 by first making the Condon approximation so that the dipole matrix elements can be moved outside the brackets that denote an equilibrium ensemble average. Each of the time-ordered exponential functions that comprise Eq. 2-21 can then be expanded to second order using Eq. 2-20. Sung and Silbey[14,21] have demonstrated that the results of this expansion can be written as:

$$\begin{aligned}
\mathbf{R}_1 &= \sum_{abcd} P_a \boldsymbol{\mu}_{ab}\boldsymbol{\mu}_{bc}\boldsymbol{\mu}_{cd}\boldsymbol{\mu}_{da} \exp\left[-i\langle\omega_{ba}\rangle t_3 - i\langle\omega_{ca}\rangle t_2 - i\langle\omega_{da}\rangle t_1\right] F^{(1)}_{abcd}(t_3,t_2,t_1) \\
\mathbf{R}_2 &= \sum_{abcd} P_a \boldsymbol{\mu}_{ab}\boldsymbol{\mu}_{bc}\boldsymbol{\mu}_{cd}\boldsymbol{\mu}_{da} \exp\left[-i\langle\omega_{dc}\rangle t_3 - i\langle\omega_{db}\rangle t_2 - i\langle\omega_{da}\rangle t_1\right] F^{(2)}_{abcd}(t_3,t_2,t_1) \\
\mathbf{R}_3 &= \sum_{abcd} P_a \boldsymbol{\mu}_{ab}\boldsymbol{\mu}_{bc}\boldsymbol{\mu}_{cd}\boldsymbol{\mu}_{da} \exp\left[-i\langle\omega_{bc}\rangle t_3 + i\langle\omega_{ca}\rangle t_2 + i\langle\omega_{da}\rangle t_1\right] F^{(3)}_{abcd}(t_3,t_2,t_1) \\
\mathbf{R}_4 &= \sum_{abcd} P_a \boldsymbol{\mu}_{ab}\boldsymbol{\mu}_{bc}\boldsymbol{\mu}_{cd}\boldsymbol{\mu}_{da} \exp\left[-i\langle\omega_{bc}\rangle t_3 + i\langle\omega_{db}\rangle t_2 + i\langle\omega_{da}\rangle t_1\right] F^{(4)}_{abcd}(t_3,t_2,t_1).
\end{aligned} \tag{2-25}$$

In Eq. 2-25, the frequency evolution of the system is now described through a series of dephasing functions, $F^{(n)}_{abcd}(t_3,t_2,t_1)$, that consist of integrals over a set of energy gap correlation functions such as that in Eq. 2-24:

$$\begin{aligned}
-\ln\left[F^{(1)}_{abcd}(t_3,t_2,t_1)\right] &= h_{bb}(t_3) + h_{cc}(t_2) + h_{dd}(t_1) + h^{+}_{bc}(t_3,t_2) \\
&\quad + h^{+}_{cd}(t_3,t_2) + f^{+}_{bd}(t_3,t_1;t_2) \\
-\ln\left[F^{(2)}_{abcd}(t_3,t_2,t_1)\right] &= \left[h_{cc}(t_3)\right]^{*} + \left[h_{bb}(t_2)\right]^{*} + h_{dd}(t_3+t_2+t_1) + \left[h^{+}_{bc}(t_3,t_2)\right]^{*} \\
&\quad + h^{-}_{cd}(t_3+t_2+t_1,t_3) + \left[f^{-}_{bd}(t_2,t_3+t_2+t_1;t_3)\right]^{*} \\
-\ln\left[F^{(3)}_{abcd}(t_3,t_2,t_1)\right]^{*} &= \left[h_{bb}(t_3)\right]^{*} + h_{cc}(t_3+t_2) + h_{dd}(t_1) + h^{+}_{cd}(t_3+t_2,t_1) \\
&\quad - f^{-}_{bc}(t_3,t_3+t_2;t_2) - f^{+}_{bd}(t_3,t_1;t_2) \\
-\ln\left[F^{(4)}_{abcd}(t_3,t_2,t_1)\right]^{*} &= h_{cc}(t_3) + h_{dd}(t_2+t_1) + \left[h_{bb}(t_3+t_2)\right]^{*} - h^{-}_{bc}(t_3,t_3+t_2) \\
&\quad + h^{+}_{cd}(t_2+t_1,t_3) - f^{-}_{bd}(t_2+t_1,t_3+t_2;t_3)
\end{aligned} \tag{2-26}$$

where:

$$h_{nm}(t) = \int_0^t d\tau_2 \int_0^{\tau_2} d\tau_1 C_{nm}(\tau_2 - \tau_1) \tag{2-27}$$

$$h^{\pm}_{nm}(t_2,t_1) = \int_0^{t_2} d\tau_2 \int_0^{t_1} d\tau_1 C_{nm}(\tau_2 \pm \tau_1) \tag{2-28}$$

$$f^{\pm}_{nm}(t_2,t_1;t_3) = \int_0^{t_2} d\tau_2 \int_0^{t_1} d\tau_1 C_{nm}(\tau_2 \pm \tau_1 + t_3). \tag{2-29}$$

Unfortunately, this simplification of Eq. 2-21 comes with a cost. Choosing to describe the fluctuations of the system using only energy gap correlation functions that are each dependent on a single time period is equivalent to assuming that the fluctuations of the system obey Gaussian statistics.[§] This has the consequence that any computed multidimensional lineshape will be symmetric with respect to the antidiagonal axis, implying that the dynamics of molecules that absorb at both low and high frequencies are identical. In the case of water, molecules that absorb at low O-H stretching frequencies participate in strong hydrogen bonds while those that instead absorb at high frequency are involved in weak or broken hydrogen bonds, and there is little reason to assume that frequency fluctuations of the O-H lineshape obey Gaussian statistics. We will indeed show that this is the case Chapter 5. Pronounced asymmetries are present in measured 2D IR spectra that result from the instability of broken hydrogen bonding configurations.[34-36] Nevertheless, this formalism at least allows us to characterize the average time scale for spectral diffusion in water and, in the case of concentrated NaOD solutions, this formalism can be extended to determine an average time scale for the structural diffusion of the deuteroxide ion.

2.4.3. Linear Absorption Lineshapes

Although linear absorption lineshapes primarily provide information on the distribution of eigenstates within a system and are only moderately sensitive to their dynamics, the calculation of linear absorption spectra can provide an additional constraint when fitting spectroscopic models or developing methods for calculating vibrational

[§] Another way of stating this is that the coupling between the system and bath, H_{SB}, is linear in the bath coordinate. Sung and Silbey[14] assume this as part of their derivation and under this condition, Eq. 2-25 is an exact result.

frequencies from MD simulations. One of the advantages of the perturbative treatment of nonlinear spectroscopy outlined in this chapter is that it can easily be generalized to any "n" order spectroscopy, including linear spectroscopy.

Following Eq. 2-11 we find that the linear polarization can be written as:

$$\mathbf{P}^{(1)}(t) = \int_0^\infty dt_1 \mathbf{R}^{(1)}(t_1)\mathbf{E}(t-\tau_1) \tag{2-30}$$

where t_1 refers to the time between the single field-matter interaction and the detection of the linear signal field. In Eq. 2-30, the first order response function, $\mathbf{R}^{(1)}(t_1)$, is given by:

$$\mathbf{R}^{(1)}(t_1) = \frac{i}{\hbar}\theta(t_1)\left\langle\left[\boldsymbol{\mu}(t_1),\boldsymbol{\mu}(0)\right]\right\rangle. \tag{2-31}$$

The linear absorption lineshape is proportional to the Fourier transform of the signal field induced by $\mathbf{P}^{(1)}(t)$. Using the same set of semiclassical approximations that were made to derive Eq. 2-22, we find that $\mathbf{R}^{(1)}(t_1)$ can be rewritten as:[12,15,28]

$$\mathbf{R}^{(1)}(t_1) = \sum_{ab} P_a \left\langle \boldsymbol{\mu}_{ab}(t_1)\boldsymbol{\mu}_{ba}(0)\exp\left[-i\int_0^{t_1}\omega_{ba}(\tau)d\tau\right]\right\rangle. \tag{2-32}$$

Within the confines of the Condon and second Cumulant approximations, $\mathbf{R}^{(1)}(t_1)$ further simplifies to:[12,15]

$$\mathbf{R}^{(1)}(t_1) = \sum_{ab} P_a \left|\boldsymbol{\mu}_{ba}\right|^2 \exp\left[-i\langle\omega_{ba}\rangle t_1 - g(t_1)\right] \tag{2-33}$$

where:

$$g(t) = \int_0^t d\tau (t-\tau)\left\langle\delta\omega_{ba}(\tau)\delta\omega_{ba}(0)\right\rangle. \tag{2-34}$$

2.4.4. Treatment of Population Relaxation and Reorientation

It should be noted that in the equations derived above, we have neglected any line broadening contributions that result from vibrational energy relaxation. The overall decay of the nonlinear signal due to this process can be added into the above formalism empirically,[9,37,38] but the means by which this is accomplished are often dependent on the exact details of the system under study. Vibrational population relaxation of the HOD molecule is accounted for phenomenologically when modeling the experimental data presented in Chapters 5 and 6, and a description of how this is accomplished appears in detail in these chapters.

The third-order polarization is a vector quantity whose polarization is dependent on that of each of the three excitation pulses used in the experiment. When calculating Eq. 2-22 from a MD simulation, it is possible to directly calculate the projection of the dipole at the time of each field-matter interaction along the polarization direction of the excitation pulse. In the case where we do not posses an atomistic description of the system, the effects of reorientation can be included in Eq. 2-25 by assuming that the orientational and vibrational degrees of freedom of the system are separable. This allows the set of $\mathbf{R}_n$ that comprise Eq. 2-25 to be written as:[14]

$$\mathbf{R}_n(t_3,t_2,t_1) = \sum_{n=1}^{4} \sum_{IJKL} \sum_{abcd} (Y_n)_{IJKL}^{abcd}(t_3,t_2,t_1)\, R_n^{abcd}(t_3,t_2,t_1). \tag{2-35}$$

Here, the functions Y_n and R_n describe the orientational and vibrational responses respectively, and the indices {I, J, K, L} refer to the directional unit vectors in the laboratory frame (i.e. X, Y, and Z). The set of R_n^{abcd} are identical to that found in Eq. 2-25, but lack the orientational information contained in the dipole matrix elements:

$$
\begin{aligned}
R_1^{abcd} &= P_a|\boldsymbol{\mu}_{ab}||\boldsymbol{\mu}_{bc}||\boldsymbol{\mu}_{cd}||\boldsymbol{\mu}_{da}|\exp\left[-i\langle\omega_{ba}\rangle t_3 - i\langle\omega_{ca}\rangle t_2 - i\langle\omega_{da}\rangle t_1\right]F_{abcd}^{(1)}(t_3,t_2,t_1)\\
R_2^{abcd} &= P_a|\boldsymbol{\mu}_{ab}||\boldsymbol{\mu}_{bc}||\boldsymbol{\mu}_{cd}||\boldsymbol{\mu}_{da}|\exp\left[-i\langle\omega_{dc}\rangle t_3 - i\langle\omega_{db}\rangle t_2 - i\langle\omega_{da}\rangle t_1\right]F_{abcd}^{(2)}(t_3,t_2,t_1)\\
R_3^{abcd} &= P_a|\boldsymbol{\mu}_{ab}||\boldsymbol{\mu}_{bc}||\boldsymbol{\mu}_{cd}||\boldsymbol{\mu}_{da}|\exp\left[-i\langle\omega_{bc}\rangle t_3 + i\langle\omega_{ca}\rangle t_2 + i\langle\omega_{da}\rangle t_1\right]F_{abcd}^{(3)}(t_3,t_2,t_1)\\
R_4^{abcd} &= P_a|\boldsymbol{\mu}_{ab}||\boldsymbol{\mu}_{bc}||\boldsymbol{\mu}_{cd}||\boldsymbol{\mu}_{da}|\exp\left[-i\langle\omega_{bc}\rangle t_3 + i\langle\omega_{db}\rangle t_2 + i\langle\omega_{da}\rangle t_1\right]F_{abcd}^{(4)}(t_3,t_2,t_1).
\end{aligned}
\tag{2-36}
$$

Analytical expressions for the set of Y_n can be derived for a single vibration:[39,40]

$$
\begin{aligned}
Y_{ZZZZ}(t_3,t_2,t_1) &= \frac{1}{9}c_1(t_1)\left(1+\frac{4}{5}c_2(t_2)\right)c_1(t_3)\\
Y_{ZZYY}(t_3,t_2,t_1) &= \frac{1}{9}c_1(t_1)\left(1-\frac{2}{5}c_2(t_2)\right)c_1(t_3)\\
Y_{ZYYZ}(t_3,t_2,t_1) &= Y_{ZYZY}(t_3,t_2,t_1) = \frac{1}{15}c_1(t_1)c_2(t_2)c_1(t_3)
\end{aligned}
\tag{2-37}
$$

where $c_\ell(t) = \left\langle P_\ell\left(\hat{\mathbf{u}}(t)\bullet\hat{\mathbf{u}}(0)\right)\right\rangle$, P_ℓ denotes the nth order Legendre polynomial and, $\hat{\mathbf{u}}(t)$ is a unit vector representing the orientation of the transition dipole of the probed vibration. Time scales associated with the decay of P_1 can be inferred on the basis of dielectric relaxation experiments[41] while nuclear magnetic resonance dipolar relaxation[42] and polarization dependent infrared pump-probe experiments[43,44] can be used to measure P_2.

2.5. Vibrational Echo Spectroscopy and Other Probes of Vibrational Dynamics

Now that we have a theoretical description for the generation of the third-order polarization, how can we use this formalism to interpret nonlinear signals in terms of the dynamics of individual molecules? This connection between theory and dynamics can be best made by making use of a simple example system. Fig. 2-3 displays the Feynman diagrams for a two-level system consisting of a ground state, $|0\rangle$, and a first excited state, $|1\rangle$.[12] These diagrams can be divided into two separate categories based on phase matching. Rephasing diagrams correspond to signals emitted in the $\mathbf{k}_{sig} = -\mathbf{k}_1 + \mathbf{k}_2 + \mathbf{k}_3$

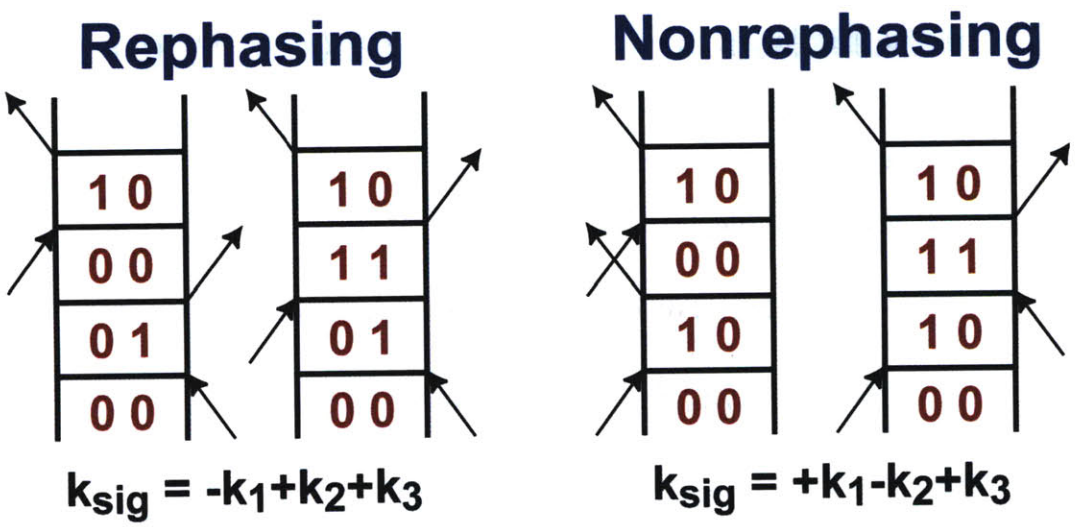


Figure 2-3: Feynman diagrams for a two-level system with ground state $|0\rangle$ and excited state $|1\rangle$. These diagrams can be divided into rephasing and nonrephasing excitation pathways on the basis of phase matching.

direction while nonrephasing diagrams are instead emitted along $\mathbf{k}_{sig} = \mathbf{k}_1 - \mathbf{k}_2 + \mathbf{k}_3$, where the subscripts 1, 2, and 3 denote the order of interaction of each signal field.

In both of the rephasing diagrams, the first field-matter interaction places the system into a coherent superposition between the ground and excited states. In a liquid sample, this corresponds to the excitation of many different oscillators that each have slightly different vibrational frequencies due to fluctuations of the surrounding environment. The coherence that is prepared for each individual molecule will oscillate between the ground and excited state at a frequency given by the energy difference between these two states. Due to the distribution of vibrational frequencies across the sample, the oscillation of the ensemble averaged coherence will dephase with time.

The second interaction in the rephasing pulse sequence causes the state of the system to collapse into either the ground or excited state. During this time spent in a population state, fluctuations of the surrounding solvent can lead to shifts in the energy

gap between the $|0\rangle$ and $|1\rangle$ states. The third pulse then creates a second coherence between the ground and excited state, but with a phase opposite to that of the coherence created during the first time period. This flip in the sign of the phase means that if frequency memory was not lost during the time spent in a population state, when t_3 is equal to t_1 a compete rephasing of the original coherent state will occur (Fig. 2-4). Physically, the rephasing of the original coherence corresponds to a macroscopic alignment of the dipoles of the excited oscillators. This serves as a source term that radiates a signal field, the vibrational echo. However, if the frequencies of the excited molecules are randomized during the population period, then the strength of the echo signal will be decreased and peaked near $\tau_3 = 0$. By systematically varying the length of the population period, we can obtain a direct measure of the time scale over which fluctuations of the bath cause the system to undergo spectral diffusion, τ_c.

Nonrephasing diagrams do not posses the ability to generate a vibrational echo since the coherences created by the first and third excitation pulses oscillate with the same phase. However, measurement of these diagrams is important in experiments that record the third-order response as a function of the τ_1 time axis. In the time domain, the nonrephasing diagrams form the negative portion of this timing axis.[1] Upon Fourier transformation to the frequency domain, the summation of rephasing and nonrephasing spectra leads to the cancellation of dispersive wings that appear in the transformed data, yielding a purely absorptive lineshape.[45]

Of course, when more energy levels are added to the system, the number of different excitation pathways probed by the experiment increases and the interpretation of the measured signal becomes more complicated. Since vibrations are inherently

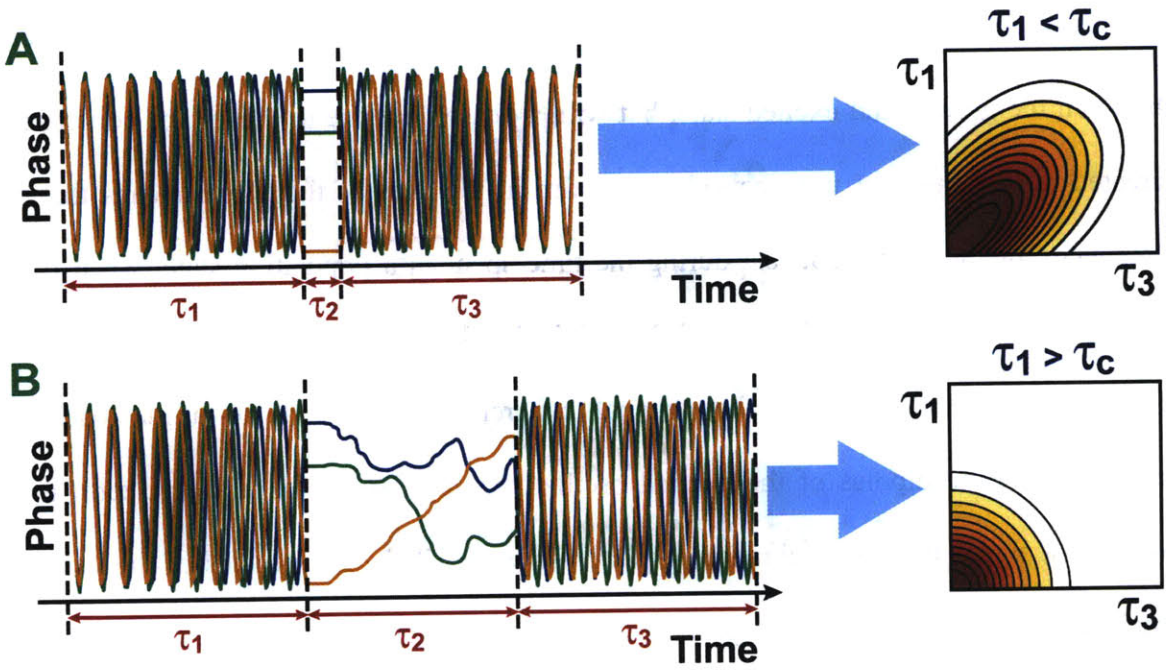


Figure 2-4: Schematic illustration of the generation of a vibrational echo. The green, blue, and yellow traces represent the phase of three separate oscillators with slightly different vibrational frequencies. At $\tau_1 = 0$, the initial excitation pulse prepares a state where each oscillator is in phase. Over time, these oscillators dephase due to their slightly different vibrational frequencies. The second pulse stops the phase of the oscillation by preparing a population state, while the third pulse creates a second coherence but with a phase opposite to that prepared by the initial pulse. In (A) frequency memory is retained during τ_2, and when $\tau_3 = \tau_1$, the original coherent state formed at $\tau_1 = 0$ is regained. This leads to the emission of a strong echo signal peaked along the $\tau_1 = \tau_3$ axis. In (B) τ_2 is lengthened, which allows the fluctuations of the surrounding solvent environment to randomize the phases and vibrational frequencies of each oscillator. This prevents the rephasing of the initial coherence, and the echo signal peaks near $\tau_3 = 0$. The time scale necessary for this loss of frequency memory is denoted the correlation time, τ_c.

multilevel systems, in the case of single vibrational transition, such as the O-H stretching transition of dilute HOD in D_2O, we need to consider not only transitions involving the v = 0 and 1 states, but also transitions involving the v = 2 state. Carrying out the sum in Eq. 2-16 over these three vibrational states, we obtain the eight Feynman diagrams displayed in Fig. 2-5.[38] The S_I and S_{II} sets of diagrams correspond to rephasing, $\mathbf{k}_{sig} = -\mathbf{k}_1 + \mathbf{k}_2 + \mathbf{k}_3$, and nonrephasing, $\mathbf{k}_{sig} = +\mathbf{k}_1 - \mathbf{k}_2 + \mathbf{k}_3$, responses respectively. S_I

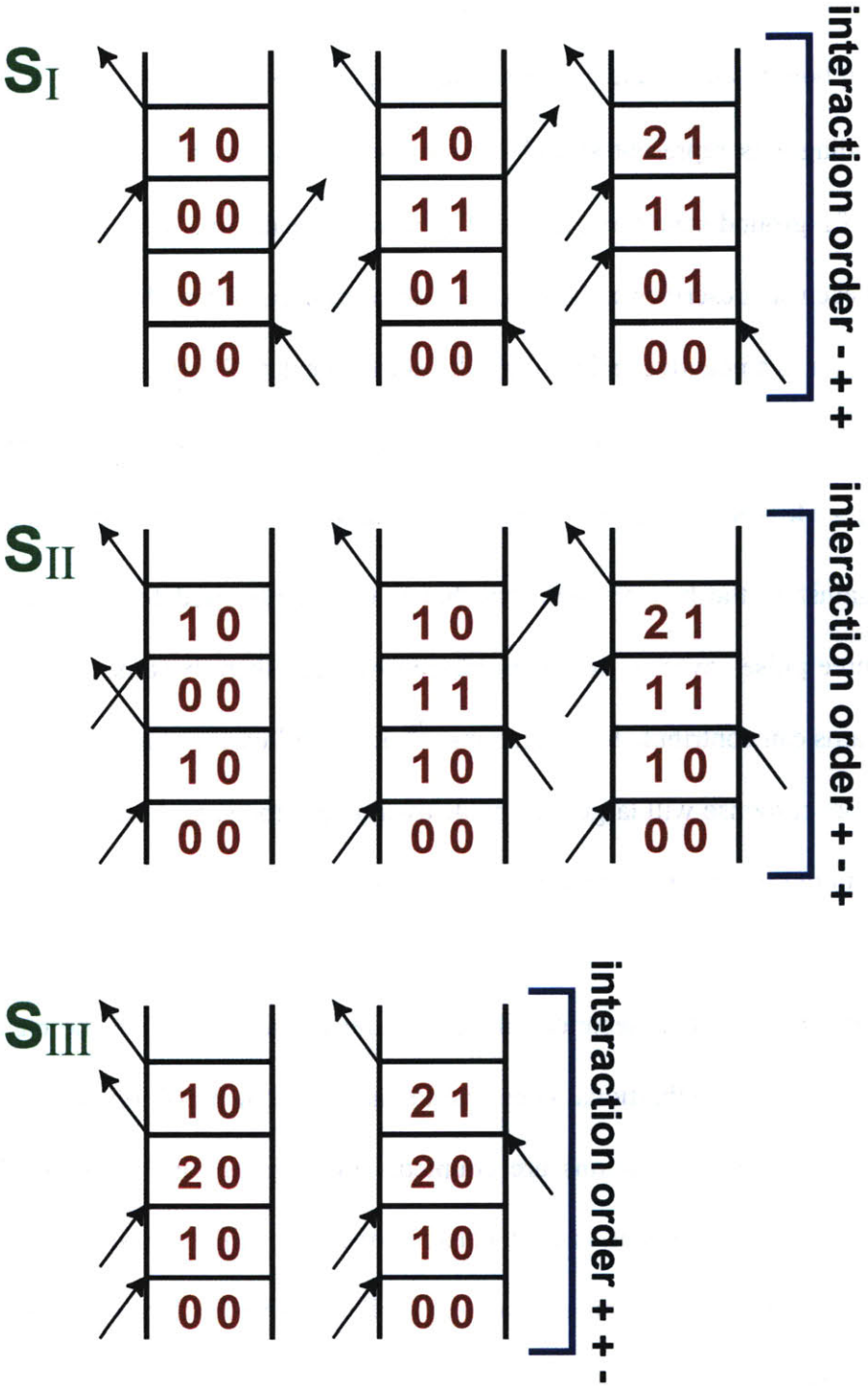


Figure 2-5: Feynman diagrams for a three-level vibrational system. The labels S_I, S_{II}, and S_{III} refer to rephasing, nonrephasing, and two-quantum diagrams respectively. In the boxcar geometry used for vibrational echo experiments, the S_{III} diagrams contribute to the signal only when all three pulses overlap.

and S_{II} both contain two diagrams that oscillate in a coherence between the v = 0 and 1 states during both τ_1 and τ_3 and exist in either the ground state or first excited state during τ_2. These diagrams represent stimulated emission from the first excited state and the formation of a ground state hole, and lead to positive peaks in 2D IR spectra. The third diagram in each set describes a photoinduced absorption involving the v = 2←1 transition, which contributes a negative, anharmonically shifted peak to 2D IR spectra.

The S_{III} diagrams are unique to multilevel systems and represent signals emitted in the $\mathbf{k}_{sig} = +\mathbf{k}_1 + \mathbf{k}_2 - \mathbf{k}_3$ phase matching direction. Although these diagrams are selected against in the boxcar geometry that is commonly used for echo experiments, when all three pulses overlap the time ordering between them becomes ambiguous, and these diagrams can contribute to the response.[38] In the following chapters, calculations of the third-order response will largely be made assuming impulsive excitation of the system, and contributions to the nonlinear response from S_{III} processes will be ignored unless noted.

In the case that two separate vibrational transitions fall within the bandwidth of the excitation pulses, a vibrational echo due to each isolated transition will be observed. However, if these two transitions are coupled, new signals can be observed that are generated by the exchange of energy between the two vibrations during the waiting period.[6] Fortunately, each of these separate contributions to the third-order signal can be separated by using coherent multidimensional spectroscopy.

2.5.1. Two-Dimensional Infrared Spectroscopy

Two-dimensional infrared (2D IR) spectroscopy is the vibrational analogue of other types of coherent multidimensional spectroscopies, such as two-dimensional NMR and electronic spectroscopy. These spectroscopies are able to identify different contributions to a nonlinear signal field by spreading the signal across two frequency axes.[5,6,46,47] As with all third-order vibrational techniques, three infrared electromagnetic fields stimulate the emission of a signal field. In 2D IR spectroscopy, this signal is detected interferometrically by overlapping it with a fourth reference pulse called the local oscillator (Fig. 2-6A), which allows for the complete characterization of the phase and amplitude of the signal field. A 2D IR spectrum is constructed by scanning the τ_1 and τ_3 time delays for a fixed value of τ_2. Fourier transform of the τ_1 and τ_3 time axes yields a frequency domain 2D spectrum with complimentary frequency axes, ω_1 and ω_3. The ω_1 frequency axis of a 2D spectrum corresponds to the frequency of interaction between the first laser pulse and the system, whereas the ω_3 axis corresponds to the frequency of the detected signal field.

For every peak that appears in the linear infrared spectrum of a sample, a corresponding peak will appear along the diagonal axis of a 2D spectrum. The shape of each transition is dictated by the degree of inhomogeneity associated with the transition. As the waiting period between excitation and detection, τ_2, is increased, transitions that dephase faster than τ_2 take on homogeneous, round shapes, whereas peaks comprised of an inhomogeneous distribution of transition energies remain diagonally elongated (Fig. 2-7). Metrics that quantify time dependent changes in the shape of peaks in 2D spectra due to spectral diffusion are given in Chapter 3. Couplings between vibrational states give

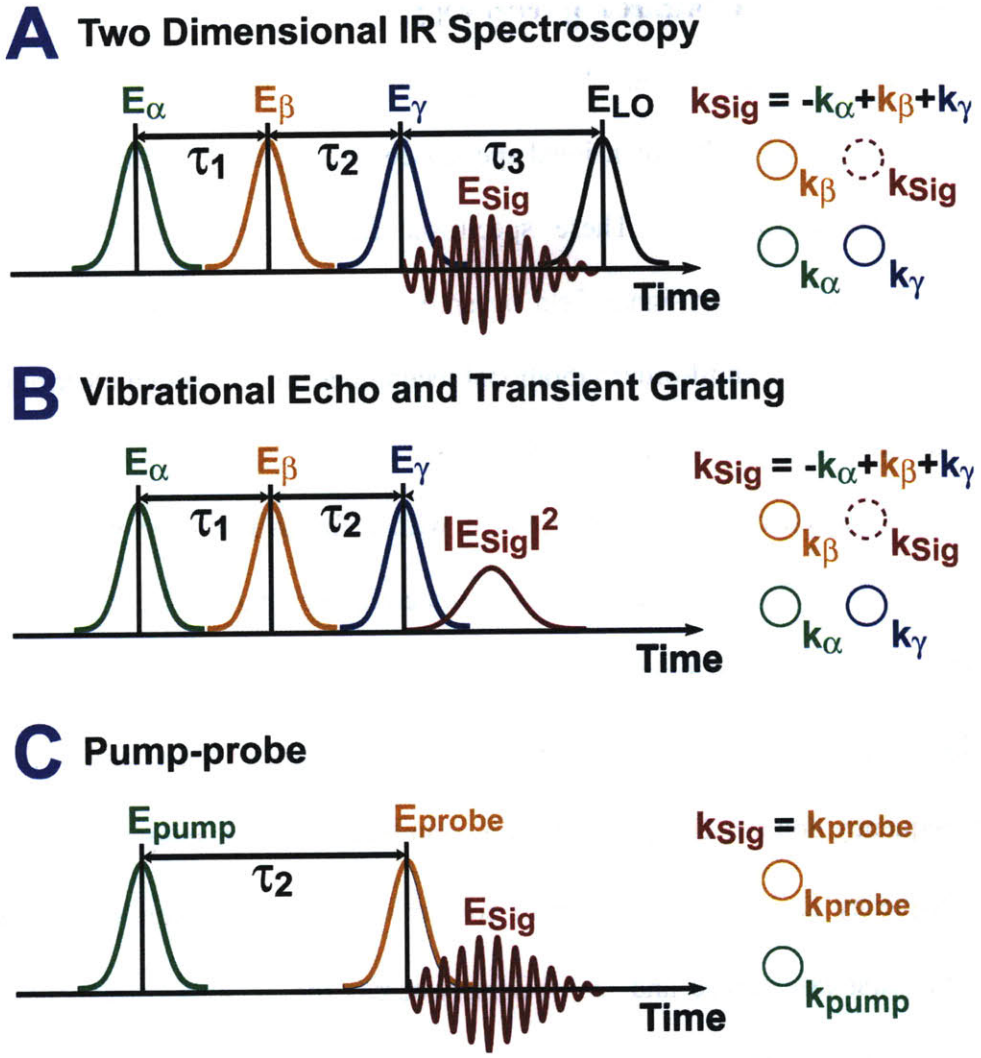


Figure 2-6: Pulse sequences, geometries, and phase matching conditions for (A) 2D IR spectroscopy, (B) vibrational echo peak shift and transient grating measurements, and (C) pump-probe experiments. In the experiments pictured in (A) and (B), a boxcar geometry is employed. Given the constraints imposed by wave vector matching, the signal is emitted in the missing corner of the box formed by the excitation pulses. In 2D IR spectroscopy, an additional reference field is overlapped with the signal that allows phase sensitive detection of the emitted signal field. In the pump-probe experiment, both a +**k** and –**k** interaction are generated by the pump pulse, causing the signal field to be emitted along the direction of the probe.

rise to cross peaks between transitions that appear along the diagonal axis. As τ_2 is increased, new cross peaks can appear that indicate the flow of population from one transition to another.[48] Since vibrational transitions are inherently multilevel systems, for

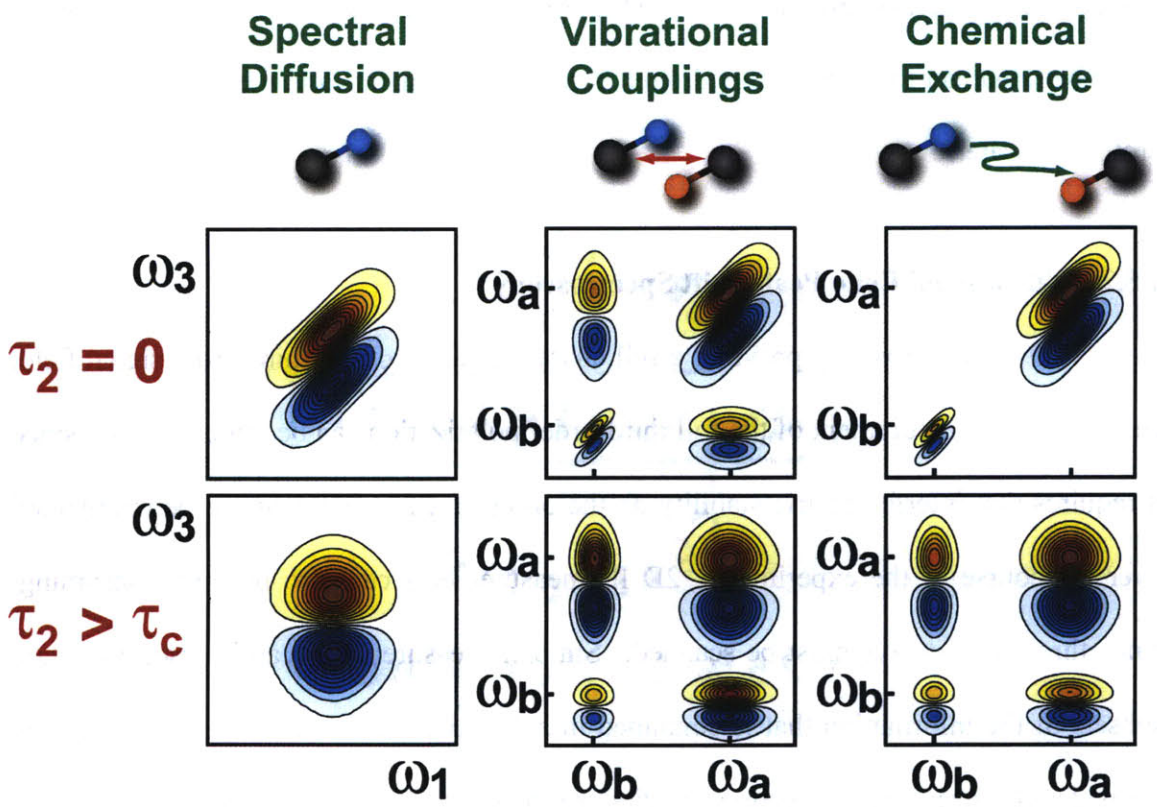


Figure 2-7: Schematic illustration of the information content of 2D IR spectra. For the anharmonic vibrations studied here, peaks in 2D IR spectra appear as positive/negative doublets. The positive peak corresponds to the ground state bleach of the v = 0←1 transition whereas the negative peak is due to excited state absorption of the v = 2←1 transition and is anharmonically shifted along ω_3. At $\tau_2 = 0$, diagonal peak appears for each excited transition that is elongated along the diagonal axis (upper left panel). As τ_2 increases and the system undergoes spectral diffusion, the peaks assume a round, homogeneous lineshape (lower left). Couplings between different vibrational transitions give rise to cross peaks in the $\tau_2 = 0$ 2D spectrum (upper middle). Chemical exchange processes can lead to the appearance of cross peaks with increasing waiting time (upper and lower right). The kinetics that give rise to this process will be discussed in Chapter 6.

each positive peak that appears in a 2D IR spectrum, a corresponding negative peak appears that is anharmonically shifted along the ω_3 axis. This negative feature corresponds to a photoinduced absorption involving a v = 2 ← 1 transition (See Fig. 2-5). Since a strong correlation exists between the frequency of the O-H stretching transition of dilute HOD dissolved in either D_2O or NaOD solution and the local hydrogen bonding environment, the time scales over which experimental 2D spectra are observed to

broaden as well as asymmetries in the 2D lineshapes are related to the fluctuations of the water bath that act to drive both hydrogen bond rearrangements and the motion of excess protons in water.

2.5.2. Vibrational Echo Peak Shift Spectroscopy

2D IR spectroscopy provides a full characterization of the third-order signal field. However, the measurement of the full third-order polarization can be quite difficult, since it requires that interferometric stability on the order of a few hundred nm be maintained over the course of the experiment. 2D IR measurements can also be time consuming, since three time delays must be scanned. Simpler measurements can be used to obtain subsets of the information that is contained in a 2D spectrum. These measurements are equivalent to measuring projections or slices of the third-order response function.

Vibrational echo peak shift spectroscopy is the homodyne analogue of the 2D IR experiment. The pulse sequence for a peak shift measurement is identical to that used for 2D IR, but no reference pulse is interfered with the emitted signal field. Thus, the measured echo intensity is equivalent to the absolute value of the third-order signal field integrated along the τ_3 time axis:[1,2,49]

$$I_{echo}(\tau_2,\tau_1) \propto \int_{-\infty}^{\infty} d\tau_3 \left|\mathbf{E}_{sig}(\tau_3,\tau_2,\tau_1)\right|^2. \tag{2-38}$$

Due to the rephasing contributions to the vibrational echo described above and illustrated in Fig. 2-4, for $\tau_2 = 0$, a strong echo signal peaked at a positive value of τ_1 will be observed. As τ_2 increases and the vibrational frequencies of the system become randomized due to fluctuations of the surrounding environment, the echo will decrease in intensity and peak at increasingly smaller values of τ_1. The value of τ_1 that maximizes

the emitted echo signal for a given value of τ_2 is referred to as the echo peak shift, and its decay is related to the loss of frequency memory due to spectral diffusion. Since the observable that is measured in peak shift spectroscopy is not dependent on the total amplitude of the recorded signal field, the peak shift is largely insensitive to effects due to population relaxation.

A major advantage that peak shift spectroscopy possesses with respect to 2D IR experiments is that the peak shift experiment does not require that stages be scanned interferometrically and only two time delays (verses three in 2D IR) need to be controlled. This allows for the rapid collection of data as a function of the waiting period, τ_2. Unfortunately, the simplistic interpretation of the peak shift experiment given above is only valid in the situation where the excitation pulses interact with a single vibrational transition. Since the peak shift is not a phase sensitive measurement, it cannot differentiate signals from different transitions based on their frequency of vibration. The peak shift is also fairly insensitive to the presence of vibrational couplings that give rise to cross peaks in 2D IR spectra. Despite these disadvantages, we shall see in Chapters 5 and 6 that the peak shift is a useful technique that can indicate how the dynamics of a system vary as a function of an external variable, such as temperature or the concentration of a particular species.

2.5.3. Pump-Probe and Transient Grating Spectroscopy

In a pump-probe experiment, only a single pulse, the pump, is used to excite the sample, and the effect of the excitation is determined by measuring the change in transmission of a reference probe pulse that is time delayed with respect to the pump. In terms of the third-order formalism described above, the first pump interacts twice with

the sample, once along both the $+\mathbf{k}_{pump}$ and $-\mathbf{k}_{pump}$ directions. The probe then stimulates the emission of the signal field along the $+\mathbf{k}_{probe}$ direction, enabling the probe to also serve as the experiment's local oscillator. Since the first two field-matter interactions occur within the envelope of the pump pulse, τ_1 is effectively equal to zero, which precludes the generation of a photon echo and lowers the sensitivity of the measurement to spectral diffusion.[50] Instead, the pump pulse rapidly creates an excited population state, and the decay of the pump-probe signal reports on how quickly energy flows out of this state and into the remaining modes of the system.

Because molecules preferentially absorb when the polarization of the excitation field lies parallel to the axis of the molecule's transition dipole, a change of the pump-probe signal can also be caused by the reorientation of excited molecules into or out of the plane of the probe pulse. For a molecule that engages in diffusive reorientation, the contribution to the pump-probe signal due to reorientation can be canceled by orienting the pump and probe pulses at the magic angle (54.7°) with respect to each other.[40] This angle can be derived by recognizing that the pump pulse excites a $\cos^2\theta$ distribution of molecules that will diffusively reorient to an isotropic distribution with time. The magic angle corresponds to the angle where these two normalized angular distributions are equivalent. Hence, signals measured at this angle are invariant to reorientation.

A relationship between the signals measured by pump-probe and 2D IR experiments can be derived by making use of the projection-slice theorem. This theorem states that the 1D projection of a 2D frequency domain spectrum onto a line that passes through the origin and has an angle θ between it and the horizontal axis forms a Fourier transform pair with the equivalent slice through the 2D time domain signal.[5,46] This has

the consequence that the projection of a 2D frequency domain spectrum onto the ω_3 axis is equivalent to the frequency resolved pump-probe signal.

Transient grating experiments are similar to pump-probe measurements in that they mainly probe vibrational population dynamics and the reorientation of molecules. While the first two interactions in a pump-probe measurement are both derived from the pump pulse, in a transient grating experiment these two interactions come from two separate pulses with different **k** vectors that are temporally overlapped in the sample. The third pulse then stimulates the emission of a signal field in a background free direction, generally allowing for improved signal to noise relative to a pump-probe measurement. Unfortunately, this improved signal to noise comes at a cost in that the transient grating experiment is a homodyne measurement. In the case that multiple vibrations contribute to the third-order polarization, the measured transient grating signal will contain cross terms between the signals generated by each of these separate vibrations that are not present in the pump-probe experiment. Additionally, terms due to the nonresonant excitation of vibrational transitions near those of interest can make large contributions to the signal field,[37,51] further complicating the analysis of transient grating experiments. Nonetheless, as with the peak shift experiment the transient grating technique can prove to be very useful when looking for changes in the dynamics of a system as an external variable is systematically changed.

References

(1) T. Joo, Y. Jia, J.-Y. Yu, M. J. Lang and G. R. Fleming, "Third-order nonlinear time-domian probes of solvation dynamics," J. Chem. Phys. 104, 6089 (1996).

(2) W. P. de Boeij, M. S. Pshenichnikov and D. A. Wiersma, "Ultrafast solvation dynamics explored by femtosecond photon echo spectroscopies," Annu. Rev. Phys. Chem. 49, 99 (1998).

(3) J. C. Deàk, Y. Pang, T. D. Sechler, Z. Wang and D. D. Dlott, "Vibrational energy transfer across a reverse micelle surfactant layer," Science 306, 473 (2004).

(4) M. D. Fayer, "Dynamics of liquids, molecules, and proteins measured with ultrafast vibrational echo chemical exchange spectroscopy," Annu. Rev. Phys. Chem. 60, 21 (2008).

(5) D. M. Jonas, "Two-dimensional femtosecond spectroscopy," Annu. Rev. Phys. Chem. 54, 397 (2003).

(6) M. Khalil, N. Demirdoven and A. Tokmakoff, "Coherent 2D IR spectroscopy: Molecular structure and dynamics in solution," J. Phys. Chem. A 107, 5258 (2003).

(7) M. Cho, "Coherent two-dimensional optical spectroscopy," Chem. Rev. 108, 1331 (2008).

(8) S. Mukamel and D. Abramavicius, "Many-Body approaches for simulating coherent nonlinear spectorscopy of electronic and vibrational excitons," Chem. Rev. 104, 2073 (2004).

(9) K. Kwak, J. Zheng, H. Cang and M. D. Fayer, "Ultrafast two-dimensional infrared vibrational echo chemical exchange experiments and theory," J. Phys. Chem. B 110, 19998 (2006).

(10) J. L. McHale, *Molecular Spectroscopy*, (Prentice Hall, Upper Saddle River, NJ, 1999).

(11) Y. R. Shen, *The Principles of Nonlinear Optics*, (Wiley-Interscience, New York, 1984).

(12) S. Mukamel, *Principles of Nonlinear Optical Spectroscopy*, (Oxford University Press, New York, 1995).

(13) S. M. Gallagher Faeder and D. M. Jonas, "Phase-resolved time-domain nonlinear optical signals," Phys. Rev. A. 62, 033820 (2000).

(14) J. Sung and R. J. Silbey, "Four-wave mixing spectroscopy for a multi-level system," J. Chem. Phys. 115, 9266 (2001).

(15) J. G. Saven and J. L. Skinner, "A molecular theory of the line shape: Inhomogeneous and homogeneous electronic spectra of dilute chromophores in nonpolar fluids," J. Chem. Phys. 99, 4391 (1993).

(16) K. Kwac, H. Lee and M. Cho, "Non-Gaussian statistics of amide I mode frequency fluctuation of N-methylacetamide in methanol solution: Linear and nonlinear vibrational spectra," J. Chem. Phys. 120, 1477 (2004).

(17) J. R. Schmidt, S. A. Corcelli and J. L. Skinner, "Pronounced non-Condon effects in the ultrafast infrared spectroscopy of water," J. Chem. Phys. 123, 044513 (2005).

(18) S. Mukamel, "On the semiclassical calculation of molecular absorption and fluorescence spectra," J. Chem. Phys. 77, 173 (1982).

(19) S. Mukamel, "Collisional broadening of spectral line shapes in two-photon and multiphoton processes," Phys. Rep. 93, 1 (1982).

(20) Y. J. Yan and S. Mukamel, "Photon Echoes of polyatomic molecules in condensed phases," J. Chem. Phys. 94, 179 (1991).

(21) J. Sung and R. J. Silbey, "Optical four wave mixing spectroscopy for multilevel systems coupled to multimode Brownian oscillators," J. Chem. Phys. 118, 2443 (2003).

(22) G. H. Herzberg, *Spectra of Diatomic Molecules*, 2nd, (Van Nostrand, New York, 1950).

(23) A. Novak, "Hydrogen bonding in solids. Correlation of spectroscopic and crystallographic data," in *Structure and Bonding*, edited by J. D. Dunitz et al., (Springer-Verlag, New York, 1974).

(24) G. C. Pimentel and A. L. McClellan, *The Hydrogen Bond*, (Freeman, San Francisco, 1960).

(25) S. A. Corcelli and J. L. Skinner, "Infrared and Raman line shapes of dilute HOD in liquid H_2O and D_2O from 10 to 90 ^{o}C," J. Chem. Phys. 109, 6154 (2005).

(26) B. Auer, R. Kumar, J. R. Schmidt and J. L. Skinner, "Hydrogen bonding and Raman, IR, and 2D-IR spectroscopy of dilute HOD in D_2O," Proc. Natl. Acad. Sci. U.S.A. 104, 14215 (2007).

(27) S. T. Roberts, P. B. Petersen, K. Ramasesha, A. Tokmakoff, I. S. Ufimtsev and T. J. Martinez, "Observation of a Zundel-like transition state during proton transfer in aqueous hydroxide solutions," Proc. Natl. Acad. Sci. U.S.A. 106, 15154 (2009).

(28) A. M. Walsh and R. F. Loring, "Time resolved stimulated light scattering from a solvated chromophore: A molecular dynamics study," J. Chem. Phys. 94, 7575 (1991).

(29) L. E. Fried and S. Mukamel, "Structure, dynamics, and the electronic absorption of benzene-argon clusters," J. Chem. Phys. 96, 116 (1992).

(30) R. Rey, K. B. Møller and J. T. Hynes, "Hydrogen bond dynamics in water and ultrafast infrared spectroscopy," J. Phys. Chem. A 106, 11993 (2002).

(31) C. P. Lawrence and J. L. Skinner, "Vibrational spectroscopy of HOD in liquid D_2O. I. Vibrational energy relaxation," J. Chem. Phys. 117, 5827 (2002).

(32) J. D. Eaves, A. Tokmakoff and P. Geissler, "Electric field fluctuations drive vibrational dephasing in water," J. Phys. Chem. A 109, 9424 (2005).

(33) T. Hayashi, T. l. C. Jansen, W. Zhuang and S. Mukamel, "Collective solvent coordinates for the infrared spectrum of HOD in D_2O based on an *ab initio* electrostatic map," J. Phys. Chem. A 109, 64 (2005).

(34) J. D. Eaves, J. J. Loparo, C. J. Fecko, S. T. Roberts, A. Tokmakoff and P. L. Geissler, "Hydrogen bonds in liquid water are broken only fleetingly," Proc. Natl. Acad. Sci. U.S.A. 102, 13019 (2005).

(35) J. J. Loparo, S. T. Roberts and A. Tokmakoff, "Multidimensonal infrared spectroscopy of water. II. Hydrogen bond switching dynamics," J. Chem. Phys. 125, 194522 (2006).

(36) S. T. Roberts, K. Ramasesha and A. Tokmakoff, "Structural rearrangements in water viewed through two-dimensional infrared spectroscopy," Acc. Chem. Res. 42, 1239 (2009).

(37) S. Yeremenko, M. S. Pshenichnikov and D. A. Wiersma, "Interference effects in IR photon echo spectroscopy of liquid water," Phys. Rev. A 73, 021804 (2006).

(38) C. J. Fecko, J. J. Loparo, S. T. Roberts and A. Tokmakoff, "Local hydrogen bonding dynamics and collective reorganization in water: Ultrafast IR spectroscopy of HOD/D_2O," J. Chem. Phys. 122, 054506 (2005).

(39) B. J. Berne and R. Pecora, *Dynamic Light Scattering with Applications to Chemistry, Biology, and Physics*, (R. E. Krieger Publishing Co., Malabar, FL, 1990).

(40) A. Tokmakoff, "Orientational correlation functions and polarization selectivity for nonlinear spectroscopy of isotropic media. I. Third order," J. Chem. Phys. 105, 1 (1996).

(41) N. Nandi, K. Bhattacharyya and B. Bagchi, "Dielectric relaxation and solvation dynamics of water in complex chemical and biological systems," Chem. Rev. 100, 2013 (2000).

(42) D. W. G. Smith and J. G. Powles, "Proton spin-lattice relaxation in liquid water and liquid ammonia," Mol. Phys. 10, 451 (1966).

(43) H. J. Bakker, Y. L. A. Rezus and R. L. A. Timmer, "Molecular reorientation of liquid water studies with femtosecond midinfrared spectroscopy," J. Phys. Chem. A 112, 11523 (2008).

(44) J. J. Loparo, C. J. Fecko, J. D. Eaves, S. T. Roberts and A. Tokmakoff, "Reorientational and configurational fluctuations in water observed on molecular length scales," Phys. Rev. B 70, 180201 (2004).

(45) M. Khalil, N. Demirdöven and A. Tokmakoff, "Obtaining absorptive lineshapes in two-dimensional infrared vibrational correlation spectra," Phys. Rev. Lett. 90, 47401 (2003).

(46) R. R. Ernst, G. Bodenhausen and A. Wokaun, *Principles of Nuclear Magnetic Resonance in One and Two Dimensions*, (Oxford University Press, Oxford, 1987).

(47) S. Mukamel, "Multidimensional femtosecond correlation spectroscopies of electronic and vibrational excitations," Ann. Rev. Phys. Chem. 51, 691 (2000).

(48) J. R. Zheng, K. Kwak, J. Asbury, X. Chen, I. R. Piletic and M. D. Fayer, "Ultrafast dynamics of solute-solvent complexation observed at thermal equilibrium in real time," Science 309, 1338 (2005).

(49) P. Hamm, M. Lim and R. M. Hochstrasser, "Non-Markovian dynamics of the vibrations of ions in water from femtosecond infrared three-pulse photon echoes," Phys. Rev. Lett. 81, 5326 (1998).

(50) D. A. Farrow, A. Yu and D. M. Jonas, "Spectral relaxation in pump-probe transients," J. Chem. Phys. 118, 9348 (2003).

(51) S. Yeremenko, *Water Dynamics Explored by Femotsecond Infrared Spectroscopy*, Ph.D Thesis, University of Groningen, Dept. of Physical Chemistry, 2004.

Chapter 3

Characterization of Spectral Diffusion from 2D Lineshapes

3.1. Introduction

The dynamics of molecules in the condensed phase are commonly studied with experiments that characterize transition energy fluctuations and spectral diffusion.[1-6] Since the vibrational or electronic energy gap of a molecule depends on interactions with its surroundings, such experiments can report on the configurational changes of the local environment and the time-scales for the evolution of the bath. As described in the previous chapter, a number of ultrafast four-wave mixing techniques capable of tracking the frequency dynamics of molecules have been developed. The spectral relaxation in such experiments is commonly modeled by making use of the Condon and second Cumulant approximations, which allows characterization of the amplitude and time scale of frequency fluctuations and spectral diffusion in terms of an energy gap time correlation function:[1,7]

$$C(\tau) = \left\langle \delta\omega_{10}(\tau)\,\delta\omega_{10}(0) \right\rangle . \tag{3-1}$$

Here, $\omega_{10} = (E_1 - E_0)/\hbar$, and denotes the difference in energy between the ground state of the system, $|0\rangle$, and the first excited state, $|1\rangle$, and $\delta\omega_{10}(\tau) = \omega_{10}(\tau) - \langle\omega_{10}\rangle$.

Although this simplistic description of a system's dynamics breaks down if the fluctuations of the system do not obey Gaussian statistics,[8] $C(\tau)$ remains a useful parameter since it describes the average time scale over which the system reorganizes itself.

Perhaps the most widely used spectroscopy for the determination of $C(\tau)$ is the three pulse photon echo peak shift experiment.[2,9] In certain limits, the peak shift measurement is directly proportional to $C(\tau)$, providing a readily available semi-quantitative approach to characterizing spectral diffusion.[10-12] However, a quantitative analysis depends on experimental pulse parameters, meaning that a trial form for $C(\tau)$ is often guessed, used to calculate the nonlinear observable, and then iteratively adjusted to give the best agreement with the measured data. Since this procedure is involved, experimental observables that can be more directly related to $C(\tau)$ would be highly advantageous.

Two dimensional optical and infrared spectroscopy are the newest methods that are being used to provide a measure of $C(\tau)$.[6,13-17] The two-dimensional lineshape is a characterization of how a distribution of frequencies evolves with time.[5,6,8,15,17,18] The 2D spectrum is closely related to the joint probability that a molecule has an initial vibrational frequency ω_1 and reaches a final vibrational frequency ω_3 after a waiting period, τ_2. Thus, a static inhomogeneous lineshape is diagonally elongated, a homogeneous system is symmetric, and the spectral diffusion observed by changing τ_2 leads from one limit to the other. Several quantities that can be calculated from changes to a 2D lineshape as a function of τ_2, have been related to the decay of $C(\tau)$. Many

groups have noted the similarity between $C(\tau)$ and the tilt of the node in either imaginary 2D electronic lineshapes or absorptive 2D IR lineshapes.[5,17-19] Fayer and co-workers[14] have suggested that the linewidth of the 2D spectrum for a constant value of ω_3, the dynamical linewidth, is related to $C(\tau)$. Hamm has shown that the covariance of the normalized 2D spectrum is equal to $C(\tau)$ under certain limits,[20] while Pshenichnikov and co-workers have proposed an analysis of the ellipticity of the 2D lineshape to determine $C(\tau)$.[21]

The goal of this chapter is to show how, within certain approximations, different observables obtained from 2D spectra are related to the frequency correlation function, $C(\tau)$. In addition to previous suggestions, we propose new metrics that characterize the decay of $C(\tau)$ independent of lifetime amplitude decay, and analytically demonstrate their relationship to $C(\tau)$. We then calculate these same metrics without making the restrictive approximations that enabled their derivation and include the effects of finite duration excitation fields in the calculation to test how well each metric estimates $C(\tau)$ when a more realistic calculation of the third-order polarization is performed. While these metrics are no longer directly equal to $C(\tau)$ when these calculations are performed, they still track the shape of the correlation function at early waiting times and show similar asymptotic behavior for large waiting times. The validity of these relationships is also analyzed for two-level and three-level systems, characteristic of single electronic and vibrational resonances, respectively.

3.2. Response Function Formalism

The modeling of spectral evolution in Fourier transform 2D IR [6,7,22] and electronic [1,23-25] experiments is based on the third-order nonlinear response function, $R^{(3)}(\tau_3,\tau_2,\tau_1)$. $R^{(3)}$ describes the evolution of the system during three consecutive time intervals and, in the short pulse limit, is directly proportional to the signal measured in these experiments. By assuming that the fluctuations of the transition frequency follow Gaussian statistics (second-order Cumulant approximation) and that the transition moment is independent of the bath variables (Condon approximation), the response function for a simple two-level system can be expressed in terms of a single dynamical quantity, the frequency correlation function, $C(\tau)$.[1]

Although analytical, the expressions are cumbersome.* However, the form can be greatly simplified through two further approximations. Here we make the short time approximation that assumes that the dephasing dynamics described by $C(\tau)$ negligibly impact the evolution of the response during τ_1 and τ_3, and for simplicity examine the high temperature limit in which $C(\tau)$ is real. Then, one can express $R^{(3)}$ as a sum of two terms, the rephasing and nonrephasing responses:[12,17,26]

$$R^{(3)}(\tau_3,\tau_2,\tau_1) = R_-^{(3)}(\tau_3,\tau_2,\tau_1) + R_+^{(3)}(\tau_3,\tau_2,\tau_1), \tag{3-2}$$

where:

$$R_\pm^{(3)} = \exp\left[-\frac{1}{2}C(0)\left(\tau_1^2+\tau_3^2 \pm 2\tau_1\tau_3\bar{C}(\tau_2)\right) + i\Omega(\pm\tau_1+\tau_3) - \tau_2/T_1\right]\theta(\tau_1)\theta(\tau_3). \tag{3-3}$$

* See Section 2.4.2 of Chapter 2 for a full description of the calculation of the third-order response function within the limits of the Second Cumulant approximation.

Here $\theta(\tau)$ is the unit step function, $\bar{C}(\tau)$ is the normalized frequency correlation function $\bar{C}(\tau) = \langle \delta\omega_{10}(\tau)\delta\omega_{10}(0)\rangle / \langle \delta\omega_{10}^2 \rangle$, and $\Omega = \langle \omega_{10} \rangle$. Population relaxation, characterized by a time scale T_1, has been included phenomenologically.

Due to the difference in the sign of the oscillation of the phase during the two coherence periods, τ_1 and τ_3, the "–" term in Eq. 3-3 describes rephasing processes that give rise to a strong echo response as long as the waiting time, τ_2, is short enough that $C(\tau)$ has not significantly decayed. The "+" term however simply decays away monotonically, closely resembling a free induction decay. As described in Chapter 2, due to their sensitivity to $C(\tau)$ the behavior of rephasing signals are most commonly used to characterize spectral diffusion. We note that a result of the short time approximation is that the rephasing signal shows no decay along the diagonal axis for $\tau_2 = 0$.

The 2D spectra that are analyzed for signatures of spectral diffusion are obtained from a two-dimensional Fourier transformation with respect to the τ_1 and τ_3 evolution:

$$S(\omega_3, \tau_2, \omega_1) = \frac{1}{2\pi} \int_{-\infty}^{\infty} \int_{-\infty}^{\infty} \exp[-i\omega_1\tau_1 - i\omega_3\tau_3] R(\tau_3, \tau_2, \tau_1) d\tau_1 d\tau_3 . \qquad (3\text{-}4)$$

The complex 2D correlation spectra $(S_C = S_C' + iS_C'')$ as a function of the conjugate variables ω_1 and ω_3 are obtained from a sum of rephasing and nonrephasing spectra $(S_C = S_+(\omega_3, \omega_1) + S_-(\omega_3, -\omega_1))$.[24,27] The real part or absorptive 2D IR correlation spectrum, S_C', is most commonly presented, but we here also examine the 2D IR phase spectrum $S_\varphi = \tan^{-1}[S_C''/S_C']$.

3.3. Analysis of Lineshapes

Fig. 3-1 shows examples of these spectra calculated for a two-level system for waiting times short and long compared to the correlation time for $C(\tau)$, $\tau_c = \int_0^\infty \bar{C}(\tau)d\tau$. These lineshapes are characteristic of the inhomogeneous and homogeneous limits. Due to the difference in the sign of the phase accumulated during the coherence periods, τ_1 and τ_3, in the rephasing spectrum (Eq. 3-3), a strong echo signal is observed along the diagonal time axis ($\tau_1 = \tau_3$) when the frequency memory of the system is largely preserved (i.e. $C(\tau)$ has not decayed). In the frequency domain, this leads to the rephasing spectrum being aligned along the diagonal axis (Fig. 3-1A). Conversely, the phase of the nonrephasing spectrum is the same during both τ_1 and τ_3, causing the frequency domain representation to be aligned along the antidiagonal axis (Fig. 3-1B). For the inhomogeneous case, the amplitude of the rephasing signal is greater than the nonrephasing signal, which leads to a diagonally elongated absorptive lineshape (Fig 3-1C). In the homogeneous limit, the rephasing and nonrephasing amplitudes equalize, giving a symmetric absorptive lineshape.[†]

This change in peak symmetry is also apparent in the phase spectrum of the complex 2D lineshape as a change of orientation for the lines of constant phase. For the complex rephasing and nonrephasing spectra, the lines of constant phase are oriented along the diagonal and antidiagonal axes respectively and do not rotate with waiting time. For early waiting times, the larger rephasing signal causes the lines of constant phase to be preferentially oriented along the diagonal axis (Fig. 3-1D). As the intensity of the

[†] Within the Bloch limit it is assumed that $C(\tau)$ decays infinitely fast during both τ_1 and τ_3, resulting in a 2D Lorentzian lineshape in the homogeneous limit.[28] Under the short time expansion however, $C(\tau)$ does not decay during the coherence periods, instead yielding a 2D Gaussian lineshape.

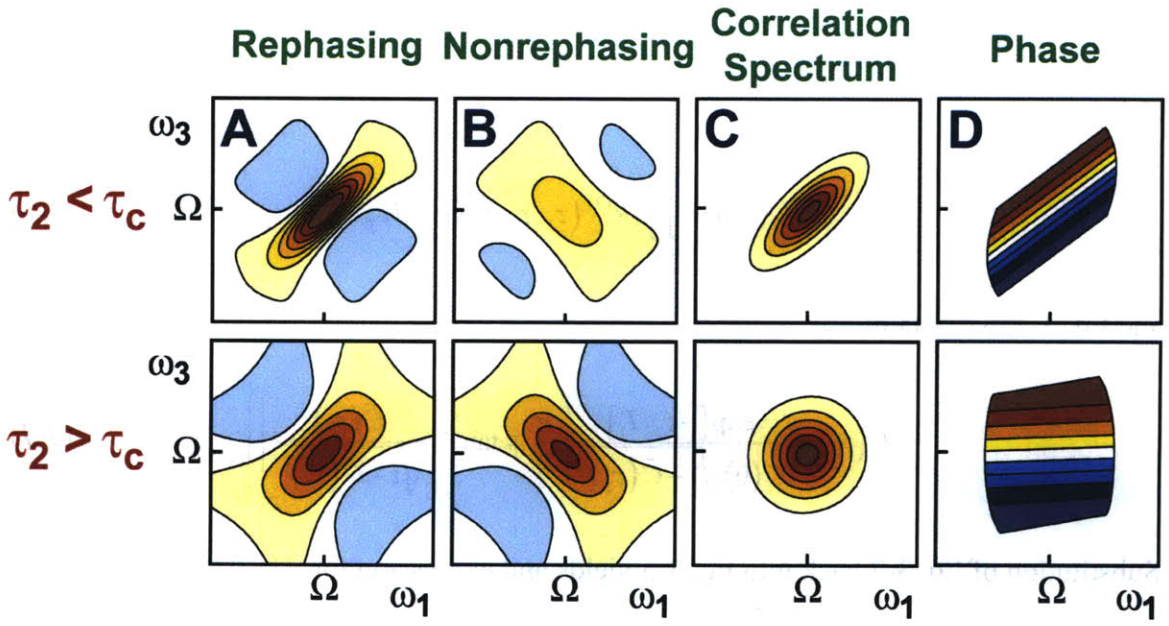


Figure 3-1: Illustration of 2D spectra in both the inhomogeneous ($\tau_2 >> \tau_C$) and homogeneous ($\tau_2 << \tau_C$) limits. The rephasing (A) and nonrephasing (B) spectra are aligned along the diagonal and antidiagonal axes respectively. For waiting times shorter than the correlation time, the rephasing signal is much stronger than the nonrephasing signal, causing the 2D surface (C) to be diagonally elongated. For waiting times much larger than the correlation time, the rephasing and nonrephasing spectra equalize in intensity leading to a symmetric lineshape. The phase (D) of the 2D surface (rephasing plus nonrephasing) reflects this loss of correlation by rotating away from the diagonal to become parallel to the ω_1 axis.

rephasing and non rephasing spectra equalize with increasing waiting time, the phase lines rotate to become parallel with the ω_1 axis.

The trends observed in Fig. 3-1 suggest a number of different spectral features that can be analyzed to obtain $C(\tau)$. Because the persistence of frequency memory is reflected in the imbalance of amplitude between the rephasing and nonrephasing signals, we postulate that the amplitude difference between these two signals is a measure of $C(\tau)$. We define a quantity, the inhomogeneity index, I, which is the normalized difference between these two signals:

$$I = \frac{A_- - A_+}{A_- + A_+} \tag{3-5}$$

Using:

$$A_\pm(\tau_2) = \int_0^\infty \int_0^\infty \left| R_\pm^{(3)}(\tau_3, \tau_2, \tau_1) \right| d\tau_1 d\tau_3 \tag{3-6}$$

and Eq. 3-3, we obtain:

$$A_\pm(\tau_2) = \frac{\exp[-\tau_2/T_1]}{C(0)\sqrt{1-\bar{C}(\tau_2)^2}} \left(\frac{\pi}{2} \mp \tan^{-1}\left[\frac{\bar{C}(\tau_2)}{\sqrt{1-\bar{C}(\tau_2)^2}} \right] \right) \tag{3-7}$$

Substitution of Eq. 3-7 back into Eq. 3-5 yields and expression for $I(\tau_2)$:

$$I(\tau_2) = -\frac{2}{\pi} \tan^{-1}\left[\frac{\bar{C}(\tau_2)}{\sqrt{1-\bar{C}(\tau_2)^2}} \right] \tag{3-8}$$

This expression can be inverted to give a simple expression for $C(\tau)$ in terms of I:

$$\bar{C}(\tau_2) = \sin\left[\frac{\pi I}{2} \right]. \tag{3-9}$$

For small values of I (i.e. for $\tau_2 > \tau_C$), $C(\tau_2)$ and $I(\tau_2)$ are directly proportional. Furthermore, looking at Eq. 3-7, we can see that the sum of the integrated absolute values of the rephasing and nonrephasing signals can be used to characterize the population relaxation time scale:

$$A_+ + A_- = \frac{\pi}{C(0)\sqrt{1-\bar{C}(\tau_2)^2}} \exp[-\tau_2/T_1]. \tag{3-10}$$

The dependence of Eq. 3-10 on $C(\tau_2)$ describes the amplitude decay of the coherent polarization as the dipoles of the ensemble dephase, and disappears as the waiting time becomes very large. Although the sum of rephasing and nonrephasing amplitudes

depends on $C(\tau)$, the combination of sum and differences can be used to separate the vibrational dynamics of population relaxation from those of frequency fluctuations and spectral diffusion.

In addition to the inhomogeneity index, the slant of the spectral phase of the 2D surface can be used to calculate $C(\tau)$. Since the imbalance in intensity between rephasing and nonrephasing signals tracks the decay of $C(\tau)$, for early waiting times the lines of constant spectral phase are primarily oriented along the diagonal axis. As τ_2 increases, the phase lines rotate to become parallel with the ω_1 axis. Normally, Eq. 3-4 provides the Fourier transform relationship that is used to obtain the rephasing and nonrephasing spectra. Rather than evaluating these separately, we note the symmetry of Eq. 3-3 with respect to τ_1, and Fourier transform the sum of these two terms:

$$S_C(\omega_3,\tau_2,\omega_1) = \frac{\exp[-\tau_2/T_1]}{2\pi} \times \int_0^\infty d\tau_3 \int_{-\infty}^\infty d\tau_1 \exp\left[-\frac{C(0)}{2}\left(\tau_1^2+\tau_3^2-2\tau_1\tau_3\bar{C}(\tau_2)\right)-i\left(\Delta_1\tau_1+\Delta_3\tau_3\right)\right] \quad (3\text{-}11)$$

Here we have defined the detunings $\Delta_1 = \omega_1 - \Omega$ and $\Delta_3 = \omega_3 - \Omega$. Evaluating Eq. 3-12, we obtain:

$$S_C(\Delta_3,\tau_2,\Delta_1) = \frac{\exp[-\tau_2/T_1]}{2C(0)\sqrt{\left(1-\bar{C}(\tau_2)^2\right)}} \times \exp\left[-\left(\frac{\Delta_3^2+\Delta_1^2-4\Delta_1\Delta_3\bar{C}(\tau_2)}{2C(0)\left(1-\bar{C}(\tau_2)^2\right)}\right)\right]\left(1-erf\left[\frac{i\left(\Delta_3-\Delta_1\bar{C}(\tau_2)\right)}{\sqrt{2C(0)\left(1-\bar{C}(\tau_2)^2\right)}}\right]\right). \quad (3\text{-}12)$$

Using this result, the phase spectrum is found to be:

$$S_{\phi}(\Delta_3,\tau_2,\Delta_1)=\tan^{-1}\left[-erfi\left[\frac{\Delta_3-\Delta_1\bar{C}(\tau_2)}{\sqrt{2C(0)\left(1-\bar{C}(\tau_2)^2\right)}}\right]\right] \tag{3-13}$$

where $erfi(x)=-ierf(ix)$.

We have shown that rotation of the lines of constant phase are related to the relaxation of $C(\tau)$.[8,18] In practice, extracting lines of constant phase from an experimentally measured 2D surface is difficult since the data is sampled on a square grid of points. As a more practical, yet equivalent approach, we calculate the slope of the spectral phase along ω_1 evaluated on resonance:

$$\beta(\tau_2)=\left.\frac{\partial S_{\phi}}{\partial\Delta_1}\right|_{\substack{\Delta_1=0\\ \Delta_3=0}}=\frac{\bar{C}(\tau_2)\sqrt{2}}{\sqrt{C(0)\pi\left(1-\bar{C}(\tau_2)^2\right)}}. \tag{3-14}$$

As with I, β can be inverted to give $C(\tau)$:

$$\bar{C}(\tau_2)=\sqrt{\frac{\beta^2\langle\delta\omega^2\rangle\pi}{2+\beta^2\langle\delta\omega^2\rangle\pi}} \tag{3-15}$$

As the waiting time becomes large, β approaches zero. In this limit the correlation function and β are directly proportional.

A third measure of $C(\tau)$ is the ellipticity of the 2D lineshape. The width of a peak appearing along the diagonal frequency axis of a 2D spectrum is related to the inhomogeneous distribution of oscillators that comprise the transition while the antidiagonal axis is related to their inherent homogeneous linewidth.[28,29] As the waiting time is increased, the effective time resolution of the experiment increases and the 2D lineshape becomes more circularly symmetric as molecules spectrally diffuse through the

available distribution of frequencies. Pshenichnikov[21] has suggested a definition for the ellipticity:

$$E = \frac{a^2 - b^2}{a^2 + b^2} \tag{3-16}$$

where a and b are the linewidths of the 2D resonance along the diagonal and antidiagonal axes, respectively. To determine these widths easily, we can rotate the reference frame to the diagonal and antidiagonal axes $\Delta_{\pm} = (\Delta_3 \pm \Delta_1)/\sqrt{2}$. The 2D surface then becomes:

$$S_c^{rot}(\Delta_-, \tau_2, \Delta_+) = \frac{\exp[-\tau_2/T_1]}{2C(0)\sqrt{\left(1-\bar{C}(\tau_2)^2\right)}} \exp\left[-\left(\frac{\Delta_-^2\left(1-\bar{C}(\tau_2)\right)+\Delta_+^2\left(1+\bar{C}(\tau_2)\right)}{2C(0)\left(1-\bar{C}(\tau_2)^2\right)}\right)\right]. \tag{3-17}$$

Setting either Δ_+ or Δ_- to zero yields a simple 2D Gaussian lineshape. Taking a and b to be the variance of these lineshapes, we find that the ellipticity is identical to the correlation function:

$$E = \bar{C}(\tau_2) \tag{3-18}$$

An additional measure of $C(\tau)$, put forth by Fayer and coworkers[14], is the dynamical linewidth. This quantity is defined as the FWHM of a slice of the real part of the 2D spectrum evaluated at $\Delta_3 = 0$. Using Eq. 3-12, we find that we can rewrite the correlation function in terms of the dynamical linewidth, Γ_{dyn}:

$$\bar{C}(\tau_2) = \sqrt{1 - \frac{\Gamma_{dyn}^2}{8\ln(2)C(0)}} \tag{3-19}$$

Finally, we note that 2D data can be used to construct another common measure of $C(\tau)$, the peak shift. This observable measured in three pulse photon echo experiments is given by the value of τ_1 that maximizes the intensity of the rephasing

signal integrated along τ_3 as a function of the waiting time. Several studies have established the close relationship between the peak shift measurement and $C(\tau)$.[10,11] For the response function given in Eq. 3-3 , the peak shift as a function of waiting time, denoted as τ_1*, is linearly dependent on $\bar{C}(\tau_2)$ in the limit where $\bar{C}(\tau_2) \ll 1$,[12,26]

$$\bar{C}(\tau_2) = \tau_1^* \sqrt{\pi C(0)}. \tag{3-20}$$

Eq. 3-9, 3-15, 3-18, and 3-19 are the most important results of this work, demonstrating how simple metrics obtained from 2D lineshapes can be formally related to the correlation function within the limit of the short time expansion. Moreover, as the waiting time becomes large, I, β, E, and τ_1^* all become linearly dependent on the correlation function, which enables the long time decay of $C(\tau_2)$ to be easily determined from these quantities. For a vibrational system, additional contributions to the rephasing and nonrephasing terms arise due to the anharmonically shifted v = 2←1 transition. As shown in Appendix 3.A, these additional contributions can be accounted for as a straightforward extension of these results, leading to somewhat modified expressions for the metrics described above.

3.4. Model Calculations & Discussion

Although, the expressions derived in the previous section are appealing because they provide simple relationships between the 2D lineshape and $C(\tau)$, they are derived on the basis of several assumptions. The short-time approximation used above will by definition break down for waiting times less than the correlation time of the bath, when the phase evolution during τ_1 and τ_3 must be considered. Also, the derived equations

neglect the effects of finite duration pulses and, for vibrational systems, the overtone transition (v = 2←1) must be taken into account during the third coherence period. These effects cannot be neglected in a quantitative extraction of $C(\tau)$ from peak shift measurements,[30] and are thereby likely to influence the other observables.

To test how well the expressions given above hold in the case of fast vibrational dynamics, we compare them to calculations of I, β, τ_1^*, E, and Γ_{dyn} for less restrictive levels of approximation. More specifically, we have calculated the full third-order response using the second Cumulant and Condon approximations.[1,7] For the purposes of this calculation, two model correlation functions were used: (1) a simple exponential decay with a correlation time of τ_c = 350 fs, and (2) our group's experimentally determined correlation function for the O-H stretching frequency of dilute HOD in D_2O,[30] which has a similar correlation time, but is characterized by a sub-100 fs initial decay, an underdamped oscillation, and a slower 1.4 ps decay. The effects of population relaxation are taken into account in both cases in a manner similar to that described previously,[30] using T_1 = 700 fs.‡

The quantitative measures of 2D lineshape relaxation obtained from these calculations are shown in Fig. 3-2. $C(\tau_2)$ is plotted along with corresponding values of I, β, τ_1^*, E, and Γ_{dyn} normalized to their initial value for case 1 in Fig. 3-2A, and for case 2 in Fig. 3-2B. Since the dynamical linewidth increases with waiting time, its asymptotic

‡ Two differences exist between the treatment of population relaxation in the current chapter and that of Ref. 30. In Ref. 30 additional contributions to the nonlinear response from the dissipation of energy upon vibrational relaxation were included, but are omitted here. Also, Ref. 30 assumed that one of the Feynman pathways that contributes to the photobleach of the fundamental transition does not undergo vibrational relaxation during τ_2 since it forms a ground state population during this time period. This is unphysical and is corrected in the modeling in this chapter.

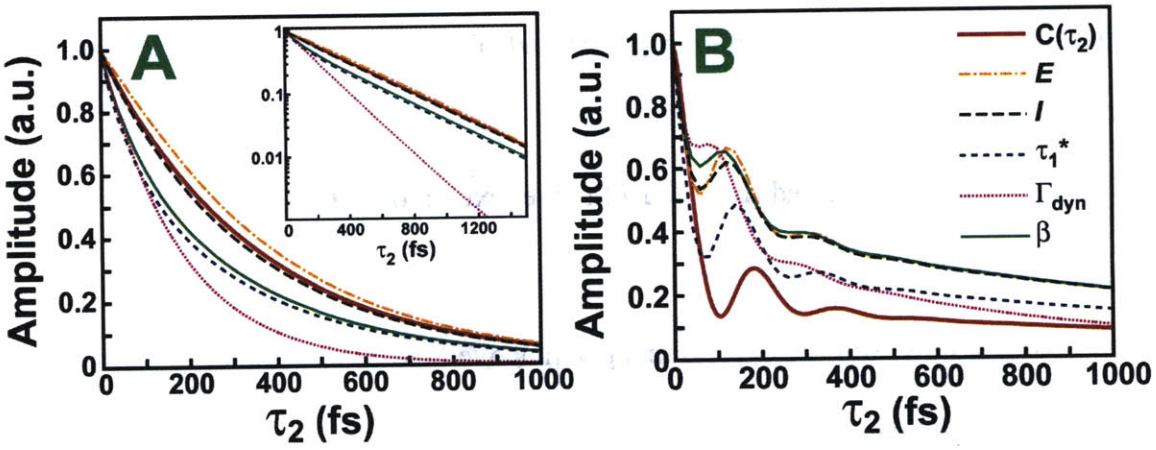


Figure 3-2: (A) Comparison between the correlation function for case 1 (thick red line) and the corresponding values of E (orange dash dotted), β (thin green line), τ_1^* (blue dashed), Γ_{dyn} (magenta dotted), and I (black long dashed) normalized to their value at $\tau_2 = 0$. (B) The same as (A) but for case 2. The inset to (A) replots the data on a log scale to highlight the similarity of the long time decay of these quantities.

value was calculated at 30 ps and subtracted from the calculated linewidth at all waiting times before normalizing the decay. Although none of the metrics except the ellipticity are explicitly equal to the correlation function in the short time approximation, the decay of each of these metrics is qualitatively similar to that of $C(\tau_2)$ for both examined cases. Moreover, after the correlation time, the decay time scales for I, β, τ_1^*, and E quantitatively match that of $C(\tau_2)$ for both trial correlation functions. Since the short time approximation assumes that $C(\tau)$ is constant during both of the coherence periods, we expect the largest difference between the metrics and $C(\tau)$ to be present at short waiting times, where $C(\tau)$ is changing most rapidly.

Fig. 3-3A and 3-3B plots $\bar{C}(\tau)$ and the inversion expressions described in Eq. 3-9, 3-16, 3-20, 3-21 and 3-22 calculated from the quantities displayed in Fig. 3-2A and

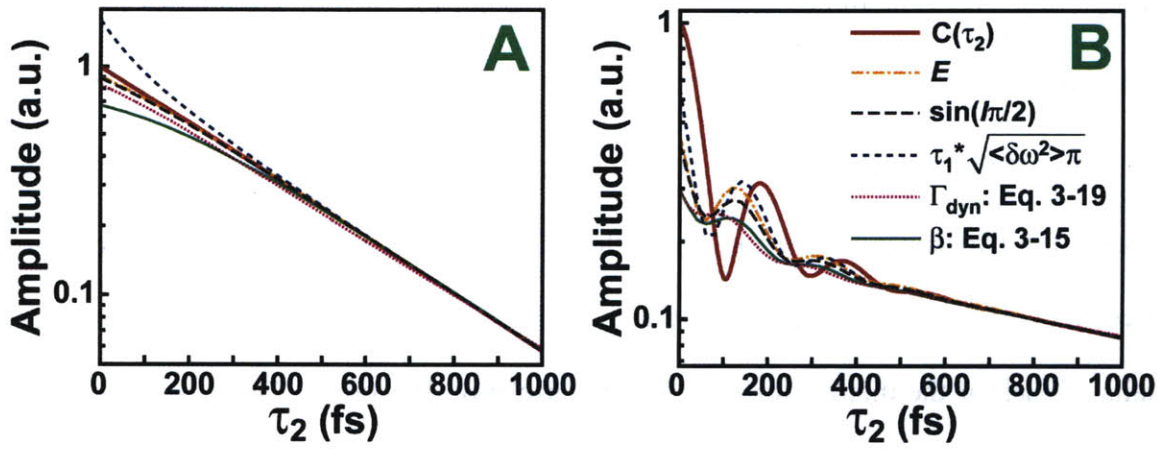


Figure 3-3: (A) Comparison between $\bar{C}(\tau_2)$ for case 1 (thick red line) and the inversion expressions given by Eq. 3-9 (black long dashed), 3-15 (thin green line), 3-18 (orange dash dotted), 3-19 (magenta dotted) and 3-20 (blue dashed). The data are normalized such that their long time tails overlap. (B) The same as (A) but for case 2.

3-2B respectively.[§] In the short time limit, the decay of each of these metrics is the same as the normalized correlation function. However, outside of this limit, each of these metrics differ from $\bar{C}(\tau)$ at early waiting times. For both model correlation functions used for these calculations, the initial values of the metrics are often too small. For case 2, the relative amplitude of the short time decay of the observables is smaller than that of $\bar{C}(\tau)$, and the first recurrence of the underdamped oscillation occurs earlier than that of $\bar{C}(\tau)$. This effect is due to a phase shift of the oscillation rather than a change of its frequency.

The origin of these discrepancies lies in the fact that the system evolves during the τ_1 and τ_3 periods. Even for a 2D lineshape that corresponds to $\tau_2 = 0$, spectral diffusion occurs over a time period roughly given by the time scale for the decay of the signal

[§] Outside of the short time approximation, the $\tau_2 = \infty$ value of the dynamical linewidth differs from *8ln(2)C(0)* as given in Eq. 3-19. Thus, in Fig. 3-3A and 3-3B this quantity has been replaced with the value of Γ_{dyn} at $\tau_2 = 30$ ps, by which time spectral diffusion is fully complete for both cases.

along these two time dimensions. The starting point for each of the metrics no longer corresponds to the same point in time as the zero time value of $C(\tau)$. However, the behavior of the metrics away from $\tau_2 = 0$ is largely unaffected by the spectral evolution during the two coherence periods, as reflected in the lack of change of the oscillation frequency of the beat in case 2, and the similarity of the decay constant of the long time tails of each of the metrics for both model correlation functions. Thus, even outside of the short time limit, the equations derived from that approximation for different metrics can be used to quantify the decay of the correlation function at long τ_2.

Although none of the metrics entirely reproduce the behavior $C(\tau)$ at early waiting times, some of the metrics are more similar to $C(\tau)$ than others. For the bare variables plotted in Fig. 3-2A and 3-2B, *I*, *β*, and *E* are very similar to the correlation function, almost perfectly matching $C(\tau)$ for the exponential decay. Γ_{dyn} differs greatly from $C(\tau)$, decaying too rapidly for both trial correlation functions. However, the inversion equation for this quantity agrees well with the trial correlation functions. Interestingly, for case 2 the time scale and intensity of the beats in the peak shift match those of $C(\tau)$ better than those of *I*, *β*, E, and Γ_{dyn}. An explanation for this comes from the fact that the all of the metrics except for the peak shift depend on the decay of the correlation function in both the τ_1 and τ_3 dimensions. While the peak shift is dependent upon the full decay of the response in the τ_3 dimension, in the τ_1 dimension its value is only dependent on the peak of the echo response. Because of this, the effective time that $C(\tau)$ must remain constant for the short time approximation to hold is smaller for the

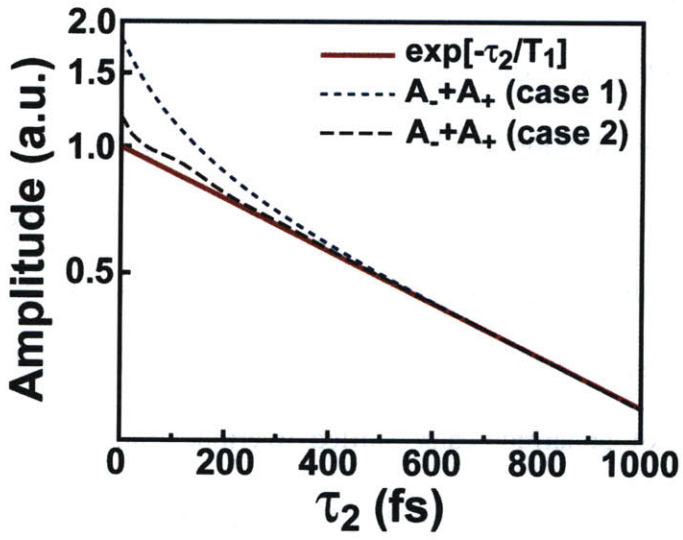


Figure 3-4: Comparison between $A_- + A_+$ for both case 1 (blue dashed), case 2 (black long dashed), and an exponential decay of T_1 = 700 fs (thick red line). The data were normalized such that their long time tails overlapped.

peak shift than for the other metrics, which causes the peak shift to have a large initial value and show recurrences later than the other metrics.

We test our ability to separate population relaxation effects from spectral evolution in Fig. 3-4. Plotted is an exponential decay with a time scale of T_1 = 700 fs compared with the sum of rephasing and nonrephasing amplitude for the two cases studied. As suggested by Eq. 3-10, these two quantities decay with a time scale of T_1 for waiting times longer than the $C(\tau)$ correlation time. The deviation in the short time behavior reflects the amplitude decay due to the dephasing of radiating dipoles, and is far less significant for the case 2 correlation function with its abrupt short time decay.

For 2D IR spectroscopy of a vibrational system, the contributions of the anharmonically shifted overtone transition (v = 2←1) must be taken into account during the second coherence period. Expressions for the metrics described in Section 3.3 can be derived taking into account the presence of the overtone and are given in Appendix 3.A.

In addition, finite duration pulses complicate the analysis of the measured signals in a 2D experiment by effectively mixing rephasing and nonrephasing signals for waiting times smaller than the pulse duration and by windowing the frequency dependent response of the system by the pulse spectrum. Some of the metrics we have identified rely on the difference between the rephasing and nonrephasing signals, and the mixing of these signals when the pulses overlap will tend to decrease the amplitude of these metrics. We analyze the effect of anharmonically shifted overtone transitions and finite duration pulses on the extraction of $C(\tau)$ from the 2D lineshape metrics in Fig. 3-5. Using the method described in Ref. 30, 2D lineshapes with these effects were calculated for the case 2 correlation function assuming an anharmonicity of 250 cm^{-1} and 45 fs transform limited pulses centered on resonance with the v = 1←0 transition.

Fig. 3-5 presents a comparison of these effects with the inversion expressions for a two-level system, a three-level system (Eq. 3-A5, 3-A10, and 3-A11), and a three-level system that accounts for finite pulse length. The addition of the overtone transition affects each of the metrics displayed in the figure in a similar fashion, effectively adding a constant offset to each of them without changing the shape of the decay. The inclusion of finite duration pulses blurs out the features of each metric, decreasing the intensity of the recurrence and initial value of the metrics. The exception to this is the peakshift, which displays a larger initial value upon the inclusion of finite duration pulses. We find in each case that a qualitative agreement is clear between each metric and $C(\tau_2)$, but that a quantitative description of the short time decay ($\tau_2 << \tau_C$: in our case a few tens of femtoseconds) cannot be solely obtained from the use of any of the variables studied.

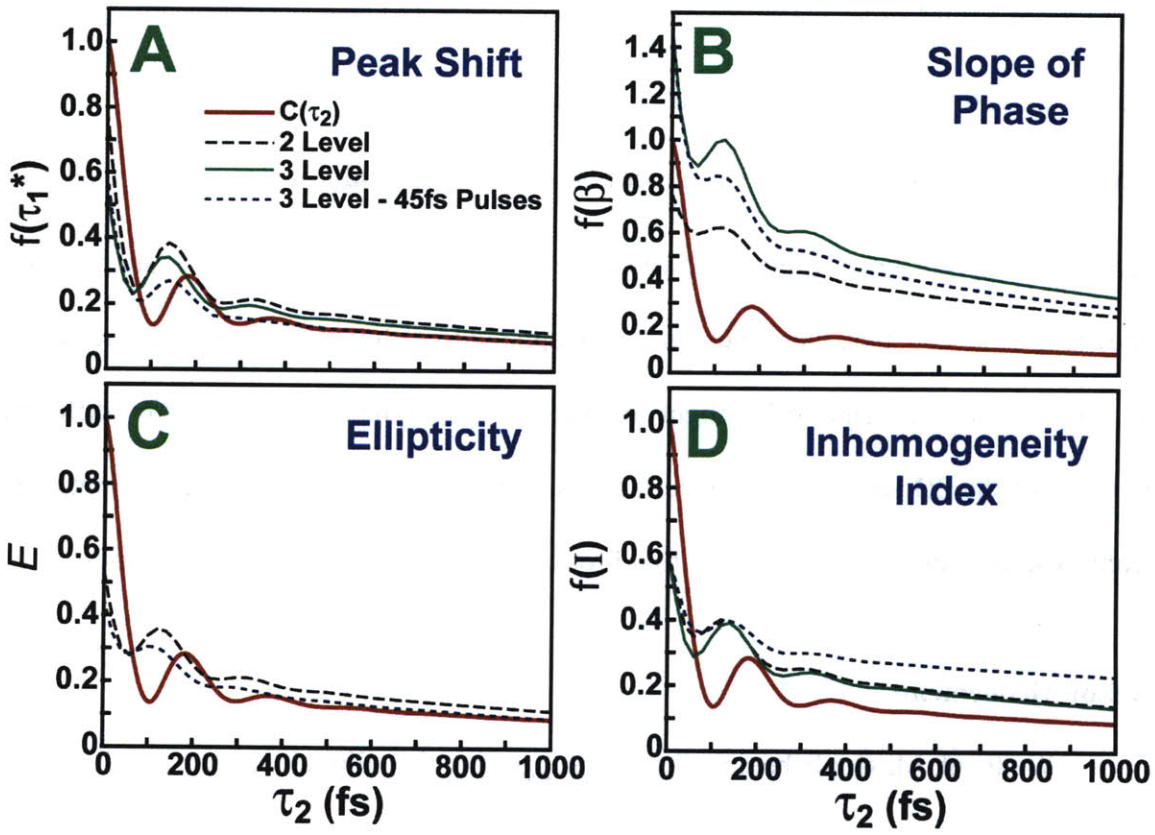


Figure 3-5: Comparison between $C(\tau)$ for case 2 (thick red line) and the inversion expressions for τ_1^* (A), E (B), β (C), and I (D) for a two-level system (black long dashed), three-level system (thin green line), and three-level system taking into account finite duration pulses (blue dashed). The inversion expressions for a two-level system are given by Eq. 3-9, 3-15, 3-18, and 3-20 and for a three-level system by 3-A5, 3-A10, and 3-A11. Since the three-level and two-level inversion expressions for the ellipticity are identical, the result from the three-level calculation is not presented.

In conclusion, we have tested the ability for a number of variables that quantify the spectral relaxation of 2D lineshapes in waiting time dependent experiments to characterize the dynamics of molecules. Within the confines of the short time expansion for the third-order response, each of these metrics can be formally related to the frequency correlation function $C(\tau)$. Outside of this approximation, these relationships break down, but each of the metrics is still sensitive to the form and time scales associated with the decay of the correlation function. Traditionally, in order to obtain

$C(\tau)$ from a third-order measurement, a trial form of $C(\tau)$ is guessed, used to calculate the signal, and then varied to give the best fit with the data. The use of these metrics provides an excellent qualitative description of $C(\tau)$ and for longer τ_2, excellent quantitative agreement. In the case where the frequency fluctuations of a system do not obey Gaussian statistics, these metrics can be applied to different portions of the resulting asymmetric 2D lineshape to highlight the difference in dynamics described by different portions of the 2D spectrum.[31] Since these variables can be quickly and easily obtained from experimental data, they should find broad use in the analysis of 2D lineshapes.

Acknowledgements

We thank Maxim Pshenichnikov for suggesting the ellipticity parameter described in Eq. 3-18.

References

(1) S. Mukamel, *Principles of Nonlinear Optical Spectroscopy*, (Oxford University Press, New York, 1995).

(2) W. P. de Boeij, M. S. Pshenichnikov and D. A. Wiersma, "Ultrafast solvation dynamics explored by femtosecond photon echo spectroscopies," Annu. Rev. Phys. Chem. 49, 99 (1998).

(3) G. R. Fleming and M. Cho, "Chromophore-solvent dynamics," Annu. Rev. Phys. Chem. 47, 109 (1996).

(4) P. Hamm, M. Lim and R. M. Hochstrasser, "Non-Markovian dynamics of the vibrations of ions in water from femtosecond infrared three-pulse photon echoes," Phys. Rev. Lett. 81, 5326 (1998).

(5) J. D. Hybl, A. Yu, D. A. Farrow and D. M. Jonas, "Polar solvation dynamics in the femtosecond evolution of two-dimensional Fourier transform spectra," J. Phys. Chem. A 106, 7651 (2002).

(6) M. Khalil, N. Demirdoven and A. Tokmakoff, "Coherent 2D IR spectroscopy: Molecular structure and dynamics in solution," J. Phys. Chem. A 107, 5258 (2003).

(7) J. Sung and R. J. Silbey, "Four-wave mixing spectroscopy for a multi-level system," J. Chem. Phys. 115, 9266 (2001).

(8) J. J. Loparo, S. T. Roberts and A. Tokmakoff, "Multidimensonal infrared spectroscopy of water. I. Vibrational dynamics in 2D lineshapes," J. Chem. Phys. 125, 194521 (2006).

(9) T. Joo, Y. Jia, J.-Y. Yu, M. J. Lang and G. R. Fleming, "Third-order nonlinear time-domian probes of solvation dynamics," J. Chem. Phys. 104, 6089 (1996).

(10) M. Cho, J.-Y. Yu, T. Joo, Y. Nagasawa, S. A. Passino and G. R. Fleming, "The integrated photon echo and solvation dynamics," J. Phys. Chem. 100, 11944 (1996).

(11) W. de Boeij, M. S. Pshenichnikov and D. A. Wiersma, "On the relation between the echo-peak shift and Brownian oscillator correlation function," Chem. Phys. Lett. 253, 53 (1996).

(12) A. Piryatinski and J. L. Skinner, "Determining vibrational solvation-correlation functions from three-pulse infrared photon echoes," J. Phys. Chem. B. 106, 8055 (2002).

(13) D. M. Jonas, "Two-dimensional femtosecond spectroscopy," Annu. Rev. Phys. Chem. 54, 397 (2003).

(14) J. B. Asbury, T. Steinel, C. Stromberg, S. A. Corcelli, C. P. Lawrence, J. L. Skinner and M. D. Fayer, "Water dynamics: Vibrational echo correlation spectroscopy and comparison to molecular dynamics simulations," J. Phys. Chem. A 108, 1107 (2004).

(15) T. Brixner, T. Mancal, I. V. Stiopkin and G. R. Fleming, "Phase-stabilized two-dimensional electronic spectroscopy," J. Chem. Phys. 121, 4221 (2004).

(16) M. T. Zanni, M. C. Asplund and R. M. Hochstrasser, "Two-dimensional heterodyned and stimulated photon echoes of N-methylacetamide-D," J. Chem. Phys. 114, 4579 (2001).

(17) K. Kwac and M. Cho, "Two-color pump-probe spectroscopies of two- and three-level systems: 2-Dimensional line shapes and solvation dynamics," J. Phys. Chem. A 107, 5903 (2003).

(18) J. D. Eaves, J. J. Loparo, C. J. Fecko, S. T. Roberts, A. Tokmakoff and P. L. Geissler, "Hydrogen bonds in liquid water are broken only fleetingly," Proc. Natl. Acad. Sci. U.S.A. 102, 13019 (2005).

(19) N. Demirdöven, M. Khalil and A. Tokmakoff, "Correlated vibrational dynamics revealed by two-dimensional infrared spectroscopy," Phys. Rev. Lett. 89, 237401 (2002).

(20) P. Hamm, "Three-dimensioinal-IR spectroscopy: Beyond the two-point frequency fluctuation correlation function," J. Chem. Phys. 124, 124506 (2006).

(21) K. Lazonder, M. S. Pshenichnikov and D. A. Wiersma, "Two-dimensional optical correlation spectroscopy applied to liquid/glass dynamics," in *Ultrafast Phenomena XV*, edited by R. J. D. Miller, A. M. Weiner, P. Corkum and D. M. Jonas, 2006

(22) J. Sung and R. J. Silbey, "Optical four wave mixing spectroscopy for multilevel systems coupled to multimode Brownian oscillators," J. Chem. Phys. 118, 2443 (2003).

(23) Y. Tanimura and S. Mukamel, "Real-time path-integral approach to quantum coherence and dephasing in nonadiabatic transitions and nonlinear optical response," Phys. Rev. E 47, 118 (1993).

(24) J. D. Hybl, A. W. Albrecht, S. M. Gallager-Faeder and D. M. Jonas, "Two-dimensional electronic spectroscopy," Chem. Phys. Lett. 297, 307 (1998).

(25) M. Cho, H. M. Vaswani, T. Brixner, J. Stenger and G. R. Fleming, "Exciton analysis in 2D electronic spectroscopy," J. Phys. Chem. B 109, 10542 (2005).

(26) K. F. Everitt, E. Geva and J. Skinner, "Determining the solvation correlation function from three-pulse photon echoes in liquids," J. Chem. Phys. 114, 1326 (2001).

(27) M. Khalil, N. Demirdöven and A. Tokmakoff, "Obtaining absorptive lineshapes in two-dimensional infrared vibrational correlation spectra," Phys. Rev. Lett. 90, 47401 (2003).

(28) K. Okumura, A. Tokmakoff and Y. Tanimura, "Two-dimensional line-shape analysis of photon-echo signal," Chem. Phys. Lett. 314, 488 (1999).

(29) A. Tokmakoff, "Two-dimensional vibrational lineshapes derived from coherent third-order nonlinear spectroscopy," J. Phys. Chem. A 104, 4247 (2000).

(30) C. J. Fecko, J. J. Loparo, S. T. Roberts and A. Tokmakoff, "Local hydrogen bonding dynamics and collective reorganization in water: Ultrafast IR spectroscopy of HOD/D_2O," J. Chem. Phys. 122, 054506 (2005).

(31) J. J. Loparo, S. T. Roberts and A. Tokmakoff, "Multidimensonal infrared spectroscopy of water. II. Hydrogen bond switching dynamics," J. Chem. Phys. 125, 194522 (2006).

3.A. Appendix: Analysis of Lineshapes for a Three-level System

For experiments on a single vibration, photoinduced absorption from the v = 1 state to v = 2 state is possible during the second coherence period. By assuming that the dynamics of the v = 2←1 transition are perfectly correlated with those of the v = 1←0 transition and that harmonic scaling of the transition dipoles holds $\left(\mu_{21} = \sqrt{2}\mu_{10}\right)$, we can rewrite the response function given in Eq. 3-3 as:

$$S_{\pm}(\tau_3,\tau_2,\tau_1) = \left(1-\exp[i\Lambda\tau_3]\right)\theta(\tau_1)\theta(\tau_3) \times \exp\left[-\frac{C(0)}{2}\left(\tau_1^2+\tau_3^2 \pm 2\tau_1\tau_3\bar{C}(\tau_2)\right) - \tau_2/T_1 + i\Omega(\tau_1-\tau_3)\right] \tag{3-A1}$$

where Λ is the anharmonicty between the v = 1←0 and v = 2←1 transitions, $\Lambda = \langle\omega_{10}\rangle - \langle\omega_{21}\rangle$. Using Eq. 3-A1, we can solve for all of the quantities described above. Since the response function including the v = 2←1 contribution is a sum of two terms, it is more mathematically convenient to integrate $|S_{\pm}|^2$ as opposed to $|S_{\pm}|$ in order to calculate the inhomogeneity index. Defining:

$$B_{\pm}(\tau_2) = \int_0^{\infty}\int_0^{\infty}\left|S_{\pm}^{(3)}(\tau_3,\tau_2,\tau_1)\right|^2 d\tau_1 d\tau_3, \tag{3-A2}$$

we find that in the limit where $\bar{C}(\tau_2) \ll 1$,

$$B_{\pm}(\tau_2) = \frac{\exp[-2\tau_2/T_1]}{C(0)\sqrt{\left(1-\bar{C}(\tau_2)^2\right)}} \times \left(\frac{\pi}{2} \mp \tan^{-1}\left[\frac{\bar{C}(\tau_2)}{\sqrt{\left(1-\bar{C}(\tau_2)^2\right)}}\right] - \frac{\pi}{2}\exp\left[-\frac{\Lambda^2}{4C(0)\left(1-\bar{C}(\tau_2)^2\right)}\right]\right), \tag{3-A3}$$

and the inhomogeneity index is:

$$\frac{B_- - B_+}{B_- + B_+} = \frac{2}{\pi}\tan^{-1}\left[\frac{\bar{C}(\tau_2)}{\sqrt{\left(1-\bar{C}(\tau_2)^2\right)}}\right] \Bigg/ \left(1-\exp\left[-\frac{\Lambda^2}{4C(0)\left(1-\bar{C}(\tau_2)^2\right)}\right]\right). \tag{3-A4}$$

This gives the approximate result:

$$\bar{C}(\tau_2) = \sin\left[\frac{\pi I}{2}\left(1-\exp\left[-\Lambda^2/4C(0)\right]\right)\right]. \tag{3-A5}$$

The sum of the rephasing and nonrephasing amplitude is,

$$B_+ + B_- = \frac{\pi \exp\left[-2\tau_2/T_1\right]}{C(0)\sqrt{\left(1-\bar{C}(\tau_2)^2\right)}}\left(1-\exp\left[-\frac{\Lambda^2}{4C(0)\left(1-\bar{C}(\tau_2)^2\right)}\right]\right), \tag{3-A6}$$

which again is dominated by the lifetime decay and exhibits a dependence on the correlation function for small waiting times. Notice that since we are integrating the square of the absolute value of the 2D surface, the sum of rephasing and nonrephasing amplitude in Eq. 3-A6 decays twice as fast as the result in Eq. 3-10.

Taking the Fourier transform of Eq. 3-A1 in a manner analogous to that described in Section 3.3, we obtain the complex 2D surface:

$$\begin{aligned} S_C(\Delta_3,\tau_2,\Delta_1) = {} & \frac{\exp\left[-\tau_2/T_1\right]}{2C(0)\sqrt{\left(1-\bar{C}(\tau_2)^2\right)}}\exp\left[-\left(\frac{\Delta_3^2+\Delta_1^2-2\Delta_3\Delta_1\bar{C}(\tau_2)}{2C(0)\left(1-\bar{C}(\tau_2)^2\right)}\right)\right] \\ & \times\left(\left(1-erf\left[i\gamma_{10}\right]\right)-\exp\left[\frac{-\Lambda^2+2\Lambda\left(\Delta_1\bar{C}(\tau_2)-\Delta_3\right)}{2C(0)\left(1-\bar{C}(\tau_2)^2\right)}\right]\left(1-erf\left[i\gamma_{21}\right]\right)\right) \end{aligned} \tag{3-A7}$$

where the quantities γ_{10} and γ_{21} are defined as:

$$\gamma_{10} = \frac{\Delta_3 - \Delta_1\bar{C}(\tau_2)}{\sqrt{2C(0)\left(1-\bar{C}(\tau_2)^2\right)}} \tag{3-A8}$$

$$\gamma_{21} = \frac{\Delta_3 + \Lambda - \Delta_1\bar{C}(\tau_2)}{\sqrt{2C(0)\left(1-\bar{C}(\tau_2)^2\right)}} \tag{3-A9}$$

In the limit where the normalized correlation function has significantly decayed, we can solve for $\bar{C}(\tau_2)$ in terms of β:

$$\bar{C}(\tau_2) = \beta\left(\frac{-C(0)}{\Lambda}\right)\frac{\left(1-\exp\left[-\Lambda^2/2C(0)\right]\right)^2 + \left(erfi\left[\Lambda/\sqrt{2C(0)}\right]\right)^2}{erfi\left[\Lambda/\sqrt{2C(0)}\right]}. \tag{3-A10}$$

Rotating the frequency axes to calculate the ellipticity shows that the antidiagonal and diagonal axes of the 2D surface are now a sum of both a positive and negative Gaussian lineshapes with equal linewidths. Thus the ellipticity can be easily calculated by fitting the diagonal and antidiagonal slices with a sum of two Gaussians of equal linewidth.

Finally, when $\bar{C}(\tau_2) \ll 1$, we can solve for the peakshift in terms of the frequency-frequency correlation function:

$$\bar{C}(\tau_2) = \tau_1^* \frac{C(0)\left(\exp\left[\Lambda^2/2C(0)\right]-1\right)}{\Lambda erfi\left[\Lambda/\sqrt{2C(0)}\right]}, \tag{3-A11}$$

and the dynamical linewidth is unchanged from Eq. 3-17. Note that for large values of the waiting time, I, β, τ_1^*, E are all linearly dependent on $C(\tau_2)$, as in the case for a two-level system.

Chapter 4

Generation of Sub-50 fs Mid-Infrared Pulses and the Measurement of Nonlinear Infrared Signals

4.1. Introduction

Due to the sensitivity of vibrational modes to fluctuations of the local solvent environment, time resolved infrared spectroscopy provides us with a means to understand how molecules interact in the condensed phase. In the case of water, nonlinear infrared experiments allow us to study the steps that lead to the rearrangement of hydrogen bonds and how these rearrangements act to guide chemical reactions, such as aqueous charge migration. The time scales for intermolecular motions in water are exceedingly fast, ranging from tens of femtoseconds to picoseconds. Thus, the generation of intense, sub-100 fs infrared pulses is needed to accurately probe water's intermolecular dynamics. As of yet, no solid state media has emerged that allows for the direct generation of high power, tunable, femtosecond pulses in the mid-infrared spectral region associated with molecular vibrations. Instead, many researchers have utilized parametric frequency down-conversion to generate pulses in the mid-infrared. Optical parametric amplifiers (OPA) pumped with the output of commercially available Ti:sapphire amplifiers have been used to generate 50-400 fs pulses with center wavelengths that are tunable from 3-

20 μm.[1] OPAs based on the down-conversion of amplified 800 nm pulses using $KNbO_3$ have been able to generate pulses centered near 3 μm, the peak of water's O-H stretching transition, that are as short as five cycles of the infrared field (~50 fs).[2,3]

Two-dimensional infrared spectroscopy (2D IR) is a powerful technique for the study of vibrational dynamics since it allows us to correlate the fluctuations of a particular vibrational eigenstate with the other vibrations of the system. The two axes of a 2D spectrum represent the frequency that a molecule is initially excited at, ω_1, and the frequency at which the excited vibration is detected, ω_3, after a set waiting period, τ_2. To construct a 2D spectrum, we might imagine using narrow band laser to excite molecules in a narrow frequency range and then use a time delayed broad band laser pulse to read out their final set of vibrational frequencies. We can then change the frequency of the excitation pulse to construct the ω_1 axis while spectral detection of the broadband probe will yield the ω_3 axis.[4] This method is often referred to as a "double resonance" experiment, and is appealing due to its simplicity. However, by choosing to use a narrow band excitation pulse a trade off is made between the frequency resolution of the excitation axis and the time resolution of the experiment. This typically limits the ability of double resonance experiments to examine processes that occur on time scales shorter than a picosecond.[5]

Fortunately, we can overcome these limitations by replacing the narrowband excitation pulse with a pair of broadband pulses. In the frequency domain, such a pulse pair forms a frequency grating, with a spacing given by the time delay separating the pulse pair. Scanning this time delay is analogous to scanning the frequency of the narrow band excitation pulse in a double resonance experiment with the exception that the

experimental time resolution is not set by the width of the excitation pulse but by the dephasing time of the excited vibration.[5,6] Typically, the three excitation pulses in broadband 2D IR experiments are not collinear, and the signal is emitted in a background free direction. Phase sensitive detection of this field can be achieved by interfering it with a reference pulse, referred to as the local oscillator, and then either scanning the local oscillator in time with respect to the signal or by spectrally dispersing the overlapped signal-local oscillator pair onto a multichannel array detector. Fourier transformation of the detected time domain signal is then used to obtain the frequency domain 2D IR spectrum.

The superior time resolution of broadband 2D IR comes with the additional complication that a precise knowledge of the time delays between each of the excitation pulses and the local oscillator is necessary to properly extract the absorptive 2D IR spectrum from the Fourier transform. Absolute timing errors between pulses can alter the tilt of 2D lineshapes while random shifts in the step size between subsequent points can lead to the appearance of side bands or ghost peaks in 2D spectra.[7] Unfortunately, the size of the errors that can lead to these distortions is quite small. Periodic timing errors on the order of 10% of the carrier oscillation period can significantly distort 2D lineshapes.[8] For the O-H stretching transition of the HOD molecule which absorbs near 3 μm, a 10% timing shift corresponds to a ±150 nm error on a retroreflecting linear stage. This level of error is close to the typical accuracy obtainable with commercial translation states that use linear encoders to determine their position. For the measurement of a 2D spectrum, one would like to have a stepping accuracy in excess of λ/50, which corresponds to a step size tolerance of only ±30 nm for 3 μm mid-infrared pulses and

retroreflecting delay stages. Hence, many groups have developed methods that allow for the precise determination of the timing axis. These methods range from the measurement of a reference interferogram that can be used to post-process data after an experiment,[9,10] the active stabilization of timing delays through a HeNe reference,[11] the creation of time delays using variable thickness windows instead of retroreflecting mirrors to decrease the timing delay created for the same distance of stage travel,[12,13] or the construction of interferometers wherein scanning a single stage moves a pair of time delays that systematically cancels timing errors due to fluctuations in pulse pointing.[14,15]

This chapter will provide a description of the laser system and Fourier transform interferometer that we have used to perform nonlinear infrared experiments that probe the O-H stretching transition of dilute HOD dissolved in both D_2O and concentrated NaOD solution. This system utilizes a home built OPA pumped with the output of a Ti:sapphire amplifier to generate sub-50 fs pulses centered at 3 μm.[3] The output of this OPA is fed into a five beam Mach-Zehnder interferometer that generates the pulse sequences used for a number of third-order experiments, including the measurement of absorptive 2D IR spectra. A description of the steps that we take to ensure the proper measurement of high signal-to-noise absorptive 2D IR spectra, which includes the proper calibration of translation stages and balanced detection, will be provided as well as a description of a novel technique that allows for the measurement of 2D spectra fully in the time domain.

4.2. Generation of Mid-Infrared Pulses

An overview of the experimental equipment necessary for the generation and detection of nonlinear infrared signals is given in Fig. 4-1. Sub 50-fs 3 μm pulses are

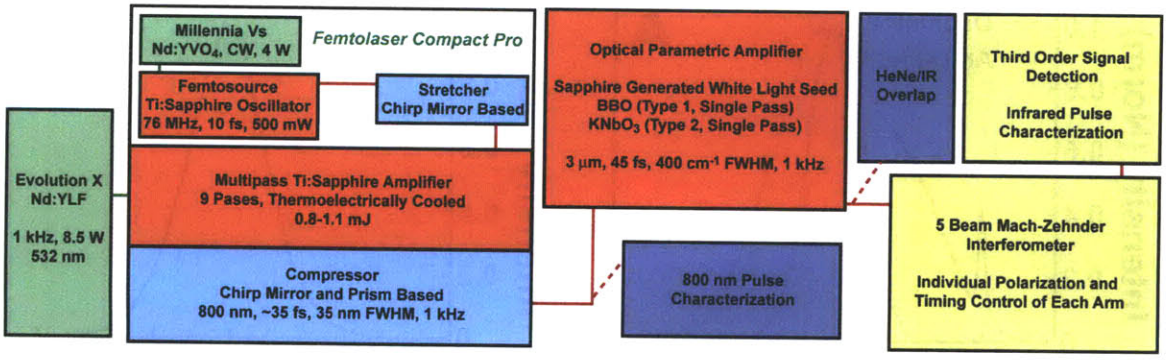


Figure 4-1: Description of the experimental setup used for nonlinear vibrational spectroscopy experiments. A commercial Ti:sapphire amplifier pumps a home built 3 μm OPA that generates 45 fs pulses. A Mach-Zehnder interferometer is used to split the generated infrared pulse into five independently controllable replicas for use in nonlinear measurements.

generated in a home built β-barium borate/potassium niobate ($BBO/KNbO_3$) based OPA that is pumped by the output of a commercially available Femtopower Compact Pro Ti:sapphire amplifier.[3,8] The amplified 800 nm source consists of a $Nd:YVO_4$ Spectra Physics Millennia Vs that powers a Femtosource Scientific Pro oscillator (76 MHz, ~10 fs duration, ~100 nm FWHM, 500 mW when modelocked), the output of which seeds a multipass amplifier after passing through a stretcher comprised of a glass slab and chirp mirrors that precompensate for third-order dispersion. The first four passes through the thermoelectrically cooled Ti:sapphire amplifier crystal increase the peak intensity of the oscillator output by $\sim 5\times10^4$. Additional amplification occurs after passing the amplified pulse train through a Pockels cell (Lasermetrics), which reduces the repetition rate to 1 kHz to match that of the Spectra Physics Evolution X Nd:YLF diode laser used to pump the amplifier. Five additional passes occur after the Pockels cell, bringing the output pulse energy up to 0.8-1.1 mJ. The beam size of the amplifier output is increased to 2 cm using a telescope and then passed through a compressor consisting of two prism pairs and a set of chirp mirrors with dispersion opposite that of the mirrors in the stretcher.

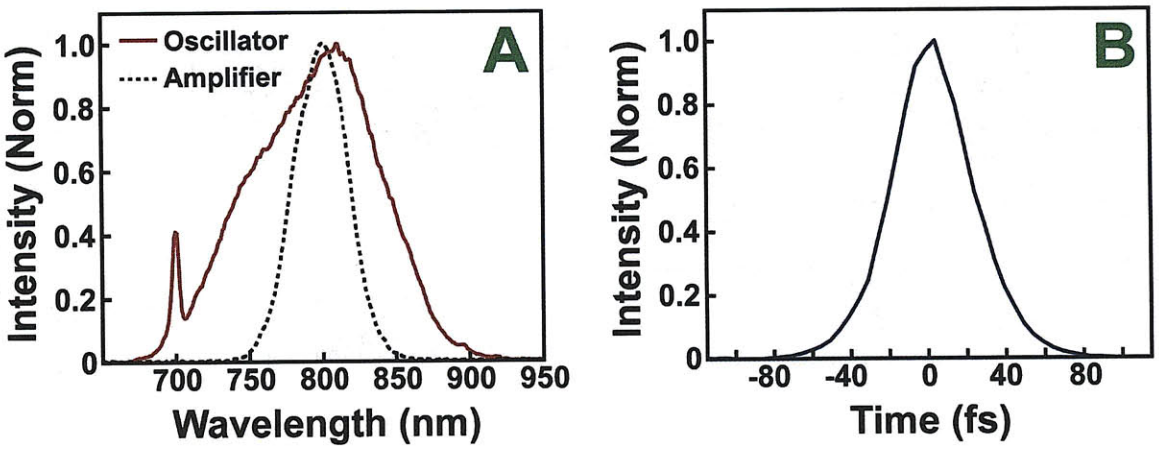


Figure 4-2: (A) Spectra of the Ti:sapphire oscillator seed and the amplified Ti:sapphire pulse. (B) Background free second Harmonic autocorrelation of the amplified Ti:sapphire pulse. The measured FWHM corresponds to a pulse duration of ~35 fs assuming a Gaussian pulse profile.

Fig. 4-2 plots typical spectra of the oscillator and amplifier as well as a second harmonic autocorrelation recorded using a 0.01 mm thick BBO crystal mounted on a 2 mm UV-grade fused silica window (EKSMA). The measured autocorrelation FWHM is consistent with a pulse duration of ~35 fs assuming a Gaussian pulse shape.

3 μm infrared pulses are generated by pumping a home built BBO/$KNbO_3$ OPA using ~0.5 mJ of the multipass amplifier output. The design of this OPA has been described in extensive detail elsewhere,[3] so only a brief description is given here. ~1% of the input amplified 800 nm pulse is used to seed a white light continuum by focusing it into a [0001]-cut sapphire plate (Meller Optics). The focusing of the 800 nm pulse and collimation of the white light continuum is performed using reflective focusing mirrors to minimize the dispersion applied to the generated continuum pulse. The white light seed and ~35% of the 800 nm pump are then mixed in a BBO crystal cut for type I phase matching (Casix), which amplifies the spectral components of the white light continuum centered near 1.1 μm, the difference frequency between 800 nm and 3 μm. BBO was

chosen for this initial amplification stage due to its high damage threshold, but it carries the disadvantage that it has an absorption resonance near 3 μm, which precludes it as a means of directly generating 3 μm pulses. The output of the BBO crystal is reflected off of a custom beamsplitter (Cascade Optical) that is designed to reflect only the amplified 1.1 μm light and the reflected beam is overlapped with the remainder of the 800 nm pump pulse in a 1 mm thick $KNbO_3$ crystal (type II, Spectrogen Inc.), which results in the generation of 3 μm pulses. The flat tuning curve of $KNbO_3$ near 3 μm ensures that the crystal can support the large spectral bandwidth needed to generate a short IR pulse.[2] However, its large dispersion limits the crystal length to relatively short thicknesses (~1 mm). After collimation, the IR beam has a diameter of 9 mm and is overlapped with a HeNe beam to aid in the alignment of optics. The overlap with the HeNe is accomplished using a 2 mm thick Ge Brewster plate. In the mid-infrared spectral range, many optical materials have opposite signs of second order dispersion. The thickness of the Ge plate was selected to add positive second order dispersion that balances the negative dispersion that arises from the CaF_2 optics in the interferometer. On a day-to-day basis, additional corrections for dispersion can be made by inserting ZnSe or CaF_2 windows into the beam which add positive or negative second order dispersion, respectively.[3,16] The OPA as well as the remaining experimental setup is enclosed in a series of Plexiglas boxes and purged with dry air to remove the effects of atmospheric water absorption that can decrease the high frequency side of the pulse spectrum.

The results of a transient grating FROG of the IR pulse measured by frequency resolving the nonresonant response of a CaF_2 window placed at the sample position is plotted in Fig. 4-3A. A fit of the displayed FROG gives a FWHM of 48 fs for the pulse

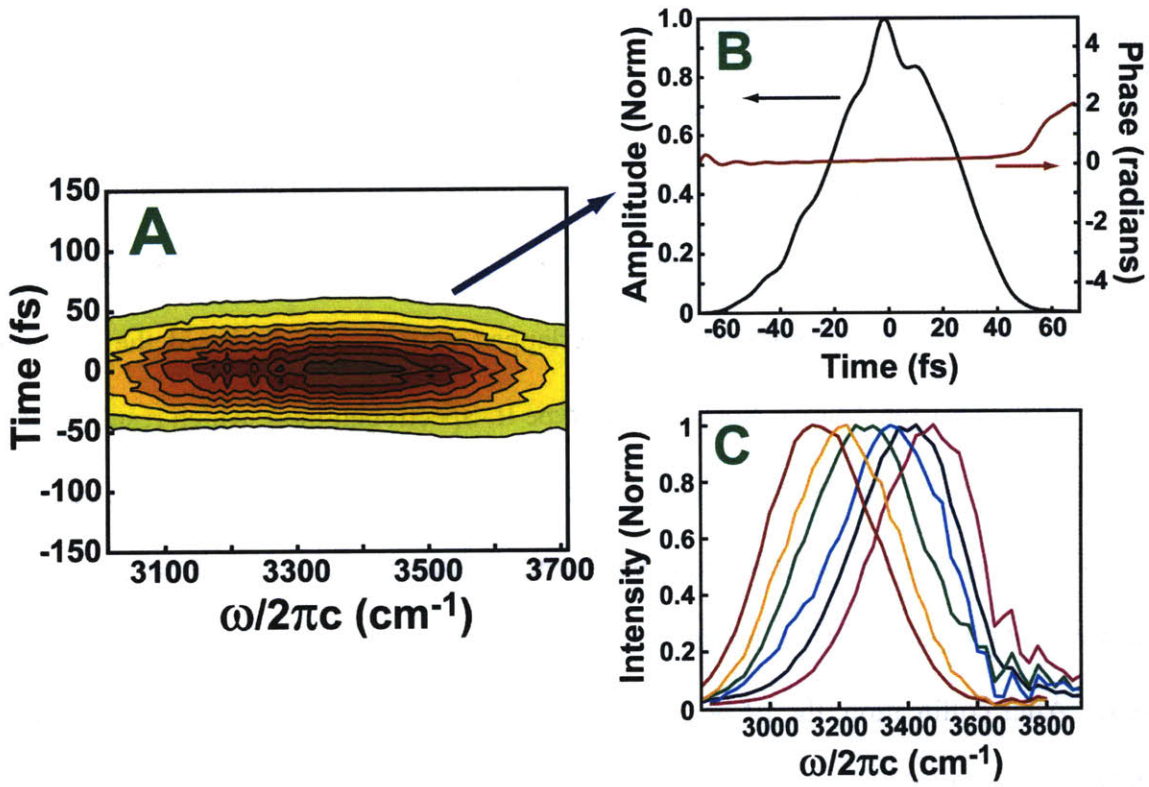


Figure 4-3: Pulse characterization of the 3 μm pulse generated by the OPA. (A) A transient grating FROG performed using the nonresonant response of CaF_2. (B) A fit to the FROG data gives an electric field duration of 48 fs with flat temporal phase. (C) The spectral range over which the infrared pulse can be tuned by rotation of the $KNbO_3$ crystal.

electric field with nearly flat temporal phase (Fig. 4-3B). Typical retrieved pulse durations are in the range of 45-50 fs,[17] although pulses as short as 42 fs have been observed. Pulse bandwidths generally range from 350-400 cm^{-1} and pulse energies of ~5 μJ are common. Due to the large acceptance bandwidth of $KNbO_3$, the center frequency of the pulse can be tuned by rotation of the $KNbO_3$ crystal in the second stage of the OPA. Fig. 4-3C plots measured pulse spectra that highlight the spectral range over which the OPA is easily tunable. The OPA is capable of generating pulses with bandwidths centered at wavelengths as long as 4 μm, although the energy output of the OPA in this spectral range is quite low.

4.3. Acquisition of Vibrational Echo Signals

The generation of third-order signals requires precise control over the polarization, timing, and wave vector of each excitation pulse utilized in the experiment. Such control is achieved through the use of a modified Mach-Zehnder interferometer, pictured schematically in Fig. 4-4A,[18] which divides the infrared pulse generated by the OPA into five independently controllable replica pulses. The interferometer employs 3 mm thick custom CaF_2 50/50 beamsplitters and compensation plates (Thin Film Laboratory) and each interferometer arm is designed to contain two passes through a CaF_2 window to ensure that the dispersion of each pulse is equal at the sample position. Independent polarization control of each pulse is obtained by inserting a MgF_2 $\lambda/2$ waveplate/CaF_2 wire grid polarizer pair (Alphalas and Molectron, respectively) into each arm of the interferometer. Computer controlled, motorized translation states (Aerotech ANT-25L, 50 nm reproducibility, ±150 nm resolution) mounted with 2" gold corner cube retroreflectors are used to generate time delays between each pulse.

The five replica pulses that are generated by the interferometer serve as the three excitation pulses used in a third-order pulse sequence (Fig. 4-4B), the local oscillator used in 2D IR experiments, and a tracer that follows the signal path of the background free signal generated in nonlinear experiments. The tracer is primarily used for the alignment of optics and is blocked during experiments. The three excitation pulses are focused into the sample using a right angle uncoated gold off-axis parabolic mirror with an effective focal length of 10 cm (Janos). The relative time delays between each excitation pulse are determined by using a 0.3 mm thick $AgGaS_2$ crystal (EKSMA) for pair wise, second harmonic autocorrelations.

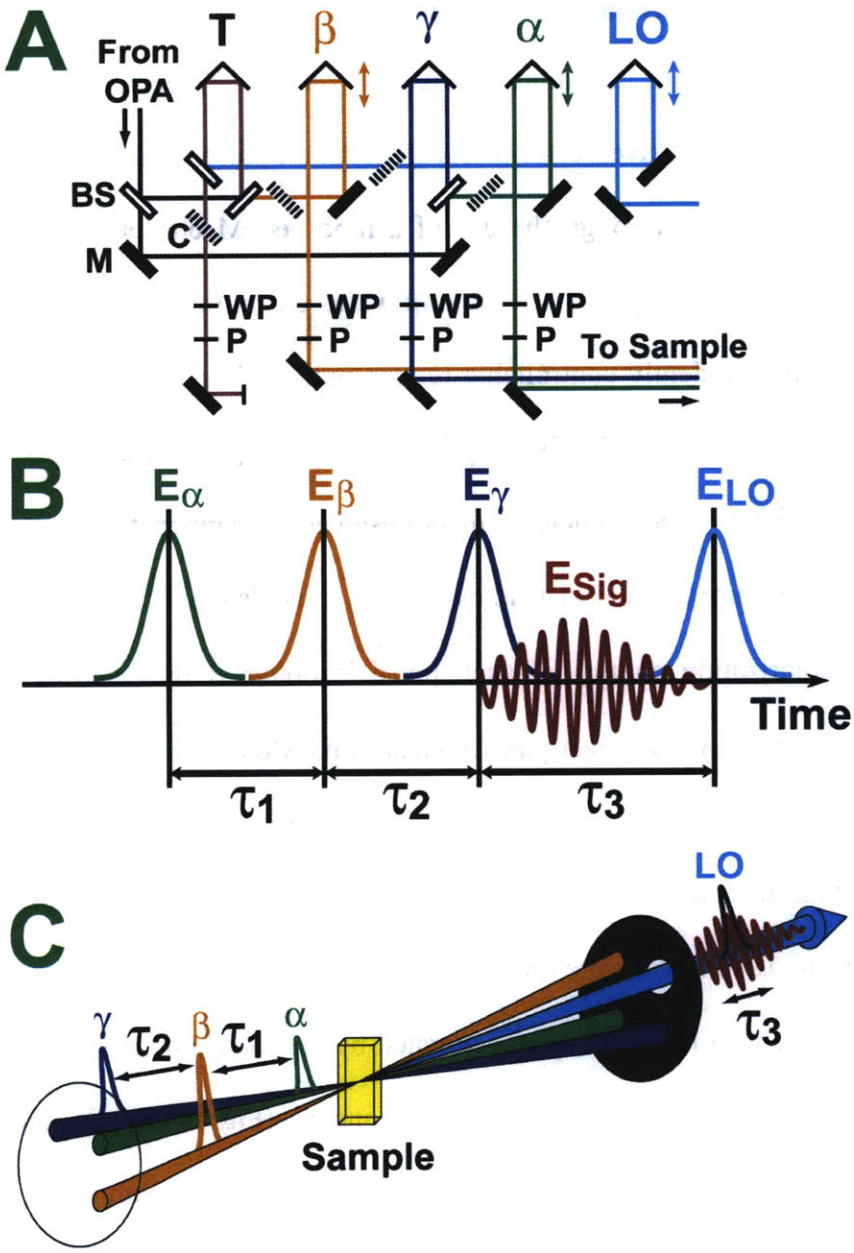


Figure 4-4: (A) Schematic showing one half of the Mach-Zehnder interferometer used for nonlinear experiments. **M** – Gold mirror. **BS** – 50/50 3 mm thick CaF_2 beamsplitter. **C** – 3 mm thick CaF_2 compensation plate. **WP** – MgF_2 tunable zero order $\lambda/2$ waveplate. **P** – CaF_2 wire grid polarizer. The interferometer is designed such that each excitation beam contains 25% of the OPA output while the tracer and local oscillator each contain only 12.5%. (B) General pulse sequence for third-order spectroscopy employing heterodyne detection. In homodyne measurements, no reference field is used. (C) Boxcar geometry employed for vibrational echo and transient grating experiments.

Fig. 4-4C shows the boxcar geometry used for vibrational echo experiments. The three excitation pulses occupy three corners of the box and stimulate the emission of a signal field into the box's missing corner, $\mathbf{k}_{Sig} = -\mathbf{k}_\alpha+\mathbf{k}_\beta+\mathbf{k}_\gamma$, where the indices α, β, and γ each refer to specific arms of the interferometer. By changing the order in which the pulses along the $\mathbf{k}_\alpha$ and $\mathbf{k}_\beta$ wave vectors interact with the sample, both rephasing ($\mathbf{k}_{Sig} = -\mathbf{k}_1+\mathbf{k}_2+\mathbf{k}_3$) and nonrephasing ($\mathbf{k}_{Sig} = +\mathbf{k}_1-\mathbf{k}_2+\mathbf{k}_3$) signals can be measured and summed to yield absorptive 2D IR spectra. The alignment of the boxcar can be optimized by maximizing the nonresonant response of a CaF_2 window that is emitted when all three excitation pulses are overlapped and time coincident on the window. This response can also be dispersed and collected as a transient grating FROG measurement, which allows retrieval of the temporal phase and amplitude of the pulse.

In experiments whose main focus was to study the behavior of dilute HOD in D_2O, samples were flowed using a 50 μm Sapphire nozzle (Meller Optics) to avoid the strong nonresonant response from CaF_2 windows that masks the sample response at waiting times less than 200 fs. Experiments involving the use of NaOD solutions could not be flowed due to the large increase in solution viscosity with increasing NaOD concentration. Instead, NaOD solutions were held between two 100 nm thick Si_3N_4 windows (Norcada) within a home built Teflon sample cell with a path length of 100 μm. The Si_3N_4 windows were found to give no nonresonant signal when excitation pulses overlap in the sample, consistent with measurements by Cowan et. al.[19] However, due to poor index matching between air and the Si_3N_4, a back reflected signal could be detected during 2D IR measurements. This signal was removed by inserting a small piece of Parafilm (~25 μm thick) into one side of the sample cell so that the two Si_3N_4 windows

were held at a small angle with respect to one another. This caused the back reflected signal to propagate in a different direction than the signal field. HOD/NaOD solutions were prepared by first diluting a 40% NaOD solution (99.5% deuteration; Cambridge Isotope Laboratories) with D_2O. A small amount of H_2O was then added to give an absorbance less than 0.4. The amount of H_2O needed to achieve this was ~1% of the solution volume.

4.3.1. Calibration of Stages for Interferometric Measurements

The measurement of purely absorptive broadband 2D IR spectra remains challenging due to the fact that 2D lineshapes can be easily distorted by improper control of the time delays between the excitation pulses. The fast Fourier transform routine that is commonly used to calculate frequency domain 2D spectra requires both a uniform step size between points and knowledge of the zero timing between each excitation pulse. Errors in either of these quantities can alter the shape of the transformed spectra or, in the worst cases, add ghost peaks to the spectra. Errors due to nonuniform step size are often related to the fact that a linear encoder is used to determine the position of each of the mechanical delay stages that control the relative timing of each excitation pulse. When a stage is required to stop at a position between two marks on the encoder, it must perform an interpolation to determine the point at which it should stop moving. Inaccuracies in this interpolation due to round-off or other complicating factors can lead to systematic step size errors. Although the stages used for the experiments described in Chapters 5 and 6 are quite accurate (±150 nm with a reproducibility of 50 nm), errors on the order of 150 nm correspond to $\lambda/10$ at 3 μm and can lead to the appearance of large side bands that distort experimental 2D spectra.

Since these improper step size errors are primarily due to inaccuracies in each mechanical stage's linear encoder, we can correct these errors by optically calibrating each stage.[18] This is accomplished by scanning each stage along the entire length of its travel and recording an interferogram using the alignment HeNe tracer that copropagates with each infrared pulse. For each stage, the interferogram is measured using quadrature detection.[20] One arm of the HeNe is passed through a λ/4 wave plate to circularly polarize it, while the other HeNe arm travels through a λ/2 wave plate before it is recombined with the circularly polarized HeNe beam on a 50/50 beamsplitter. The recombined beam is then passed through a polarizing beam cube that allows detection of the interference in both the horizontal and vertical directions on two matched ThorLabs det210 photodiode detectors. The angle of the λ/2 wave plate is adjusted to ensure that the fringe depth measured by both detectors is equal. Due to the phase shift between the horizontal and vertical components in one arm of the interferometer due to the λ/4 wave plate, the detected S and P components of the interference correspond to the sine and cosine of the accumulated phase between the two arms. This phase can be extracted by taking the inverse tangent of the ratio of two measured interferograms:

$$\phi = \tan^{-1}\left(\frac{I_P}{I_S}\right), \tag{4-1}$$

where I_P and I_S correspond to the measured S and P components of the interferogram. For perfect stage motion, the accumulated phase should increase linearly with the difference in path length between the two stages with a slope given by the inverse of the HeNe wavelength:

$$d\phi = \frac{4\pi}{\lambda_{HeNe}} dx. \tag{4-2}$$

In Eq. 4-2, $d\phi$ refers to the change in accumulated phase due to a change in the stage position of length dx and λ_{HeNe} denotes the HeNe wavelength of 632 nm.* Deviations of the measured phase from Eq. 4-2 are largely due to errors that stem from the inaccuracy of the encoder.

Fig. 4-5A displays a sample of the extracted timing error plotted in fs for a 150 μm long section of the stage, the length of which corresponds to a 1 ps time delay. The extracted error is found to be on the order of λ/10 (1 fs at 3 μm) and is quite periodic. To correct this error, we take advantage of the high reproducibility of our delay states (50 nm) and have constructed a look up table that contains the measured stage error for a given position on each delay stage. When the Labview software that operates a stage directs it to move to a certain position, the software corrects the distance of travel by the measured stage error contained in the lookup table. Before applying this correction, a Fourier transform of a measured HeNe interferogram contained numerous side bands due to inaccuracies in the stage step size (Fig. 4-5B). However, after applying the correction and measuring a second HeNe interferogram, a single peak is observed in the Fourier transform centered at the HeNe wavelength. The measured phase error after the stage calibration is significantly improved, on the order of λ/60 at 3 μm. Because this error is a property of the encoder, once a stage has been calibrated, there is no need to repeat the calibration unless a significant change has been made to the physical position of the stage on the optical table. Repeating the calibration procedure once every ~6 months was found to be sufficient to maintain λ/60 phase stability within the interferometer.

* Note, there is an extra factor of 2 included in Eq. 4-2 to account for the fact that the beam is retroreflected from the moving stage.

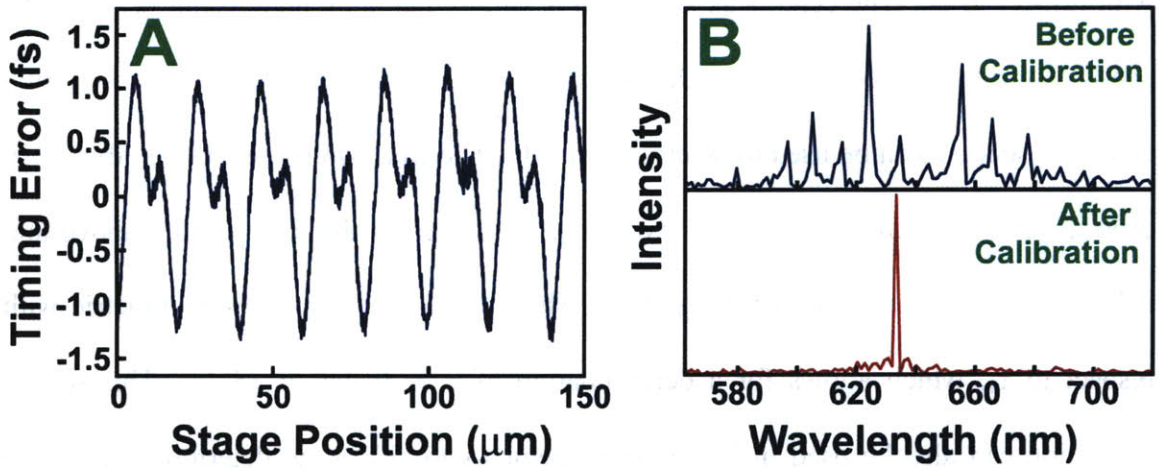


Figure 4-5: (A) Timing error extracted using the stage calibration procedure described in the text. The strong periodicity of the error suggests that it is due to a systematic error of the linear encoder used to determine the stage position. (B) Fourier transform of a HeNe interferogram recorded before and after applying the stage calibration. Without the calibration, numerous side bands appear. By applying the calibration, a single strong peak at the HeNe wavelength of 632 nm is observed with minimal side bands.

4.3.2. Photon Echo Peak Shift Experiments

In a photon echo peak shift experiment, the emitted echo signal is measured as a function of both τ_1 and τ_2. The peak shift corresponds to the value of τ_1 that maximizes the signal intensity for a given value of τ_2. No reference pulse is used to collect the echo, hence the intensity of the echo signal is integrated along the τ_3 time axis. As described in Chapter 2, the decay of the peak shift with increasing τ_2 is related to the average time scale over which the system undergoes spectral diffusion. For vibrational systems that rapidly dephase, such as the O-H stretching transition of water, the initial value of the peak shift can be quite small (<30 fs)[21] and accurate knowledge of the timings between each pulse is needed prevent errors that can distort the measured peak shift.

Precise determination of the peak shift is typically accomplished by adopting an equilateral triangle geometry.[22,23] While this geometry is not perfectly phase matched, its symmetry allows for the simultaneous emission of two echo signals that are symmetric

with respect to τ_1. The echo peak shift then is simply the point equidistant between the peaks of the two echo signals. In the boxcar geometry pictured in Fig. 4-4C, a similar detection scheme can be used to determine $\tau_1 = 0$. The first two pulses in the vibrational echo experiment generate a pair of two pulse echo signals that are emitted above and below this excitation pulse pair (Fig. 4-6). These two echo signals are symmetric with respect to τ_1, which allows for a determination of $\tau_1 = 0$ within ±5 fs. This timing correction can also be used in 2D IR measurements to aid in the determination of the absolute phase of the signal.

The detection of both the echo signal as well as the two pulse echoes used to correct the τ_1 time axis was accomplished through the use of a set of single channel liquid nitrogen cooled InSb detectors (Infrared Systems Development), which were gated using a boxcar integrator (Stanford Research Systems SR-250). The boxcar outputs were each fed into a separate lock-in amplifier referenced to the phase of an optical chopper that modulated one of the excitation beams at 500 Hz, which allowed for the subtraction of scatter from the other two excitation beams. In practice, it was found that removing scatter even at the cost of losing echo signal intensity by irising off the echo response was crucial for the success of the experiment. At very long waiting times, when the signal is small due to vibrational population relaxation, any type of scatter that propagates at a wave vector similar to that of the signal can interfere with it at the detector, yielding an echo response that contains spurious interference fringes that prevent a proper determination of the maximum of the echo response.

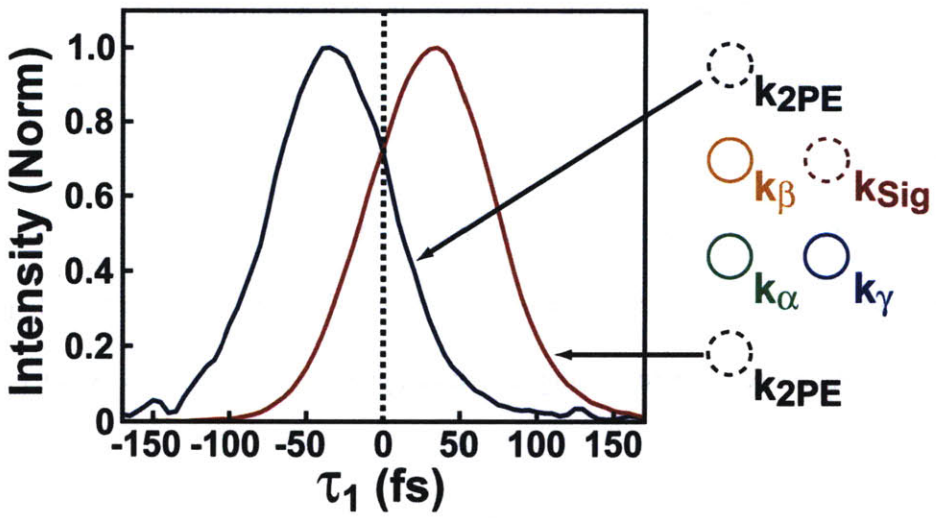


Figure 4-6: Example two pulse echo signals measured during a photon echo peak shift experiment. The two measured signals are symmetric about $\tau_1 = 0$.

4.3.3. Two-Dimensional Infrared Spectroscopy

In a 2D IR experiment, the emitted signal field is overlapped with a reference pulse, the local oscillator, using a beamsplitter and the interference between these two fields is detected using a square law detector. The intensity measured at the detector is proportional to the amplitude of the sum of the two fields:

$$I_{\text{det}} = \left|E_{Sig} + E_{LO}\right|^2 = \left|E_{Sig}\right|^2 + \left|E_{LO}\right|^2 + \left|E_{Sig}\right|\left|E_{LO}\right|\cos\left(\phi_{Sig} - \phi_{LO}\right) \qquad (4\text{-}3)$$

where ϕ_{Sig} and ϕ_{LO} correspond to the phase of the signal field and the local oscillator respectively. The $\left|E_{Sig}\right|^2$ term is often small and can be ignored while the $\left|E_{LO}\right|^2$ term can be removed by either using an optical chopper or by balanced detection of the two local oscillator/signal pairs generated by the beamsplitter (See below). The retrieved signal is then linearly proportional to the amplitude of the signal field and depends on the phase of the signal relative to that of the local oscillator. Knowledge of the absolute phase of the local oscillator (i.e. the time delay between it and the signal) as well as that of each of the

excitation pulses is needed to prevent mixing of the real and imaginary parts of the signal upon Fourier transformation. These values can be determined to an accuracy on the order of a single 3 μm infrared fringe (±5 fs) using second harmonic autocorrelations, but this alone is not precise enough to prevent distortions to the 2D spectra upon Fourier transformation. To correct for small errors in the absolute timing of each pulse, we multiply each measured 2D rephasing and nonrephasing spectrum by a constant phase correction factor:

$$\begin{aligned} \phi_R &= \exp\left[i\omega_1 \Delta\tau_1^R + i\omega_3 \Delta\tau_3 \right] \\ \phi_{NR} &= \exp\left[i\omega_1 \Delta\tau_1^{NR} + i\omega_3 \Delta\tau_3 \right]. \end{aligned} \tag{4-4}$$

Here, the set of $\Delta\tau$ values denote the small timing error of each stage.[†] The value of each of these parameters is set to satisfy the projection-slice theorem,[7] which in the context of 2D IR spectroscopy has been used to show the equivalence of a spectrally dispersed pump-probe measurement and the projection of the absorptive Fourier transform 2D correlation spectrum onto the ω_3 frequency axis.[9,24] For each measured 2D spectrum, a corresponding dispersed pump-probe is measured at the same value of the waiting time. The set of $\Delta\tau$ values in Eq. 4-4 are then varied until agreement between the projection of the 2D spectrum and the measured dispersed pump-probe is found (Fig. 4-7).

The measurement of a broadband 2D IR spectrum requires that the interference between the overlapped signal/local oscillator pair be detected by either spectrally resolving the interference or by scanning the local oscillator in time with respect to the signal field. We have utilized both of these approaches for the collection of multidimensional spectra, and a schematic description of these two methods appears in

[†] Different values are used for the τ_1 timing error for the rephasing and nonrephasing spectra since this time axis is determined by scanning two separate motorized translation stages in the boxcar geometry.

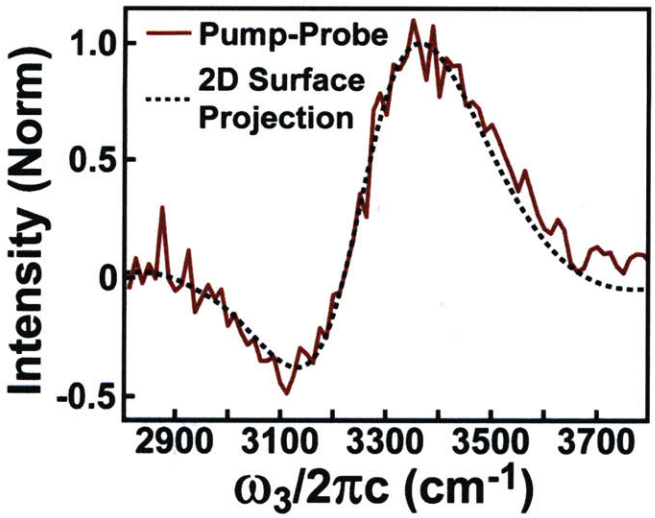


Figure 4-7: Comparison between the projection onto the ω_3 axis of a 2D IR spectrum for a sample of ~1% HOD dissolved in 10.6M NaOD/D_2O measured a waiting time of 50 fs and a dispersed pump-probe of the same sample solution measured at a corresponding waiting time. The value of the constant phase added to the 2D spectrum (Eq. 4-4) was adjusted until sufficient agreement between the ω_3 projection and the pump-probe measurement was found. This ensures that the 2D lineshape obtained upon Fourier transformation corresponds to the absorptive response of the sample.

Fig. 4-8. In the mixed time/frequency domain approach, the overlapped signal and local oscillator are spectrally dispersed onto a multichannel infrared array detector. By spectrally dispersing the interferogram, the interference between the local oscillator and the signal is collected simultaneously at each frequency that comprises the ω_3 axis of the 2D spectrum, thereby eliminating the need to scan the local oscillator stage. Collection of the excitation dimension of a 2D spectrum is obtained by scanning the τ_1 time delay, yielding a mixed time/frequency 2D data set. A numerical Fourier transform of the data along the τ_1 axis yields a frequency domain 2D spectrum.

This mixed time/frequency domain scanning method was adopted to collect the 2D spectra that appear in Chapter 5 and some of the spectra found in Chapter 6. After the sample, the signal and local oscillator fields were combined using a 50/50 beamsplitter,

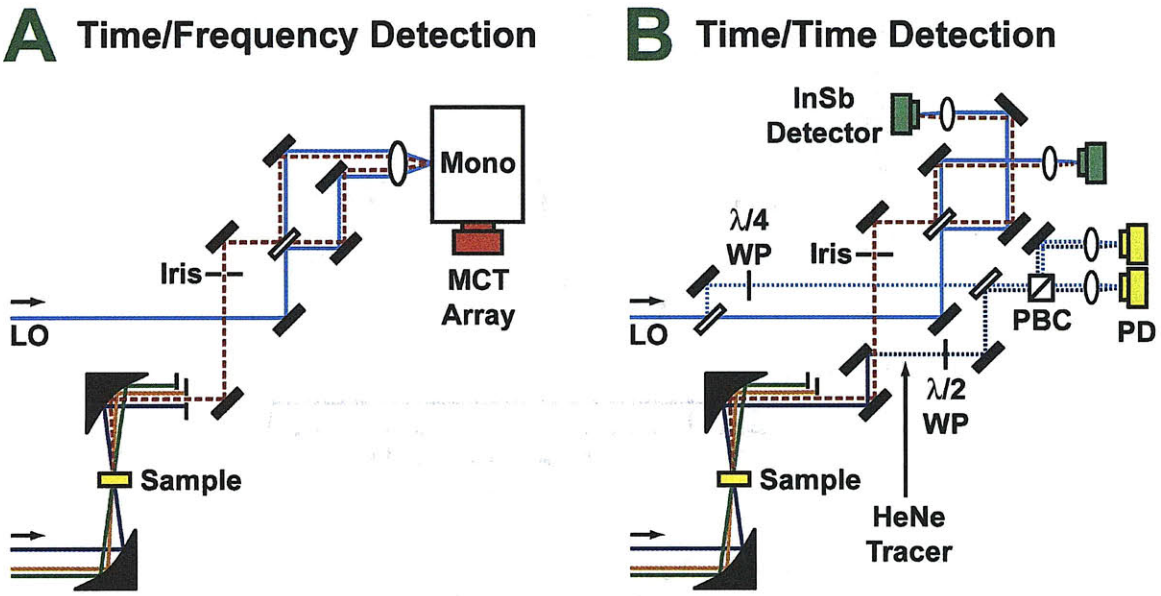


Figure 4-8: Schematic descriptions of the experimental layouts used to record 2D spectra using (A) mixed time/frequency domain detection and (B) pure time domain detection. The signal emitted by the sample is denoted by the long dashed red line, while the HeNe tracers that copropagate with the third IR excitation field and the local oscillator are represented by the dotted blue and cyan lines respectively. **LO** – Local oscillator. **PCB** – Polarizing beam cube. **WP** – Wave plate. **PD** – Photodiode. **MCT** – Mercury Cadmium Telluride. **Mono** – Grating monochromator.

generating two overlapped signal/local oscillator pairs that were both collected by spectrally dispersing each using a Triax 190 single grating spectrometer (Jobin Yvon) onto a single strip of a 2 x 64 liquid nitrogen cooled multichannel HgCdTe array detector (Infrared Systems Development). The frequency detected by each pixel on the array was determined by Fourier transforming a measured interferogram between the local oscillator and the nonresonant response generated by a CaF_2 window placed at the sample position. A 2D correlation spectrum for a set value of τ_2 was measured by scanning the E_α and E_β time delays shown in Fig. 4-4 to generate rephasing and nonrephasing spectra respectively. For the data that appears in Chapter 5, the τ_1 time axis was moved in step sizes of 2 fs and scanned for a total range of 400 fs, 200 fs each for rephasing and

nonrephasing spectra. This total scan range was slightly increased to 500 fs to record the data in Chapter 6, and was again evenly split between rephasing and nonrephasing spectra. An optical chopper was used to modulate one of the excitation beams at 500 Hz, which allowed for the subtraction of homodyne contributions to the measured interferogram. The timing between the signal and local oscillator was set by ensuring that the interferograms measured at a delay of ±600 fs between the signal and local oscillator were identical. Data were zero padded to 2048 time points along the τ_1 axis before Fourier transformation.

Two different array/spectrometer pairs were used for the collection of 2D data. Both spectrometers used a 75 g/mm grating optimized for the reflection of 3 μm light, however slight differences in the design of the spectrometer resulted in different spectral resolutions for both experimental setups. The resolution of the spectrometer/array used to record the spectra in Chapter 5 was found to be ~5 cm^{-1}/pixel which allowed a total bandwidth of 320 cm^{-1} to be dispersed onto the array. This bandwidth is somewhat smaller than that of each of the excitation pulses and also limited the ability to simultaneously record spectra for both the $v = 1 \leftarrow 0$ and anharmonically shifted $v = 2 \leftarrow 1$ stretching transitions of the HOD molecule. For each 2D correlation spectrum, two separate experiments were run back to back with the spectrometer centered at a frequency near the peak of the $v = 1 \leftarrow 0$ and $v = 2 \leftarrow 1$ transitions. The measured data where Fourier transformed, phased separately, and then averaged together in the spectral range of overlap (~20 cm^{-1}) between the two recorded spectra to give a 2D correlation spectrum that spans ~550 cm^{-1} along the ω_3 axis. The data in Chapter 6 recorded using mixed time/frequency detection were measured using the second spectrometer/array setup which

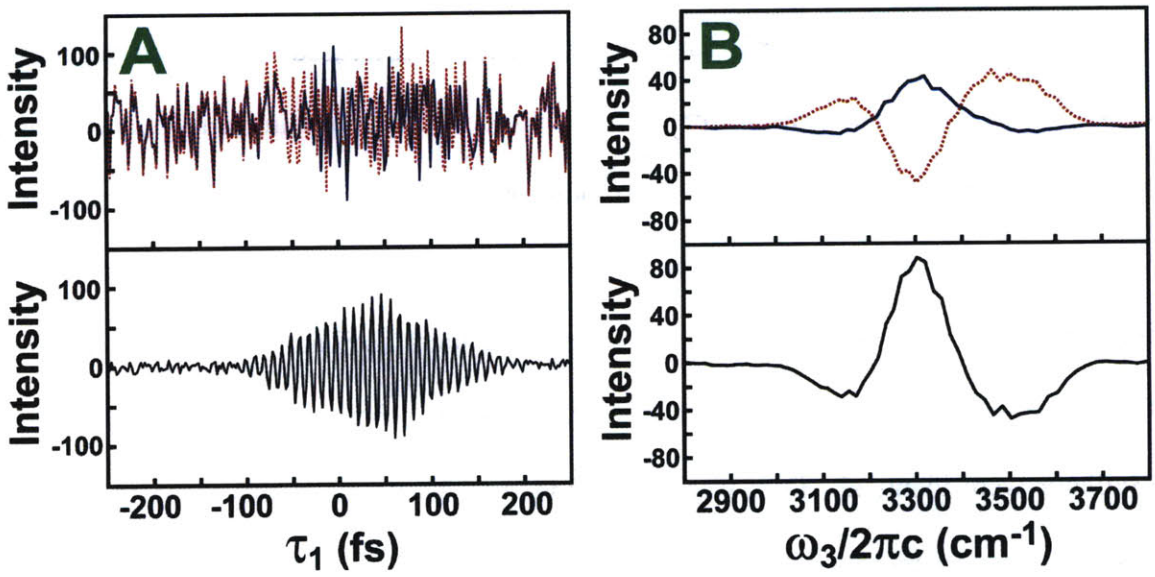


Figure 4-9: Demonstration of balanced detection in both the time and frequency domains. The solid blue and red dashed traces in (A) correspond to the interference measured at two vertically displaced pixels of the array. As τ_1 is scanned, the interference between the signal and local oscillator measured at these two pixels is out of phase. Significant noise obscures the signal which peaks at $\tau_1 = 50$ fs. Subtraction of the data measured by each pixel allows removal of much of the scatter and local oscillator intensity fluctuations that are common to both pixels, yielding the clear interferogram shown in black. (B) The two spectrally dispersed out of phase signals at $\tau_1 = 0$ fs are shown in dashed red and blue. Their subtraction yields the spectrum in black.

had a frequency resolution of 8.1 cm^{-1}/pixel. This resolution was large enough to measure a 2D correlation spectrum without having to move the spectrometer grating.

Due to the change in the phase of a pulse that occurs upon reflection, there is a π phase shift between the two signal/local oscillator pairs generated by the beam splitter (Fig. 4-9). The detection of both pairs and their subsequent subtraction allows for the removal of any homodyne contribution to the interferogram due to the local oscillator and also reduces scatter that is common to both overlapped signal/local oscillator pairs. The quality of the noise suppression that results from the subtraction is highly sensitive to variations in the local oscillator intensity placed on each stripe as well as the alignment of each beam into the spectrometer. To ensure that the signal/local oscillator interference

was equal for both stripes, a delay of 600 fs between the signal and local oscillator was introduced, which created a number of interference fringes in the detected response. The alignment into the array as well as small changes in the polarization[‡] and intensity of the local oscillator were made to ensure that the measured interference was π phase shifted and equal in intensity on both stripes of the array. Additional small corrections for variations in signal intensity between the two stripes were made in software by normalizing the interferogram measured on each stripe by the intensity of the local oscillator measured on that stripe. When properly performed, balanced detection can result in a 10x signal-to-noise improvement.

Fig. 4-10 shows a sample 2D spectrum of dilute HOD in D_2O at a waiting time of 200 fs recorded using this scanning procedure. For each τ_1 value, the data spread across the ω_3 axis was averaged for 1500 laser shots, which allowed the surface to be recorded in ~10 minutes. Along the τ_1 time axis the signal oscillates at the frequency of detection along the ω_3 dimension. τ_1 values less than zero correspond to the portion of the signal due to nonrephasing excitation pathways while positive τ_1 values denote the rephasing portion of the 2D spectrum. The fact that the rephasing portion of the spectrum extends further in τ_1 shows that at this waiting time spectral diffusion is not yet complete. Fourier transform of the τ_1 time dimension yields the absorptive correlation spectrum pictured to the right in Fig. 4-10. The positive tilt of the spectrum along the diagonal axis is a result of the residual frequency memory retained at this waiting time.

While time/frequency detection of 2D spectra eliminates the need to scan the local

[‡] The 50/50 beam splitters employed for the recombination of the signal and local oscillator are slightly polarization dependent. By making small changes in the local oscillator polarization, the amount of the local oscillator that travels alongside both of the two signal replicas created by the beamsplitter can be adjusted.

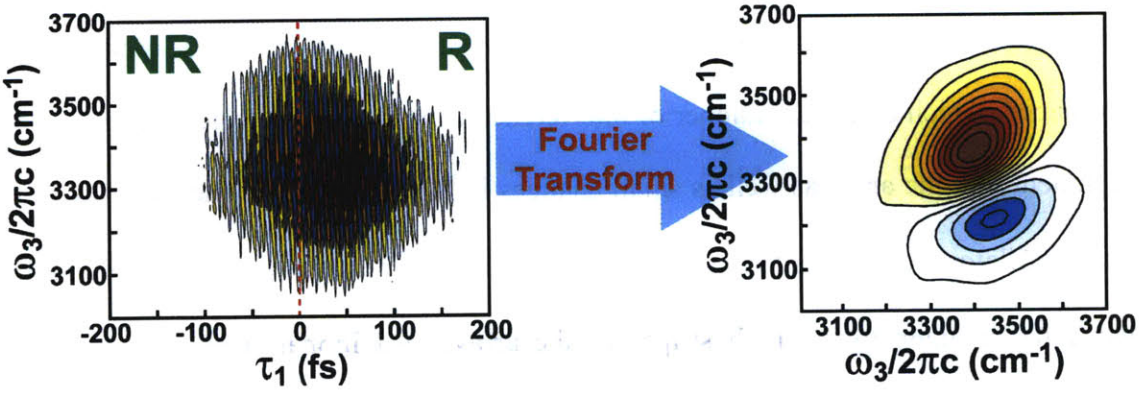


Figure 4-10: Example 2D spectrum recorded using mixed time/frequency domain detection. The sample consists of ~1% HOD dissolved in D_2O and the measured waiting time corresponds to $\tau_2 = 200$ fs. The signal that appears along the negative portion of the τ_1 time axis is due to nonrephasing processes whereas the signal at positive τ_1 time delays arises from rephasing pathways. Fourier transformation of the spectrum along τ_1 yields the spectrum displayed to the right.

oscillator stage, there are some disadvantages to this technique that can be overcome by switching to a pure time domain detection scheme. For example, in time/frequency detection, the spectral resolution along the ω_3 dimension is set by the dispersion of the grating and the spacing of the pixels in the array detector, which are not adjustable parameters. In the case where the dispersion of the grating poorly matches the width of the vibrational transition of interest, multiple 2D spectra must be recorded and patched together. In time domain scanning, the spectral resolution is instead set by the total length of time scanned along the τ_3 dimension and the signal sampling rate, which can be adjusted depending on experimental needs and constraints. A second disadvantage of time/frequency scanning is that by spectrally dispersing the signal, the total energy of the signal field is dispersed along the elements of the array, which decreases the intensity that is detected per pixel with respect to that measured on a single channel detector. This intensity/pixel loss coupled with the fact that many infrared gratings are at most ~70% efficient means that very weak signals can be more easily detected using time domain

scanning vs. mixed time/frequency detection. Lastly, infrared array detectors are generally quite expensive, often costing in the range of $70,000-$90,000. The pair of liquid nitrogen cooled single channel detectors we employed for time domain detection cost only ~$3,000, making this technique an attractive alternative in the absence of funds for a multichannel array detector.

Of course, the major disadvantage of direct time domain detection is that the local oscillator needs to be scanned in time with respect to the signal field, which can be extremely time consuming. For example, a 2D surface obtained by scanning the τ_1 and τ_3 time delays a total of 500 fs in each dimension using 2 fs steps and an acquisition time of 60 ms per time point would take ~ 1 hour. This estimate does not include time spent moving each stage from point to point as well as the equilibration time for the detection electronics (~120 ms/point), which can triple the length of the measurement. A long acquisition time for a 2D surface makes the measurement problematic since small changes in the path length of any of the interferometer arms over this time period can distort the results of the measurement. For systems with narrow spectral features and long dephasing times, the constraints on the phase stability of the system are increased since a longer time delay in both the τ_1 and τ_3 dimensions must be scanned.

We have devised a method that allows us to rapidly acquire 2D spectra in the time domain by using a fast scanning technique that is analogous to the operation of many commercial FT-IR interferometers. In such an instrument, a spectral interferogram is measured by moving one arm of the interferometer at constant velocity as data is continuously collected. The interference fringes of a HeNe tracer that copropagates with the infrared light are counted to determine the position of the stage at each time point.

Our experimental setup is displayed in Fig. 4-8B. Similar to the mixed time/frequency domain approach described above, balanced detection of the signal field is employed using two single channel liquid nitrogen cooled InSb detectors (Infrared Systems Development) that are each gated using separate boxcar integrators. Instead of step scanning the τ_3 time delay for a given τ_1 value, we rapidly acquire data along this time axis by moving the local oscillator stage at constant velocity starting from a negative τ_3 value (typically 200-300 fs before the emission of the signal field) to a large, positive time delay. As the stage moves, the interference between the signal and local oscillator is measured for each laser shot using a 250 kilo-samples per second DAQ card (National Instruments). Once a rapidly scanned τ_3 data set is measured, τ_1 is incremented using a 2 fs step size made with respect to the calibrated lookup table described in Section 4.3.1 and another rapid τ_3 scan is performed until a full (τ_1, τ_3) data set spanning a τ_1 range of 250 fs for both rephasing and nonrephasing signals is obtained. When the two boxcar outputs were properly balanced, it was found that homodyne contributions could be adequately removed from the measured temporal interferograms by subtraction of the signals alone, eliminating the need to modulate the signal field using an optical chopper as the local oscillator stage is scanned. Using this technique, a full 2D correlation spectrum can be measured in under 8 minutes. While this acquisition time is comparable to that of the mixed time/frequency method described above, the time/frequency technique could only be used to measure spectra up to a waiting time of 1.5 ps due to population relaxation of the HOD molecule (T_1 = 700 fs[25]). Instead, due to the enhanced signal-to-noise of the direct time domain measurement, spectra up to waiting times of 10 ps were measured (See Chapter 6).

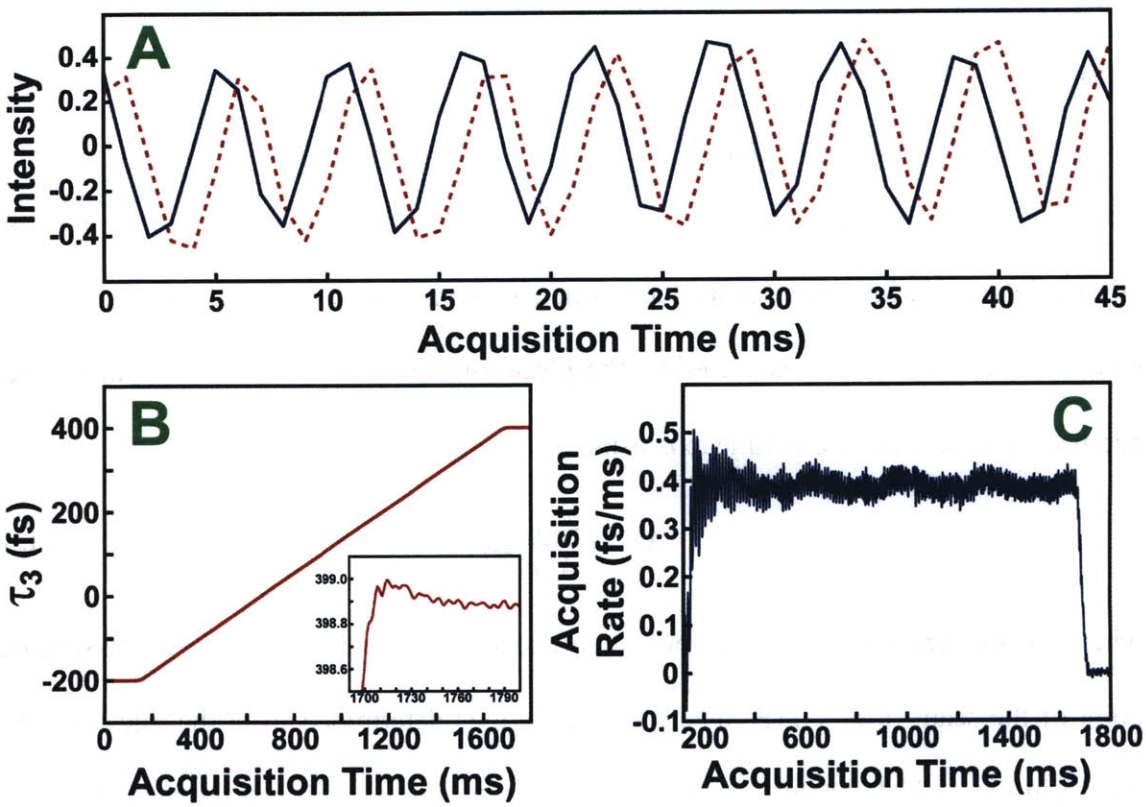


Figure 4-11: Determination of the τ_3 time axis for a rapidly scanned time domain 2D spectrum. (A) In quadrature interferograms recorded between the HeNe tracer of the local oscillator and the third excitation beam as the local oscillator is moved at constant velocity. (B) The extracted τ_3 time delay as a function of time. (Inset) The phase extraction procedure is accurate enough to show that the stage overshoots its final position by ~15 nm before backtracking to its target final position. (C) The extracted velocity profile for the stage motion. Since it is not constant, the data acquired during a fast scan is first interpolated to an equally spaced grid of points before Fourier transformation.

To determine the value of τ_3 that corresponds to each individual laser shot, quadrature detection of the interference between the HeNe alignment beams that copropagate with the local oscillator and the third excitation pulse is used. The quadrature detection setup that is employed is identical to that already described in the context of the stage calibrations in Section 4.3.1. This interference is measured using two matched photodiodes and is acquired at a 1 kHz sampling rate using the DAQ card described above. An example section of an interferogram acquired during the

measurement of a 2D surface is given in Fig. 4-11A. The velocity of the moving stage is set at 58 nm/ms so that ~5 points along each HeNe fringe are recorded as the local oscillator stage moves. This has the added benefit that the measured infrared interferogram is highly oversampled (~25 pts/infrared fringe), which allows the easy elimination of spurious data points due to fluctuations in laser intensity. Once a pair of in quadrature interferograms is recorded, the phase of the interference can be unwrapped and used to determine the τ_3 time axis using:

$$\Delta\tau_3 = \frac{\lambda_{HeNe}}{4\pi c}\Delta\phi, \tag{4-5}$$

where $\Delta\phi$ and $\Delta\tau_3$ refer to the accumulated phase and τ_3 time delay relative to the starting point of the scan. Fig. 4-11B displays the time axis determined from the interferogram shown in Fig. 4-11A. After a brief equilibration period of ~150 ms, the velocity of the stage appears to be roughly constant, giving an equal spacing between each of the acquired points. However, upon closer inspection we find that the stage velocity displays small deviations from constant velocity (Fig. 4-11C). To correct for the variations in the velocity profile, the recorded data is interpolated to an evenly spaced grid with a point separation of 2 fs. The time domain data set was zero padded to 2048 points along both dimensions prior to Fourier transformation.

An example of a 2D time domain spectrum of the O-H stretching transition of a solution of dilute HOD in D_2O at a waiting time of 200 fs measured using the described fast scanning technique appears in Fig. 4-12. Interference fringes are observed to oscillate in phase along the antidiagonal time axis, indicating that no phase drift due to interferometer instabilities occurs over the course of the measurement. Slices along the τ_1 and τ_3 dimensions of the 2D data set show strong modulation depths along both the

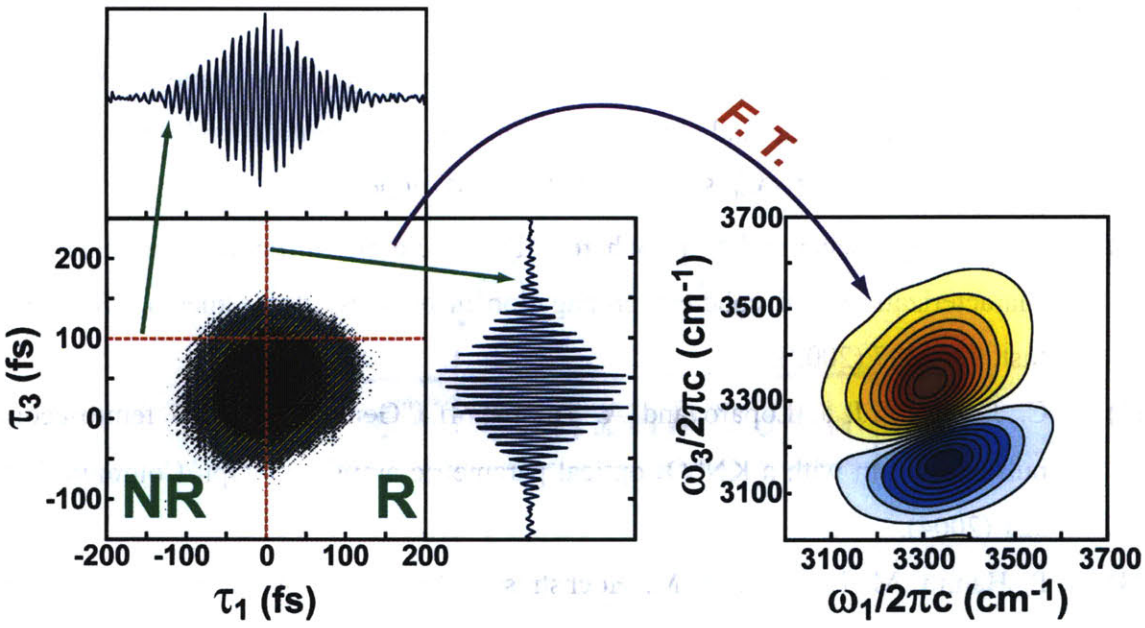


Figure 4-12: Example 2D spectrum recorded in the time domain using the rapid scanning procedure described in the text. As in Fig. 4-10, the sample consists of a solution of ~1% HOD in D_2O and the data was recorded for a waiting time of 200 fs. Strong fringe modulation is observed along both the rapidly (τ_3) and step scanned (τ_1) time dimensions. A 2D Fourier transform yields a frequency domain spectrum that displays no discernable ghost peaks or other transform errors.

rapidly and step scanned dimensions. A two dimensional Fourier transform of the time domain data yields the frequency domain correlation spectrum displayed in the right portion of Fig. 4-12. This spectrum is comparable in signal-to-noise to that obtained using mixed time/frequency domain detection despite the fact that each measured (τ_1, τ_3) time point corresponds to a single laser shot.[§]

Acknowledgements

I am indebted to Joseph Loparo for his help in building the first version of the time domain acquisition setup detailed in Section 4.3.3.

[§] The differences in the position of the peak of the frequency domain 2D spectra shown in Fig. 4-10 and 4-12 largely stem from differences in the center position of the excitation pulses used to record the data. The data in Fig. 4-10 was recorded using a pulse tuned to the maximum of the HOD linear IR absorption peak at 3400 cm^{-1} while the data in Fig. 4-12 was measured using a red shifted pulse peaked at 3350 cm^{-1}.

References

(1) R. A. Kaindl, M. Wurm, K. Reimann, P. Hamm, A. M. Weiner and M. Woerner, "Generation, shaping, and characterization of intense femtosecond pulses tunable from 3 to 20 μm," J. Opt. Soc. Am. B 17, 2086 (2000).

(2) J. A. Gruetzmacher and N. F. Scherer, "Few-cycle mid-infrared pulse generation, characterization, and coherent propagation in optically dense media," Rev. Sci. Inst. 73, 2227 (2002).

(3) C. J. Fecko, J. J. Loparo and A. Tokmakoff, "Generation of 45 femtosecond pulses at 3 μm with a $KNbO_3$ optical parametric amplifier," Opt. Commun. 241, 521 (2004).

(4) P. Hamm, M. Lim and R. M. Hochstrasser, "Structure of the amide I band of peptides measured by femtosecond nonlinear-infrared spectroscopy," J. Phys. Chem. B 102, 6123 (1998).

(5) V. Cervetto, J. Helbing, J. Bredenbeck and P. Hamm, "Double-resonance versus pulsed Fourier transform two-dimesional infrared spectroscopy: An experimental and theoretical comparison," J. Chem. Phys. 121, 5935 (2004).

(6) J. D. Eaves, J. J. Loparo, C. J. Fecko, S. T. Roberts, A. Tokmakoff and P. L. Geissler, "Hydrogen bonds in liquid water are broken only fleetingly," Proc. Natl. Acad. Sci. U.S.A. 102, 13019 (2005).

(7) R. R. Ernst, G. Bodenhausen and A. Wokaun, *Principles of Nuclear Magnetic Resonance in One and Two Dimensions*, (Oxford University Press, Oxford, 1987).

(8) J. J. Loparo, *Ultrafast structural fluctuations and rearrangements of water's hydrogen bonded network*, Ph.D Thesis, Massachusetts Institute of Technology, Dept. of Chemistry, 2006.

(9) J. D. Hybl, A. A. Ferro and D. M. Jonas, "Two-dimensional Fourier transform electronic spectroscopy," J. Chem. Phys. 115, 6606 (2001).

(10) M. Khalil, N. Demirdoven and A. Tokmakoff, "Coherent 2D IR spectroscopy: Molecular structure and dynamics in solution," J. Phys. Chem. A 107, 5258 (2003).

(11) T. Zhang, C. N. Borca, X. Li and S. T. Cundiff, "Optical two-dimensional Fourier transform spectroscopy with active interferometric stabilization," Optics Express 13, 7432 (2005).

(12) T. Brixner, I. V. Stoipkin and G. R. Fleming, "Tunable two-dimensional femtosecond spectroscopy," Opt. Lett. 29, 884 (2004).

(13) L. P. DeFlores, R. A. Nicodemus and A. Tokmakoff, "Two-dimensional Fourier transform spectroscopy in the pump-probe geometry," Opt. Lett. 32, 2966 (2007).

(14) M. L. Cowan, J. P. Ogilvie and R. J. D. Miller, "Two-dimensional spectroscopy using diffractive optics based phased-locked photon echoes," Chem. Phys. Lett. 386, 184 (2004).

(15) U. Selig, F. Langhojer, F. Dimler, T. Lohrig, C. Schwarz, B. Gieseking and T. Brixner, "Inherently phase-stable coherent 2D spectroscopy using only conventional optics," Opt. Lett. 33, 2851 (2008).

(16) W. J. Tropf, M. E. Thomas and T. J. Harris, "Properties of crystals and glasses," in *Handbook of Optics*, edited by M. Bass, 2, (Optical Society of America, New York, 1995).

(17) C. J. Fecko, J. J. Loparo, S. T. Roberts and A. Tokmakoff, "Local hydrogen bonding dynamics and collective reorganization in water: Ultrafast IR spectroscopy of HOD/D_2O," J. Chem. Phys. 122, 054506 (2005).

(18) J. J. Loparo, S. T. Roberts and A. Tokmakoff, "Multidimensonal infrared spectroscopy of water. I. Vibrational dynamics in 2D lineshapes," J. Chem. Phys. 125, 194521 (2006).

(19) M. L. Cowan, B. D. Bruner, N. Huse, J. R. Dwyer, B. Chugh, E. T. J. Nibbering, T. Elsaesser and R. J. D. Miller, "Ultrafast memory loss and energy redistribution in the hydrogen bond network of liquid H_2O," Nature 434, 199 (2005).

(20) L. Lepetit, G. Chériaux and M. Joffre, "Linear techniques of phase measurement by femtosecond spectral interferometry for applications in spectroscopy," J. Opt. Soc. Am. B 12, 2467 (1995).

(21) C. J. Fecko, J. D. Eaves, J. J. Loparo, A. Tokmakoff and P. L. Geissler, "Ultrafast hydrogen bond dynamics in the infrared spectroscopy of water," Science 301, 1698 (2003).

(22) T. Joo, Y. Jia, J.-Y. Yu, D. M. Jonas and G. R. Fleming, "Dynamics in isolated bacterial light harvesting antenna (LH2) of *Rhodobacter sphaeroides* at room temperature," J. Phys. Chem. 100, 2399 (1996).

(23) S. A. Passino, Y. Nagasawa, T. Joo and G. R. Fleming, "Three-pulse echo peak shift studies of polar solvation dynamics," J. Phys. Chem. A 101, 725 (1997).

(24) D. M. Jonas, "Two-dimensional femtosecond spectroscopy," Annu. Rev. Phys. Chem. 54, 397 (2003).

(25) J. J. Loparo, C. J. Fecko, J. D. Eaves, S. T. Roberts and A. Tokmakoff, "Reorientational and configurational fluctuations in water observed on molecular length scales," Phys. Rev. B 70, 180201 (2004).

Chapter 5

Structural Rearrangements in Water Viewed Through Two-Dimensional Infrared Spectroscopy

5.1. Introduction

Although key to many chemical and biological processes, a molecular understanding of how the structure of liquid water evolves with time continues to challenge researchers. The structures of many simple liquids are dictated by repulsive Lennard-Jones forces that prevent the interpenetration of neighboring molecules. While interactions of this type are at play in liquid water, its structure is equally shaped by attractive forces due to water's unique ability to both accept and donate two hydrogen bonds. Due to the directionality of these attractive interactions, liquid water forms an extended tetrahedral network held together by hydrogen bonds.[1] While strong compared to other attractive intermolecular forces, hydrogen bonds are 2-3 orders of magnitude weaker than many common covalent bonds. At room temperature, thermal fluctuations allow water's tetrahedral network to rearrange over time scales that range from femtoseconds to picoseconds.[2,3] The rapid nature of these fluctuations, coupled with the water molecule's large dipole moment forms the heart of aqueous reactivity, allowing water to rapidly respond to changes in solute electronic structure[4] and guide the motion of protons through solution.[5]

When discussing the "structure" of liquid water, it is common to adopt a perspective based on instantaneous configurations of the liquid and the variation of hydrogen bond distances and angles within these liquid "snapshots." The distribution of structures in liquid water under ambient conditions remains a topic of debate[6,7] despite decades of experiments, theory, and computer simulation. Some researches picture water as a continuum of hydrogen bonding configurations that fluctuate about an average structure whereas others describe water as a mixture of two or more distinct, stable hydrogen bonding species.[8] Experimentalists often implicitly evoke this latter view of water when fitting components to features that appear in Raman and infrared absorption measurements. The presence of isosbestic points have often been looked to as a means of justifying a two component model of water.[9,10] However, calculations by Geissler[11] have shown that isosbestic points can arise in linear spectra even for a continuous distribution of transition frequencies. Recent x-ray absorption measurements have added a new side to this debate by calling into question water's tetrahedral arrangement of molecules, suggesting instead that water forms ring or chain structures in which each molecule accepts and donates one weak and one strong hydrogen bond.[6,12,13]

Attempts such as these to describe water's structure solely in terms of the instantaneous structure of the liquid can be misleading because they ignore the fact that only small barriers exist between different liquid configurations. In an instantaneous "snapshot" of the liquid, many water molecules will be engaged in large fluctuations about a stable configuration, and it is difficult to separate these unstable transient fluctuations from those that correspond to minima on water's free energy surface. Only by following the dynamics of water molecules can stable liquid configurations be

identified. A perspective that we adopt here is that questions regarding water's structure can be better addressed by rephrasing them in terms of its dynamics. Specifically, what are the magnitude and time scales over which hydrogen bonding configurations in water fluctuate, and what is the mechanism by which hydrogen bonds rearrange in water? Given that many definitions of a hydrogen bond are based on instantaneous geometric criteria,[14,15] should we instead consider a hydrogen bond definition that includes a characteristic time scale?

A large number of the conceptual descriptions that have been proposed for water's structure have been steeped in the language of static configurations since many of the traditional experimental probes used to study liquids cannot view changes in water's structure over femtosecond time scales. Neutron and X-ray scattering measure the average spacing between atoms in the liquid, but these experiments are not time resolved.[16,17] Infrared absorption and Raman scattering measurements provide information on the distribution of different structures present in the liquid, but are only marginally sensitive to liquid dynamics.[18] Dielectric relaxation and nuclear magnetic resonance dipolar relaxation can measure an average reorientation time scale of water molecules within some approximations, but these techniques cannot distinguish the fluctuations due to different subensembles that may exist in the liquid.[19] Optical Kerr effect measurements[2,20,21] and electronic solvation dynamics experiments[4,22] have femtosecond time resolution, but are often difficult to interpret due to a lack of a well defined relationship between the observable in these experiments and the underlying dynamics of water's hydrogen bonding network.

From a computational perspective, classical molecular dynamics (MD) simulations have allowed researchers to test proposals for water's structure in microscopic detail. Simulations clarify the types of orientational and translational fluctuations that water molecules undergo within a stable configuration on femtosecond time scales and suggest that hydrogen bond rearrangements on picosecond or longer time scales involve the loosely correlated motion of many molecules.[14,23-25] However, MD simulations are based on models often parameterized to reproduce bulk thermodynamic properties, and it is not clear whether their predictions for microscopic fluctuations are accurate. Simulations need to be compared with experimental benchmarks to prove their validity for the description of water dynamics.

Two-dimensional infrared spectroscopy (2D IR) has the ability to fill the gap between experiment and simulation due to both its high time resolution and structural sensitivity. The time resolution of a 2D IR experiment is set by the dephasing time of the vibration under study, which generally lies in the sub-picosecond range for many commonly studied vibrational transitions. In the case of water, nonlinear infrared experiments have primarily focused water's OH stretching transition since the frequency of this transition, ω_{OH}, shifts depending on the strength of the hydrogen bond formed by the O-H bond.[25-27] The formation of a hydrogen bond weakens the bond, broadening the proton stretching potential and decreasing ω_{OH}. Water molecules participating in strong hydrogen bonds tend to absorb on the low frequency side of the O-H line shape, whereas molecules in weak or broken hydrogen bonds absorb at higher frequency. Experimentalists have primarily studied isotopically dilute solutions of HOD in D_2O to avoid complications due to the intramolecular and intermolecular couplings of degenerate

oscillators, allowing fluctuations in ω_{OH} to be interpreted solely in terms of changes in the HOD molecule's local environment.[3,28-31] 2D IR spectroscopy enables us to measure time dependent shifts in ω_{OH} that can be related to changes in water's hydrogen bonding structure. Recent advances in simulation techniques have allowed for the development of mixed quantum-classical methodologies that can be used to calculate multidimensional spectra from classical simulation models,[26,32-36] thereby allowing the origin of spectral features observed in 2D IR experiments to be determined in mechanistic detail.

This chapter describes the results of ultrafast 2D IR measurements that have provided new information on the stability of different hydrogen-bonding configurations in liquid water.[37-40] A 2D IR spectrum is related to the probability of observing a molecule at given initial and final frequencies after a fixed waiting period. 2D IR spectra of the O-H stretching transition of HOD in D_2O are found to be highly asymmetric. As the waiting time increases, the 2D spectrum preferentially broadens on the high frequency side of the lineshape over a time scale of ~60 fs, consistent with librations (hindered rotations) of water molecules. This broadening indicates that configurations wherein molecules participate in weak or broken hydrogen bonds are unstable and reorient rapidly to return to a hydrogen bonded configuration. MD simulations support this conclusion and suggest that water molecules undergo a large-angle reorientation during the course of hydrogen bond exchange. The transition state for hydrogen bond rearrangements can be well described as a bifurcated hydrogen bond. Roughly half of the hydrogen bond exchange events in the simulation are found to involve the insertion of a water molecule across a hydrogen bond, suggesting that hydrogen-bond exchange in

water is a correlated process that involves the coordinated motion of many water molecules.

5.2. Experimental and Theoretical Methods

A detailed description of the measurement and interpretation of 2D IR spectra appear in Chapters 2 and 4 of this thesis, so only a brief description is given here. The 2D IR spectra that appear in Fig. 5-3 were recorded at zzzz polarization (parallel excitation beams and signal field) using the mixed time-frequency detection method described in Section 4.3.3. The sample for these measurements consisted of a ~1% solution of dilute HOD in D_2O prepared by adding a small amount of H_2O to a D_2O solution and was flowed as a 50 μm jet using a sapphire nozzle. The 1D metrics displayed in Fig. 5-4 and the 2D anisotropy spectra in Fig. 5-15 were calculated from surfaces acquired using the pure time domain technique also described in Section 4.3.3. For these experiments, the sample was held between two 100-nm thick Si_3N_4 windows using a home made Teflon cell.

MD simulations employing the commonly used simple point charge/extended (SPC/E) empirical water potential were performed to aid in the microscopic interpretation of experimentally measured 2D lineshapes. The simulations were carried out using a home built simulation code that has been described elsewhere.[35,41] A periodically replicated box consisting of a single HOD molecule and 107 D_2O molecules was simulated using the Velocity-Verlet algorithm with a 3 fs time step. This time step was sufficient to keep the energy fluctuations of the system on the order of 10^{-4} of the average system energy. Unless noted otherwise, simulations were performed at 298 K and the size of the simulation box was set to reproduce the density of D_2O at this temperature,

1.104 g/cm^3.[42] Velocities were rescaled every 10 ps to ensure that the temperature did not deviate significantly from the equilibrium set value.

The calculation of 2D IR spectra from MD simulation requires a methodology for the calculation of vibrational frequencies. The approach that we have employed uses a model Hamiltonian:[27,35]

$$H = H_S + H_B + H_{SB} \tag{5-1}$$

that describes the interaction of a single quantum mechanical degree of freedom, the O-H stretching vibration (H_S), with the classical translational and rotational degrees of freedom of the bath (H_B). H_S is taken from a Morse potential fitted to gas phase data by Reimers and Watts.[43] We can make an adiabatic separation between the system and bath coordinates since the motions of the bath are typically much slower than the vibrational period of the O-H bond. For a given bath configuration, the total potential energy of the system is only a function of the displacement along the O-H bond, and we can calculate H_{SB} by stretching the bond. Generally, H_{SB} varies slowly along this coordinate, and a Taylor series truncated at second order can provide a sufficient approximation for the system-bath Hamiltonian. With an estimate of H_{SB} in hand, the shift in the energy of each of the system eigenstates due to H_{SB} can be determined using time independent second order perturbation theory:

$$E_n^{(2)} = \langle n | H_{SB} | n \rangle + \sum_{k,\, n \neq k} \frac{\left| \langle n | H_{SB} | k \rangle \right|^2}{E_n^{(0)} - E_k^{(0)}}, \tag{5-2}$$

where the set of $\{E_n^{(0)}, |n\rangle\}$ represents the unperturbed energies and eigenstates of the system. With a fluctuating frequency trajectory in hand, 2D IR spectra can be calculated

using the results of Chapter 2. Section 5.6 describes in detail the calculation of 2D spectra of the HOD molecule using a set of fluctuating frequency trajectories.

5.3. Frequency-Structure Correlations

Before we can interpret the frequency shifts measured in 2D IR experiments in terms of the time evolution of water structure, we must first establish a clear connection between ω_{OH} and intermolecular structure. It has been known for some time from studies of hydrogen bonding crystals that a correlation exists between ω_{OH} and R_{OO}, the oxygen-oxygen separation between the hydrogen bond donor and acceptor.[44] Modeling of infrared spectroscopy with classical MD simulations using mixed quantum-classical approaches has established the underlying physical origin of this observation. Near-perfect correlation is found between ω_{OH} and the projection of the electric field from all other molecules in the simulation along the O-H bond at the position of the proton (Fig. 5-1A).[27] This can be understood by recognizing that the first order perturbative correction to the isolated O-H frequency due to the motions of the surrounding liquid resembles a Stark-shift Hamiltonian.[35] Due to its close proximity to the proton, the dominant contribution to the field is from the oxygen of the nearest hydrogen bonding partner. Changes in the position of this partner relative to the O-H bond induce changes in ω_{OH}.

With a structural description of ω_{OH}, simulations can be used to explore its sensitivity to hydrogen bonding configuration. Fig. 5-1B displays the static frequency distribution for ω_{OH} calculated from the MD simulations described in the previous section. By defining a hydrogen bond using geometric criteria such as R_{OO} and the hydrogen

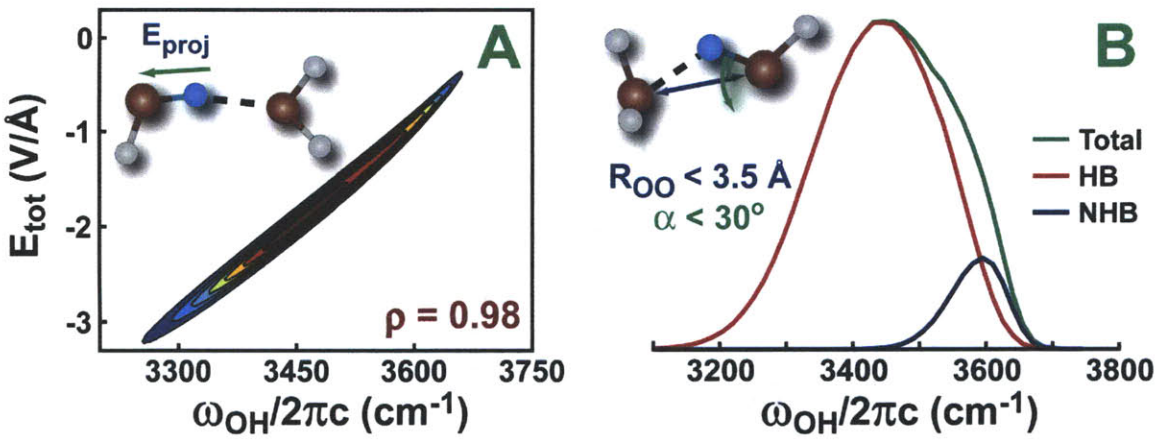


Figure 5-1: (A) Joint probability distribution of ω_{OH} calculated from MD simulation and the projection of the total electric field due to the surrounding water bath onto the HOD molecules O-H bond at the position of the proton. From Ref. 35. (B) Static frequency distribution for ω_{OH} (green) which is divided up into HB (red) and NHB (blue) based on geometric criteria ($R_{OO} \leq 3.5$ Å and HOO angle $\leq 30°$).

bonding angle,[14,15] we can divide up the ω_{OH} distribution into contributions from hydrogen bonding (HB) and non-hydrogen bonding (NHB) configurations. At any given time, ~10% of the O-H bonds in the simulation correspond to NHB and absorb preferentially on the high frequency side of the line shape.

5.4. Scenarios for Hydrogen Bond Exchange

Given the correlation between ω_{OH} and the HOD molecule's hydrogen bonding configuration, one can study the dynamics by which a hydrogen bond switches from one acceptor to another. Two limiting scenarios, concerted and stepwise hydrogen bond rearrangements, are distinguished by their view of NHB configurations and are described by the free energy surfaces in Fig. 5-2. In a stepwise process, a thermal fluctuation ruptures the initial hydrogen bond, but a new acceptor for that bond is not yet available. The entropically stabilized (or dangling) hydrogen bond persists until another fluctuation presents a new hydrogen bond acceptor. In this case, HB and NHB occupy stable

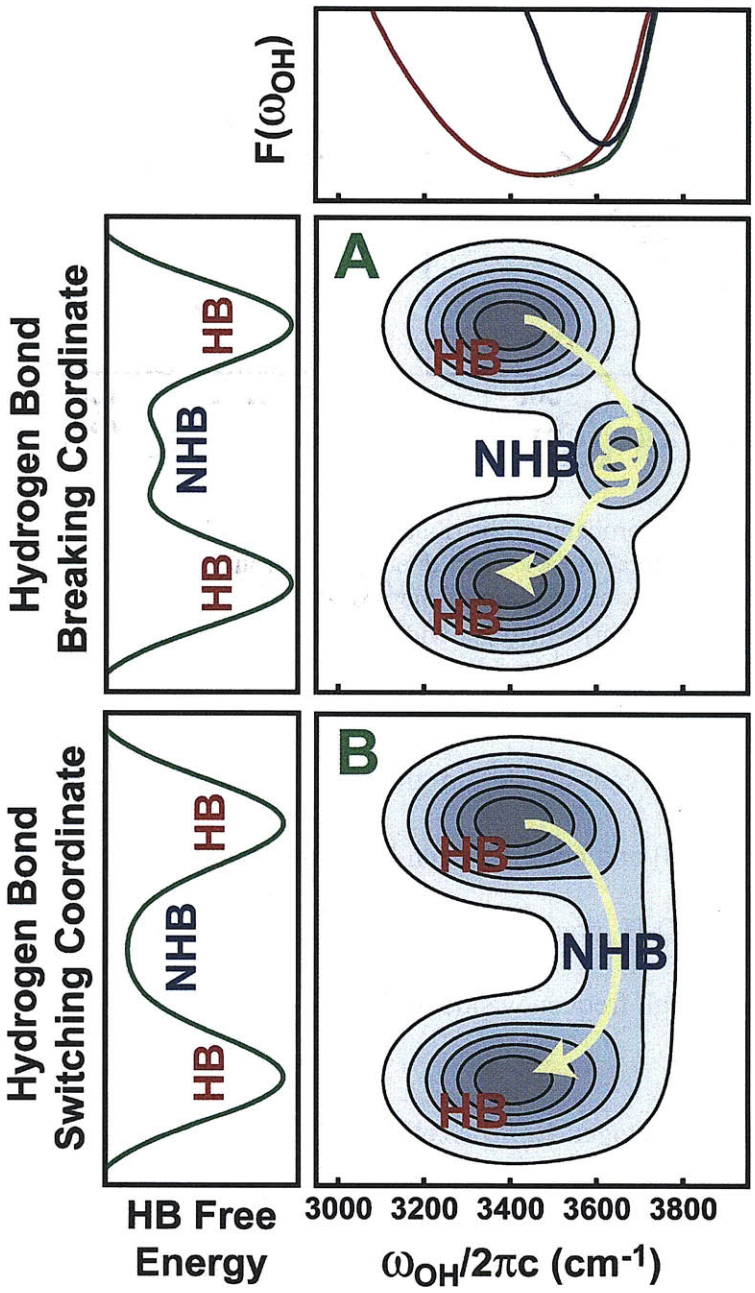


Figure 5-2: Cartoon free energy surfaces describing hydrogen bond exchange for (A) a mixture picture of water and (B) a continuous distribution of structures. In both cases, the free energy along ω_{OH} (above) is the same but the dynamics along this coordinate will differ.

minima on water's free energy surface with a barrier larger than kT separating them (Fig. 5-2A). An alternative view is that the rearrangement of hydrogen bonds from one acceptor to another happens in a single concerted step involving the correlated motion of

multiple molecules including the HB donor and the initial and final hydrogen bond acceptors. Here, NHB configurations are not stable and form a saddle point visited during the course of hydrogen bond exchange (Fig. 5-2B). In both pictures, the free energy projected along the frequency axis is the same, but qualitatively different dynamics will be observed in ω_{OH}. If NHB configurations form a metastable state, a separation of time scales between the relaxation within both the NHB and HB wells and the exchange between them will be observed. If NHB configurations are unstable, they should return to the HB wells on a time scale of the intermolecular motions of the liquid. 2D IR measurements can discriminate between these scenarios by tracking how the stretching frequencies of molecules in a given initial configuration change with time.

5.5. Two-Dimensional Infrared Spectroscopy of HOD in D_2O

Fig. 5-3 shows 2D IR spectra for a 1% solution of HOD in D_2O as a function of τ_2.[38] At early waiting times the spectra appear diagonally elongated, but broaden as τ_2 increases and become largely homogeneous by a waiting time of 700 fs. The loss of frequency memory in 2D IR lineshapes can be quantified by a number of one-dimensional metrics, including the ellipticity of the line shape,[45] the slope of the nodal line separating the fundamental and overtone transitions,[37,46,47] and the center line slope.[48] Chapter 3 shows how, within certain approximations, many of these metrics can be related to the decay of a frequency correlation function:

$$C(\tau_2) = \left\langle \delta\omega_{OH}(\tau_2)\,\delta\omega_{OH}(0) \right\rangle, \tag{5-3}$$

where $\delta\omega_{OH}(t) = \omega_{OH}(t) - \langle\omega_{OH}\rangle$. $C(\tau_2)$ describes the time period over which the system retains memory of its initial excitation frequency. Fig. 5-4 displays two of these

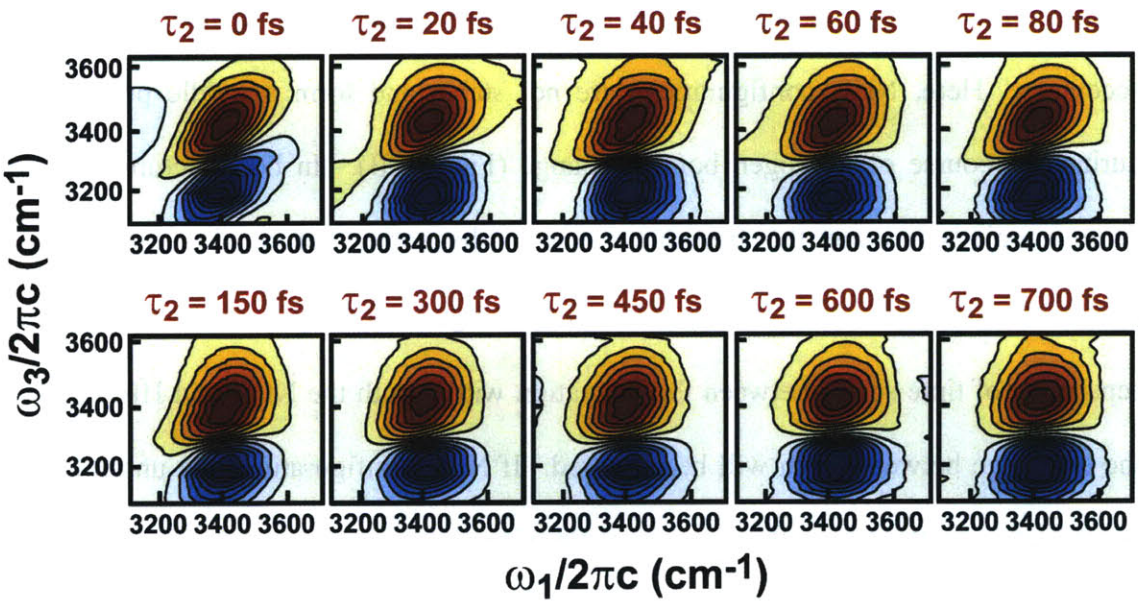


Figure 5-3: 2D IR spectra for a ~1% HOD in D_2O solution recorded at zzzz polarization as a function of waiting time.

metrics, the slope of the spectral phase along the ω_1 frequency axis evaluated at (ω_1, ω_3) = 3400 cm^{-1}, the peak of the linear absorption of the O-H stretching transition, and the photon echo peak shift reconstructed from the 2D data. Both of the calculated metrics show a sub-100 fs decay, a recurrence near 150 fs due to an underdamped hydrogen bond oscillation (O-H···O oxygen-oxygen stretch), and a slower picosecond decay. This slow decay component has often been associated with the time scale for hydrogen bond breakage and reformation,[25,49] although we instead interpret this time scale more generally as that for hydrogen bond equilibration and structural deformation of the first solvation shell about a water molecule[35] (See Section 5.7). The dashed green curves that appear in both plots are derived from 2D spectra calculated using our previously extracted $C(\tau)$ that was determined on the basis of photon echo peak shift measurements.[3] These calculations use the second order Cumulant approximation

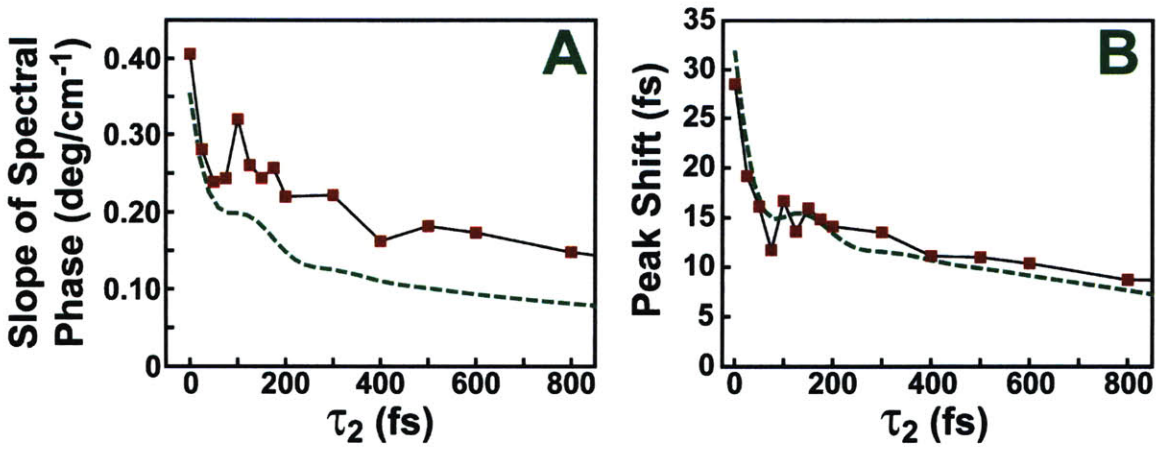


Figure 5-4: (A) The slope of the spectral phase evaluated at the peak of the O-H stretching transition and (B) the photon echo peak shift calculated from 2D IR data (red squares) each provide measures of the average time scale for the spectral diffusion of ω_{OH}. These experimentally determined metrics agree well with predictions based on our previously extracted frequency-frequency correlation function (green dashed).

described in Chapter 2 to calculate 2D lineshapes and also account for effects due to finite pulse duration when calculating the nonlinear polarization.[38] The calculations are able to well reproduce the experimentally derived peak shift decay and the time scales but not the magnitude of the decay of the slope of the spectral phase.

More interesting are the frequency-dependent changes to the 2D spectra with increasing τ_2. The $\tau_2 = 0$ spectrum shows that the high frequency side of the line shape ($\omega_{OH} \geq 3500$ cm^{-1}) is broader along the antidiagonal axis than at low frequency ($\omega_{OH} \leq 3300$ cm^{-1}), leading to a pear-like shape. As τ_2 increases, the discrepancy in line width between the high and low frequency sides becomes more distinct as the blue side of the line shape broadens while at lower frequency it remains compact. If molecules forming strong and weak hydrogen bonds behave similarly, a line shape that is symmetric about the diagonal axis should be observed at all waiting times. The asymmetry of the 2D line shape indicates that molecules in HB configurations undergo qualitatively different

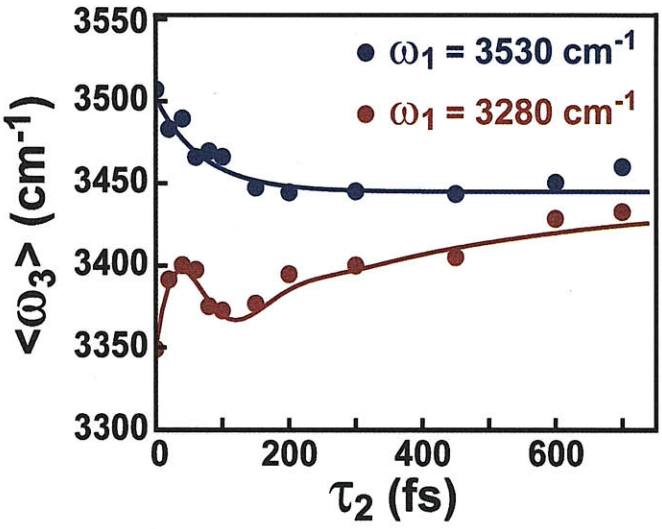


Figure 5-5: The first moment of the positive amplitude of slices of the 2D IR spectra for set values of ω_1.

relaxation that those in NHB geometries.

This difference in dynamics can be quantified by examining vertical slices through the 2D spectra.[39] By analogy with hole-burning experiments, such slices correspond to the relaxation of a subensemble prepared at a given frequency, and their time-dependent evolution can be quantified through their first moments (Fig. 5-5). The first moment of slices taken at ω_1 = 3250 cm^{-1} displays a sharp increase toward band center followed by a pronounced recurrence at 130 fs. This recurrence is indicative of the hydrogen bond oscillation observed in the 1D metrics displayed in Fig. 5-4, but it is more prominent. This strong recurrence indicates that the vibrational frequencies of hydrogen bonded oscillators are rapidly modulated as the distance between the proton and the hydrogen bonding partner changes. At high frequency, no oscillation is observed and the first moment returns to band center within 100 fs (time constant of ~60 fs). If NHB species are stable, they should persist longer than the time scale of the slowest intermolecular motions of the liquid (~200 fs). Given the time scale and the

completeness of this decay, NHB configurations do not correspond to stable minima on water's free energy surface. Furthermore, the time scale for the relaxation of the high frequency side of the lineshape corresponds well with that for librations in water, implying that reorientational motion plays an important role in hydrogen bond rearrangement.

5.6. 1D and 2D Lineshapes Calculated from Classical MD Simulations

MD simulations can be used to determine the molecular origins of the spectral relaxation observed in 2D IR spectra in atomistic detail. Once a fluctuating frequency trajectory has been calculated using the methodology described in Section 5.2, 2D IR spectra can be calculated using Eq. 2-22 of Chapter 2. Due to the use of an isotopically dilute system, the O-H stretch of the HOD molecule is largely decoupled from all other vibrations of the system and only the v = 0, 1, and 2 states of the O-H stretch need to be considered when calculating 2D spectra. Carrying out the sum in Eq. 2-22 over just these three eigenstates yields the following expression for the third-order polarization in the limit of delta function pulses:

$$\begin{aligned} S_{\pm}(\tau_3,\tau_2,\tau_1) = 2\Big\langle \boldsymbol{\mu}_{10}^{(\mathrm{LO})}(\tau_3+\tau_2+\tau_1)\boldsymbol{\mu}_{10}^{(3)}(\tau_2+\tau_1)\boldsymbol{\mu}_{10}^{(2)}(\tau_1)\boldsymbol{\mu}_{10}^{(1)}(0)\phi_{\pm}^{(10)}\Big\rangle \\ -\Big\langle \boldsymbol{\mu}_{21}^{(\mathrm{LO})}(\tau_3+\tau_2+\tau_1)\boldsymbol{\mu}_{21}^{(3)}(\tau_2+\tau_1)\boldsymbol{\mu}_{10}^{(2)}(\tau_1)\boldsymbol{\mu}_{10}^{(1)}(0)\phi_{\pm}^{(21)}\Big\rangle, \end{aligned} \tag{5-4}$$

where:

$$\begin{aligned} \phi_{\pm}^{(10)} &= \exp\left[\mp i\int_0^{\tau_1}\omega_{10}(t)\,dt - i\int_{\tau_1+\tau_2}^{\tau_1+\tau_2+\tau_3}\omega_{10}(t')\,dt'\right] \\ \phi_{\pm}^{(21)} &= \exp\left[\mp i\int_0^{\tau_1}\omega_{10}(t)\,dt - i\int_{\tau_1+\tau_2}^{\tau_1+\tau_2+\tau_3}\omega_{21}(t')\,dt'\right]. \end{aligned} \tag{5-5}$$

In Eq. 5-4 and 5-5, S_- and S_+ denote the signal due to rephasing and nonrephasing excitation pathways, respectively. These two types of signals are measured separately and summed to yield a 2D IR spectrum. $\boldsymbol{\mu}_{nm}^{(i)}$ represents the projection of the dipole operator onto the direction of either the "ith" excitation field or the local oscillator:

$$\boldsymbol{\mu}_{nm}^{(i)}(t) = \langle n|\boldsymbol{\mu}(t)\bullet\hat{\boldsymbol{\varepsilon}}_i|m\rangle, \tag{5-6}$$

and $\omega_{nm}(t) = \left(E_n(t) - E_m(t)\right)/\hbar$. We can rewrite the expression for the dipole matrix elements in a form more conducive to calculation via MD simulation by expanding $\boldsymbol{\mu}$ to first order in the O-H stretching coordinate, r_{OH}, about the minimum of the potential, r_{eq}:[33]

$$\boldsymbol{\mu}_{nm}^{(i)} \approx \langle n|\boldsymbol{\mu}_o\bullet\hat{\boldsymbol{\varepsilon}}_i|m\rangle + \langle n|r_{OH}\left(d\boldsymbol{\mu}/dr_{OH}\right)\big|_{r_{OH}=r_{eq}}\bullet\hat{\boldsymbol{\varepsilon}}_i|m\rangle = \mu' r_{nm}\hat{\boldsymbol{\mu}}\bullet\hat{\boldsymbol{\varepsilon}}_i. \tag{5-7}$$

Here, r_{nm} is the matrix element of the position operator, $r_{nm} = \langle n|r_{OH}|m\rangle$. μ' is the magnitude of the derivative of the dipole operator evaluated at the minimum of the stretching potential, $\mu' = \left(d\mu/dr_{OH}\right)\big|_{r_{OH}=r_{eq}}$, and $\hat{\boldsymbol{\mu}}\bullet\hat{\boldsymbol{\varepsilon}}_i$ is the dot product of the unit vectors pointing along the O-H bond* and one of the excitation fields or the local oscillator.

The Condon approximation assumes that both r_{nm} and μ' are independent of the bath degrees of freedom, which means that only a change in the orientation of the HOD molecule can affect the dot products in Eq. 5-4. However, this approximation is not expected to hold in the case of hydrogen bonding systems since it is well known that a large increase in the infrared absorption cross section accompanies an increase in

* As Ref. 33 has noted, in the gas phase the transition dipole of the O-H stretch of the HOD molecule is not oriented along the O-H bond but is rotated by 25.2° from this axis, while in ice the transition dipole rotates to lie along the O-H bond.[50] Following Ref. 33, we assume that in the liquid phase the O-H transition dipole lies along the bond axis since the hydrogen bonding configurations found in water are on average not significantly different from those found in ice.

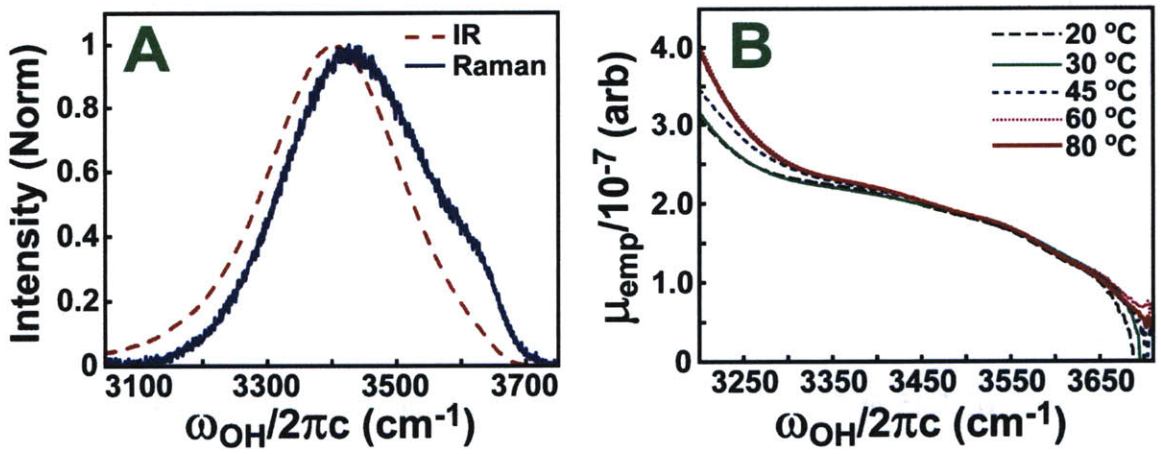


Figure 5-6: (A) IR and Raman spectra of dilute HOD in D_2O recorded at 20 °C. (B) Extracted value of μ_{emp} for different temperatures. Raman spectra were taken from Ref. 54.

hydrogen bonding strength.[44,51] In the case of dilute HOD in D_2O, the results of DFT calculations carried out on water molecule clusters predicted a dramatic breakdown of the Condon approximation.[33,52,53] The results showed a strong correlation between μ' and ω_{OH}, with μ' increasing with decreasing ω_{OH}.[†] The calculations also showed that the Raman polarizability of the stretching transition has only a small dependence on ω_{OH}. Experimental Raman and IR absorption data of dilute HOD in D_2O support this conclusion (Fig. 5-6). The peaks of the Raman and infrared lineshapes corresponding to ω_{OH} are shifted by ~50 cm^{-1} and the Raman spectrum shows a shoulder on the high frequency side of the lineshape that is absent in the infrared spectrum. Equations for the infrared absorption and Raman scattering intensities appear in Ref. 55. Comparison of these expressions shows that is it possible to extract the frequency dependence of μ_{OH}

[†] While a strong correlation between μ' and ω_{OH} was observed in Ref. 33, only a slight dependence of the matrix elements, r_{nm}, on ω_{OH} was found. For the spectra calculated in this chapter, we have chosen to ignore the frequency dependence of r_{nm}. Instead, we assume that r_{nm} does not differ significantly from the values calculated from the eigenfunctions of the unperturbed potential of Reimers and Watts.[43] Under this assumption, we find that r_{nm} scales nearly harmonically, $r_{21} = (1.0125)\sqrt{2}r_{10}$.

from the square root of the ratio of the infrared and Raman lineshapes provided that the Raman polarizability is frequency independent. We have used this assumption to calculate an empirically determined transition dipole, μ_{emp}, which is shown in Fig. 5-6B. μ_{emp} displays a nonlinear dependence on ω_{OH}, and across the range of frequencies that comprise the bulk of the infrared absorption lineshape (3270 to 3530 cm^{-1}), μ_{emp} varies by a factor of 1.45 at 20 °C. Although both the Raman and IR lineshapes shift and change in intensity with increasing temperature due to a weakening of water's hydrogen bonding network, μ_{emp} is only slightly temperature dependent. This suggests that this method of extracting the transition dipole is robust over a number of different liquid configurations. To use μ_{emp} in the calculation of linear and nonlinear spectra from our MD model, we fit μ_{emp} at 20 °C with a sixth order polynomial:

$$\begin{aligned}\mu_{emp}/\mu_{ref} = &-8.7258374\times10^{-13}\,cm^5\omega_{OH}^5 + 1.51752318\times10^{-8}\,cm^4\omega_{OH}^4 \\ &-1.04185686\times10^{-4}\,cm^3\omega_{OH}^3 + 0.36002993\,cm^2\omega_{OH}^2 \\ &-622.081735\,cm\;\omega_{OH} + 429953.22\end{aligned} \tag{5-8}$$

where μ_{ref} corresponds to the value of μ_{emp} calculated for ω_{OH} = 3650 cm^{-1}.

Fig. 5-7A examines the influence of non-Condon effects on linear absorption spectra by comparing the lineshape calculated within the Condon approximation to that calculated by including non-Condon effects through the use of μ_{emp}. The lineshape calculated within the Condon approximation is asymmetric due to the presence of a shoulder on the high frequency side of the lineshape. When we account for the increase in the O-H transition dipole with decreasing frequency, we find that the peak of the absorption lineshape decreases by 10 cm^{-1}, and the lineshape's high frequency shoulder is suppressed. This comparison between the Condon and non-Condon lineshapes resembles

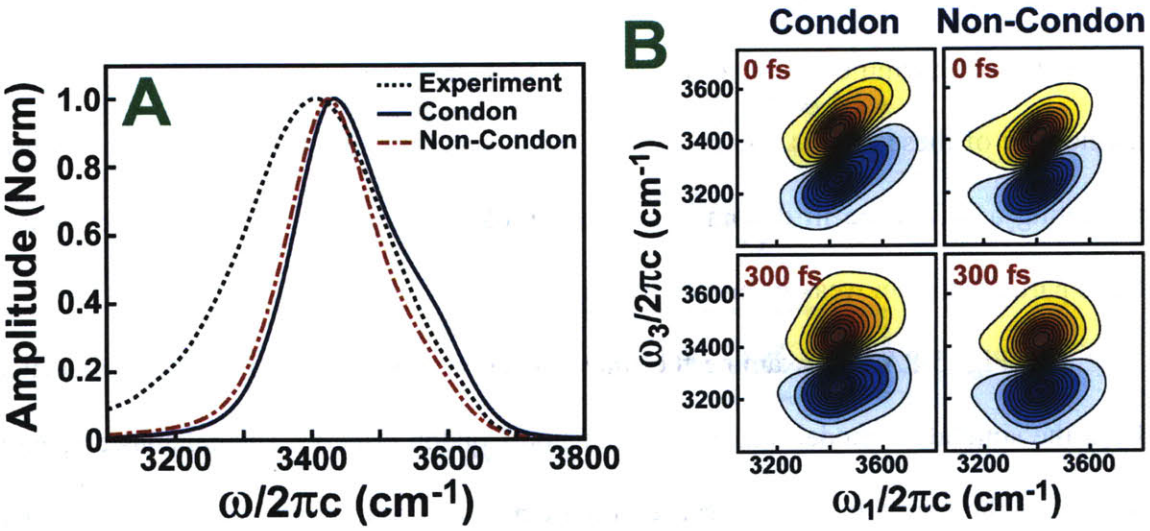


Figure 5-7: (A) Comparison between absorption lineshapes calculated using our simulation model and experiment. The inclusion of non-Condon effects shifts the lineshape to lower frequency and suppresses its high frequency shoulder. The calculated non-Condon lineshape has a linewidth (FWHM = 165 cm^{-1}) much to narrow compared to experiment (FWHM = 260 cm^{-1}) and is peaked to the blue of the experimental absorption lineshape. (B) 2D IR spectra calculated within the Condon approximation and with the inclusion of non-Condon effects.

that of the experimental Raman and infrared lineshapes displayed in Fig. 5-6A. However, this is only a qualitative resemblance since the linewidths of the calculated lineshapes are much too narrow with respect to experiment and are peaked to the blue of the experimental spectra. The lack of agreement between experiment and simulation in part reflects the simulation's inability to properly reproduce the full set of possible liquid configurations.

In Fig. 5-7B, we plot a similar comparison between Condon and non-Condon lineshapes for 2D IR spectra calculated for two waiting times, 0 fs and 300 fs. Similar to the experimental data in Fig. 5-3, the spectra calculated within the Condon approximation appear diagonally elongated at $\tau_2 = 0$, but have broadened significantly at high frequency by $\tau_2 = 300$ fs. Similar to the 1D case, the inclusion of non-Condon effects acts to shift

the center frequency of the 2D spectra to a smaller value along the diagonal axis and suppresses the asymmetry of the lineshape at high frequency. However, even after the application of these effects, the calculated 2D spectra still appear distinctly asymmetric, indicating a difference in dynamics between molecules in strong hydrogen bonds and those participating in weak or broken hydrogen bonds.

In Fig. 5-8A, we examine the time dependence of the 2D IR spectra calculated from the simulation model that account for non-Condon effects. The calculated spectra reproduce the experimentally observed time dependent asymmetry and center diagonal frequency well but are too narrow along the diagonal axis, indicating that the magnitude of the fluctuations in the simulation may be too small relative to experiment. Fig. 5-8B displays the photon echo peak shift calculated from the simulation data. Similar to the experiment,[27] this data displays a bi-exponential decay and an underdamped hydrogen bond oscillation. The calculated peak shift qualitatively resembles the frequency-frequency correlation function calculated from an MD frequency trajectory (Fig. 5-8C) although the magnitudes of the decay components and hydrogen bond oscillation differ. In general, each of the time scales associated with the simulated frequency correlation function are faster than those observed in our experimentally determined $C(\tau)$. The hydrogen bond oscillation occurs at 120 fs in the simulation vs. 180 fs in the experiment and the long decay time constant is ~750 fs, which is about half that found experimentally (1.4 ps).[3] This disagreement between experiment and simulation has been attributed to the simulation's simplistic treatment of intermolecular interactions. For example, allowing the charges on each of the molecular sites of the water simulation model to fluctuate in response to environmental changes has been shown to slow the

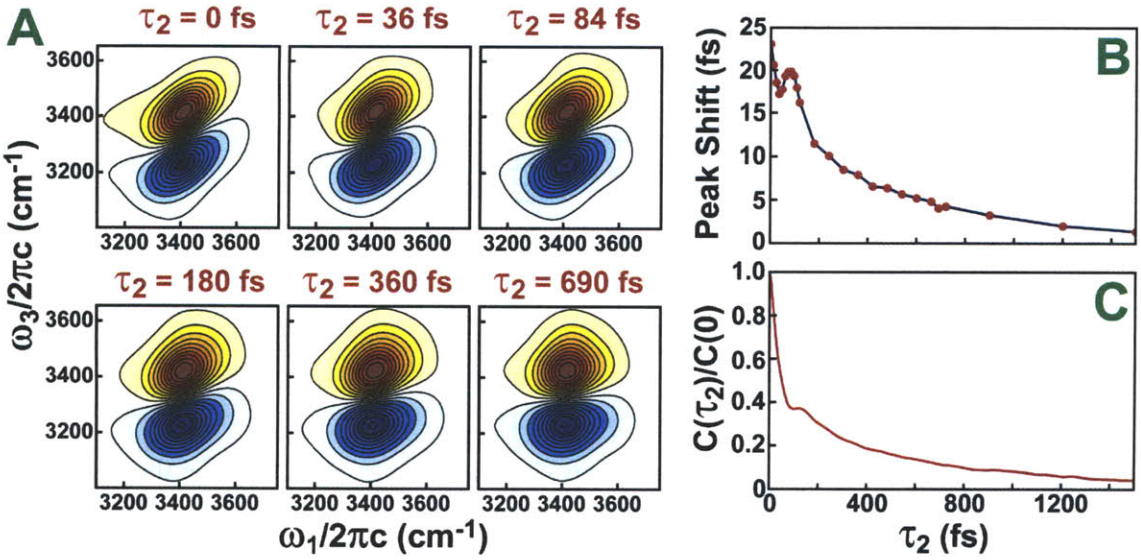


Figure 5-8: (A) Calculated 2D IR spectra (B) photon echo peak shift and (C) frequency-frequency correlation function for the simulation model described in the text. Spectra were calculated for zzzz polarization.

fluctuations associated with the rearrangement of hydrogen bonds.[56,57] Nonetheless, the qualitative agreement between the simulation and experiment suggests that we can use classical simulations to understand the origin of the observed asymmetries in 2D IR spectra in mechanistic detail.

In Section 5.5, we highlighted the difference in dynamics exhibited by molecules in different hydrogen bonding configurations by calculating the first moment of slices taken along the ω_3 dimension for values of ω_1 at both high and low frequency. On the low frequency side of the lineshape, these slices display a strong hydrogen bond oscillation while at high frequency, they rapidly decay on the time scale of librational motion (Fig. 5-5). Fig. 5-9A plots the equivalent result calculated from our simulation model. Similar to experiment, the first moment of slices taken on the low frequency side of the lineshape (ω_1 = 3300 cm^{-1}) displays an initial rapid increase towards the center of the O-H stretching transition that gives way to a recurrence at 100 fs due to a strong,

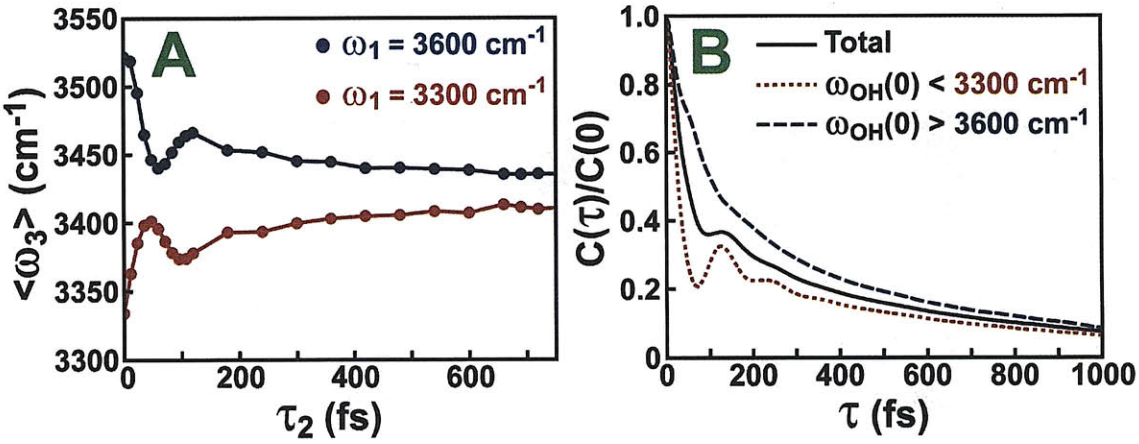


Figure 5-9: (A) The first moment of the positive amplitude of slices taken through the 2D IR spectra calculated from our simulation model for set values of ω_1. (B) Comparison between the frequency-frequency correlation function (black) calculated from the simulation model described in the text and correlation functions calculated with the additional constraint that the initial value of ω_{OH} be above 3600 cm^{-1} or below 3300 cm^{-1}. These two correlation functions correspond to the relaxation of HB and NHB configurations.

underdamped hydrogen bond stretch. At high frequency (ω_1 = 3600 cm^{-1}) a similar hydrogen bond oscillation is found and peaks at a slightly later time (120 fs) indicating the formation of a weaker hydrogen bond than that formed by molecules that initiate at lower frequency. However, this result lies in contrast to the experiment which shows no evidence for such an oscillation at high frequency. This disagreement with experiment may indicate that either our treatment of non-Condon effects overemphasizes contributions to the 2D IR lineshape due to hydrogen bonded water molecules or that the simulation potential is biased in favor of hydrogen bonding.

As an alternative to these slices, we can separately follow the relaxation of HB and NHB species by defining a frequency-frequency correlation function similar to $C(\tau)$ but with the additional constraint that the initial value of ω_{OH} is either above or below a given cutoff frequency. Fig. 5-9 displays the frequency correlation function displayed in

Fig. 5-8C and two additional correlation functions that have been calculated by applying the constraint that either $\omega_{OH}(0) \geq 3600$ cm^{-1} or $\omega_{OH}(0) \leq 3300$ cm^{-1}. These correlation functions provide information that is complimentary to the first moments displayed in Fig. 5-5, but avoid complications due to non-Condon effects and the v = 2←1 transition that interferers with the fundamental v = 1←0 transition. The correlation function corresponding to HB (low frequency) shows a rapid initial decay and a strong hydrogen bond oscillation, indicating that molecules in strong hydrogen bonds undergo large frequency shifts as the hydrogen bond expands and contracts. However, 2D IR spectra at low frequency appear narrow because HB configurations are relatively stable. Even though molecules in strong hydrogen bonds experience large changes in vibrational frequency as the hydrogen bonds expand and contract, motional narrowing averages these fluctuations over the period of the hydrogen bond oscillation, yielding a narrow 2D IR spectrum (See Appendix 5.A).

In the case of NHBs, no oscillation consistent with an underdamped hydrogen bond is observed. This correlation function can be well fit with a sum of two nearly equal amplitude exponential decays with time constants of 90 and 670 fs. While the slow decay time is similar to that observed in the total frequency-frequency correlation function, the fast time scale corresponds to twice the librational period of the HOD molecule in this simulation model (45 fs), which lends support to the conclusion drawn from the experimental 2D IR spectra that librations play a role in the relaxation of NHB configurations. Even though the correlation functions in Fig. 5-9 show that the spectral diffusion of NHB is slower than that of HB, there is no restoring force that causes these molecules to remain at high frequency and they largely return to the median of the O-H

frequency distribution within the time scale of intermolecular motions of the liquid. This overdamped behavior leads to the preferential broadening on the high frequency side of the calculated 2D IR lineshapes when the effects of motional narrowing are taken into consideration.

5.7. Energetics of Water's Hydrogen Bonding Network

Before continuing our discussion of the heterogeneous dynamics that exist between HB and NHB, it is worth discussing the origin of the 1.4 ps decay component that appears in the experimental O-H stretch frequency-frequency correlation function.[3] This decay component implied as an indicator of the time scale associated with the breakage and reformation of hydrogen bonds.[25,49] On the basis of MD simulation, Fecko et al.[27] found that many additional parameters associated with water structure, such as R_{OO}, electric field fluctuations at the position of the proton, and the tetrahedrality of a water molecule's first solvation shell, each show similar decay time scales. This lead them to propose that this decay corresponds not just to hydrogen bond breakage and reformation involving the HOD molecule, but instead to a global restructuring time scale that includes the exchange of water molecules into and out of the HOD molecule's solvation shell. The energy required to drive this restructuring can be determined by examining the temperature dependence of $C(\tau)$.

Fig. 5-10A displays frequency-frequency correlation functions calculated from our simulation model at eight representative temperatures. While the amplitude and time scale of the initial sub-100 fs decay is found to be largely invariant to temperature, the slower decay component of the correlation function decreases with increasing

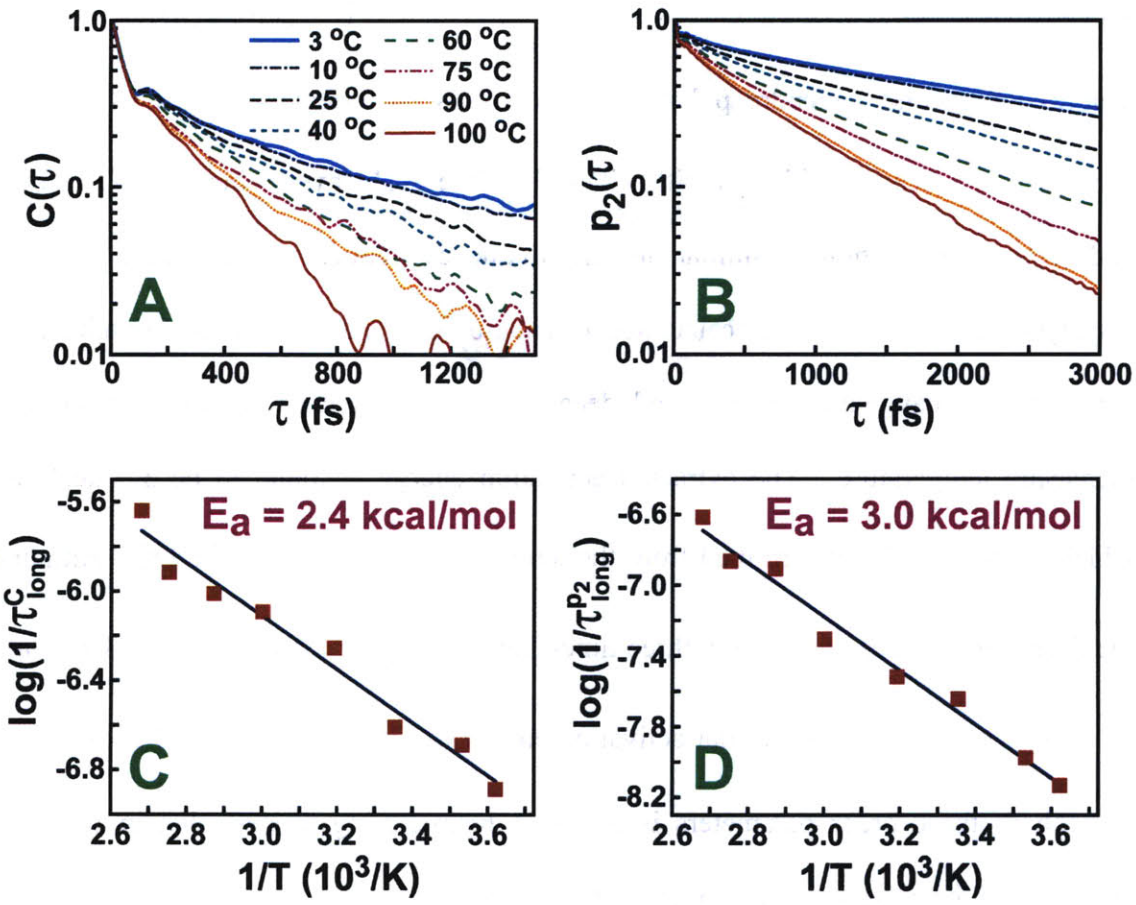


Figure 5-10: Temperature dependence of (A) $C(\tau)$ and (B) $p_2(\tau)$ calculated from the simulation model. Each trace was fit using a sum of two exponential decays and the time constants determined from the slower decay rate were used to construct the Arrhenius plots in (C) and (D).

temperature, changing from 980 fs at 3 °C to 370 fs at 90 °C. Each of the pictured correlation functions was fit to a bi-exponential decay and the inverse log of the slow time constant of each fit was used to construct the Arrhenius plot displayed in Fig. 5-10C. A linear fit to the data yields an activation energy of 2.4 kcal/mol, which is roughly half the energy estimated for a hydrogen bond in water on the basis of dielectric constant data (5-6 kcal/mol).[58]

Provided that this time scale describes the reorganization of the local solvation shell about a water molecule, other structural parameters should show similar temperature

dependencies. Fig. 5-10B plots the decay of $p_2(\tau) = \left\langle P_2\left(\hat{r}_{OH}(\tau)\bullet\hat{r}_{OH}(0)\right)\right\rangle$, where P_2 denotes the second Legendre polynomial and $\hat{r}_{OH}$ is the orientation of the O-H bond vector. The decay of this quantity gives the time scale over which the O-H bond undergoes reorientation. Similar to the frequency-frequency correlation functions displayed in Fig. 5-10A, the calculated orientation correlation functions exhibit a bi-exponential decay with a picosecond decay component that decreases in value with increasing temperature. The extracted activation energy is found to be 3.0 kcal/mol, which is close to that determined from the temperature dependence of $C(\tau)$. Although the decay time scales are roughly three times longer for $p_2(\tau)$, ranging from 3.4 ps at 3 °C to 0.96 ps at 90 °C, the similar activation energy to $C(\tau)$ implies that the long decay of each of these order parameters is due to a restructuring process that involves the evolution of the solvation shell about the HOD molecule.

5.8. Reorientation During Hydrogen Bond Exchange

The experimental and theoretical results described in Sections 5.5 and 5.6 support that hydrogen bond exchange scenario proposed in Fig. 5-2B. Broken hydrogen bonds form a conduit passed through as a water molecule exchanges hydrogen bonding partners. However, a proper reaction coordinate for hydrogen bond exchange is not obvious. It is to be expected that the rearrangement of hydrogen bonds involves many water molecules, as described through studies of the vibrational modes associated with inherent structures, configurations of the liquid that correspond to minima of the liquid's potential energy surface.[23,24] The local motions involved and the relevant length scale over which the

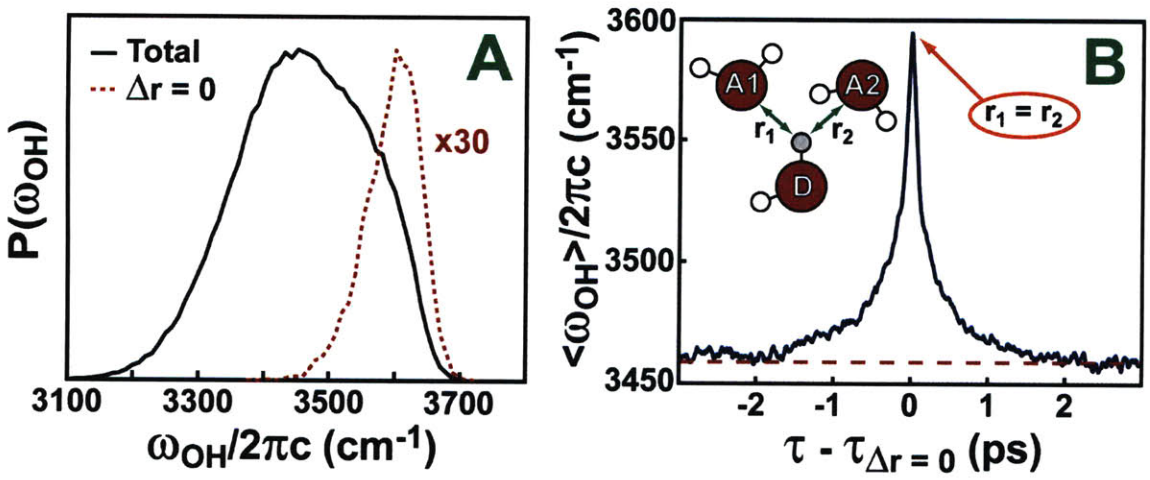


Figure 5-11: (A) Frequency distribution of molecules in bifurcated geometries relative to the total frequency distribution and (B) average relaxation behavior of ω_{OH} about HB exchange events. The dashed red line denotes the average value of ω_{OH} in the simulation, 3458 cm^{-1}.

motions of water molecules are coupled remains unclear. The observation that NHB configurations return to HB frequencies on the time scale of librational motion suggests that reorientation of the O-H bond is critical for switching. It is reasonable to assume that the transition state for switching resembles a bifurcated hydrogen bond. This hypothesis can be tested using the simulation model. A bifurcated transition state suggests that the differences in distance between the lines connecting the hydrogen of the HOD molecule and the two oxygen atoms of the initial and final acceptors, $\Delta r = R_1 - R_2$, can serve as a reaction coordinate for hydrogen bond exchange. Fig. 5-11A plots the frequency distribution for molecules with $\Delta r = 0$.[39] Compared with the total frequency distribution, molecules in bifurcated geometries are blue-shifted and follow essentially the same frequency distribution as NHB configurations. Fig. 5-11B shows that bifurcated molecules quickly return to frequencies indicative of hydrogen bonds, with time constants of 80 and 500 fs. These time scales are similar to those observed for the NHB

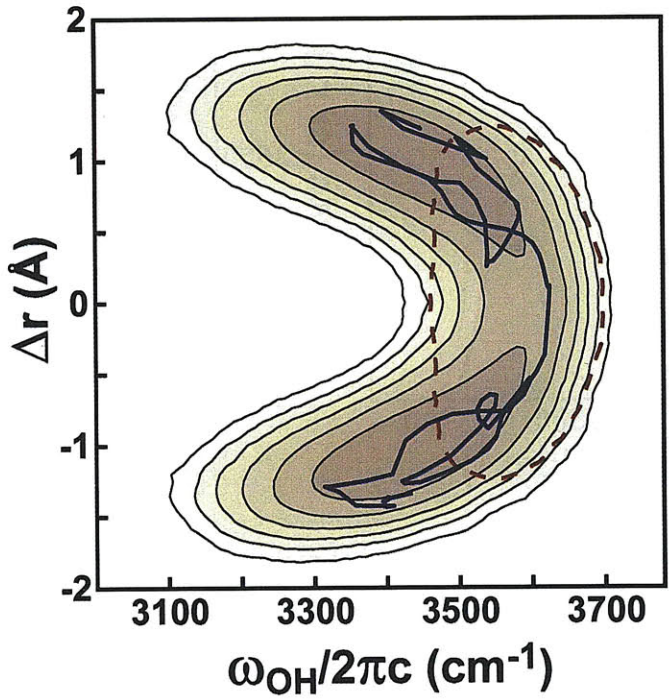


Figure 5-12: Free energy surface for ω_{OH} and the hydrogen bond exchange coordinate, Δr. Black contours correspond to units of kT. The dashed red contour contains 98% of molecules in NHB configurations, and the blue line is a representative exchange trajectory from MD simulation.

frequency-frequency correlation function in Fig. 5-9B and roughly correspond to twice the librational period and that for structural rearrangement of the liquid.

Fig. 5-12 shows the free energy surface calculated as a function of ω_{OH} and Δr. It closely resembles that proposed in Fig. 5-2B. The high frequency side of the line shape serves as a passage for hydrogen bond exchange, and no stable minimum is observed in the NHB region. Plotted on top of this surface is a sample trajectory wherein a HOD molecule undergoes underdamped oscillations in the HB region before rapidly moving through the NHB region to form a new hydrogen bond. It should be noted that only 35% of the molecules that enter the NHB region go on to form a new hydrogen bond. A highly blue-shifted frequency is not a unique indicator of the transition state for hydrogen

bond exchange.[59] Rather, a blue-shifted frequency can arise from either molecules undergoing exchange or large fluctuations about a stable hydrogen bond. In both of these cases, we would observe the rapid motion of a blue-shifted frequency to the center of the O-H stretching transition, indicating the return of these molecules to a hydrogen bonded state.

A detailed description of the reorientational motion of water molecules in the process of switching has been presented in the recent simulations of Laage and Hynes.[59-61] They suggested that a number of geometric parameters that describe liquid structure undergo large changes concomitant with hydrogen bond exchange. The exchange occurs as a rapid, large angle rotation of the HOD molecule (~68°) concurrent with an increase in R_{OO} for the original hydrogen bond acceptor and a decrease in R_{OO} for the new acceptor. Leading up to the exchange, the original hydrogen bond acceptor becomes over-coordinated and the new hydrogen bond acceptor becomes under-coordinated, suggesting that density fluctuations may play a role in the exchange.

5.9. The Connection Between Reorientation and Frequency Shifts

Given the role that reorientation plays in hydrogen bond exchange, experiments that probe molecular reorientation such as pump-probe anisotropy measurements should display a dependence on ω_{OH}. MD results support this conclusion, finding that the magnitude of the inertial decay time scale in orientational correlation functions is enhanced for molecules initially at high frequency.[25] Experimental attempts to measure frequency dependence of the anisotropy have yielded conflicting results due in part to the differing pump and probe frequencies used as well as a lack of pulses short enough to

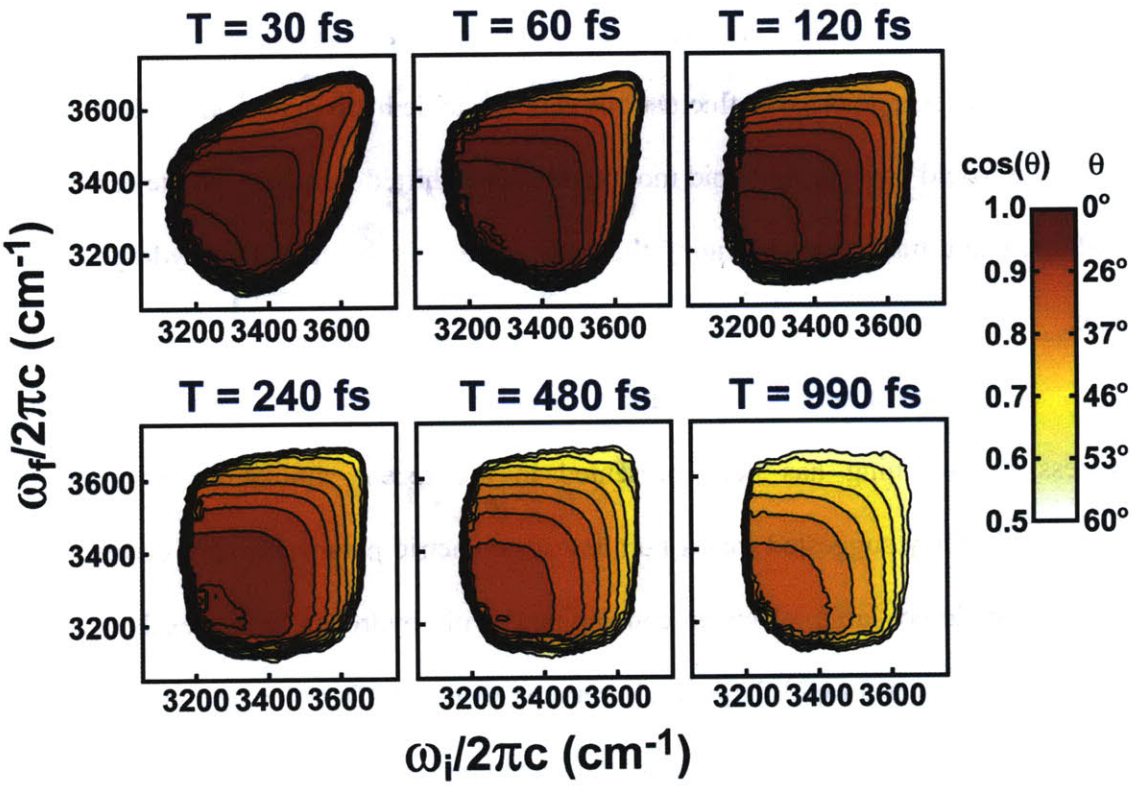


Figure 5-13: Joint probabilities for angular reorientation. Plotted is the average value of the cosine of the angle rotated through by molecules that start at a frequency, ω_i, and reach a frequency, ω_f, after a time, T.

resolve the inertial decay.[62-64] Recent work by Moilanen et. al.[65] has shown a slight frequency dependence to the anisotropy decay of the O-D stretch of HOD in H_2O. Although the first 100 fs of the decay was not resolved, at a delay time of 100 fs the anisotropy at high frequency has decayed to a lower value than at low frequency.

In Fig. 5-13, we extend the frequency dependent orientational correlation functions shown in Ref. 25 to two dimensions. For a given value of time, T, we examine each pair of MD time steps spaced by T and determine the initial and final values of ω_{OH} for the HOD molecule, ω_i and ω_f. We then determine $\cos(\theta)$, where θ is the angle between the O-H bond vectors of the initial and final configurations. Fig. 5-13 shows the

average value of $\cos(\theta)$ plotted as a function of T, ω_i, and ω_f. Even at values of T as early as 30 fs the value along the diagonal axis is largest at low frequency, suggesting that molecules that remain in strong hydrogen bonds undergo smaller angular fluctuations than molecules in weak or broken hydrogen bonds. Also apparent is an inverted "L" shape that indicates that molecules that undergo exchange from red to blue frequencies must undergo a larger degree of reorientation with respect to molecules that remain at hydrogen bonded frequencies.

Although the orientational correlation functions displayed above show strong evidence of a frequency dependence to angular reorientation, experiments that can directly measure this distribution are not yet available. Reorientation time scales are typically measured in nonlinear experiments through the construction of the anisotropy parameter from polarization dependent pump-probe experiments. Since pump-probe experiments and 2D IR spectroscopy both rely on the third-order nonlinearity of the sample, equations relating the tensor elements of pump-probe signals equally apply to 2D IR spectroscopy.[66] This allows us to construct a 2D anisotropy surface using:

$$r = \frac{S_{zzzz} - S_{zzyy}}{S_{zzzz} + 2S_{zzyy}} \tag{5-9}$$

where S_{zzzz} and S_{zzyy} correspond to 2D signals measured with the first two excitation pulses polarized parallel and perpendicular to the third excitation pulse and signal field respectively. Fig. 5-14A displays 2D anisotropy surfaces calculated from the simulation model for the v = 1←0 transition as a function of waiting time. At $\tau_2 = 0$, the anisotropy uniformly adopts a value of 0.4. However, by $\tau_2 = 120$ fs, the anisotropy has decayed to a lower value at high frequency along the diagonal axis and in the off-diagonal regions,

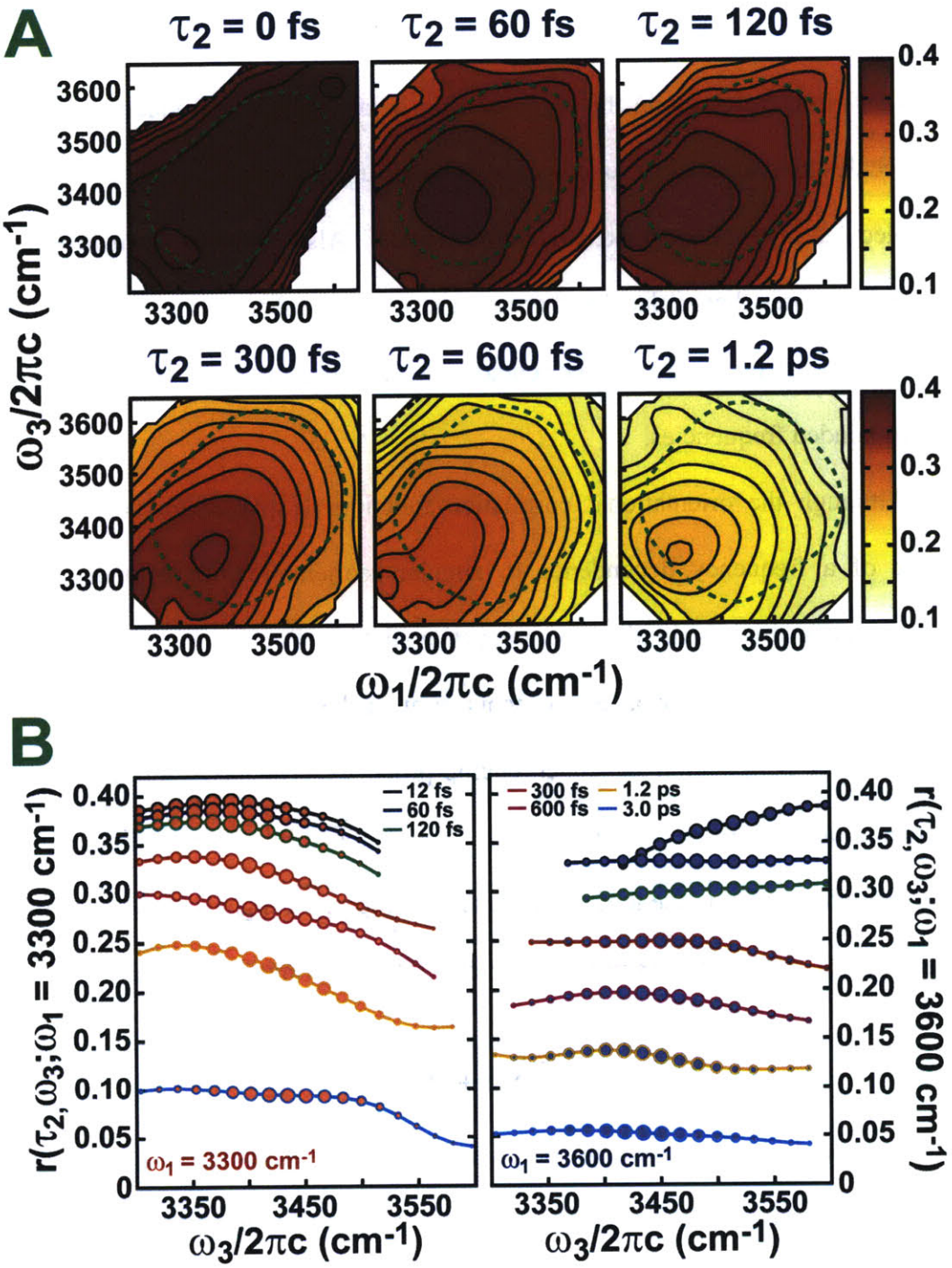


Figure 5-14: (A) Calculated 2D IR anisotropy spectra from MD simulation. The dashed green contour on each surface indicates the point where the isotropic response ($S_{zzzz} + 2S_{zzyy}$) is equal to 10% of its maximum value. (B) Slices of the calculated spectra for $\omega_1 = 3300$ cm^{-1} and 3600 cm^{-1} as a function of τ_2. The size of the plotted symbols represents the amplitude of the computed isotropic response for each slice, which tracks how the motionally narrowed population of molecules initially on the high and low frequency sides of the absorption line shape return to band center.

indicating that molecules prepared in NHB states undergo a large degree of reorientation along the course of returning to a hydrogen bond. This behavior qualitatively resembles that of the orientational joint probabilities displayed in Fig. 5-13 and suggests that the measurement of 2D anisotropy surfaces may be a way to directly view concerted hydrogen bond rearrangements.

Slices through the calculated 2D anisotropy for ω_1 = 3300 cm^{-1} and 3600 cm^{-1} are shown in Fig. 5-14B. For molecules that initiate at high frequency, the anisotropy relaxes from 0.4 to a uniform value of 0.25 within 300 fs. For those molecules that manage to return to hydrogen bonded frequencies within 24 fs, a mean rotation of 30° is necessary. For molecules that initiate from strongly hydrogen bonded states, little change in anisotropy is observed in the first 300 fs. Only as molecules transition to NHB configurations are significant drops in the anisotropy observed.

Fig. 5-15 plots three experimentally measured 2D anisotropy surfaces for a ~1% solution of HOD in D_2O. zzzz and zzyy spectra were subsequently recorded for a given waiting time by rotating the wave plates and polarizers of the first two excitation pulses. Measured zzzz and zzyy spectra were phased separately using dispersed pump-probe measurements recorded for the appropriate polarization. At τ_2 = 100 fs we observe a strong decrease of the anisotropy from 0.4 to 0.24 as we move along the diagonal axis from 3300 cm^{-1} to 3460 cm^{-1}. This variation in the value of the anisotropy is much larger than that found in the simulation. In the offdiagonal region we find that the anisotropy is lower than along the diagonal axis at low frequency, similar to the simulated 2D anisotropies, and lends support to the notion that reorientation is necessary to move from HB to NHB. As the waiting time increases, the anisotropy decays further at all

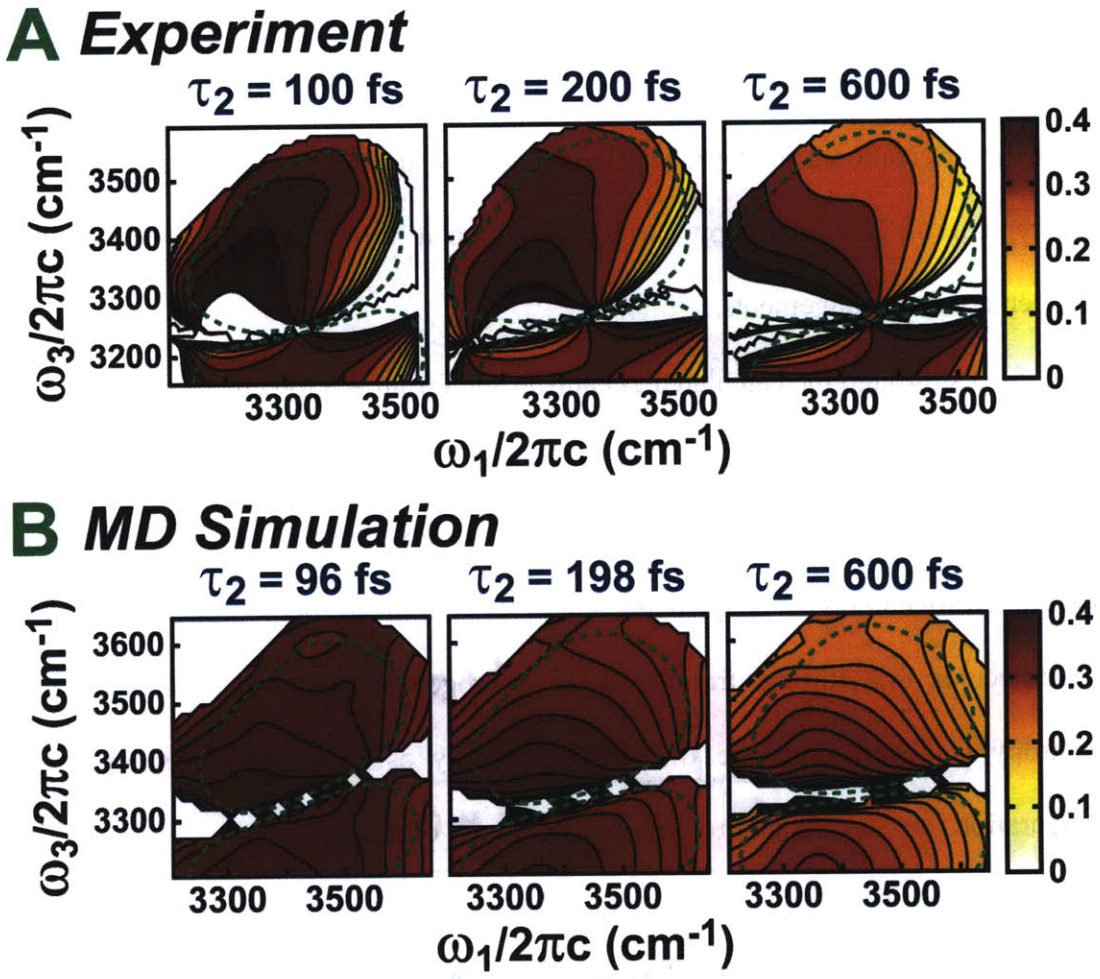


Figure 5-15: (A) Experimental and (B) simulated 2D anisotropy spectra. The simulated spectra includes contributions from the anharmonically shifted v = 2←1 transition for a proper comparison to the measured experimental data. The dashed green contour in each plot indicates where the absolute value of the absorptive isotropic response ($S_{zzzz} + 2S_{zzyy}$) is equal to 10% of its maximum.

frequencies, but the general frequency dependent trends are preserved, giving the spectra an inverted "L" shape at all waiting times similar to the joint probabilities displayed in Fig. 5-13.

While the general trends observed in the experimental data are consistent with the calculations displayed in Fig. 5-14, it must be kept in mind that the presence of the v = 2←1 transition complicates the measurement of 2D anisotropy spectra and, at present,

prevents a full quantitative analysis of the results. The v = 2←1 transition interferers strongly with the v = 1←0 transition at low frequency, causing the anisotropy adopt values well above 0.4, the theoretical maximum value of the anisotropy, near the node separating these two oppositely signed signals. How far this interference extends along the diagonal axis is difficult to estimate, and the larger change in the experimentally measured anisotropy with frequency may be the result of this interference. Nonetheless, the data appears to support the conclusions we have drawn regarding the exchange of HB and NHB.

5.10. Switching Through Water Insertion

Although the jump diffusion model put forth by Laage and Hynes[59-61] and the instability of NHB configurations determined by our 2D IR experiments are consistent, questions remain about the mechanism for hydrogen bond exchange. The results of our experiments and simulations suggest that hydrogen bond exchange involves the correlated motion of at least three water molecules, the hydrogen bond donor and the original and new acceptors. However, it is unclear whether this correlated exchange involves the motion of water molecules beyond the first or second solvation shells. Work examining inherent structures in water seems to suggest that such correlations do exist, but the determination of the length scale over which these correlations extend is difficult.[23] The minima of the free energy surface in Fig. 5-12 near $\Delta r = \pm 1.25$ Å implies that hydrogen bond switching involves the exchange of water molecules in the first and second solvation shells of the switching molecule, which necessitates the rearrangement of molecules outside of this molecule's first solvation shell.

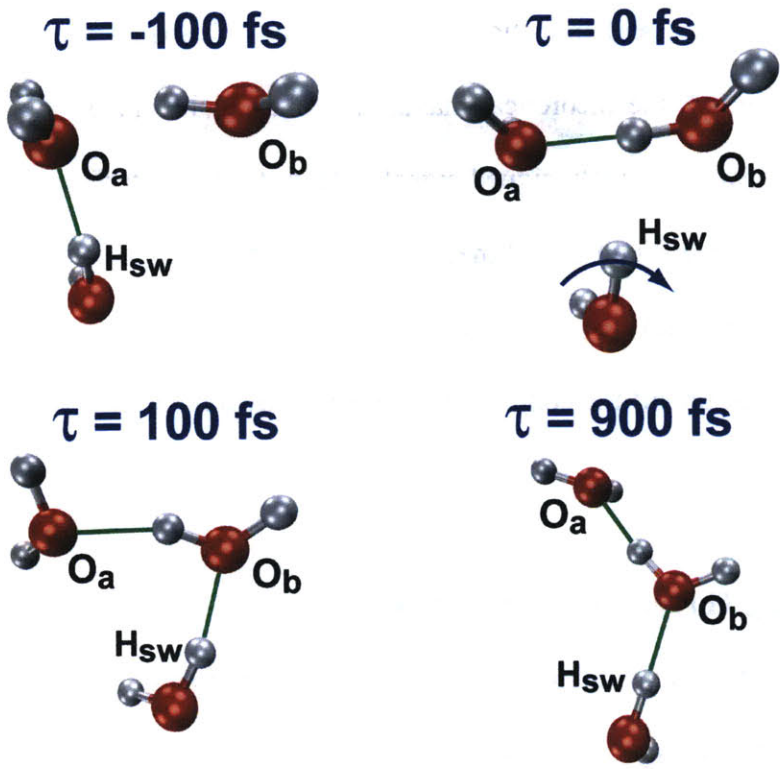


Figure 5-16: Snapshots taken from MD simulation over the course of a water insertion event.

One proposal that can address these questions is a rearrangement process that involves the insertion of a second solvation shell water molecule across a hydrogen bond. Fig. 5-16 shows snapshots from a simulation of SPC/E water that illustrate the course of a hydrogen bond exchange event. The switching hydrogen atom, H_{sw}, undergoes a large angular rotation that breaks the hydrogen bond between it and O_a, forming a new hydrogen bond with O_b. At the bifurcated transition state for the exchange event, one of the hydrogen atoms covalently bonded to O_b has formed a hydrogen bond to O_a. If we examine these three water molecules after the switching event, we find that the new hydrogen bond acceptor has inserted across the original hydrogen bond formed by H_{sw}

and O_a. Such an insertion mechanism would provide for concerted rearrangements of multiple molecules in a dense liquid. We observe that in ~50% of the hydrogen bond exchange events that occur in the MD simulation a hydrogen bond is formed between the original and new hydrogen bond acceptors, which suggests that this water insertion mechanism is quite robust. Naturally, microscopic reversibility requires that the expulsion of a water molecule from a hydrogen bonded chain to form a new hydrogen bond will also be present in a roughly equal number of cases.

5.11. Conclusions

Through the use of a combination of 2D IR experiments and classical MD simulations we have gained new insight into the dynamic structure of liquid water. Hydrogen bonding defects are found to be extremely short lived, returning to HB configurations on the time scale of water's fastest intermolecular motions. The rotation of individual water molecules is found to play a strong role in hydrogen bond exchange, and a bifurcated transition state is consistent with the experimental and theoretical results. Hydrogen bond switching involves the concerted motion of at least three water molecules although the collective participation of molecules as far away as the second solvation shell is implicated.

The detailed nature of these results is possible because 2D IR spectroscopy has the unique ability to identify short lived transition states provided that a spectroscopic signature of that state exists. In this case, NHB configurations could be identified due to the way that the dynamics of these configurations project onto ω_{OH}. In the following two chapters, we will use 2D IR spectroscopy to identify signatures of a transition state for the proton transfer reaction between a water molecule and a hydroxide ion in aqueous

solution. When a hydroxide ion accepts a proton from one of its hydrogen bonding partners, the stretching potential of the shared proton is highly perturbed, and can be best envisioned as a double well potential whose exact shape is rapidly modulated by the motion of molecules surrounding the complex. As this potential responds to the fluctuations of the surrounding liquid, the vibrational transitions associated with the potential undergo large changes in frequency, and transitions between vibrational eigenstates of the potential that are normally disallowed can begin to carry a great deal of oscillator strength. These effects give rise to a strong, transient spectral signature that 2D IR can observe and use to determine the lifetime of these shared proton states.[36]

Acknowledgements

I would like to thank Joseph Loparo for measuring the 2D spectra displayed in Fig. 5-3, Joel Eaves and Phill Geissler for developing the methodology used to calculate vibrational frequencies from the simulation model, Krupa Ramasesha for aid in calculating 2D anisotropy spectra, and Jared Smith and Richard Saykally for providing the temperature dependent Raman spectra.

References

(1) P. Ball, *Life's Matrix: A Biography of Water*, (University of California Press, Berkeley, CA, 2001).

(2) E. W. Castner, Jr., Y. J. Chang, Y. C. Chu and G. E. Walrafen, "The intermolecular dynamics of liquid water," J. Chem. Phys. 102, 653 (1995).

(3) C. J. Fecko, J. J. Loparo, S. T. Roberts and A. Tokmakoff, "Local hydrogen bonding dynamics and collective reorganization in water: Ultrafast IR spectroscopy of HOD/D_2O," J. Chem. Phys. 122, 054506 (2005).

(4) R. Jimenez, G. R. Fleming, P. V. Kumar and M. Maroncelli, "Femtosecond solvation dynamics of water," Nature 369, 471 (1994).

(5) N. Agmon, "The Grotthuss mechanism," Chem. Phys. Lett. 244, 456 (1995).

(6) P. Wernet, D. Nordlund, U. Bergmann, M. Cavalleri, M. Odelius, H. Ogasawara, L. Å. Näslund, T. K. Hirsch, L. Ojamäe, P. Glatzel, L. G. M. Pettersson and A. Nilsson, "The structure of the first coordination shell in liquid water," Science 304, 995 (2004).

(7) J. D. Smith, C. D. Cappa, K. R. Wilson, B. M. Messer, R. C. Cohen and R. J. Saykally, "Energetics of hydrogen bond network rearrangements in liquid water," Science 306, 851 (2004).

(8) D. Eisenberg and W. Kauzmann, *The Structure and Properties of Water*, (Clarendon Press, Oxford, 1969).

(9) W. B. Monosmith and G. E. Walrafen, "Temperature dependence of the Raman OH-stretching overtone from liquid water," J. Chem. Phys. 81, 669 (1984).

(10) M. G. Sceats and K. Belsley, "A conjecture on the overtone OH stretching spectrum of HDO in liquid water," Mol. Phys. 40, 1389 (1980).

(11) P. L. Geissler, "Temperature dependence of inhomogeneous broadening : On the meaning of isosbestic points," J. Am. Chem. Soc. 127, 14930 (2005).

(12) M. Odelius, M. Cavalleri, A. Nilsson and L. G. M. Pettersson, "X-ray absorption spectrum of liquid water from molecular dynamics simulations: Asymmetric model," Phys. Rev. B: Condens. Matter 73, 024205 (2006).

(13) C. Huang, K. T. Wikfeldt, T. Tokushima, D. Nordlund, Y. Harada, U. Bergmann, M. Niebuhr, T. M. Weiss, Y. Horikawa, M. Leetmaa, M. P. Ljungberg, O. Takahashi, A. Lenz, L. Ojamäe, A. P. Lyubartsev, S. Shin, L. G. M. Pettersson and A. Nilsson, "The inhomogeneous structure of water at ambient conditions," Proc. Natl. Acad. Sci. U.S.A. 106, 15214 (2009).

(14) A. Luzar and D. Chandler, "Effect of environment on hydrogen bond dynamics in liquid water," Phys. Rev. Lett. 76, 928 (1996).

(15) R. Kumar, J. R. Schmidt and J.L.Skinner, "Hydrogen bonding definitions and dynamics in liquid water," J. Chem. Phys. 126, 204107 (2007).

(16) T. Head-Gordon and G. Hura, "Water structure from scattering experiments and simulation," Chem. Rev. 102, 2651 (2002).

(17) A. K. Soper, "The radial distribution functions of water and ice from 220 to 673 K and at pressures up to 400 MPa," Chem. Phys. 258, 121 (2000).

(18) C. P. Lawrence and J. L. Skinner, "Vibrational spectroscopy of HOD in liquid D_2O. II. Infrared line shapes and vibrational Stokes shift," J. Chem. Phys. 117, 8847 (2002).

(19) D. W. G. Smith and J. G. Powles, "Proton spin-lattice relaxation in liquid water and liquid ammonia," Mol. Phys. 10, 451 (1966).

(20) S. Palese, L. Schilling, R. J. D. Miller, P. R. Staver and W. T. Lotshaw, "Femtosecond optical Kerr effect studies of water," J. Phys. Chem. 98, 6308 (1994).

(21) C. J. Fecko, J. D. Eaves and A. Tokmakoff, "Isotropic and anisotropic Raman scattering from molecular liquids measured by spatially masked optical Kerr effect spectroscopy," J. Chem. Phys. 117, 1139 (2002).

(22) W. Jarzeba, G. C. Walker, A. E. Johnson, M. A. Kahlow and P. F. Barbara, "Femtosecond microscopic solvation dynamics of aqueous solutions," J. Phys. Chem. 92, 7039 (1988).

(23) I. Ohmine, "Liquid water dynamics: Collective motions, fluctuation, and relaxation," J. Phys. Chem. 99, 6767 (1995).

(24) I. Ohmine and S. Saito, "Water dynamics: fluctuation, relaxation, and chemical reactions in hydrogen bond network rearrangement," Acc. Chem. Res. 32, 741 (1999).

(25) C. P. Lawrence and J. L. Skinner, "Vibrational spectroscopy of HOD in D_2O. III. Spectral diffusion, and hydrogen-bonding and rotational dynamics," J. Chem. Phys. 118, 264 (2003).

(26) R. Rey, K. B. Møller and J. T. Hynes, "Hydrogen bond dynamics in water and ultrafast infrared spectroscopy," J. Phys. Chem. A 106, 11993 (2002).

(27) C. J. Fecko, J. D. Eaves, J. J. Loparo, A. Tokmakoff and P. L. Geissler, "Ultrafast hydrogen bond dynamics in the infrared spectroscopy of water," Science 301, 1698 (2003).

(28) H. Graener, G. Seifert and A. Laubereau, "New spectroscopy of water using tunable picosecond pulses in the infrared," Phys. Rev. Lett. 66, 2092 (1991).

(29) S. Woutersen, U. Emmerichs, H.-K. Nienhuys and H. J. Bakker, "Anomalous temperature dependence of vibrational lifetimes in water and ice," Phys. Rev. Lett. 81, 1106 (1998).

(30) G. M. Gale, G. Gallot, F. Hache, N. Lascoux, S. Bratos and J.-C. Leicknam, "Femtosecond dynamics of hydrogen bonds in liquid water: A real time study," Phys. Rev. Lett. 1068 (1999).

(31) J. C. Deàk, S. T. Rhea, L. K. Iwaki and D. D. Dlott, "Vibrational energy relaxation and spectral diffusion in water and deuterated water," J. Phys. Chem. A 104, 4866 (2000).

(32) C. P. Lawrence and J. L. Skinner, "Vibrational spectroscopy of HOD in liquid D_2O. I. Vibrational energy relaxation," J. Chem. Phys. 117, 5827 (2002).

(33) S. A. Corcelli and J. L. Skinner, "Infrared and Raman line shapes of dilute HOD in liquid H_2O and D_2O from 10 to 90 ^{o}C," J. Chem. Phys. 109, 6154 (2005).

(34) T. l. C. Jansen, T. Hayashi, W. Zhuang and S. Mukamel, "Stochastic Liouville equations for hydrogen-bonding fluctuations and their signatures in the two-dimensional vibrational spectroscopy of water," J. Chem. Phys. 123, 114504 (2005).

(35) J. D. Eaves, A. Tokmakoff and P. Geissler, "Electric field fluctuations drive vibrational dephasing in water," J. Phys. Chem. A 109, 9424 (2005).

(36) S. T. Roberts, P. B. Petersen, K. Ramasesha, A. Tokmakoff, I. S. Ufimtsev and T. J. Martinez, "Observation of a Zundel-like transition state during proton transfer in aqueous hydroxide solutions," Proc. Natl. Acad. Sci. U.S.A. 106, 15154 (2009).

(37) J. D. Eaves, J. J. Loparo, C. J. Fecko, S. T. Roberts, A. Tokmakoff and P. L. Geissler, "Hydrogen bonds in liquid water are broken only fleetingly," Proc. Natl. Acad. Sci. U.S.A. 102, 13019 (2005).

(38) J. J. Loparo, S. T. Roberts and A. Tokmakoff, "Multidimensonal infrared spectroscopy of water. I. Vibrational dynamics in 2D lineshapes," J. Chem. Phys. 125, 194521 (2006).

(39) J. J. Loparo, S. T. Roberts and A. Tokmakoff, "Multidimensonal infrared spectroscopy of water. II. Hydrogen bond switching dynamics," J. Chem. Phys. 125, 194522 (2006).

(40) S. T. Roberts, K. Ramasesha and A. Tokmakoff, "Structural rearrangements in water viewed through two-dimensional infrared spectroscopy," Acc. Chem. Res. 42, 1239 (2009).

(41) J. D. Eaves, *Vibrational dynamics in water from the molecule's perspective*, Ph.D Thesis, Massachusetts Institute of Technology, Dept. of Chemistry, 2005.

(42) M. Nakamura, K. Tamura and S. Murakami, "Isotope effects on thermodynamic properties: Mixtures of x(D_2O or H_2O) + (1-x)CH_3CN at 298.15 K," Thermochim. Acta 253, 127 (1995).

(43) J. R. Reimers and R. O. Watts, "A local mode potential function for the water molecule," Mol. Phys. 52, 357 (1984).

(44) A. Novak, "Hydrogen bonding in solids. Correlation of spectroscopic and crystallographic data," in *Structure and Bonding*, edited by J. D. Dunitz et al., (Springer-Verlag, New York, 1974).

(45) K. Lazonder, M. S. Pshenichnikov and D. A. Wiersma, "Easy interpretation of optical two-dimensional correlation spectra," Opt. Lett. 31, 3354 (2006).

(46) K. Kwac and M. Cho, "Two-color pump-probe spectroscopies of two- and three-level systems: 2-Dimensional line shapes and solvation dynamics," J. Phys. Chem. A 107, 5903 (2003).

(47) S. T. Roberts, J. J. Loparo and A. Tokmakoff, "Characterization of spectral diffusion from two-dimensional line shapes," J. Chem. Phys. 125, 084502 (2006).

(48) K. Kwak, D. E. Rosenfeld and M. D. Fayer, "Taking apart the two-dimensional vibrational echo spectra: More information and elimination of distortions," J. Chem. Phys. 128, 204505 (2008).

(49) J. B. Asbury, T. Steinel, C. Stromberg, S. A. Corcelli, C. P. Lawrence, J. L. Skinner and M. D. Fayer, "Water dynamics: Vibrational echo correlation spectroscopy and comparison to molecular dynamics simulations," J. Phys. Chem. A 108, 1107 (2004).

(50) E. Whalley and D. D. Klug, "Effect of hydrogen bonding on the direction of the dipole-moment derivative of the O–H bond in the water molecule," J. Chem. Phys. 84, 78 (1986).

(51) G. C. Pimentel and A. L. McClellan, *The Hydrogen Bond*, (Freeman, San Francisco, 1960).

(52) J. R. Schmidt, S. A. Corcelli and J. L. Skinner, "Pronounced non-Condon effects in the ultrafast infrared spectroscopy of water," J. Chem. Phys. 123, 044513 (2005).

(53) B. Auer, R. Kumar, J. R. Schmidt and J. L. Skinner, "Hydrogen bonding and Raman, IR, and 2D-IR spectroscopy of dilute HOD in D_2O," Proc. Natl. Acad. Sci. U.S.A. 104, 14215 (2007).

(54) J. D. Smith, C. D. Cappa, K. R. Wilson, R. C. Cohen, P. L. Geissler and R. J. Saykally, "Unified description of temperature-dependent hydrogen-bond rearrangements in liquid water," Proc. Natl. Acad. Sci. U.S.A. 102, 14171 (2005).

(55) J. J. Loparo, S. T. Roberts, R. A. Nicodemus and A. Tokmakoff, "Variation of the transition dipole moment across the stretching band of water," Chem. Phys. 341, 218 (2007).

(56) S. A. Corcelli, C. P. Lawrence, J. B. Asbury, T. Steinel, M. D. Fayer and J. Skinner, "Spectral diffusion in a fluctuating charge model of water," J. Chem. Phys. 121, 8897 (2004).

(57) E. Harder, J. D. Eaves, A. Tokmakoff and B. J. Berne, "Polarizable models in the vibrational spectroscopy of water," Proc. Nat. Acad. Sci. 102, 11611 (2005).

(58) S. J. Suresh and V. M. Naik, "Hydrogen bond thermodynamic properties of water from dielectric constant data," J. Chem. Phys. 113, 9727 (2000).

(59) D. Laage and J. T. Hynes, "On the molecular mechanism of water reorientation," J. Phys. Chem. B 112, 14230 (2008).

(60) D. Laage and J. T. Hynes, "Do more strongly hydrogen-bonded water molecules reorient more slowly?," Chem. Phys. Lett. 433, 80 (2006).

(61) D. Laage and J. T. Hynes, "A molecular jump mechanism of water reorientation," Science 311, 833 (2006).

(62) S. Woutersen, U. Emmerichs and H. J. Bakker, "Femtosecond mid-IR pump-probe spectroscopy of liquid water: evidence for a two-component structure," Science 278, 658 (1997).

(63) Y. L. A. Rezus and H. J. Bakker, "Oreintational dynamics of isotopically diluted H_2O and D_2O," J. Chem. Phys. 125, 144512 (2006).

(64) H. J. Bakker, Y. L. A. Rezus and R. L. A. Timmer, "Molecular reorientation of liquid water studies with femtosecond midinfrared spectroscopy," J. Phys. Chem. A 112, 11523 (2008).

(65) D. E. Moilanen, E. E. Fenn, Y.-S. Lin, J.L.Skinner, B. Bagchi and M. D. Fayer, "Water inertial reorientation: Hydrogen bond strength and the angular potential," Proc. Natl. Acad. Sci. U.S.A. 105, 5295 (2008).

(66) A. Tokmakoff, "Orientational correlation functions and polarization selectivity for nonlinear spectroscopy of isotropic media. I. Third order," J. Chem. Phys. 105, 1 (1996).

5.A. Appendix. The Role of Motional Narrowing in 2D Lineshapes

A point on a 2D spectrum is commonly interpreted as the probability of observing a molecule at given initial and final frequencies after a set waiting period. While this analogy is attractive due to its simplicity, it neglects the fact that the time resolution in a broadband 2D IR experiment is set by the dephasing time of the vibration under study. Even at $\tau_2 = 0$, 2D spectra are broadened due to dynamics that take place during the τ_1 and τ_3 coherence periods. Spectra can appear motionally narrowed when exchange processes or coherent dynamics occur on the time scale of the dephasing time of the probed vibration.

Given that the dynamics that guide hydrogen bond rearrangements in water are quite fast, we have used the MD simulation to calculate two-dimensional joint probability distributions for comparison with simulated 2D lineshapes to investigate the role of motional narrowing in 2D IR spectra of HOD in D_2O. These distributions represent the probability of observing the evolution of an initial instantaneous frequency, ω_1, to a final frequency, ω_3, after a time period, τ_2:

$$P(\omega_1,\omega_3,\tau_2) = \left\langle \delta\left(\omega_{OH}(\tau_2) - \omega_3\right)\delta\left(\omega_{OH}(0) - \omega_1\right)\right\rangle \tag{5-A1}$$

We can relate this expression to an absorptive 2D spectrum by first recognizing that the delta functions in Eq. 5-A1 can be rewritten as the Fourier transform of a cosine:

$$\delta\left(\omega_{OH}(\tau) - \omega_1\right) = \frac{1}{2\pi}\int_{-\infty}^{\infty} d\tau_1 e^{-i\omega_1\tau_1} e^{-i\omega_{OH}(\tau)\tau_1} \tag{5-A2}$$

Using this relationship, we can rewrite Eq. 5-A1 as:

$$P(\omega_1,\omega_3,\tau_2) = \frac{1}{4\pi^2}\int_{-\infty}^{\infty} d\tau_3 \int_{-\infty}^{\infty} d\tau_1 e^{-i\omega_3\tau_3} e^{-i\omega_1\tau_1} \left\langle \exp\left[-i\omega_{OH}(\tau_2)\tau_3 - i\omega_{OH}(0)\tau_1\right]\right\rangle \tag{5-A3}$$

By applying the Condon approximation and neglecting contributions due to rotations and the v = 2←1 transition, the two-dimensional Fourier transform of Eq. 5-4 can be rewritten in a form similar to Eq. 5-A3:

$$S_{\pm}(\omega_3,\omega_1,\tau_2)=\frac{1}{2\pi^2}\int_{-\infty}^{\infty}d\tau_3\int_{-\infty}^{\infty}d\tau_1 e^{-i\omega_3\tau_3}e^{-i\omega_1\tau_1}\left\langle \exp\left[\mp i\left\langle\omega_{OH}(t)\right\rangle_{\tau_1}\tau_1 - i\left\langle\omega_{OH}(t)\right\rangle_{\tau_3}\tau_3\right]\right\rangle \quad \text{(5-A4)}$$

where we have used the definition of the time average:

$$\left\langle A\right\rangle_t=\frac{1}{t}\int_0^t A(\tau)d\tau, \quad \text{(5-A5)}$$

to rewrite the integrals over τ_1 and τ_3 as the average of ω_{OH} during these time periods. In the static limit where frequencies do not evolve during the coherence periods, Eq. 5-A3 and 5-A4 yield identical results. However, if the system evolves during either τ_1 or τ_3, a motionally averaged lineshape will result.

The first two columns of Fig. 5-A1 displays a comparison between the joint probability distributions determined from our simulation model and 2D spectra calculated within the Condon approximation and neglecting contributions due to both reorientation and the v = 2←1 transition. At τ_2 = 0, the joint probability is simply a straight line stretched along the diagonal axis since no frequency evolution has occurred. As τ_2 increases, the probability distribution broadens rapidly at low frequency, a result that is not observed in calculated 2D spectra. This broadening is maximized at τ_2 = 60 fs, but as τ_2 increases to 120 fs the distribution narrows. The driving force behind this rapid broadening and contraction is the underdamped hydrogen bond stretch observed in the simulation's frequency-frequency correlation function (Fig. 5-8C). 60 and 120 fs correspond to the half and full periods of this oscillation. The high frequency side of the

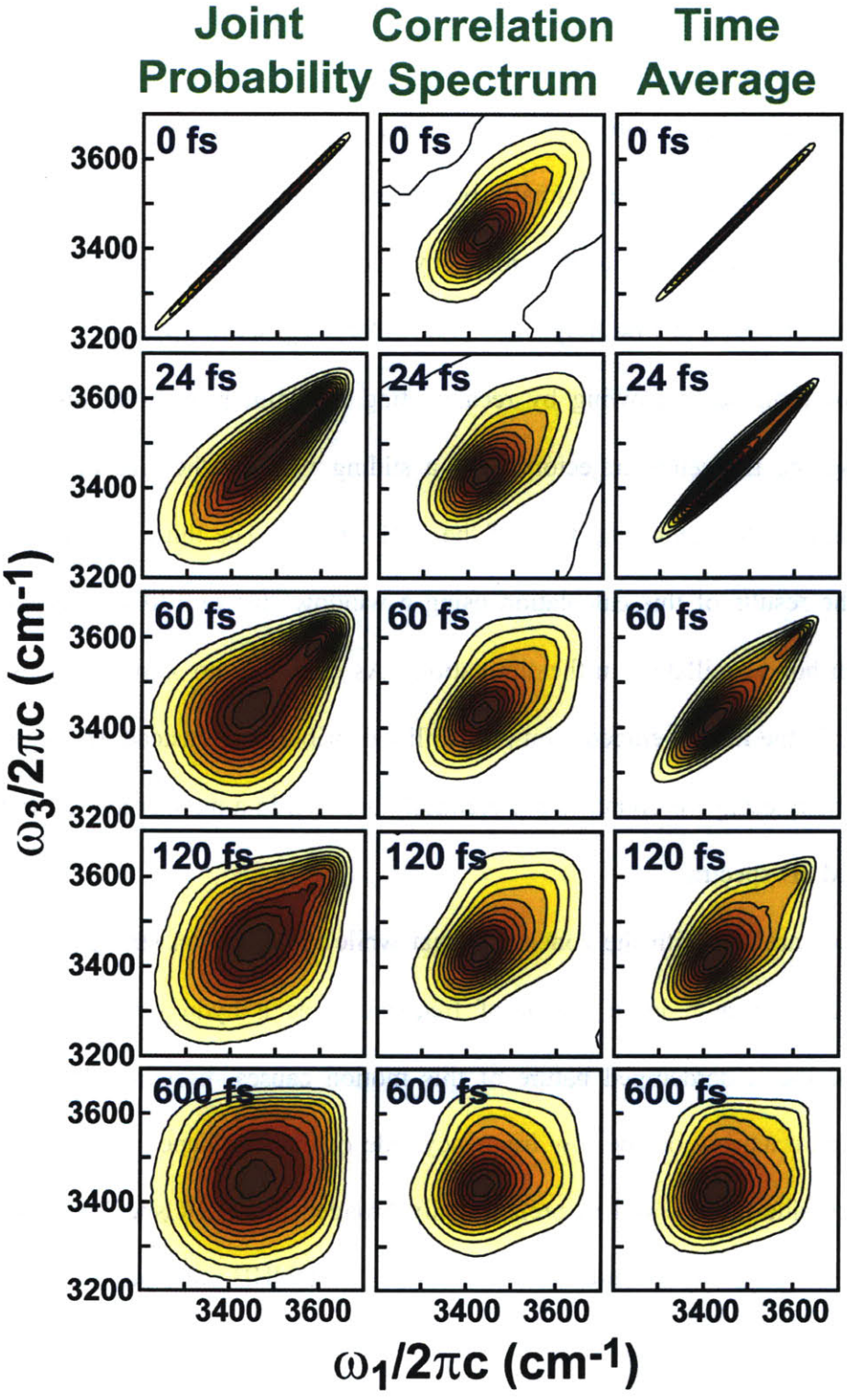


Figure 5-A1: Joint probability distributions of ω_{OH} (left), 2D IR spectra calculated using Eq. 5-A4 (middle), and joint probability distributions calculated after averaging the ω_{OH} frequency trajectory using a sliding 120 fs window.

distribution is also found to broaden rapidly, but the range of spanned frequencies is not as large as on the red side of the distribution.

While the joint probability shows a large, rapid broadening at low frequency, the calculated 2D spectrum preferentially broadens at high frequency as in the experiment. Motional narrowing leads to this result by averaging over the strong hydrogen bond oscillation observed at low frequency. Eq. 5-A4 suggests that we can approximate the effects of motional narrowing by recalculating the joint probability distribution after averaging the frequency trajectory over a sliding window the size of which roughly corresponds to the dephasing time of the O-H stretch. The third column of Fig. 5-A1 shows the results of this calculation using a window size of 120 fs, the period of the hydrogen bond oscillation in the simulation. As expected, no sign of this oscillation is observed in the time averaged joint probability distributions. Instead, the high frequency side of the lineshape is found to preferentially broaden in a manner similar to that of the calculated 2D spectra.

We are left with the conclusion that while molecules in strong hydrogen bonds rapidly experience a large breath of frequencies as a hydrogen bond expands and contracts, the underdamped nature of this motion causes measured 2D IR spectra to remain quite narrow on the low frequency side of the lineshape. In contrast, the high frequency side is observed to preferentially broaden in 2D IR spectra since no strong restoring force exists to return molecules that leave NHB configurations back to their initial configurations.

Chapter 6

Different Stages of Proton Transfer in Aqueous Hydroxide Solutions Visualized using Ultrafast Infrared Spectroscopy

6.1. Introduction

Under ambient conditions, one in every 10^{14} water molecules will dissociate, yielding both a hydronium, H_3O^+, and a hydroxide ion, OH^-. While the equilibrium properties and thermodynamics of solutions of these ions are well understood, a description of their microscopic structure and behavior continues to elude researchers. Hydronium and hydroxide ions both display anomalously high diffusion rates compared to ions of similar size and charge density.[1] Researchers have rationalized this excess diffusion by recognizing that each ion can undergo a proton transfer reaction with a neighboring water molecule, leading to a translocation of the ion's structural motif rather than the diffusion of a specific set of covalently bound atoms. Thus, water's hydrogen bonding network serves as a scaffolding upon which excess protons and protons holes can migrate. This conceptual picture of proton transport is prevalent in the discussion of systems where the motion of the proton is highly unidirectional, such as membrane proteins that serve as proton pumps,[2] proton transfer among different residues of a protein molecule,[3] or the conduction of protons between water molecules confined within carbon nanotubes.[4] Hydrogen bonded water chains present in the core of these systems are

thought to serve as "water wires" along which excess protons can be conducted from one location to another.[5]

While the motion of protons along hydrogen bonds provides an elegant general picture of proton conduction in water, many questions concerning the details of this mechanism remain unanswered. Most notably, what is the structure of the excess proton? Researchers commonly identify two limiting configurations, the Eigen cation,[6] a triply solvated hydronium ion ($H_3O^+ \bullet 3H_2O$), and the Zundel ion,[7] a proton equally shared between two water molecules ($H_5O_2^+$ or $H_2O \cdot\cdot H^+ \cdot\cdot OH_2$). Proton transport is often described in terms of the exchange between these two species.[8,9] The energy that separates these configurations is small, on the order of a hydrogen bond (2-3 kcal/mol),[10] which allows Eigen-like and Zundel-like structures to interconvert as the hydrogen bonding network surrounding the excess proton fluctuates over femtosecond to picosecond time scales.[11] The length scale over which hydrogen bond fluctuations can influence proton transport can be quite large. Polarization fluctuations of the solvent were hypothesized by Zundel[7,12] to play a strong role in the structural diffusion of the excess proton, while recent multistate empirical valence bond molecular dynamics (MS-EVB) simulations have shown that the breakage and formation of hydrogen bonds as far away as the second solvation shell of the excess proton can affect the proton's motion.[13] Given the strong coupling of the motion of the proton to that of the surrounding hydrogen bonding network, this suggests that the structure of the excess proton cannot be described simply in terms of static Eigen and Zundel cations, but instead as a rapidly evolving continuum of structures that oscillates between these two limiting cases.[8] Thus, a more appropriate description of the ion can be gained by asking questions regarding its

dynamics. What are the primary fluctuations of the hydrogen bonding network that act to guide the motion of the proton? Over what time and length scales do these fluctuations occur?

Similar questions also exist regarding the transport of the hydroxide ion. Traditionally, the structural diffusion of this ion has received much less experimental and theoretical investigation compared to that of the excess proton and a great deal of debate still exists regarding both the limiting structures of the ion and its transport mechanism. An initial proposal for the transport of the ion described it as the mirror image of that of the hydronium ion and postulated the existence of two limiting structures, a triply solvated $H_7O_4^-$ ion ($HO^-\bullet 3H_2O$) and a $H_3O_2^-$ ion ($HO\cdot\cdot H\cdot\cdot OH^-$) that are the analogues of the Eigen and Zundel structures of the excess proton.[14] The rate limiting step in this mechanism was suggested to be the cleavage of a hydrogen bond in the first solvation shell of a $H_7O_4^-$ ion, which promotes its conversion into a $H_3O_2^-$ structure since the hydrogen bonding connectivity of this structure will be identical on either side of the ion. This picture is supported by DFT based *ab initio* simulations which found that while the hydroxide ion most often accepts three hydrogen bonds, the ion's coordination number is quite labile, and the $H_3O_2^-$ ion comprises a prominent subspecies that is formed during proton transfer events.[15]

Recent Car-Parrinello molecular dynamics (CPMD) simulations have called this mechanism into question.[16-18] The results of these simulations suggest that the three lone pair electrons on the oxygen atom of the hydroxide ion can blend together, forming a ring of delocalized charge that can accept up to four hydrogen bonds from surrounding water molecules. Under ambient conditions, the most stable form of the ion is found to be a

"hypercoordinated" $H_9O_5^-$ ion. The simulations also suggest that a breakage of a hydrogen bond to this 4-coordinate complex facilitates proton transfer since the two oxygen atoms of a $H_3O_2^-$ ion can each support up to 3 hydrogen bonds (including the shared proton). Tuckerman et al.[19] describe this mechanism as "presolvation" because the transport of the OH^- ion only occurs when solvent fluctuations prepare a liquid configuration that can optimally solvate the proton transfer transition state.

While the concept of presolvation provides an insightful view of proton transport in aqueous hydroxide solutions, care must be used when interpreting CPMD simulations since their results display a strong dependence on the density functional employed for the simulation.[19,20] The results described above made use of the BLYP density functional. However, simulations performed with the PW91 functional were found to contain few 4-coordinate structures, instead containing primarily 3-coordinate hydroxide ions. Moreover, a simulation performed with the HCTH density functional only contained 4-coordinate ions. While the conclusions drawn from the BLYP based simulations are supported by the fact that the diffusion constant calculated for the ion agrees best with experiment with respect to simulations using other density functionals, the diffusion constant calculated from BLYP based simulations is still only ~2/3 of the value determined on the basis of experiment.[19] The origin of this discrepancy is as of yet unclear.

Debate between these conceptual views of the transport of the hydroxide ion continues in part due to the lack of definitive experimental evidence that supports one picture over the other. Thermochemical measurements[21] and infrared spectra[22] of gas phase clusters suggest that the oxygen atom of the hydroxide ion accepts only three

hydrogen bonds, consistent with the formation of an $H_7O_3^-$ ion. In contrast, neutron scattering[23,24] and x-ray diffraction[25] results imply a coordination number between 3 and 4 that varies with the concentration of the ion, consistent with CPMD simulation, and found that the ion's hydrogen atom donates only a weak hydrogen bond to the surrounding liquid. Measurements of infrared absorption spectra of the O-D stretch of dilute HOD in alkali hydroxide solutions were interpreted as showing no evidence for the formation of a stable $H_3O_2^-$ ion.[26] However, this conclusion was reached on the assumption that the measured infrared spectra can be decomposed into a series of contributions from species with different solvation shell structures, which is dubious given that the fluctuations of water's hydrogen bonding network are expected to drive the rapid exchange of different solvation shell structures of the ion.

Raman spectra support the conclusion reached from neutron scattering experiments regarding the donation of a hydrogen bond by the hydroxide ion. At high concentration, a narrow peak appears on the high frequency side of the O-H stretching transition that has been attributed to the weakly hydrogen bound OH^- stretch.[27,28] Recent core-level photoelectron emission measurements[29] have found evidence of a transiently formed hydrogen bond to the hydrogen atom of the hydroxide ion but were unable to determine the lifetime of this interaction. This raises the question if the formation of such a bond is important in the transport of the hydroxide ion.

Time resolved measurements have provided evidence for both fast and slow relaxation time scales involving the hydroxide ion. Nienhyus et al.[30] observed a fast decay of 160 fs in transient hole burning measurements of the O-H stretch of dilute HOD dissolved in a 10 M NaOD solution, and attributed this decay to HOD molecules in the

solvation shell of OD^- ions that undergo induced population relaxation when the OD^- ion accepts a proton from a neighboring water molecule. The authors also reported that the rotational anisotropy of this system showed no visible decay during the first 1.7 ps after excitation, which implies that while the transfer of the charge defect can be quite fast, hydrogen bond dynamics in concentrated hydroxide solutions can be quite slow. At much lower hydroxide ion concentrations (40 mM KOH), rotational anisotropy measurements[31] of the charge transfer to solvent band of the hydroxide ion were demonstrated to track that reported for the reorientation of water at temperatures above 290 K, and implies that the reorientation of the hydroxide ion is dictated by the surrounding solvent. Below this temperature, the time scale for the anisotropy decay increases above that of water, which suggests that the formation of strong hydrogen bonds between the ion and the solvent cause the ion to drag its solvation shell along with it as it reorients.

From the discussion above it is clear that there is little experimental consensus concerning the structure and dynamics of the aqueous hydroxide ion. Gas phase studies and scattering experiments give different results for the average size of the ion's solvation shell. While the hydrogen bonding to the proton of the ion is certainly weak on average, it is unclear if the formation of a bond to this proton facilitates the ion's ability to accept a proton from a hydrogen bonded partner. Transient studies show a mixture of time scales that range from very fast (160 fs) to picosecond or longer time scales and it is not clear what processes these time scales represent or how each contributes to the ion's structural diffusion.

Nonlinear infrared spectroscopy provides a unique means of probing the structural diffusion of the hydroxide ion since the frequency of the O-H stretching transition, ω_{OH}, of a dilute solution of HOD dissolved $NaOD/D_2O$ is sensitive to the strength of the hydrogen bond formed by the HOD molecule. Short, linear hydrogen bonds between a HOD molecule and an OD^- ion appear red shifted from the main O-H stretching band whereas weak hydrogen bonds of the type formed by the proton of an OH^- ion appear at high frequency. Time dependent changes in ω_{OH} result from the dynamics of the solvent that enable the donation of a proton from a HOD molecule to an OD^- ion and the subsequent solvation of the newly formed ion.

In this and the following chapter, we present the results of a series nonlinear infrared experiments[32] carried out on an isotopically dilute solution of HOD dissolved in $NaOD/D_2O$ and the calculation of spectra from a recently developed MS-EVB simulation model[33,34] of aqueous NaOH. Upon the addition of NaOD, a new spectral feature appears in both pump-probe and transient grating measurements that relaxes on a 110 fs time scale. Two-dimensional infrared spectroscopy (2D IR) experiments show that this feature corresponds to a broad component that absorbs across the entire frequency range probed by the experiments. In Chapter 7, we will show that spectra calculated from the MS-EVB simulations indicate that this spectral feature arises from Zundel-like states, wherein a proton is delocalized between a HOD molecule and a deuteroxide ion. Once the decay of this feature is complete, photon echo peak shift measurements display an offset that increases linearly with NaOD concentration, indicating a slowing of the dynamics of the system. Beyond a waiting time of ~2 ps however, the offset observed in the peak shift decays uniformly to zero primarily as the result of a non-equilibrium

heating of the bath modes surrounding excited HOD molecules after they have undergone population relaxation. 2D IR spectra measured for waiting times in this picosecond regime show the existence of new spectral features that are indicative of chemical exchange between the center of the O-H stretching transition and the high frequency side of the lineshape, a spectral range indicative of the absorption of the OH^- ion.

We have built a spectral model that can qualitatively explain the behavior of the measured pump-probe, echo peak shift, and 2D IR spectra that takes into account the effects of both chemical exchange between different species induced by proton transfer to the hydroxide ion and the heating of the bath upon vibrational energy relaxation. The results of this model suggest that while protons shared in Zundel-like configurations undergo rapid relaxation within 110 fs, the solvation of the newly formed hydroxide ion is much slower, occurring over a time scale of at least 3 ps. The existence of this relatively slow relaxation time scale associated with the solvation of a newly formed OD^- charge defect may in part help to explain the strong increase in solvent viscosity with increasing NaOD concentration.

6.2. Experimental Methods

A description of the acquisition of pump-probe and vibrational echo signals is contained in Chapter 4, consequently only a brief description of the experimental setup and sample preparation is given here. Samples were prepared through the dilution of 40% NaOD (99.5% deuteration; Cambridge Isotope Laboratories) and 40% KOD (98% deuteration; Aldrich) stock solutions with D_2O. A small amount of H_2O (typically less than 1% of the sample volume) was added to each solution to give an absorbance of the O-H stretch no greater than 0.4 after subtraction of the D_2O background. FT-IR

measurements were performed by holding each sample solution between two CaF_2 windows with a path length of 50 μm. Due to the overwhelming nonresonant response that arises from CaF_2 windows when all three pulses are overlapped in the sample, solutions used for nonlinear experiments were held between two Si_3N_4 windows (Norcada) within a home built Teflon sample cell with a path length of 100 μm. 500 nm thick windows were used for photon echo peak shift experiments while all other measurements were carried out using 100 nm windows. Both sets of windows were found to give no measurable nonresonant response. Due to poor index matching with air, a significant back reflected signal could be measured during 2D IR experiments. To remove this signal a small piece of Parafilm (~25 μm thick) was inserted into one side of the sample cell so that the two Si_3N_4 windows were held at a small angle with respect to one another, and caused the back reflected signal to propagate in a different direction than the signal.

Pump-probe experiments were performed using 45 fs pulses containing ~350 cm^{-1} of bandwidth centered at 3325 cm^{-1}. The polarization of each beam was controlled with λ/2 wave plates (Alphalas) and CaF_2 wire-grid polarizers (Molectron). The pump pulse was oriented at the magic angle (54.7°) with respect to the probe to remove effects due to the reorientation of excited molecules.[35] The probe was passed through an analyzing polarizer and a narrow band-pass filter (FWHM ~50 cm^{-1}, Spectrogon) centered at 3400 cm^{-1} after the sample to reduce interference with the $v = 2 \leftarrow 1$ transition. To reduce noise from fluctuations of the pump intensity, a weak reflection of the pump pulse before the sample was used for shot-to-shot normalization.

The pulses used for transient grating and photon echo peak shift measurements were also 45 fs in duration, but centered at 3375 cm^{-1}. Similar to the pump-probe experiments, transient grating measurements were carried out with the first two excitation pulses set at the magic angle with respect to the third pulse to suppress contributions to the signal due to diffusive reorientation. The echo peak shift measurements were carried out at zzzz polarization (all pulses parallel) to help enhance the low signal intensity at waiting times longer than a few picoseconds. In both measurements, the excitation pulses were arranged in a boxcar geometry and a single channel liquid nitrogen cooled InSb detector (Infrared Systems Development) gated by a boxcar integrator (Stanford Research Systems SR-250) was used to detect the background free signal. One of the excitation pulses was modulated at 500 Hz using an optical chopper, which allowed the boxcar output to be detected using a lock-in amplifier. In the case of the peak shift experiments, the pair of two pulse echo signals stimulated by the first two excitation pulses were also collected to properly calibrate the zero timing position of the τ_1 time axis. These two signals were recorded simultaneously with the three pulse echo signal using two separate single channel InSb detectors.

All of the 2D IR spectra that appear in this chapter were recorded using the time domain acquisition technique described in Chapter 4 with the exception of the difference spectra that appear in Fig. 6-7, which were measured using the mixed time-frequency scanning technique also described in Chapter 4. All spectra were recorded using ~45 fs pulses and at zzzz polarization. The excitation pulses were centered at 3400 cm^{-1} for all presented data sets with the exception of the spectra shown in Fig. 6-6, which were measured using pulses centered at 3350 cm^{-1}. The larger contribution of the photo

induced absorption of the v = 2←1 transition to the spectra in Fig. 6-6 is due to this small shift in the center frequency of the excitation pulses.

6.3. Infrared Spectroscopy of Isotopically Dilute Hydroxide Solutions

Fig. 6-1 displays linear absorption spectra of ~1% HOD dissolved in $NaOD/D_2O$ solution as a function of NaOD concentration. As this concentration increases, the spectra broaden significantly to low frequency. This broadening is similar to that observed in strong acids or bases,[7,36-38] which display a continuum absorption that spans the entire mid-infrared region below the peak of the O-H stretching transition (See Fig. 1-3). The formation of a hydrogen bond imparts an attractive perturbation to the O-H stretching potential, causing it to broaden and decreasing ω_{OH}. In the case of a mid-strength hydrogen bond to water, this decrease is ~300 cm^{-1} relative to the gas phase. However, in the case of a hydrogen bond formed between a HOD molecule and an OD^- ion, the interaction between the ion and HOD molecule is much stronger, yielding frequency shifts well in excess of 400 cm^{-1}. During proton exchange, this interaction increases to the point that the proton becomes equally shared between the two species. In this case, the proton stretching potential is better described as a double well potential with a vanishingly small barrier separating the two wells,[39] resulting in a very large red shift of ω_{OH}. Argon predissociation spectra of the gas phase $H_3O_2^-$ ion have shown that the shared proton stretching transition can reach values as low as 697 cm^{-1}.[40] In the liquid, it is expected that the stretching potential of the bridging proton will be modulated by the surrounding solvent. The broad absorption that appears across the mid-infrared range is the result of a continuum of shared proton structures that rapidly evolve and interconvert with time.[7]

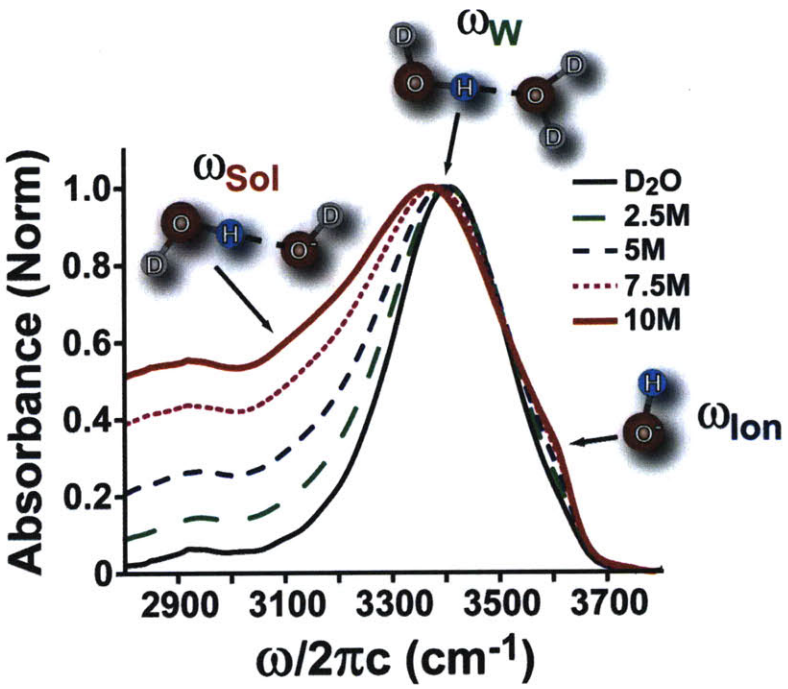


Figure 6-1: FT-IR spectra of ~1% HOD in varying concentrations of NaOD/D_2O normalized to the absorption maximum. For each presented spectrum, a background of the appropriate concentration of NaOD/D_2O was subtracted before normalization so that only contributions to the spectra due to proton (H) vibrations are pictured. As the NaOD concentration increases, a new feature appears at 3600 cm^{-1} because of the OH^- stretch, and a strong broadening appears at low frequency because of HOD molecules hydrogen bonded to OD^- ions. We can broadly label the frequency regions corresponding to the OH^- stretch, HOD molecules hydrogen bonded to D_2O, and HOD molecules that donate a hydrogen bond to an OD^- ion by ω_{Ion}, ω_W, and ω_{Sol}, respectively.

In addition to the continuum absorption at low frequency, a peak at 3600 cm^{-1} is also found to appear with increasing NaOD concentration. Although this peak is only a small shoulder in the infrared spectra of Fig. 6-1, Raman spectra of alkali hydroxides display a strong, sharp scattering peak at ~3610 cm^{-1} that has been attributed to the OH^- stretch.[27,28,41,42] Because of the negative charge on the OH^- ion, its proton can only act as a weak hydrogen bond donor. This leads to a blue shift of its O-H stretching frequency relative to that of a HOD molecule hydrogen bonded to D_2O. Neutron scattering results

support this conclusion drawn from the spectra, finding little evidence for the presence of a hydrogen bond donated by the hydroxide ion.[23,24]

As an initial test of how the dynamics of the system change upon the addition of NaOD, we performed pump-probe transient absorption measurements of the O-H stretching transition (Fig. 6-2). The addition of deuteroxide was found to lead to the appearance of a fast decay component whose amplitude grows monotonically with hydroxide concentration. To properly determine the time scale of this fast decay feature, we must also account for the fact that the HOD/D_2O trace also shows a small rapid decay at early waiting times. This initial fast decay as well as the small oscillations in the signal at early waiting times are due to the influence of the underdamped hydrogen bond stretch that modulates ω_{OH} (see Chapter 5) and these contributions to the pump-probe signal can be reproduced by calculations using our group's previously measured O-H stretch frequency-frequency correlation function that take into account the finite time duration of the excitation pulses.[43,44] To include this coherent contribution due to HOD molecules interacting with the D_2O bath, the decay trace for HOD/D_2O was fit with a single exponential function and the residual was then fit using a pair of damped exponential decays. This residual was included in each of the subsequent biexponential fits for the NaOD solutions, but the ratio of the amplitude of the residual and that of the long decay component determined from the fit to the HOD/D_2O decay trace was held constant.

Following our fitting procedure, we find that the decay of each trace can be well described using only two decay time constants, 710 and 110 fs, whose relative contributions to the measured decay change with concentration. The 710 fs decay time scale is consistent with previous measurements of the vibrational lifetime of the O-H

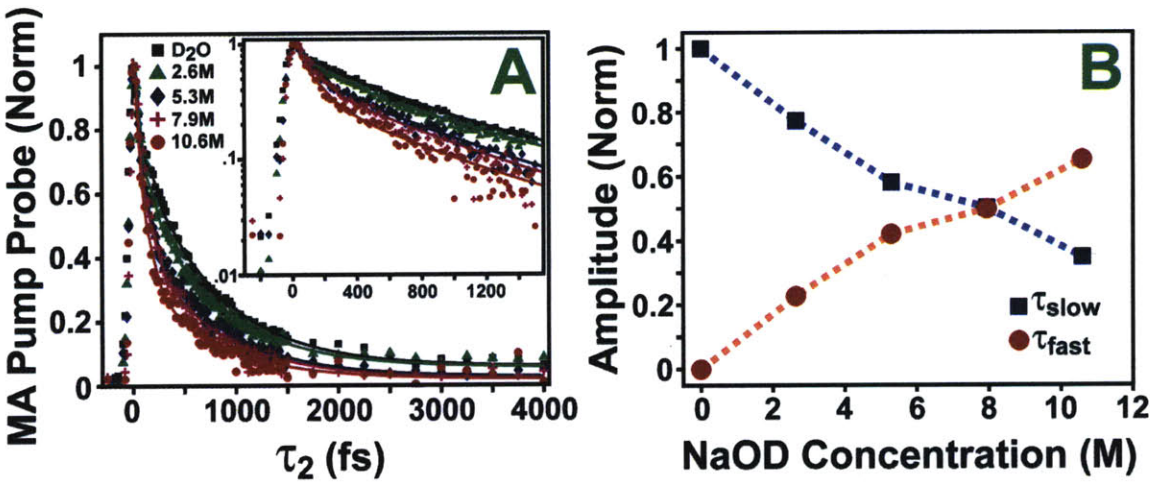


Figure 6-2: (A) Pump-probe decay traces of the O-H stretching region for differing concentrations of NaOD, along with biexponential fits determined as described in the text. As the NaOD concentration decreases, the measured decay acquires a fast component of 110 fs. (B) Relative amplitudes of the fast and slow decay components to the measured pump-probe signal.

stretch of HOD in D_2O.[43-46] The rapid decay time scale was hinted at in transient hole burning measurements of a 10 M NaOD solution, where a decay on the order of the experimental time resolution, ~160 fs, was observed.[30]

Since changes in ω_{OH} are largely determined by the configuration of the proton's hydrogen bonding partner, we believe that this fast decay time scale is associated with a process involving the deuteroxide ions present in solution. Previous measurements of water dynamics in electrolyte solutions have shown that the observed water dynamics in ultrafast infrared experiments primarily reflect interactions between water and dissolved anions.[47] Cations were found to only have a minimal influence on the measured dynamics.[48] However, in the absence of a control experiment it is unclear whether the Na^+ ions present in solution have a direct influence on the measured decay traces. To determine if there is any contribution due to the counterion to the measured data in Fig. 6-2, we carried out transient grating measurements of HOD dissolved in both $NaOD/D_2O$

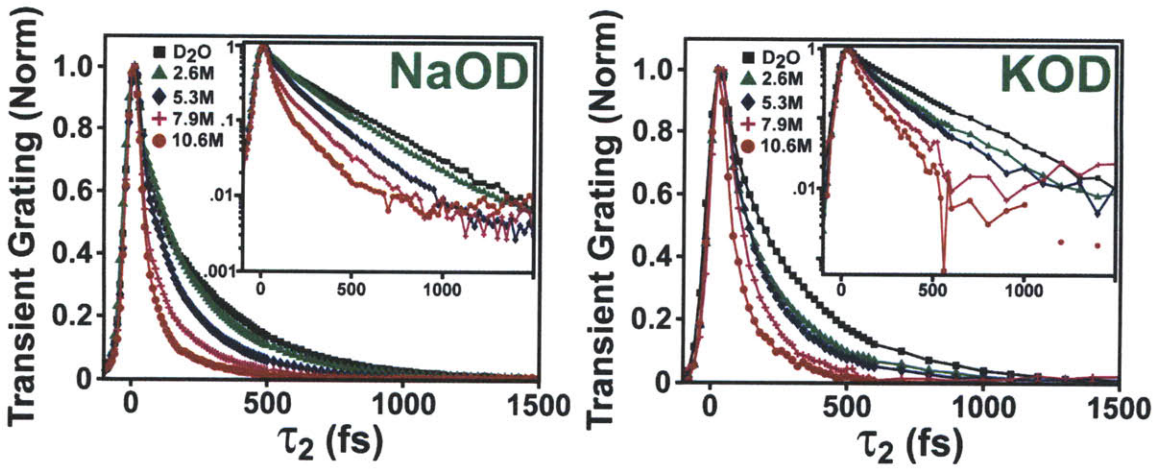


Figure 6-3: Transient grating decay traces for ~1% HOD in NaOD/D_2O and KOD/D_2O as a function of the deuteroxide concentration. The decay traces for both sets of solutions are quite similar, suggesting that the rapid initial decay that appears with increasing concentration is due to the influence of the OD^- ion and not the cation.

and KOD/D_2O as a function of the deuteroxide concentration (Fig. 6-3). Since the first two pulses in the transient grating measurement prepare an excited population state, the decay of the grating signal is largely related to vibrational population relaxation, similar to the pump-probe measurement. However, since the signal in a transient grating experiment is not phase resolved, it is related to the square of the pump-probe decay which complicates the extraction of decay time scales from the data. Nonetheless, the transient grating signals for NaOD solutions appear qualitatively similar to the pump-probe transient displayed in Fig. 6-2. As the NaOD concentration increases, an initial rapid decay of the transient grating signal is observed, consistent with the growth of the 110 fs decay component found in the pump-probe data. The transient grating decay traces measured for KOD solutions are almost identical to those measured using NaOD solutions in terms of both the amplitude and time scale of each decay component. This leads us to the conclusion that the observed fast decay is entirely due to the influence of OD^- ions.

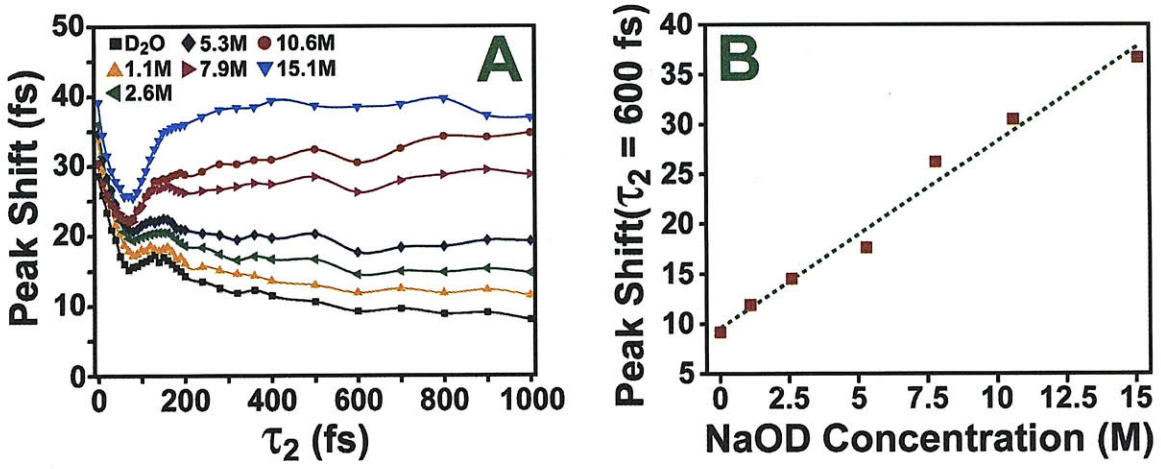


Figure 6-4: (A) Photon echo peak shift of HOD in NaOD/D_2O measured for solutions of increasing NaOD concentration. (B) The value of the peak shift at τ_2 = 600 fs increases linearly with NaOD concentration and suggests that the presence of NaOD slows the overall dynamics of the system.

To determine how the presence of OD^- ions influences the spectral diffusion of the surrounding water, we measured the decay of the photon echo peak shift of ω_{OH} as a function of the NaOD concentration (Fig. 6-4A). As described in Chapter 3, the decay of the echo peak shift can be related to a frequency-frequency correlation function for ω_{OH}, $C(\tau) = \langle \delta\omega_{OH}(\tau)\,\delta\omega_{OH}(0) \rangle$, where $\delta\omega_{OH}(\tau) = \omega_{OH}(\tau) - \langle \omega_{OH} \rangle$. In the case of HOD/$D_2O$, the peak shift displays a sub-100 fs decay, a recurrence at 160 fs due to the oscillation of an underdamped hydrogen bond, and a longer 1.2 ps decay time scale. With increasing NaOD concentration, the initial decay of the peak shift appears to remain largely the same, however the offset of the peak shift at longer waiting times is found to increase. Fig. 6-4B plots the value of the peak shift at a waiting time of 600 fs and shows that this offset increases linearly with increasing NaOD concentration. The lack of an observed decay over this range of waiting times suggests that the addition of NaOD slows down the average dynamics of the system. This decrease in the overall time scale for

spectral diffusion is not unexpected given that the viscosity of alkali hydroxide solutions are known to strongly increase with the number of dissolved hydroxide ions.[49]

More interesting is the fact that at concentrations greater than 5.3 M, after a waiting time of ~80 fs the peak shift undergoes a large increase before reaching its offset. If the peak shift decay originated from a single vibrational transition, an increase in the peak shift would indicate that this transition becomes more inhomogeneous with waiting time, a surprising result. More likely, the complicated behavior of the peak shift indicates the presence of multiple absorbing species under the O-H lineshape, each with different spectral diffusion time scales and vibrational lifetimes. This prevents a simple analysis of the peak shift in terms of $C(\tau)$. A more specific explanation for this recurrence may be that the rapidly decaying feature observed in both the pump-probe and transient grating measurements undergoes rapid spectral shifts, leasing to an initial decay of the peak shift. As this component undergoes relaxation, the contribution to the peak shift due to the slower dynamics of the solvent will come to dominate the signal, causing the observed rise in the peak shift.

In Fig. 6-5 we expand the time axis of Fig. 6-4 and plot the decay of the peak shift out to 10 ps. Unexpectedly, at a waiting time of ~2 ps each of the measured peak shift traces were found to decay uniformly to zero regardless of the deuteroxide concentration. One possible intriguing explanation for this decay is that it is due to proton transfer. As spectral diffusion slows down due to the increased viscosity of the solution, proton transfer can serve as a means of converting a high frequency free OH^- stretch into a lower frequency, water-like stretch. This shift in frequency associated with this exchange would cause a decrease in the measured peak shift. CPMD simulations have suggested

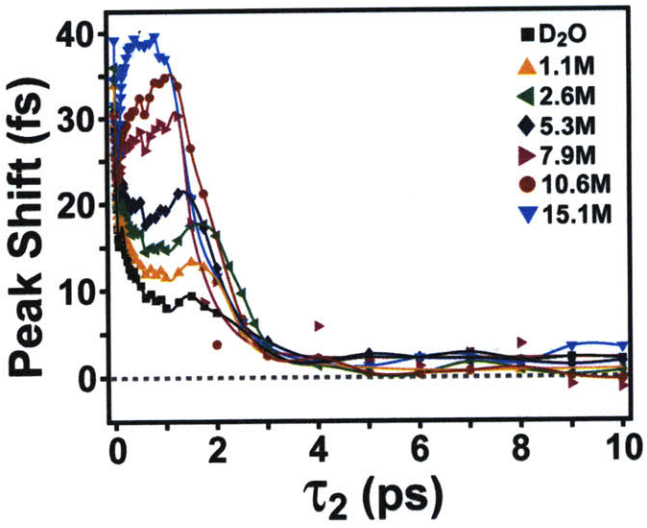


Figure 6-5: The photon echo peak shift data of HOD in NaOD/D_2O displayed in Fig. 6-4A, but now plotted for waiting times up to 10 ps.

that in deuterated solutions, the structural diffusion of the OD^- ion occurs on a 1.7 ps time scale,[20] which would agree well with our experimental results provided that the decay is in fact due to proton transfer.

An equally plausible second explanation is that the decay of the peak shift is dueto a non-equilibrium heating of the solvent surrounding excited HOD molecules. When an excited molecule undergoes vibrational relaxation, the energy deposited in the O-H stretch by the excitation pulses eventually funnels down to the low frequency modes of the bath, making the local solvent environment surrounding the HOD molecule appear as if it has been heated.[50] This can shift the absorption spectrum of the molecule so that the initially prepared photobleach of the O-H stretch does not refill upon population relaxation. In pump-probe measurements, this "hot ground state" absorption contributes a static offset to the decay that persists over 10's of picoseconds.[44,51] In photon echo peak shift measurements of HOD/D_2O, it has been shown that both recurrences and decays of the peak shift at time delays corresponding to a few ps can be observed

depending on both the bandwidth and center frequency of the excitation pulses.[52,53] Echo peak shifts measured with pulses tuned to the red edge of ω_{OH} can show strong recurrences near waiting times of 2 ps due to interference effects that arise from relaxation induced heating.[50] If we wish to determine if information concerning the structural diffusion of the OD^- ion is contained in the decay of the echo peak shift, it is clear that we must first develop a model that can account for the effects of non-equilibrium heating.

6.4. Observation of Proton Transfer Dynamics using 2D IR Spectroscopy

From the experiments described in the previous section, we find evidence for both fast and slow spectral dynamics. As a new spectral feature that relaxes on a 110 fs time scale is found to appear with increasing NaOD concentration, the overall dynamics of the system appear to slow down. Additionally, the process that leads to the relaxation of the peak shift measurements near 2 ps is unclear. To help explain the origin of these spectral features, we carried out 2D IR measurements of the O-H stretching transition as a function of NaOD concentration. 2D IR is well suited the study of short-lived species that arise and disappear during the course of proton transport because it combines the time resolution needed to observe transient species with the frequency resolution necessary to isolate their spectral signatures. Additionally, time scales for the exchange of different species that absorb under a congested linear spectrum can be measured by observing the growth of cross peaks between different transitions that appear along the diagonal axis of a 2D spectrum.

2D IR spectra for 10.6 and 5.3 M NaOD are plotted against spectra of neat HOD/D_2O in Fig. 6-6A. As τ_2 increases, we find that the 10.6 M NaOD data remains

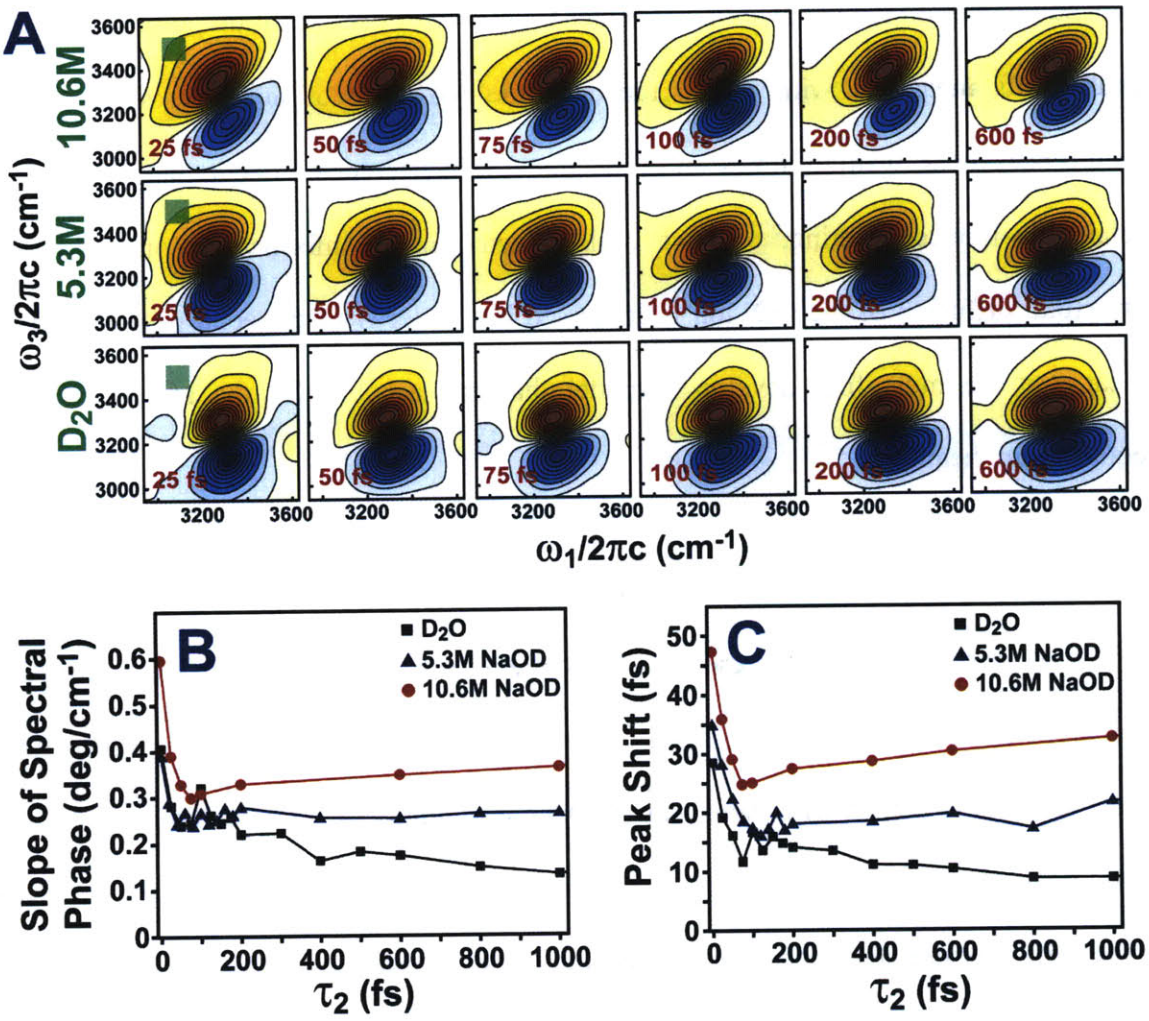


Figure 6-6: 2D IR spectra for 10.6 M NaOD, 5.3 M NaOD, and neat HOD:D_2O as a function of waiting time. The shaded green region highlights a spectral range showing strong off-diagonal broadening at early waiting times that quickly relaxes as τ_2 increases (See Fig. 6-7). (B & C) The slope of the spectral phase at the peak of the O-H stretching transition of HOD:D_2O and the echo peak shift constructed from the 2D data. The increasing offsets of these metrics with NaOD concentration show that the addition of NaOD slows the picosecond dynamics of the system.

strongly elongated along the diagonal axis while the data measured for neat D_2O solution is found to broaden, becoming more homogeneous with waiting time. We can quantify the loss of frequency memory in each of the pictured spectra through the use of two of the metrics for quantifying spectral diffusion in 2D lineshapes described in Chapter 3. Fig. 6-6B and 6-6C display the slope of the spectral phase along the ω_1 dimension

evaluated at (ω_1, ω_3) = 3400 cm^{-1}, the peak of the linear absorption of the O-H stretching transition in D_2O solution, and the echo peak shift calculated from the 2D data.* Both of these metrics appear qualitatively similar to the peak shift data displayed in Fig. 6-4A. The addition of NaOD leads to an increase in the offset of these metrics in the 100 fs – 1 ps waiting time range, and reflects the conclusion drawn from the peak shift data that the addition of NaOD slows the average dynamics of the system.

While the diagonal elongation of the 2D spectra corroborates the general observations drawn from the decay of the peak shift, the more interesting feature observed in the spectra is the strong off-diagonal broadening that is present in the NaOD spectra at early waiting times whose intensity scales linearly with increasing NaOD concentration (Fig. 6-7A). This broadening is observed at all probed frequencies and quickly relaxes as τ_2 increases, nearly disappearing from the spectra by a waiting time of 100 fs (Fig. 6-7B). This collapse of intensity with increasing τ_2 is the opposite of what is expected in 2D IR exchange experiments, where cross peaks or off-diagonal intensities appear over the time scale during which two species exchange environments.[54] Off-diagonal intensity can also be observed in systems containing coupled oscillators.[55] However, given that the solutions under investigation are isotopically dilute, the probability of two separate O-H oscillators encountering each other is small. Instead, the large broadening observed at early waiting times shows that a subset of O-H vibrations samples the entire probed frequency range within a few tens of femtoseconds. At sub ~100 fs waiting times, the measured 2D spectra consist of a superposition of two spectral

* To calculate the peak shift, the time domain 2D data was Fourier filtered to remove the 3 μm carrier oscillations. The resulting time domain envelopes were then squared, projected onto the τ_1 time axis, and fit using a Gaussian lineshape to determine the peak of the envelope.

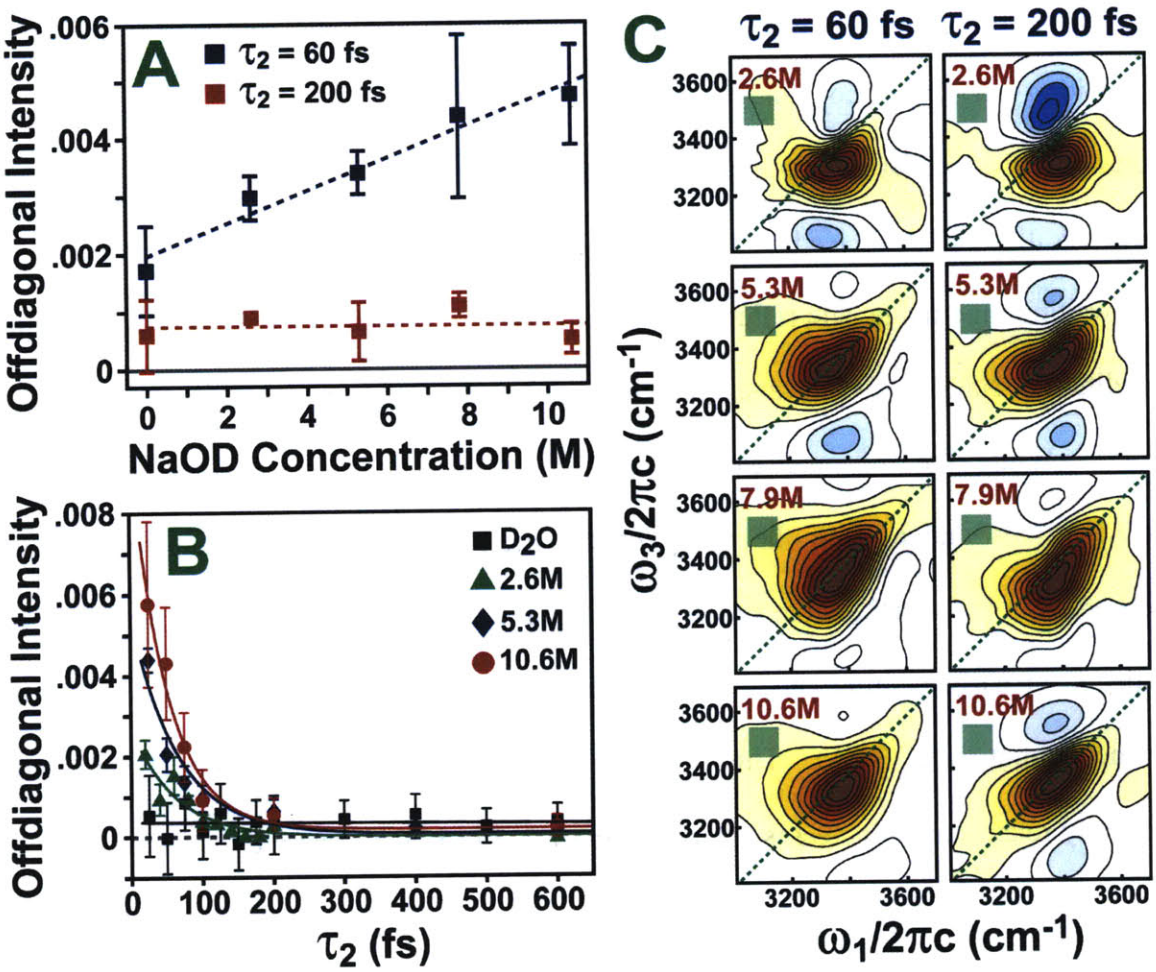


Figure 6-7: Intensity of the off-diagonal region of the 2D IR spectra as a function of NaOD concentration and waiting time. (A) The integrated area ω_1 = 3050 – 3150 cm^{-1} and ω_3 = 3450 – 3550 cm^{-1} for τ_2 = 60 and 200 fs normalized by the integrated absolute value spectrum at the earliest recorded waiting time for each data set. The green boxes overlaid on the spectra in (C) and Fig. 6-6 denote the integrated frequency region. (B) The decay of this integrated spectral range as a function of τ_2. (C) Difference spectra for waiting times of 60 and 200 fs calculated as noted in the text. Contours are plotted in equal increments relative to the maximum of each computed spectral difference.

features, a diagonally elongated lineshape corresponding to the relaxation of HOD molecules moving in a slowed D_2O bath and a broad feature that has moved across the frequency range probed by our excitation pulses within a few tens of femtoseconds. Given that the fast relaxation of the off-diagonal intensity of the 2D data occurs on a time

scale similar to that observed in the pump-probe measurements in Fig. 6-2, these two spectral features appear to have a common origin.

We can attempt to isolate the lineshape associated with the rapidly decaying spectral feature by trying to remove the contribution to the spectra due to the relaxation of HOD/D_2O through the calculation of difference spectra between data recorded for $NaOD/D_2O$ and neat D_2O solution. Since we want to isolate the spectral features associated with the rapid decay observed in the pump-probe measurement, each 2D IR data set for a given NaOD concentration was normalized to the peak of the dispersed pump-probe measurement at $\tau_2 = 200$ fs before subtraction. By this waiting time, the 110 fs feature in the pump-probe spectra has largely disappeared, leaving only the response of the remaining system. Fig. 6-7C plots difference spectra calculated at two waiting times, 60 and 200 fs. At all concentrations, the calculated difference spectra at a given waiting time appear similar, but with decreasing signal-to-noise as the NaOD concentration lessens and the spectral differences between the spectra for NaOD solution and D_2O become small. At $\tau_2 = 200$ fs, we find that the intensity of the NaOD 2D spectra is increased relative to D_2O along the diagonal axis, but decreased in the regions above and below the diagonal. A difference spectrum of this type is what we would assume for the subtraction of a homogenous 2D lineshape from a diagonally elongated inhomogeneous lineshape. The difference spectrum at this waiting time simply indicates the slowing of the average dynamics of the water bath observed in both the peak shift measurement and the spectral diffusion metrics calculated from the 2D spectra.

At $\tau_2 = 60$ fs, the difference spectra appear qualitatively different. Positive intensity appears throughout the majority of the pictured spectral range and supports our

hypothesis that a subset of the O-H oscillators in the system rapidly samples the 3 μm frequency range. The small negative features that appear in the difference spectra can be explained by noting that the difference spectra at τ_2 = 200 fs shows that the remaining response of the system cannot be properly subtracted due to the slowing of the system dynamics with increasing concentration. The difference spectra at τ_2 = 60 fs are then a superposition of the difference observed at τ_2 = 200 fs and a broad feature that absorbs across the entire plotted frequency region.

Different scenarios can be put forth that can explain the existence of this rapidly decaying spectral feature. A fast decay component has previously been observed in IR transient hole burning measurements of isotopically dilute hydroxide solutions.[30] The authors of that report hypothesized that as a deuterium atom is transferred back and forth between an OD^- ion and a D_2O molecule, the hydrogen bonds of the remaining spectator water molecules in the OD^- solvation shell will be rapidly modulated, leading to the observed relaxation. A second explanation is that the spectral feature arises from transferring protons themselves as the O-H stretching potential flattens during proton transfer, causing a large decrease in ω_{OH}. Such spectral evolution of shared protons has been invoked as an explanation for the absorption continua in IR spectra of strong acids and bases.[7] Another explanation recognizes that as the O-H stretching potential broadens during proton transfer, transitions from the ground state to higher lying vibrational states can move into resonance with the probing pulses. A continuum of rapidly evolving structures with different proton potentials will allow a continuum of excitation pathways involving these states to contribute to the measured 2D IR spectra. This creates the possibility for excitation pathways involving vibrational overtone transitions that are

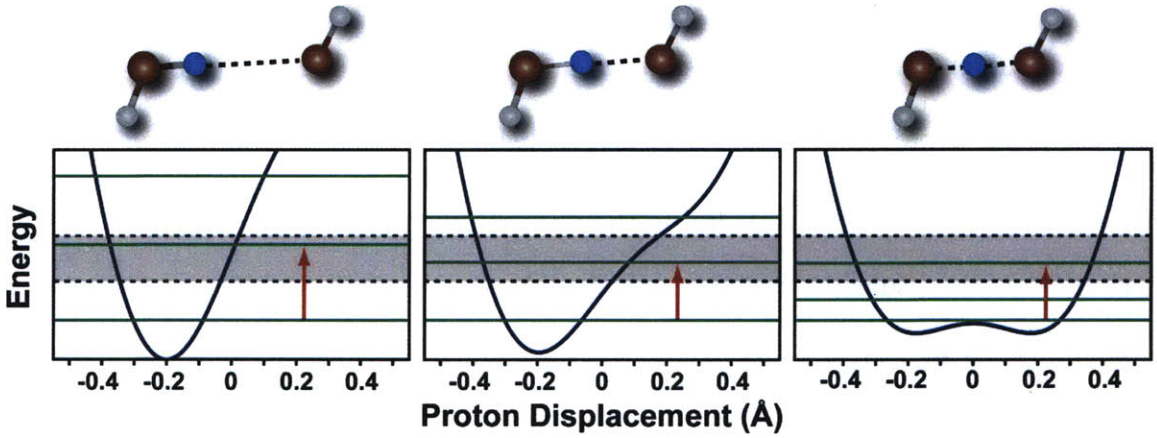


Figure 6-8: Cartoon illustrating how the eigenstates of the O-H stretching potential shift leading up to a proton transfer event. For a well localized proton (left) only the v = 1←0 transition is expected to fall with the spectral bandwidth of the excitation pulses (grey shaded region). As the proton potential broadens as the proton becomes delocalized, the v = 1←0 transition exits the experimentally probed frequency region and the v = 2←0 transition can move into the bandwidth of the excitation pulses.

traditionally neglected in the calculation of nonlinear vibrational spectra to contribute to the experimental 2D data.

In Fig. 6-8 we plot a series of one-dimensional O-H stretching potentials that serve as an illustrative example of this last possibility. Each of the pictured 1D potentials is plotted so that the energy of the lowest eigenstate of the system is the same and the shaded grey region of each plot represents the frequency region accessible by our experiments. The O-H stretching potential pictured on the left represents a HOD molecule that participates in a weak hydrogen bond with a deuteroxide ion. The proton is localized on the HOD molecule and we expect only the v = 1←0 transition to be resonant with our excitation pulses. As the proton becomes more equally shared with the OD^- ion, the v = 1←0 transition will gradually red shift and in the extreme case of an equally shared proton pictured on the right, this transition will exit our experimentally accessible frequency region. However, as this occurs other transitions of the potential can move

into the bandwidth of the excitation pulses, such as the v = 2←0 transition in the case pictured. Given that v = 2←0 transition of the shared proton stretch of the $H_3O_2^-$ ion in the gas phase is predicted to appear as low as 1718 cm^{-1} for an equally shared proton,[56] and that a nonlinear scaling of the O-H transition dipole with frequency is known to occur,[57,58] it is reasonable that overtone transitions of such Zundel-like species absorb strongly in the frequency range of our experiments. Rapid fluctuation of the stretching potential can then lead to contributions to the signal that arise from a sequence of v = 1←0 and v = 2←0 excitations during the short period over which the proton is delocalized.

In Chapter 7 we will present 2D IR spectra calculated from an MS-EVB simulation of aqueous hydroxide that lend support to this hypothesis. The rapid decay observed in both the measured pump-probe and 2D IR spectra can be explained through the inclusion of excitation pathways that involve overtone transitions of Zundel-like states.[32] The rapid modulation of the O-H potential that occurs during the course of proton transfer causes the frequencies of these transitions to sweep through a large frequency range within a few 10s of fs, thereby yielding the broad lineshapes observed experimentally. Since these excitation pathways are only accessible when a proton is delocalized within a $DO{\cdot\cdot}H{\cdot\cdot}OD^-$ complex, the 110 fs time scale that we measure in pump-probe experiments corresponds to the time needed for the proton potential to shift in such a way as to localize the proton on either of the two oxygen atoms of the complex.

6.5. Signatures of Chemical Exchange Processes in 2D IR Spectra

Although we now possess a qualitative explanation for the rapidly decaying feature that appears in our measurements at short waiting times, the process that leads to

the decay of the echo peakshift at a waiting time near 2 ps is still unclear. To further investigate the origin of this relaxation process, we carried out 2D IR measurements for waiting times up to 10 ps and a subset of these spectra are displayed in Fig. 6-9.

Examining the spectra recorded for HOD in D_2O, at τ_2 = 1 ps, we find that the nodal line separating the v = 1←0 and v = 2←1 transitions has rotated to be nearly parallel to the ω_1 axis, indicating that spectral diffusion is largely complete by this waiting time. As τ_2 increases further, the negative peak corresponding to the v = 2←1 transition disappears from the 2D spectrum. The loss of this transition can be attributed to the vibrational relaxation of the v = 1←0 transition that occurs on a 710 fs time scale and the corresponding rise of the "hot ground state" absorption described near the end of Section 6-3. Upon vibrational relaxation, energy deposited in the O-H stretching transition of a HOD molecule is passed to other modes of the system and eventually reaches the low frequency modes of the surrounding bath molecules. The excitation of these bath modes makes the system appear as if it is heated, which slightly decreases the degree of hydrogen bonding in the system and shifts the O-H lineshape to higher frequency as a result. This spectral shift prevents the ground state hole formed by the excitation pulses from refilling upon vibrational relaxation, and gives rise to a long lasting bleaching signal.[44,50-53] The calculation of 2D IR spectra of HOD/D_2O for waiting times well past the vibrational lifetime of the O-H stretch have shown that measured spectra can be well reproduced by a decorrelated 2D lineshape that when projected onto the ω_1 axis approximates the linear absorption spectrum of the O-H stretch, and resembles the difference of the linear absorption spectrum recorded at room temperature and a temperature elevated by 1-2 °C when projected along the ω_3 axis.[51,53,59]

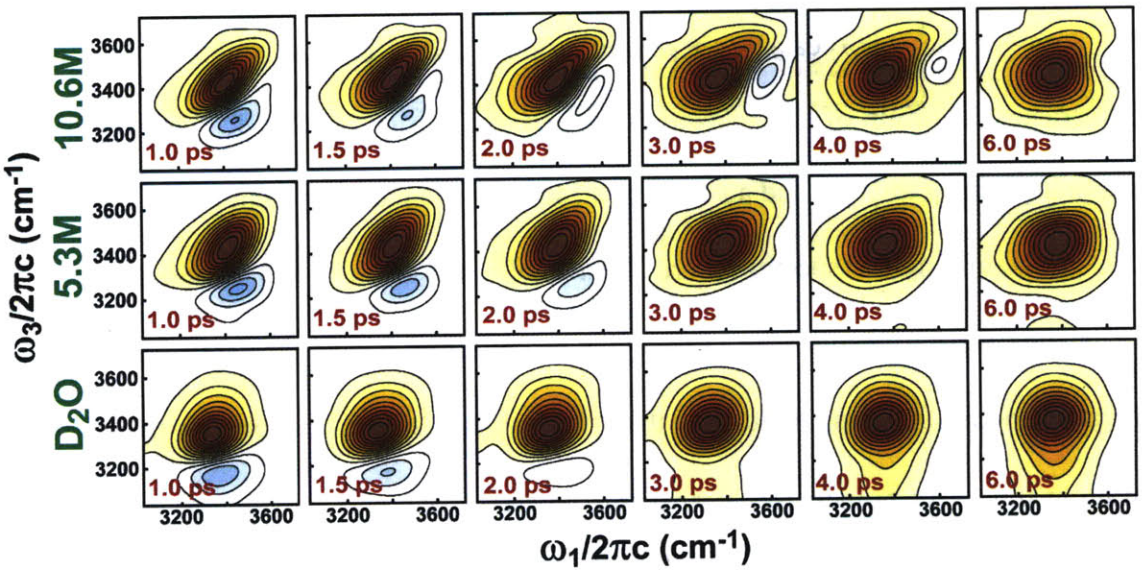


Figure 6-9: 2D IR spectra for 10.6 M NaOD, 5.3 M NaOD, and neat HOD/D_2O for waiting times between 1 ps and 6 ps. Over this range of waiting times, 2D spectra of HOD/D_2O simply display signatures of non-equilibrium heating. Spectra for NaOD solution show similar signatures of heating, but are also suggestive of exchange between the free OH^- stretch near 3600 cm^{-1} and the main HOD/D_2O absorption band near 3400 cm^{-1}.

In the 2D spectra measured for 10.6 M NaOD solution, we observe spectral changes that are consistent with the disappearance of the v = 2←1 transition due to vibrational relaxation, but with a few important differences with respect to the spectra recorded for neat D_2O. As the v = 2←1 transition disappears due to the growth of the hot ground state, we observe a shift of negative amplitude along the direction of the diagonal axis to frequencies near 3600 cm^{-1} along the ω_1 axis. This is most prominently seen in the 2D spectra for τ_2 = 3 ps, where only a small negative peak is observed below the diagonal axis at ω_1 = 3600 cm^{-1}/ω_3 = 3450 cm^{-1}. This frequency region along the ω_1 axis is indicative of the free OH^- stretch that appears in the FT-IR spectra in Fig. 6-1. The persistence of the photoinduced absorption of the OH^- v = 2←1 transition beyond the appearance of the hot ground state absorption at lower frequency suggests that the

vibrational lifetime of the OH^- stretch is longer than the 710 fs lifetime of the O-H stretch of HOD dissolved in D_2O. This result is not unexpected since the main pathway for the vibrational relaxation of the O-H stretch of the HOD molecule is believed to be intramolecular in origin and involves the transfer of energy from the O-H stretch to the molecule's first bending overtone.[60,61] Since the OH^- ion possesses no vibrational modes other than its stretch, it can only undergo vibrational relaxation through intermolecular pathways. Vibrational lifetimes for similar diatomic molecules in D_2O that undergo relaxation by intermolecular energy transfer can be quite slow, reaching time scales as long as 71 ps in the case of the CN^- ion.[62] Given the low density of high frequency acceptor modes present in an isotopically dilute solution of HOD/NaOD, we expect the vibrational lifetime of the OH^- ion in these solutions to be longer than that of the HOD molecule.

Additional examination of the 2D spectrum of 10.6 M NaOD at a waiting time of 3 ps shows the growth of a new positive spectral feature below the negative $v = 2 \leftarrow 1$ peak of the OH^- stretch at $\omega_1 = 3600\ cm^{-1}/\omega_3 = 3300\ cm^{-1}$. The appearance of this positive spectral feature is reflected above the diagonal axis by an intensification of the ridge extending away from the diagonal axis along $\omega_3 = 3600\ cm^{-1}$. Both of these spectral features are found to increase with waiting time and are suggestive of the growth of a cross peak between the free OH^- stretch at $3600\ cm^{-1}$ and the main HOD/D_2O absorption band near $3400\ cm^{-1}$. The growth of such a peak would indicate an exchange process wherein an OH^- ion accepts a deuteron from a hydrogen bonded D_2O molecule to form HOD and the reverse process whereby a HOD molecule donates its deuteron to a nearby OD^- ion. In each case, the solvation of the newly formed species will lead to a

shift of their vibrational frequencies, giving rise to a cross peak in the 2D IR spectrum that appears over the characteristic time scale of the exchange process.

To highlight the growth of this cross peak feature, we have calculated difference spectra of the 2D surfaces measured for 10.6 M NaOD and D_2O solutions (Fig. 6-10A).[†] At a waiting time of 600 fs, we see that the 10.6 M NaOD data is more intense along the diagonal axis between 3300 and 3600 cm^{-1}, which reflects both the presence of the OH^- absorption near 3600 cm^{-1} and the fact that spectral diffusion slows with increasing NaOD concentration. Near a waiting time of 2 ps, we see a ridge beginning to extend horizontally along the ω_1 axis at ω_3 = 3600 cm^{-1} that strengthens with waiting time. Likewise, as τ_2 increases we gradually observe a change in the region below the diagonal at ω_1 = 3600 cm^{-1} from negative to positive, consistent with the appearance of a new peak. Due to interference with the v = 2←1 transition, the growth of the off-diagonal intensity below the diagonal axis does not have the same asymptotic limit as that found above the diagonal axis. Nevertheless, the growth of intensity in both off-diagonal regions can be well described by a rising exponential with a time constant of 1.9 ps. This time scale is similar to the delay time at which the echo peak shift measurement in Fig. 6-5 is observed to have completed its decay, and suggests that the decay of the peak shift may be the result of the appearance of cross peaks in the 2D spectra.

However, before any definitive conclusions can be reached concerning the appearance of new peaks in the 2D spectra over this range of waiting times, we must first

[†] To best remove the contributions to the difference spectra due to HOD molecules interacting with D_2O, each measured 2D spectrum was convolved with the band-pass filter used in the pump-probe measurements along the ω_3 axis and the result was integrated to approximate the pump-probe signal from each sample. The 10.6 M NaOD data set was then scaled by a single multiplicative constant to make the long time decay of its calculated pump-probe signal match that calculated from the HOD/D_2O spectra before subtraction to give the difference spectra in Fig. 6-10.

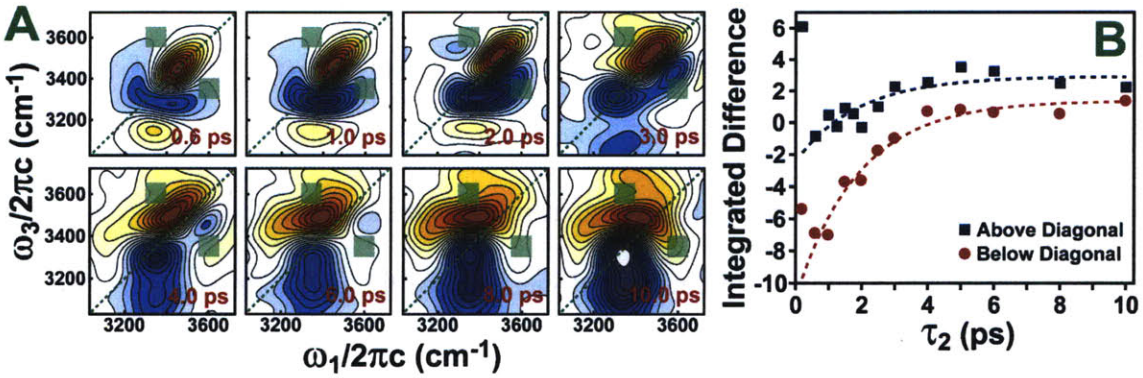


Figure 6-10: (A) Difference 2D IR spectra of HOD in 10.6 M NaOD and D_2O. (B) Plots of the integrated difference in the off-diagonal regions highlighted by the shaded green squares above and below the diagonal axis (ω_1 = 3300 – 3400 cm^{-1}, ω_3 = 3550 – 3600 cm^{-1} and its reflection about the diagonal). The growth of excess intensity in these regions can be well described by an exponential function with a 1.9 ps time constant.

determine how the non-equilibrium heating effects that greatly alter the spectra of neat HOD/D_2O affect the 2D spectra of NaOD solutions. The growth of a decorrelated "hot ground state" absorption may create spectral features that resemble exchange cross peaks. Additionally, given that we expect the O-H stretch of HOD and the free hydroxide ion stretch to have different vibrational lifetimes, it is not clear how the growth of intensity displayed in Fig. 6-10B is related to the exchange time scale between these two types of hydride stretches. To account for how each of these effects influence our measured spectra, we apply a fitting model that accounts for the varying population relaxation of different hydride species, their exchange, and the effects of non-equilibrium heating. This model can adequately reproduce our measured FT-IR, pump-probe, echo peak shift, and 2D IR data, and allows us to estimate a lower bound for the exchange of the free OH^- stretch and the main HOD absorption band due to proton transfer.

6.6. Treatment of Chemical Exchange in 2D IR Lineshapes

Chemical exchange refers to a process by which two states of a system interconvert with one another under equilibrium conditions. Many processes that occur in liquid solution at room temperature, such as molecular isomerization,[63] the transport of protons, and the migration of molecules into and out of the solvation shell of a solute[64] can be viewed as chemical exchange reactions. 2D IR spectroscopy can be used to deduce the time scale over which an exchange process occurs by measuring the growth of cross peaks between vibrational modes that correspond to the initial and final states of the exchange reaction.[64-66] A schematic illustration of 2D spectra indicating the presence of chemical exchange appears in Fig. 6-11A. In this example, a molecule undergoes an exchange process that converts it from state "*a*" to state "*b*". The exchange causes a corresponding shift in the frequency of one of its vibrations, changing it from "ω_a" to "ω_b". At $\tau_2 = 0$, no exchange has yet occurred, and the 2D IR spectrum simply contains the diagonal peaks corresponding to the inhomogeneously broadened ω_a and ω_b transitions. As the waiting time increases past the characteristic exchange time scale for states *a* and *b*, cross peaks appear between the two diagonal peaks, indicating the exchange. The intensities of the diagonal peaks that appear at ω_a and ω_b are related to the vibrationally excited populations of *a* and *b* respectively, whereas the intensities of the cross peaks are related to the excited population that exchanges between these two states.

Fig. 6-11B displays an example calculation of how each of these excited populations vary as a function of time. In the case of the diagonal peaks, the excited populations in *a* and *b* simply decrease with increasing τ_2 due to vibrational relaxation. As τ_2 increases and exchange is allowed to proceed, the number of excited molecules that

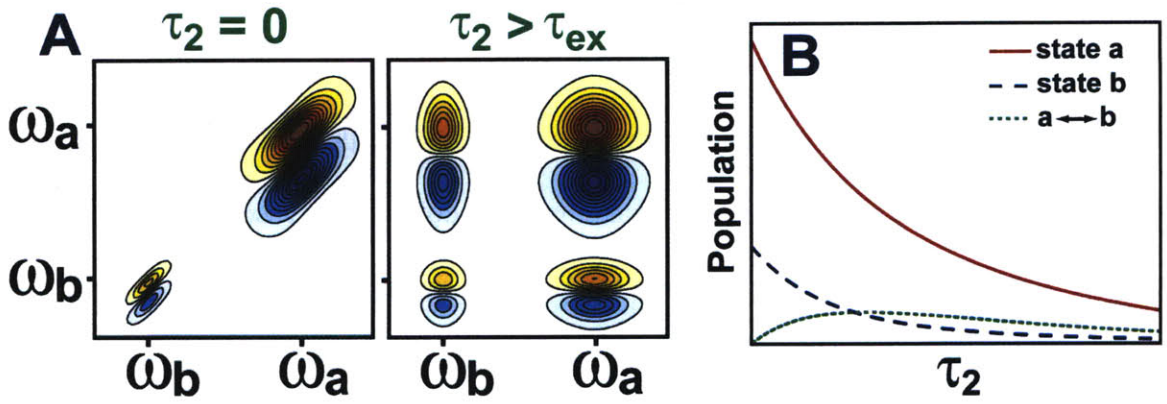


Figure 6-11: (A) Schematic illustration of chemical exchange in 2D IR lineshapes. As the waiting time increases past the time scale over which a molecule in state "a" converts to a state "b" (τ_{ex}), cross peaks appear between the vibrational transitions associated with these two states. (B) Cartoon showing the vibrational excited populations in state *a*, state *b*, and that which has interchanged between the two states as a function of waiting time.

have exchanged from $a \rightarrow b$ builds, but as τ_2 increases further this population gradually decays due to vibrational relaxation. The time scale for the growth of the cross peak represents a competition between the vibrational lifetimes of *a* and *b* and the exchange rate between these transitions. In the case that the vibrational lifetimes of the two exchanging transitions are much longer than the exchange rate of these transitions, the exchange time scale may be estimated from a simple fitting of the amplitude of the exchange peaks, but more generally a modeling of the behavior of the full 2D spectrum as a function of τ_2 is needed to properly determine the exchange time scale.[67] Since the exchange process occurs at chemical equilibrium, detailed balance dictates that an equal number of molecules exchange from state $a \rightarrow b$ and from state $b \rightarrow a$. This causes the cross peaks that appear in the 2D spectra to be equal in intensity.

Recently, theoretical methods[67,68] have been developed that allow a description of chemical exchange processes to be incorporated into the commonly used perturbative, semi-classical modeling formalism of 2D IR spectra within the context of the Condon

and second Cumulant approximations.[‡] These two approximations neglect the variation of the O-H transition dipole with vibrational frequency and asymmetries that appear in the shape of peaks of the 2D spectrum respectively. While the results of the previous chapter have stressed that these approximations break down in the case of HOD/D_2O, by making these two approximations, we can use our experimental data to extract an exchange time scale between the free OH^- stretch and the main HOD/D_2O vibrational transition. Following the formalism outlined in Ref. 67, we can describe exchange between the two states of our example, *a* and *b*, according to the reaction scheme:

$$\overset{T_1^a}{\leftarrow} a \underset{k_{b\to a}}{\overset{k_{a\to b}}{\rightleftharpoons}} b \overset{T_1^b}{\rightarrow} \tag{6-1}$$

where $k_{a\to b}$ denotes the rate constant for exchange from $a \rightarrow b$ and T_1^a denotes the vibrational lifetime of state *a*. The left and right pointing arrows represent vibrational relaxation which leads to a decrease of all peaks in the 2D spectrum, and is explicitly included in this model.

Since 2D IR experiments are performed using polarized excitation fields, orientational relaxation can rotate molecules out of the plane of the excitation fields and also cause a decrease in the intensity of features in the 2D spectrum.[69] Orientational relaxation of the O-H stretch of HOD in D_2O can be well described by a bi-exponential decay, involving a small, rapid 50 fs component due to librational motion which gives way to a 3 ps decay that describes the diffusive reorientation of the HOD molecule and hydrogen bond exchange events.[44,70] Given that this 3 ps time scale is much longer than those associated with both spectral diffusion and vibrational relaxation, the contribution

[‡] A description of the calculation of 2D IR spectra within these two approximations is given in detail in Section 2.4.2 of Chapter 2.

to the third-order response due to orientation was found to be small on time scales longer than 100 fs.[71] Furthermore, for 10 M NaOD solution, pump-probe anisotropy measurements have shown that no detectable orientational relaxation occurs within the first 1.7 ps following vibrational excitation.[30] Since we are primarily interested in exchange processes that occur in this concentration regime, we will make the simplifying assumption that the orientational contribution to the third-order response can be neglected. Note, this does not necessarily mean that we assume that reorientation does not play a role in the solvation of new species formed during the course of proton transport. Molecular dynamics simulations have recently shown that large, rapid rotations of water molecules plays a role in the migration of water molecules into and out of the solvation shell of the Cl^- anion.[72] The change in the size of the hydroxide ion's solvation shell that is believed to play a role in guiding the transport of the ion[19,20] necessitates the reorientation of molecules as they enter and leave the solvation shell. We are simply neglecting the line broadening processes that are due to the reorientation of the frame of each excited molecule.

For the reaction scheme given in Eq. 6-1, it is possible to derive the following expressions for the populations of vibrationally excited molecules in state *a* (N_a), state *b* (N_b), and those that have transferred from *a* → *b* ($N_{a\to b}$) and from *b* → *a* ($N_{b\to a}$):[67]

$$\begin{aligned} N_a(t) &= N_a(0)e^{-\alpha t}\left(\cosh(\beta t)-\gamma\sinh(\beta t)\right) \\ N_b(t) &= N_b(0)e^{-\alpha t}\left(\cosh(\beta t)+\gamma\sinh(\beta t)\right) \\ N_{a\to b}(t) &= N_a(0)\frac{k_{a\to b}}{\beta}e^{-\alpha t}\sinh(\beta t) \\ N_{b\to a}(t) &= N_b(0)\frac{k_{b\to a}}{\beta}e^{-\alpha t}\sinh(\beta t) \end{aligned} \qquad (6\text{-}2)$$

where the parameters α, β, and γ are given by:

$$\alpha = \frac{k_{a\to b} + k_{b\to a} + 1/T_1^a + 1/T_1^b}{2}$$
$$\beta = \sqrt{\alpha^2 - \left(1/T_1^a T_1^b + k_{a\to b}/T_1^b + k_{b\to a}/T_1^a\right)} \qquad (6\text{-}3)$$
$$\gamma = \frac{1/T_1^a - 1/T_1^b + k_{a\to b} - k_{b\to a}}{2\beta}.$$

As noted above, since the system is at chemical equilibrium the rate of transfer from *a* → *b* is related to that for transfer from *b* → *a* by detailed balance:

$$N_a(0)k_{a\to b} = N_b(0)k_{b\to a}. \qquad (6\text{-}4)$$

Feynman diagrams that describe each of the excitation pathways relevant to chemical exchange appear in Fig. 6-12. Each of the pictured pathways begins with a molecule initially in state *a* that then undergoes exchange during the waiting time. An equivalent set of Feynman pathways can be drawn for molecules that are in state *b* at the start of the experiment. During the waiting time, a molecule can participate in multiple exchange events, and only molecules that undergo an odd number of exchanges will contribute to the formation of cross peak in the 2D spectrum. The diagrams that appear on the left side of Fig. 6-12 describe the rephasing and nonrephasing pathways that correspond to these successful exchange events. Molecules that instead participate in an even number of exchanges will contribute to the diagonal peaks of the 2D spectrum (right side of Fig. 6-12) since they have returned to state *a* by the end of τ_2. Of course, exchange can also take place during the two coherence periods, τ_1 and τ_3, but these periods are often quite short compared to the time scale over which exchange processes are expected to occur. Given that the echo signal of the O-H stretch finishes its decay by (τ_1, τ_3) = 250 fs and we are interested in exchange processes that occur on picosecond or longer time scales, in our modeling we neglect exchange that may occur during the

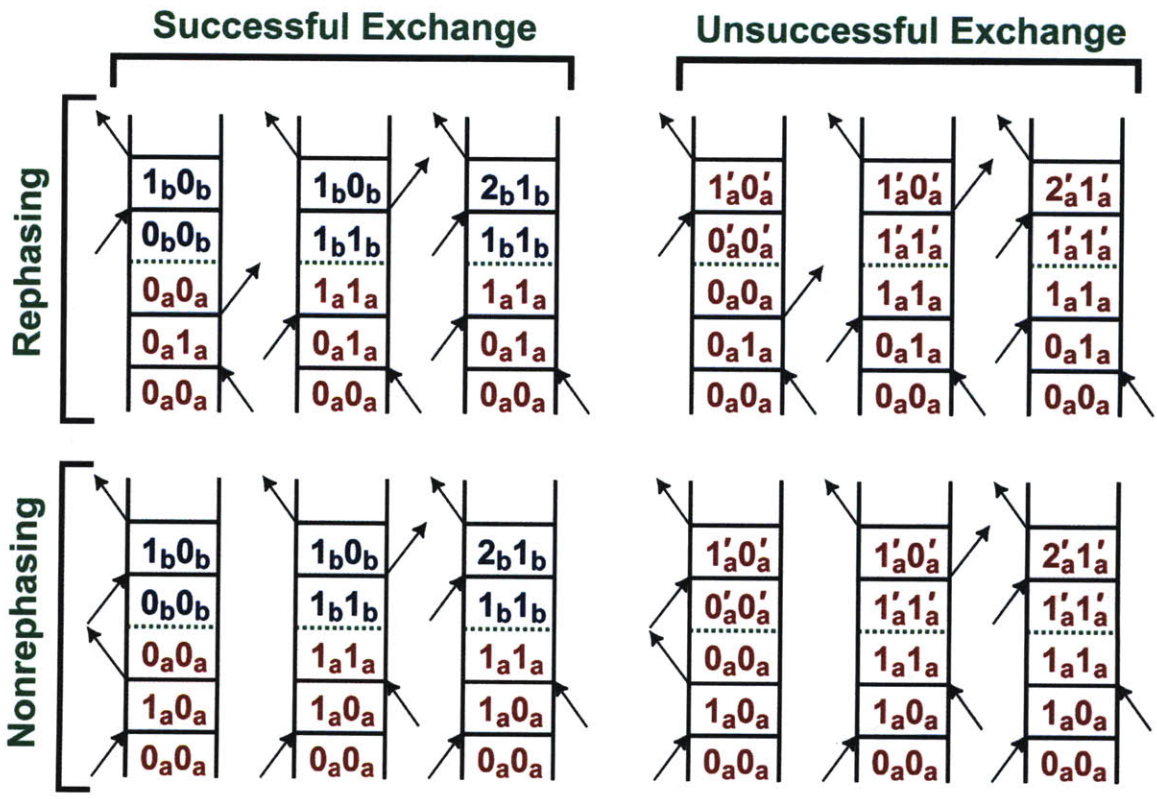


Figure 6-12: Feynman pathways describing chemical exchange. In each diagram, the dotted green line that appears during τ_2 denotes a series of exchange events. In the diagrams labeled successful exchange, an odd number of exchanges occur, resulting in a net conversion of $a \rightarrow b$. Conversely, the diagrams on the right describe instances where an even number of exchange events occur, which result in the loss of correlation of transitions appearing along the diagonal axis.

coherence periods.

In the formalism set forth by Kwak et al.[67] an additional assumption is made that the frequency fluctuations of state *b* are not correlated with those of state *a*. Under this assumption, dynamics that occur during the waiting time are ignored, and peaks that appear due to exchange are simply equivalent to the product of the one dimensional lineshapes associated with ω_a and ω_b. The validity of this assumption in the system described here is questionable. The difference in frequency between the O-H stretches of a HOD molecule hydrogen bonded to D_2O and an OH^- ion comes about due to the fact

that these two types of O-H bonds possess different hydrogen bonding configurations. After an OH^- ion accepts a deuteron from a hydrogen bonded partner, the decrease of its O-H stretching frequency will be induced by changes in the organization of the D_2O molecules in its first solvation shell, and may involve the formation of a hydrogen bond to the newly formed HOD molecule. These solvation processes can occur on a time scale that is long enough as to invalidate the assumption of an instantaneous jump in frequency upon chemical exchange. However, in the absence of a better theory for the calculation of 2D lineshapes using a simplistic fitting model, we will make this assumption and note where its breakdown may influence the results of the model calculations.

6.7. Model of Chemical Exchange in Isotopically Dilute Deuteroxide Solution

With the ability to model exchange between two vibrational transitions in hand, we can begin to build a spectral model for proton transfer in isotopically dilute deuteroxide solutions. Since our nonlinear experiments primarily focus on vibrational transitions that appear in the spectral region centered near 3 μm, we will only include O-H vibrations in our model that appear in this frequency range. Examining the FT-IR spectra in Fig. 6-1, we can identify three spectral features that correspond to different types of O-H oscillators. The deuteroxide free spectrum shows that HOD molecules hydrogen bonded to D_2O primarily absorb near 3400 cm^{-1} (ω_W). As NaOD is added to the system, we see the appearance of the free OH^- absorption near 3600 cm^{-1} (ω_{Ion}) and the growth of a broad continuum absorption to the red side of the O-H stretch due to HOD molecules that donate a hydrogen bond to OD^- ions (ω_{Sol}). We will attempt to model each of our experiments by assuming that these three different types of O-H

species each give rise to a separate peak in the linear absorption spectrum and that exchange between a subset of these species can be observed in 2D IR experiments.

Fig. 6-13 displays exchange processes that may be observed in 2D IR experiments. In Fig. 6-13A, a proton is transferred from a HOD molecule to an OD^- ion, forming a new HOD molecule. While the $v = 1 \leftarrow 0$ transition associated with this shared proton state absorbs at low frequency, outside of the range of our experiments, overtone transitions of shared proton states can make a strong contribution to the third-order signal (See Chapter 7). Our spectral model must account for the transient signal that arises from these configurations at short waiting times. Fig. 6-13B shows an example of an exchange event where the deuterium atom of a HOD molecule is passed to an OD^- ion, creating a new OH^- ion. Exchange of this type will result in a cross peak between ω_W and ω_{Ion} and will be accounted for in our model. In Fig. 6-13C we see an exchange scenario that would lead to a cross peak between ω_{Sol} and ω_W, wherein a HOD molecule hydrogen bonded to an OD^- ion breaks its hydrogen bond and migrates out of the OD^- solvation shell. While a cross peak is expected to appear due to this process, given that the majority of our experimental data was recorded using excitation pulses tuned in closer resonance with ω_W and ω_{Ion}, we expect this process to make minimal contributions to our measurements and neglect exchange of this type in our analysis. Lastly, Fig. 6-13D pictures an exchange process involving two separate OD^- ions that we only expect to take place at high concentration, but would lead to a cross peak between ω_{Sol} and ω_{Ion}. In this process a HOD molecule forms hydrogen bonds to two OD^- ions, and the transfer of the HOD molecule's deuterium atom results in the formation of a new OH^- ion. However, since we expect exchange of this type to occur only at high concentration and given that

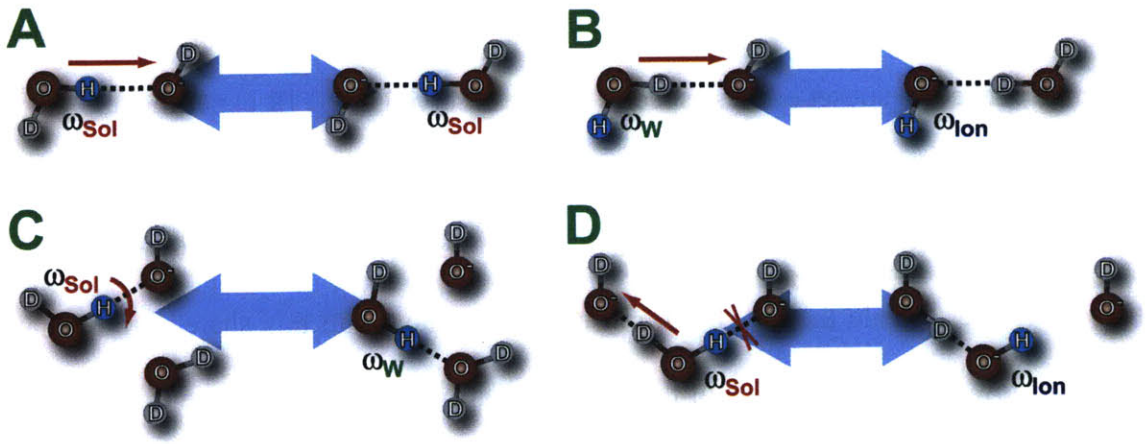


Figure 6-13: Different types of exchange processes that can contribute to 2D IR spectra. Only processes of the type pictured in A and B are included within our spectral model.

our excitation pulses were centered on ω_W and ω_{Ion} to better view exchange between these transitions, we will not include exchange of the type pictured in Fig 6-13D in our model.

We begin our description of the third-order response, S^{Total}, by writing it as a sum of three separate terms:

$$S^{Total} = S^{Diag} + S^{Cross} + S^{Therm}. \tag{6-5}$$

S^{diag} denotes the diagonal contributions to ω_W, ω_{Ion}, and ω_{Sol} and the transient signature of Zundel-like configurations that appears at short waiting times. The diagonal contributions to ω_W and ω_{Ion} are further subdivided among molecules that do not engage in exchange during τ_2 ($S^{W,S}$ and $S^{Ion,S}$, Eq. 6-9) and those that engage in an even number of exchange events ($S^{W,Ex}$ and $S^{Ion,Ex}$, Eq. 6-14):

$$S^{Diag} = S^{W,S} + S^{Ion,S} + S^{W,Ex} + S^{Ion,Ex} + S^{Sol} + S^{Zundel}. \tag{6-6}$$

S^{cross} contains the contributions to the nonlinear response from successful exchange events between ω_{Ion} and ω_W that give rise to cross peaks between these two transitions in the 2D spectra (Eq. 6-13):

$$S^{Cross} = S^{W \to Ion} + S^{Ion \to W}. \tag{6-7}$$

Finally, S^{therm} describes the thermal redistribution of energy within the sample upon vibrational relaxation:

$$S^{therm} = S^{W,Therm} + S^{Ion,Therm} + S^{Sol,Therm} + S^{Therm}_{D_2O}. \tag{6-8}$$

In Eq. 6-8, $S^{W,Therm}$, $S^{Ion,Therm}$, and $S^{Sol,Therm}$ each describe long lived ground state bleaches that are related to the vibrational relaxation of ω_W, ω_{Ion}, and ω_{Sol} (Eq. 6-15), while $S^{Therm}_{D_2O}$ describes a thermal signal generated by the D_2O bath (Eq. 6-17).[52,53] In each of the following subsections, we will provide expressions for each of the terms in Eq. 6-6 through 6-8 and provide a description of the methodology we used to determine each of the unknown parameters that appear in each term.

6.7.1. Treatment of Diagonal and Exchange Cross Peaks

The expressions that we employ for the diagonal peaks due to ω_W, ω_{Ion}, and ω_{Sol} in the absence of exchange are derived from the expressions for the third-order response given in Section 2.4.2 of Chapter 2, and allow us to calculate 2D lineshapes using a frequency-frequency correlation function for each transition. These correlation functions will serve as a set of fitting parameters that will be optimized to match the experimental data. For ω_W, the rephasing and nonrephasing contributions to the third-order response can be calculated by evaluating the sum in Eq. 2-25 over the set of S_I and S_{II} diagrams that appear in Fig. 2-7, giving the result:

$$
\begin{aligned}
S_R^{W,S}(t_3,t_2,t_1) &= \left|\mu_{10}^W\right|^4 N_W^S(t_2)\exp\left[i\left\langle\omega_{10}^W\right\rangle t_1 - i\left\langle\omega_{10}^W\right\rangle t_3 - (t_1+t_3)/2T_1^W\right] \\
&\times\left(F_{0101}^{(3)W}(t_3,t_2,t_1)+F_{0101}^{(4)W}(t_3,t_2,t_1)\right)-\left|\mu_{21}^W\right|^2\left|\mu_{10}^W\right|^2 N_W^S(t_2) \\
&\times\exp\left[i\left\langle\omega_{10}^W\right\rangle t_1 - i\left\langle\omega_{21}^W\right\rangle t_3 - (t_1+3t_3)/2T_1^W\right]F_{0121}^{(2)W}(t_3,t_2,t_1) \\
S_{NR}^{W,S}(t_3,t_2,t_1) &= \left|\mu_{10}^W\right|^4 N_W^S(t_2)\exp\left[-i\left\langle\omega_{10}^W\right\rangle t_1 - i\left\langle\omega_{10}^W\right\rangle t_3 - (t_1+t_3)/2T_1^W\right] \\
&\times\left(F_{0101}^{(1)W}(t_3,t_2,t_1)+F_{0101}^{(2)W}(t_3,t_2,t_1)\right)-\left|\mu_{21}^W\right|^2\left|\mu_{10}^W\right|^2 N_W^S(t_2) \\
&\times\exp\left[-i\left\langle\omega_{10}^W\right\rangle t_1 - i\left\langle\omega_{21}^W\right\rangle t_3 - (t_1+3t_3)/2T_1^W\right]F_{0121}^{(4)W}(t_3,t_2,t_1).
\end{aligned}
\tag{6-9}
$$

The definitions of the dephasing functions $F_{abcd}^{(n)}(t_3,t_2,t_1)$ are given in Eq. 2-26 of Chapter 2, $\{\mu_{10}, \mu_{21}\}$ and $\{\omega_{10}, \omega_{21}\}$ denote the transition dipole matrix elements and frequencies of the v = 1←0 and v = 2←1 transitions, and the superscript *W* denotes that each of these parameters correspond to HOD molecules hydrogen bonded to D_2O.[§] Expressions describing the behavior of the isolated diagonal peaks of ω_{Ion} and ω_{Sol} can be similarly written.

In Eq. 6-9 we have included the effects of population relaxation during the t_1 and t_3 time periods by assuming that relaxation during these coherence periods can be described as a superposition of the corresponding relaxation times for population states. Thus, defining $\Gamma_{11} = 1/T_1$, we have $\Gamma_{ab} = (\Gamma_{aa} + \Gamma_{bb})/2$.[44,73] We also assume that the relaxation time scales for higher lying vibrational excited states scale as a harmonic oscillator linearly coupled to a harmonic bath, $\Gamma_{aa} = a\Gamma_{11}$.[74,75] By using these scaling

[§] For consistency, in writing Eq. 6-4 we have adopted the notation of Chapter 2, and use the variables t_1, t_2, and t_3 to denote the time periods between each field matter interaction and the detection of the third-order signal. The variables τ_1, τ_2, and τ_3 denote the peak of each of the excitation pulses and local oscillator. In a real experiment, with finite duration pulses, these two sets of variables are not necessarily the same. However, for the model presented here, wherein we neglect the finite duration of the excitation pulses, these sets of indices are interchangeable.

relationships, we can describe the vibrational relaxation of ω_W, ω_{Ion}, and ω_{Sol} by specifying a single time scale for the relaxation of each transition.

Population relaxation during τ_2 is described through extension of the results given Eq. 6-2. In our model, chemical exchange is assumed to lead to a loss of frequency correlation, so the contribution to $N_a(t)$ and $N_b(t)$ in Eq. 6-2 from population that undergoes an even number of exchanges during t_2 must be determined. Kwak et al.[67] accomplish this by calculating $N_a(t)$ in the absence of any exchange by setting $k_{a\to b}$ to zero. The difference between the population of state a and $N_a(t)$ calculated with a nonzero value of $k_{a\to b}$ then gives the population that engages in multiple exchanges, $N_a^{Ex}(t) = N_a(t;k_{a\to b}=0) - N_a(t)$. Through the conservation of population, we can likewise determine the number of molecules that do not engage in any exchange events during t_2, $N_a^S(t) = N_a(t) - N_a^{Ex}(t)$.

Each of the dephasing functions that appear in Eq. 6-9 are comprised of a sum of integrals over a set of energy gap correlation functions (See Eq. 2-26):

$$h_{nm}(t) = \int_0^t d\tau_2 \int_0^{\tau_2} d\tau_1 C_{nm}(\tau_2 - \tau_1) \tag{6-10}$$

where:

$$C_{nm}(t - t_o) = \left\langle \delta\omega_{na}(t)\,\delta\omega_{ma}(t_o) \right\rangle. \tag{6-11}$$

To calculate each of the dephasing functions in Eq. 6-9, we must first specify a set of frequency-frequency correlation functions for ω_W, ω_{Ion}, and ω_{Sol}. To reduce the number of unique correlation functions that must be determined, we will assume that harmonic scaling relationships apply, which allows us to describe the fluctuations of high lying

vibrational states of a potential in terms of the fluctuations between the ground and first excited state: $C_{22}(t) = 2C_{21}(t) = 2C_{12}(t) = 4C_{11}(t) = 4C(t)$.[44,55] As a functional form for $C^{H}(t)$, $C^{W}(t)$, and $C^{Sol}(t)$, we will use a sum of two exponentially decaying functions, a static offset, and an underdamped oscillatory decay to account for the hydrogen bond oscillation that appears in the data at early delay times:

$$C(t) = \Delta_{static} + A_{fast}\exp\left[-t/\tau_{fast}\right] + A_{slow}\exp\left[-t/\tau_{slow}\right] + A_{osc}\exp\left[-t/\tau_{osc}\right]\left(\cos(\omega_{osc}t) + (\tau_{osc}/\omega_{osc})\sin(\omega_{osc}t)\right). \quad (6\text{-}12)$$

Since the hydroxide ion can only donate a weak hydrogen bond, we disregard the oscillatory component of $C(t)$ when describing the behavior of ω_{Ion}, and set $\cos(\omega_{osc}t) + (\tau_{osc}/\omega_{osc})\sin(\omega_{osc}t) = 1$. The choice of this functional form is motivated by our previous measurements on HOD/D_2O,[44] which used a similar functional form to model both pump-probe experiments and the decay of the photon echo peak shift.

By examining the Feynman diagrams in Fig. 6-12, we can write down contributions to the third-order response that correspond to exchange between ω_{Ion} and ω_W. The rephasing and nonrephasing contributions to the off-diagonal peaks for $\omega_{Ion} \rightarrow \omega_W$ are:

$$
\begin{aligned}
S_R^{Ion\to W}(t_3,t_2,t_1) &= \left|\boldsymbol{\mu}_{10}^{Ion}\right|^2\left|\boldsymbol{\mu}_{10}^{W}\right|^2 N_{Ion\to W}(t_2)\exp\left[i\left\langle\omega_{10}^{Ion}\right\rangle t_1 - i\left\langle\omega_{10}^{W}\right\rangle t_3 - t_1/2T_1^{Ion} - t_3/2T_1^{W}\right] \\
&\times\left(\exp\left[-h_{10}^{Ion*}(t_1) - h_{10}^{W}(t_3)\right] + \exp\left[-h_{10}^{Ion*}(t_1) - h_{10}^{W*}(t_3)\right]\right) \\
&-\left|\boldsymbol{\mu}_{21}^{W}\right|^2\left|\boldsymbol{\mu}_{10}^{Ion}\right|^2 N_{Ion\to W}(t_2)\exp\left[i\left\langle\omega_{10}^{Ion}\right\rangle t_1 - i\left\langle\omega_{21}^{W}\right\rangle t_3 - t_1/2T_1^{Ion} - 3t_3/2T_1^{W}\right] \\
&\times\exp\left[-h_{10}^{Ion*}(t_1) - h_{21}^{W}(t_3)\right] \\
S_{NR}^{Ion\to W}(t_3,t_2,t_1) &= \left|\boldsymbol{\mu}_{10}^{Ion}\right|^2\left|\boldsymbol{\mu}_{10}^{W}\right|^2 N_{Ion\to W}(t_2)\exp\left[-i\left\langle\omega_{10}^{Ion}\right\rangle t_1 - i\left\langle\omega_{10}^{W}\right\rangle t_3 - t_1/2T_1^{Ion} - t_3/2T_1^{W}\right] \\
&\times\left(\exp\left[-h_{10}^{Ion}(t_1) - h_{10}^{W}(t_3)\right] + \exp\left[-h_{10}^{Ion}(t_1) - h_{10}^{W*}(t_3)\right]\right) \\
&-\left|\boldsymbol{\mu}_{21}^{W}\right|^2\left|\boldsymbol{\mu}_{10}^{Ion}\right|^2 N_{Ion\to W}(t_2)\exp\left[-i\left\langle\omega_{10}^{Ion}\right\rangle t_1 - i\left\langle\omega_{21}^{W}\right\rangle t_3 - t_1/2T_1^{Ion} - 3t_3/2T_1^{W}\right] \\
&\times\exp\left[-h_{10}^{Ion}(t_1) - h_{21}^{W}(t_3)\right]
\end{aligned}
\tag{6-13}
$$

where the functions, $h_{nm}(t)$, are defined by Eq. 6-10. A similar set of expressions exist for the process $\omega_W \rightarrow \omega_{Ion}$. In writing Eq. 6-13, we make the assumption that the exchange process induces a loss of frequency correlation and Eq. 6-13 is simply related to the product of the linear absorption spectra of ω_{Ion} and ω_W. We can also write out the contribution to the ω_W diagonal peak due to molecules that participate in multiple exchange events, which are assumed to induce the loss of frequency correlation:

$$
\begin{aligned}
S_R^{W,Ex}(t_3,t_2,t_1) &= \left|\boldsymbol{\mu}_{10}^{W}\right|^4 N_W^{Ex}(t_2)\exp\left[i\left\langle\omega_{10}^{W}\right\rangle t_1 - i\left\langle\omega_{10}^{W}\right\rangle t_3 - (t_1+t_3)/2T_1^{W}\right] \\
&\times\left(\exp\left[-h_{10}^{W*}(t_1) - h_{10}^{W}(t_3)\right] + \exp\left[-h_{10}^{W*}(t_1) - h_{10}^{W*}(t_3)\right]\right) \\
&-\left|\boldsymbol{\mu}_{21}^{W}\right|^2\left|\boldsymbol{\mu}_{10}^{W}\right|^2 N_W^{Ex}(t_2)\exp\left[i\left\langle\omega_{10}^{W}\right\rangle t_1 - i\left\langle\omega_{21}^{W}\right\rangle t_3 - (t_1+3t_3)/2T_1^{W}\right] \\
&\times\exp\left[-h_{10}^{W*}(t_1) - h_{21}^{W}(t_3)\right] \\
S_{NR}^{W,Ex}(t_3,t_2,t_1) &= \left|\boldsymbol{\mu}_{10}^{W}\right|^4 N_W^{Ex}(t_2)\exp\left[-i\left\langle\omega_{10}^{W}\right\rangle t_1 - i\left\langle\omega_{10}^{W}\right\rangle t_3 - (t_1+t_3)/2T_1^{W}\right] \\
&\times\left(\exp\left[-h_{10}^{W}(t_1) - h_{10}^{W}(t_3)\right] + \exp\left[-h_{10}^{W}(t_1) - h_{10}^{W*}(t_3)\right]\right) \\
&-\left|\boldsymbol{\mu}_{21}^{W}\right|^2\left|\boldsymbol{\mu}_{10}^{W}\right|^2 N_W^{Ex}(t_2)\exp\left[-i\left\langle\omega_{10}^{W}\right\rangle t_1 - i\left\langle\omega_{21}^{W}\right\rangle t_3 - (t_1+3t_3)/2T_1^{W}\right] \\
&\times\exp\left[-h_{10}^{W}(t_1) - h_{21}^{W}(t_3)\right].
\end{aligned}
\tag{6-14}
$$

As with Eq. 6-13, a similar set of expressions for ω_{Ion} can be written based on Eq. 6-14.

To account for the broad, transient contribution to the experimental 2D IR data that we observe at early waiting times due to protons shared in a Zundel-like configuration, we include an additional transition along the diagonal axis that is centered at the same frequency as ω_W, and whose linewidth is set such that it covers the entire experimental frequency range:

$$\begin{aligned} S_R^{Zundel}(t_3,t_2,t_1) &= K_{Zundel}\exp\left[i\left\langle\omega_{10}^{Zundel}\right\rangle t_1 - i\left\langle\omega_{10}^{Zundel}\right\rangle t_3 - (t_1+2t_2+t_3)/2T_1^{Zundel}\right] \\ &\quad\times\left(F_{0101}^{(3)Zundel}(t_3,t_2,t_1)+F_{0101}^{(4)Zundel}(t_3,t_2,t_1)\right) \\ S_{NR}^{Zundel}(t_3,t_2,t_1) &= K_{Zundel}\exp\left[-i\left\langle\omega_{10}^{Zundel}\right\rangle t_1 - i\left\langle\omega_{10}^{Zundel}\right\rangle t_3 - (t_1+2t_2+t_3)/2T_1^{Zundel}\right] \\ &\quad\times\left(F_{0101}^{(1)Zundel}(t_3,t_2,t_1)+F_{0101}^{(2)Zundel}(t_3,t_2,t_1)\right). \end{aligned} \tag{6-15}$$

Since we do not know the number of transiently shared protons that contribute to this peak, we forgo the inclusion of an explicit transition dipole and number density in Eq. 6-15 and instead describe the intensity of this feature using an empirical scaling factor, K_{Zundel}, whose value is set based on the scaling between the relative contributions of the fast and slow components of the pump-probe signal (Fig. 6-2B). The frequency fluctuations of this transition are described using a single exponential decay with a time constant of 35 fs, as determined from our fits to the echo peak shift data (See Section 6.8.2).

We believe that the decay of this feature is due to the vibrational frequencies associated with a shared proton moving out of the bandwidth of our pump pulses as the proton forms a stable covalent bond. The decay of this feature is not necessarily related to population relaxation. However, no theoretical treatment yet exists for the calculation of broad, transient signals such as that which arises from Zundel-like configurations using a set of simple fitting parameters. The main purpose of this spectral model is to

provide an estimate of the time scale for the exchange of ω_{Ion} and ω_W, which we expect to have a value of a few picoseconds. To ensure that this feature does not contribute to the signal at delay times where chemical exchange is believed to occur, we input a relaxation time of 110 fs, consistent with our pump-probe measurements. This choice is purely one of convenience as it allows us to include a transient feature in our model so that we can match the behavior of the peak shift and pump-probe at short delay times. Our decision is not meant to mean that we believe the disappearance of S^{Zundel} is the result of population relaxation.

6.7.2. Treatment of Thermal Effects

We also include contributions to the signal that come about due to heating of the bath upon the relaxation of excited molecules. It has been shown that this thermalization effect results in a ground state bleach that persists over picosecond time scales.[44,51] The lineshape of this bleach resembles the linear absorption spectrum of the sample when projected along the ω_1 frequency axis and the difference of the linear absorption spectrum measured at room temperature and a temperature elevated by a few degrees when projected along the ω_3 frequency axis.[44,51-53] To describe this heating effect, we include the additional contribution to the response:

$$\begin{aligned} S_R^{W,Therm}(t_3,t_2,t_1) &= K_{therm}^W \left|\boldsymbol{\mu}_{10}^W\right|^4 N_W(0) N_{therm}^W(t_2) \exp\left[i\left\langle\omega_{10}^W\right\rangle t_1 - i\left\langle\omega_{10}^W\right\rangle t_3\right] \\ &\quad \times \exp\left[-h_{10}^{W*}(t_1) - h_{10}^W(t_3)\right]\left(1 - \left|\Delta\boldsymbol{\mu}_{10}^W\right|^2 \exp\left[-i\Delta\omega_3^W t_3\right]\right) \\ S_{NR}^{W,Therm}(t_3,t_2,t_1) &= K_{therm}^W \left|\boldsymbol{\mu}_{10}^W\right|^4 N_W(0) N_{therm}^W(t_2) \exp\left[-i\left\langle\omega_{10}^W\right\rangle t_1 - i\left\langle\omega_{10}^W\right\rangle t_3\right] \\ &\quad \times \exp\left[-h_{10}^W(t_1) - h_{10}^W(t_3)\right]\left(1 - \left|\Delta\boldsymbol{\mu}_{10}^W\right|^2 \exp\left[-i\Delta\omega_3^W t_3\right]\right). \end{aligned} \tag{6-16}$$

We also include analogous expressions for both ω_{Sol} and ω_{Ion} in our model. Eq. 6-16 represents a difference spectrum between the product of the linear absorption spectrum of ω_W multiplied along both the ω_1 and ω_3 axes and this same quantity which has been shifted by $\Delta\omega_3^W$ along the ω_3 axis and decreased in intensity by $\left|\Delta\boldsymbol{\mu}_{10}^W\right|^2$. These two fitting parameters are set such that the projection of the thermal response onto the ω_3 frequency axis at a waiting time of 10 ps matches the experimentally measured dispersed pump-probe signal. K_{therm} is an adjustable parameter that sets the intensity of the thermal signal relative to that of the resonant contributions to the third-order response. This parameter is determined by matching the offset of the experimental pump-probe signal.

The growth of this thermal response with t_2 is described by the term $N_{therm}(t_2)$, and researchers have postulated different functional forms for the growth of the thermal signal. Yeremenko et. al.[52] and Fecko et. al.[44] have assumed that the growth of this signal can be well described by an exponential growth towards an asymptotic limit. Since the relaxation of the HOD molecule is believed to proceed through a series of intramolecular modes before populating the low frequency modes of the bath,[61,76] Rezus and Bakker[77] postulated that the growth of the thermal response could be described by assuming that the O-H stretch relaxed first to an intermediate state before reaching the low frequency modes of the system. We have chosen to describe $N_{therm}(t_2)$ using this latter approach. The analytical solution for the growth of the thermal signal is then given by:[1]

$$N_{therm}^W(t_2) = 1 + \frac{\left(1/T_1^W\right)\exp\left[-t_2/T_1^{Int}\right] - \left(1/T_1^{Int}\right)\exp\left[-t_2/T_1^W\right]}{1/T_1^W - 1/T_1^{Int}} \qquad (6\text{-}17)$$

where T_1^{Int} is the lifetime of the intermediate state, which will be adjusted to properly fit the experimental data.

As a final contribution to the third-order response, we note that Yeremenko and coworkers[52,53] have found that an additional contribution to the thermal signal can originate from the direct excitation of the D_2O solvent. Although the absorptive component of the O-D stretch is well detuned from the 3 μm region of the mid-infrared spectrum that we are probing, the dispersive component of this transition has a large tail that extends to high frequency and facilitates the non-resonant excitation of the O-D stretch. Since this excitation process is non-resonant, we expect the thermal signal that arises from the relaxation of the O-D stretch to be $\pi/4$ phase shifted from the signal field, and should not contribute to the absorptive third-order response measured in heterodyne detected experiments such as pump-probe and 2D IR spectroscopy. However, homodyne measurements such as the photon echo peak shift and transient grating, which contain contributions from both absorptive and dispersive changes of the sample, will be sensitive to this thermal signal. We add the following term used by Yeremenko and coworkers[52,53] to account for the non-resonant absorption of D_2O:

$$S_{D_2O}^{Therm}(\omega_3, t_2, \omega_1) = e^{i\pi/4} K_{D_2O}\left(1 - \exp\left[-t_2/T_1^{D_2O}\right]\right) S_{pulse}(\omega_3, \omega_1) \qquad (6\text{-}18)$$

where K_{D_2O} is a scaling factor that is determined by matching the decay of the peak shift experiment, and $T_1^{D_2O}$ is the vibrational lifetime of the O-D stretch of D_2O, which is set to the experimentally determined value of 400 fs.[78] The phase factor at the start of this term ensures that it is $\pi/4$ phase shifted from the signal field. Since the O-D stretch is largely detuned from the frequency range probed by our experiments, the spectral shape of the

thermal signal is simply given by the experimental pulse spectrum multiplied in both the ω_1 and ω_3 dimensions, $S_{pulse}(\omega_3, \omega_1)$, normalized to its maximum value.

6.7.3. Constraints for Fitting Parameters

Admittedly, this model contains a large number of fitting parameters, but many of these values can be constrained based on both our measurements and experiments by other groups. Table 6-1 provides a summary of the methods that we have used to determine each of the parameters that comprise our model. Values of the center frequencies and transition dipole strengths of ω_W, ω_{Ion}, and ω_{Sol} are found by fitting FT-IR spectra as a function of NaOD concentration. Based on these values, we calculate the values of the transition dipole matrix elements and center frequencies for the v = 2←1 transitions of ω_W, ω_{Ion} and ω_{Sol} using DFT generated frequency maps described in Chapter 7.

To determine the frequency-frequency correlation functions that describe the spectral diffusion of ω_W, ω_{Ion}, and ω_{Sol}, we used our previously determined $C(\tau)$ for HOD/D_2O[44] as an initial guess for the correlation function of each transition. The calculated decay of the echo peak shift was found to be very sensitive to the parameters that comprise each correlation function, which allowed amplitudes of each component in these functions to be determined by fitting the peak shift decay. As will be discussed in greater detail in Section 6.8.2, during the course of fitting the data we found that we could adequately reproduce the peak shift decay at each NaOD concentration by varying only the amplitudes of each component of the correlation function. The initial values of

Parameter	Constraint/Principle Method of Determination
$\langle\omega_{10}^{W}\rangle$, $\langle\omega_{10}^{Ion}\rangle$, $\langle\omega_{10}^{Sol}\rangle$, $\lvert\boldsymbol{\mu}_{10}^{W}\rvert$, $\lvert\boldsymbol{\mu}_{10}^{Ion}\rvert$, $\lvert\boldsymbol{\mu}_{10}^{Sol}\rvert$	Determined from FT-IR spectra (Fig. 6-1)
$\langle\omega_{21}^{W}\rangle$, $\langle\omega_{21}^{Ion}\rangle$, $\langle\omega_{21}^{Sol}\rangle$, $\lvert\boldsymbol{\mu}_{21}^{W}\rvert$, $\lvert\boldsymbol{\mu}_{21}^{Ion}\rvert$, $\lvert\boldsymbol{\mu}_{21}^{Sol}\rvert$	Calculated using DFT based frequency and transition dipole maps (See Chapter 7)
$\langle\omega_{10}^{Zundel}\rangle$	Constrained to match $\langle\omega_{10}^{W}\rangle$
T_1^{W}, T_1^{Zundel}	Determined from the bi-exponential fit to the pump-probe data (Fig. 6-2)
K_{Zundel}	Determined from the amplitudes of the fast and slow components of the pump-probe decay (Fig. 6-2B)
T_1^{Sol}	Constrained to match T_1^{W}
T_1^{Int}, K_{Therm}^{W}, K_{Therm}^{Ion}, K_{D_2O}	Determined from the behavior of the peak shift decay (Fig. 6-5) and pump-probe (Fig. 6-2) at $\tau_2 > 1.5$ ps
$T_1^{D_2O}$	From Ref. 78
$\Delta\omega_3$, $\lvert\Delta\boldsymbol{\mu}_{10}\rvert$	Determined from fits to dispersed pump-probe data at $\tau_2 = 10$ ps
τ_C^{Zundel}	Determined from fits to the peak-shift at τ_2 < 200 fs, held constant for all [NaOD]
$C^{W}(0)$, $C^{Ion}(0)$, $C^{Sol}(0)$, $C^{Zundel}(0)$	Determined from fits to FT-IR spectra, held constant for all [NaOD]
A_{fast}, A_{slow}, A_{osc}, Δ_{static}	Determined from fits to peak shift data (Fig. 6-5)
τ_{fast}, τ_{slow}, τ_{osc}, ω_{osc}	Constrained from our previous work on HOD/D_2O (Ref. 44), held constant for all [NaOD]
T_1^{Ion}	Floated to fit 2D IR data
$\tau_{Ion\rightarrow W}$	Floated to fit 2D IR data

Table 6-1: Summary of each of the parameters contained by our spectral model as well as a description of their principle means of determination. Many of the parameters can be constrained on the basis of either our 1D measurements (Pump-probe, echo peak shift, and FT-IR data) or literature values. This leaves only two free parameters when fitting the 2D IR spectra.

$C^{W}(\tau)$, $C^{Ion}(\tau)$, and $C^{Sol}(\tau)$ were set to match the linewidth of the experimental FT-IR spectra. We found that we did not need to vary these linewidths with the concentration of NaOD.

Time scales for population relaxation were determined from magic angle pump-probe experiments. Parameters describing thermalization effects were initially unknown, but the amplitude and rate of growth of the thermal signal was found to be sensitive to the asymptotic behavior of the peak shift and pump-probe signals at large waiting times. Parameters that govern the shape of the "hot ground state" absorption were set to match the results of dispersed pump-probe measurements carried out at τ_2 = 10 ps. At this waiting time well past the vibrational lifetime of the O-H stretch, thermal effects are expected to dominate the third-order signal.

On the basis of our 1D measurements alone (FT-IR, pump-probe, and echo peak shift), we can constrain all of the parameters that enter into our fitting model except for two, the vibrational lifetime of the OH^- stretch, T_1^{Ion}, and the exchange time scale between ω_{Ion} and ω_W, $\tau_{Ion \to W}$. These two parameters were adjusted iteratively to fit our experimental 2D IR spectra at a NaOD concentration of 10.6M.

6.8. Comparison Between Model Calculations and Experiment

6.8.1. FT-IR and Magic Angle Pump-Probe Experiments

In Fig. 6-14 we present a comparison between our experimental FT-IR spectra and that calculated using our spectral model as a function of NaOD concentration. In fitting the FT-IR data, the values of the transition dipole matrix elements, linewidths of each transition, and the center frequencies $\langle \omega_{10}^{W} \rangle$ and $\langle \omega_{10}^{Ion} \rangle$ were held constant across the entire data series. $\langle \omega_{10}^{Sol} \rangle$ was allowed to vary linearly with NaOD concentration. A set of tables containing the parameters used to fit each of our experimental observables appears in Appendix 6.B of this chapter. Near quantitative agreement with the measured

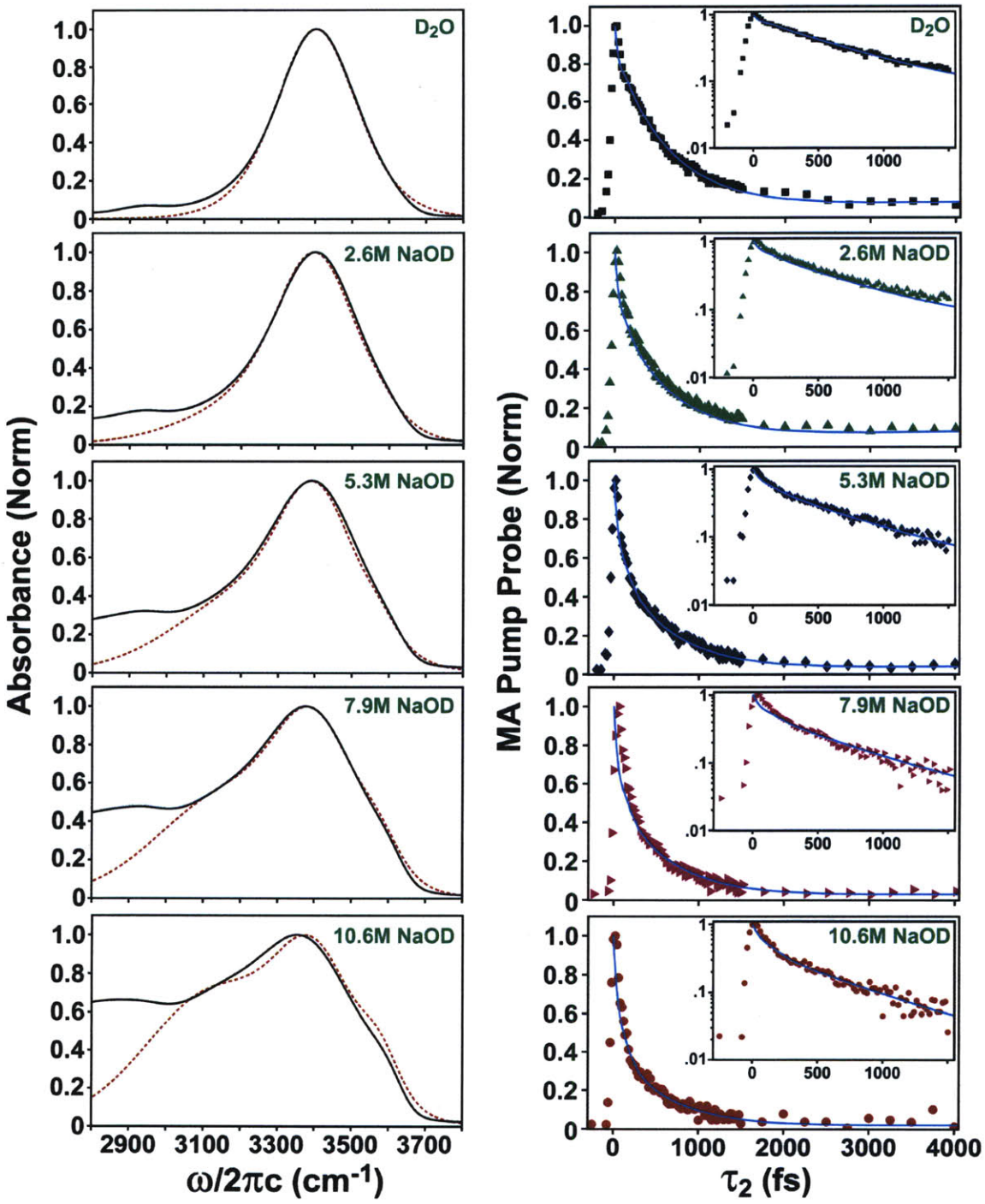


Figure 6-14: (Left) Comparison between experimental FT-IR spectra (black) and that calculated from our spectral model (red dotted) as a function of NaOD concentration. (Right) Comparison between the pump-probe signals displayed in Fig. 6-2 and that calculated from the spectral model (cyan). Good agreement is found for the overall scaling between the fast and slow contributions to the pump-probe decay, although a slight disagreement is observed between the data at short delay times since the model does not account for the finite duration of the excitation pulses.

[NaOD] (M)	% N_W	% N_{Sol}	% N_{Ion}	Density (g/mL)
0.0	1.000	0.000	0.000	1.10
1.1	0.953	0.037	0.010	1.16
2.6	0.885	0.092	0.023	1.21
5.3	0.772	0.181	0.046	1.30
7.9	0.678	0.253	0.070	1.38
10.6	0.591	0.314	0.094	1.45
15.1	0.469	0.392	0.139	1.55

Table 6-2: Percentage of hydrogen atoms that neighbor D_2O (% N_W), an OD^- ion (% N_{Sol}), or exist as OH^- (% N_{Ion}) as estimated from the know densities of NaOH solutions at different concentrations and from neutron scattering data. Also included is the density of NaOD solutions under the assumption that the spatial composition of these solutions is identical to NaOH.

spectra is obtained for frequencies above 3100 cm^{-1} except in the case of 10.6 M NaOD solution, where the peak corresponding to ω_W appears at too high a frequency since our model does not allow its center frequency to vary with concentration.

The relative populations of each of the species that contribute to ω_W, ω_{Ion}, and ω_{Sol} as a function of NaOD concentration was needed as an input to the fitting routine. These values were estimated from a combination of the known densities of NaOH solutions[49]** and neutron scattering results,[24] which provide an estimate of how the coordination number of the OH^- ion changes with NaOH concentration. Table 6-2 displays our estimates of the relative populations of hydrogen atoms whose nearest neighbor is a D_2O molecule, an OD^- ion, or exist as an OH^- ion as a function of NaOD concentration. In determining these values, we have assumed that no hydrogen bonds are donated to the Na^+ ion, that only O-H bonds that are directly hydrogen bonded to the oxygen atom of a OD^- ion contribute to ω_{Sol}, and that on average, only a minor amount of

** To calculate the values listed in Table 6-2, we have assumed that the spatial composition of an isotopically dilute HOD in NaOD/D_2O solution is identical to that of a NaOH solution of equivalent concentration since values for the density of NaOD solutions are not readily available. Given that the molarity of pure D_2O only varies by ~0.5% from that of pure H_2O, we believe that this assumption is valid.

ion pairing occurs in solution. This last assumption is expected to break down at concentrations near 10.6 M and above, where only 4.8 water molecules exist per OD^- ion.

Also displayed in Fig. 6-14 is the agreement between our spectral model and the pump-probe data pictured in Fig. 6-2. In general, the agreement is quite good and the fits reproduce both the magnitude of the fast decay component of the pump-probe and the offset at large values of τ_2 that is largely determined by the magnitude of the thermal contribution to the third-order response. The insets to each plot display the comparison with the data on a logarithmic scale and highlight that in each case the decay of the experimental pump-probe signal is preceded by a slight rise that is not captured by our model since it does not take into account the finite time duration of the excitation pulses. Nevertheless, the fact we can reproduce the remaining aspects of the pump-probe signal gives us further confidence in the ability of our model to provide a qualitative picture of the dynamics of charge migration within deuteroxide solution.

6.8.2. Photon Echo Peak Shift

Fig. 6-15 shows a comparison between the photon echo peak shift calculated from the model and the experimental data of Fig. 6-4 and 6-5. The decay of the peak shift is highly sensitive to the form of the frequency-frequency correlation functions used for ω_W, ω_{Ion}, and ω_{Sol}. As a starting point, for each transition we used a correlation function that is similar to our previously measured $C(t)$ for HOD/D_2O.[43,44,79] This function contains three decay components, an exponential 110 fs decay, an underdamped oscillation at with a frequency of 160 cm^{-1} corresponding to an underdamped hydrogen bond stretch, and a longer 1.4 ps exponential decay. This functional form was used as an initial input for

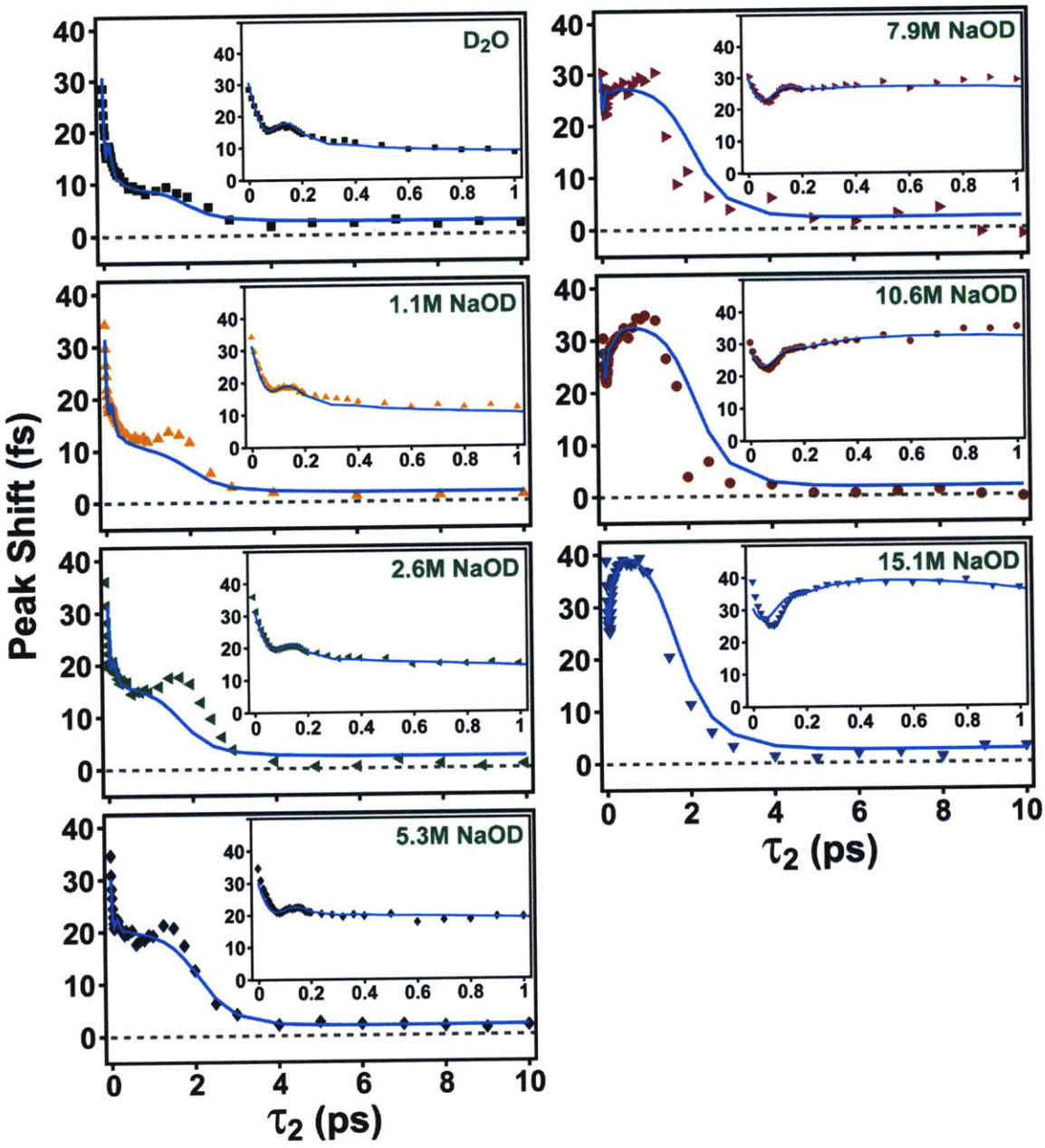


Figure 6-15: Comparison between the experimental echo peak shift data displayed in Fig. 6-4 and 6-5 and that calculated from our spectral model. The decay of the peak shift near ~2 ps at all concentrations is found to largely be the result of solvent induced heating.

$C^{W}(t)$ and $C^{Sol}(t)$, but since the OH^{-} stretch is only weakly hydrogen bonded, we removed the underdamped oscillatory component of $C^{Ion}(t)$ and retained only its fast and slow decay components. The amplitudes of the various components of $C^{W}(t)$,

$C^{Sol}(t)$, and $C^{Ion}(t)$ were then varied to fit the decay of the echo peak shift at each NaOD concentration. While iteratively fitting the data, we found that $C^{W}(t)$ and $C^{Sol}(t)$ often converged to the same functional form. Thus, to eliminate superfluous fit parameters from our model we have constrained both of these functions to vary only in terms of their time zero values to properly fit the linear absorption spectrum. Likewise, the relative scaling of the fast and slow components of $C^{H}(t)$ matched that of $C^{W}(t)$ and $C^{Sol}(t)$, so have also set this ratio to be the same. This enables us to describe spectral diffusion through the use of a single frequency-frequency correlation function for each NaOD concentration.

The inset to each panel of Fig. 6-15 displays the behavior of the peak shift up to a waiting time of 1 ps. At all concentrations smaller than 5.3 M NaOD, we observe an initial fast decay followed by a recurrence due to an underdamped hydrogen bond oscillation that is well reproduced by our fitting model. At higher concentrations, the initial fast decay is still present, but then gives way to a rise in the peak shift signal. This rise is due to the relaxation of the broad, transient contribution to the third-order response from Zundel-like states and is captured by our fitting model at concentrations of 7.9 and 10.6 M NaOD. While our model is unable to match the initial value of the peak shift of the 15.1 M NaOD data, presumably due to an improper treatment of the lineshape of the Zundel-like feature, our model is able to describe the rise in the peak shift in the 0.2-1 ps waiting time regime.

When fitting the data for waiting times between 0.2 – 2 ps, we discovered that we could not adequately reproduce the observed increase in the value of the peak shift with NaOD concentration without the inclusion of a static offset. The relative contribution of

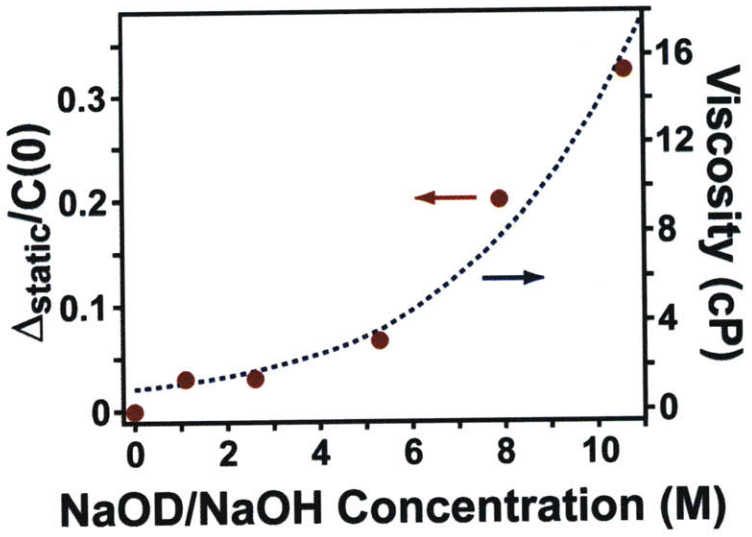


Figure 6-16: The static contribution to the frequency-frequency correlation function determined from our spectral model. This static component is found to follow the increase in solvent viscosity with NaOH concentration. This suggests that the viscosity increase may be related to new relaxation pathways associated with the structural diffusion of OD^- ions.

this static component to $C(t)$ is plotted in Fig. 6-16. With increasing NaOD concentration, the intensity of the offset first appears to grow linearly, but near a concentration of 5.3 M, the increase in the offset deviates from linearity. The amplitude of the static component matches well the increase in the viscosity of aqueous NaOH with concentration. Given that at concentrations of 5.3 M and below, our fitting model requires a small but significant contribution from the 1.4 ps relaxation time scale to properly fit the data in the 0.2 – 1 ps waiting time regime, we believe that we are justified in positing the existence of a relaxation time scale that is longer than our experimental window of a few ps.

The existence of a long relaxation time scale in electrolyte solutions is supported by 2D IR measurements of the O-D stretch of HOD in NaBr solution which displays a slow down of spectral diffusion with increasing NaBr concentration.[80] Although this

result was interpreted as showing a slow down of the dynamics of water's hydrogen bonding network with electrolyte concentration, pump-probe studies[47,81] have suggested that the water dynamics outside of anion solvation shells are only weakly affected by the presence of the anion. Likewise, molecular dynamics simulations[72,82] have suggested that the initial behavior of water molecules near anionic solvation shells are similar to that of bulk water. Recent simulations[83] of aqueous NaBr have suggested the existence of an additional slow time scale in the 6 – 40 ps range associated with rearrangements of the solvation shell of the Br^- ion. These rearrangements involve the exchange of water molecules into and out of the ion's solvation shell and may play a role in the diffusion of the ion. While we are unable to determine a value for this long time relaxation process due to interference that arises from the "hot ground state" absorption near 2-3 ps, this slow relaxation process may be related to the solvation of a newly formed HOD molecule following proton transfer, and may serve as a partial microscopic explanation for the increase in viscosity observed in these solutions. In Chapter 7, we will use a MS-EVB simulation model of aqueous NaOH to show that the structural diffusion of the hydroxide ion involves processes that occur in the 5-10 ps time scale range.

At a waiting time of ~2 ps we observe a decay of the peak shift to zero that is independent of NaOD concentration. This decay is suggestive of chemical exchange but may also be explained by solvent induced heating. The fits from our model show that both of these processes contribute to the decay of the peak shift, but that the solvent induced heating effect forms the dominant contribution to the decay. At a waiting time of 1 ps and concentration of 10.6 M, varying the exchange time scale $\tau_{Ion\to W}$, defined as $\tau_{Ion\to W} = 1/k_{Ion\to W}$, from 500 fs to 1 ns changed the value of the ps by only 2 fs. At all

other values of τ_2 at this concentration, the variation of the calculated peak shift with $\tau_{Ion \to W}$ was generally smaller than 2 fs, leading us to conclude that the peak shift is relatively insensitive to frequency shifts induced by the exchange process in Fig. 6-13B. We can perhaps rationalize this insensitivity by examining Table 6-1. Even at high concentration, the number of hydrogen atoms that form OH^- ions is small relative to the number of HOD molecules hydrogen bonded to D_2O. This means that the contribution of exchange events to the total third-order signal will be small relative to the signals due simply to the dynamics of ω_{Ion} and ω_W. However, since exchange events appear as spectrally separated cross peaks in 2D IR experiments, measurements of this type are better suited to the determination of $\tau_{Ion \to W}$.

It is worth noting that while we can reproduce the overall decay of the peak shift near ~2 ps, our model cannot well reproduce the recurrence in the peak shift near 1.5 ps at concentrations of 5.3 M and below. A recurrence of this type has been shown to arise in echo peak shift measurements of HOD in D_2O using pulses that are somewhat longer than ours (90 fs) when the pulses are tuned toward the red edge of the O-H absorption spectrum.[50] Yeremenko and coworkers[52,53] demonstrated that this recurrence grows in intensity as the experimental pulse spectrum is narrowed and detuned farther from resonance with the O-H stretch, and that this feature can be reproduced by taking into account both the thermal redistribution term displayed in Eq. 6-18 as well as a change in the refractive index of the D_2O solvent upon the transfer of vibrational energy to the low frequency modes of the bath. In an earlier version of our model, we included this change in the solvent refractive index but found that it only had a minimal effect on the calculated peak shift. However, we have found that by artificially narrowing and red

shifting our experimental pulse spectrum, we can better reproduce the recurrence near 1.5 at low NaOD concentration. It is well known that the transition dipole of the O-H stretch of the HOD molecule increases with the strength of the hydrogen bond to the proton.[57,58] This non-Condon effect can bias our experimental measurements in favor of signals that arise from the low frequency side of the O-H absorption lineshape despite the fact that our pulses span a large portion of ω_{OH}. The lack of inclusion of these effects in our spectral model may explain our inability to properly reproduce the recurrence present in our experimental results.

6.8.3. Determining an Exchange Time scale from 2D IR Measurements

In Fig. 6-17 we plot a comparison between our experimental 2D IR data measured for 10.6 M NaOD solution and the spectra calculated from our spectral model using a value of $\tau_{Ion \rightarrow W}$ = 3 ps, which was determined to be the optimum value of the exchange time from a least squares fitting of the 2D IR data. The simulation model reproduces many of the features found in the experiment, such as the appearance of the v = 2←1 transition of the OH^- stretch with increasing waiting time, and the asymmetry of the 2D spectra along the diagonal axis that persists at large values of τ_2. Also reproduced are the elongation of the diagonal OH^- peak near 3600 cm^{-1} along the ω_1 axis and the appearance of a positive feature below the diagonal at (ω_1, ω_3) = (3600 cm^{-1}, 3300 cm^{-1}). These two features were postulated in Section 6.5 to correspond to cross peaks denoting chemical exchange. By plotting different contributions to our model, we indeed find that enhancement in these regions is due to cross peaks that appear as a result of chemical exchange. While the elongation of the 2D spectra above the diagonal axis is primarily

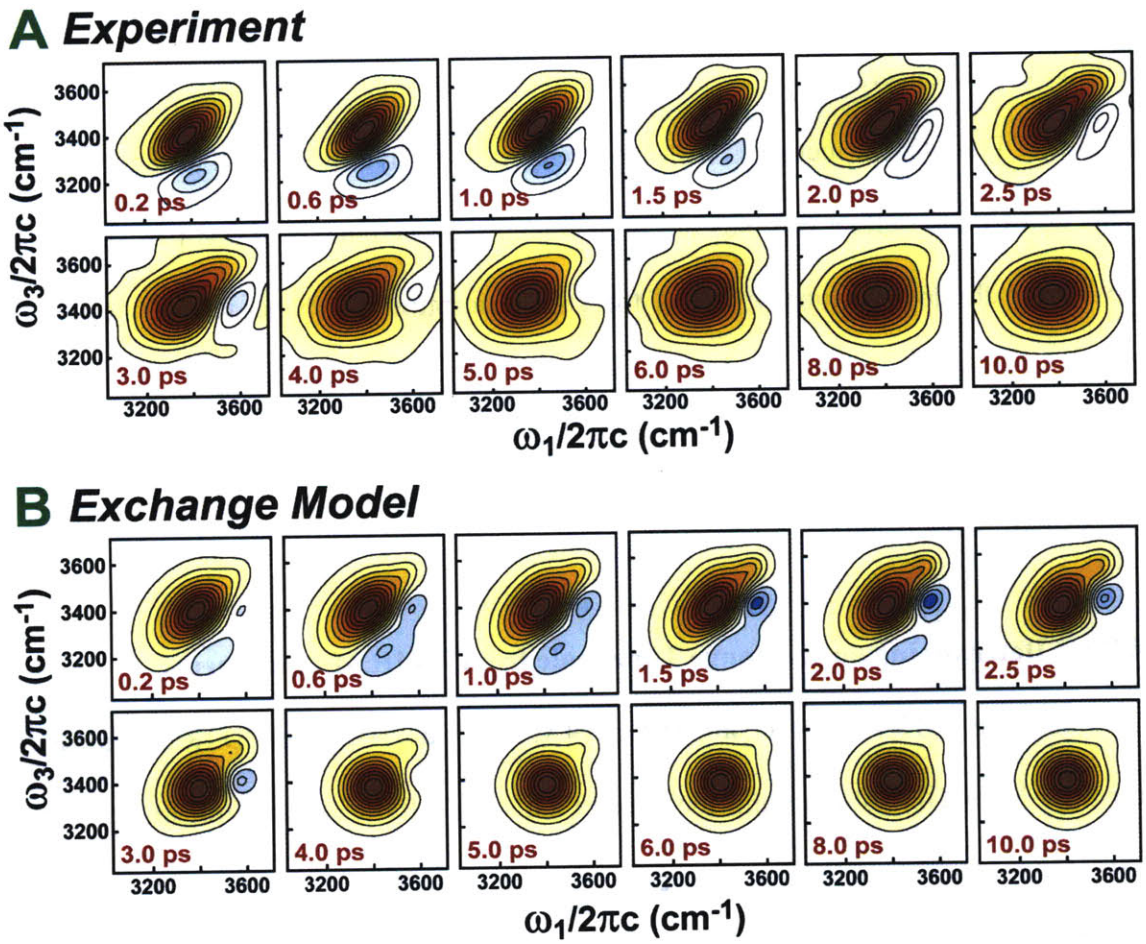


Figure 6-17: Comparison between experimentally measured 2D IR spectra for a NaOD concentration of 10.6 M (A) compared to the results of our spectral model (B). The spectra calculated from our model were convolved with the experimental pulse spectrum used to measure the data shown in (A) along both the ω_1 and ω_3 dimensions.

due to chemical exchange, the peak that appears below the diagonal results from both chemical exchange and the growth of the hot ground state absorption, which complicates the determination of $\tau_{Ion \to W}$ from our spectral model. Interference between these features as well as the fact that the vibrational relaxation time scales of the system are faster than the determined exchange rate can explain why the optimum exchange time scale differs from the 1.9 ps rise observed above and below the diagonal axis of the experimental 2D data (Fig. 6-10B).

Beyond a waiting time of ~6 ps, the 2D spectrum predicted by our model is no longer observed to change, indicating a completion of the growth of the thermal response. This calls into question our ability to determine if the optimum value of $\tau_{Ion \to W}$ instead corresponds to a value that is larger than 3 ps, as estimated from our model. To test the ability of our model to uniquely determine a value of $\tau_{Ion \to W}$, in Fig. 6-18 we compare our experimental 2D spectra to spectra calculated from our model for $\tau_{Ion \to W}$ = 500 fs, which would correspond to extremely rapid exchange, $\tau_{Ion \to W}$ = 3 ps as optimally determined from our model, and $\tau_{Ion \to W}$ = 1 ns, which would lead to effectively no exchange over our experimental time window.

Examining the spectra calculated using an exchange time of 500 fs, we find that the cross peak ridge that appears above the diagonal is much too intense at τ_2 = 0.6 ps. To highlight this observation, to the right of the 2D data we plot a comparison of slices of the experimental and calculated spectra along the ω_1 axis for a value of ω_3 = 3600 cm^{-1} at this waiting time. Along this direction, the calculated spectra for $\tau_{Ion \to W}$ = 500 fs appears bimodal, with two peaks centered near 3400 cm^{-1} and 3525 cm^{-1}. The higher frequency of these two peaks is due to the diagonal peak of ω_{Ion}, while the peak at lower frequency corresponds to a cross peak between ω_W and ω_{Ion}, indicating the exchange of these two transitions. Unfortunately, this bimodal distribution due to the exchange of ω_W and ω_{Ion} is not seen in the experimental data at this waiting time, and indicates that $\tau_{Ion \to W}$ must be larger than 500 fs. Increasing $\tau_{Ion \to W}$ to 3 ps acts to suppress the peak at 3400 cm^{-1} and increases the agreement with experiment, but does not completely remove the exchange

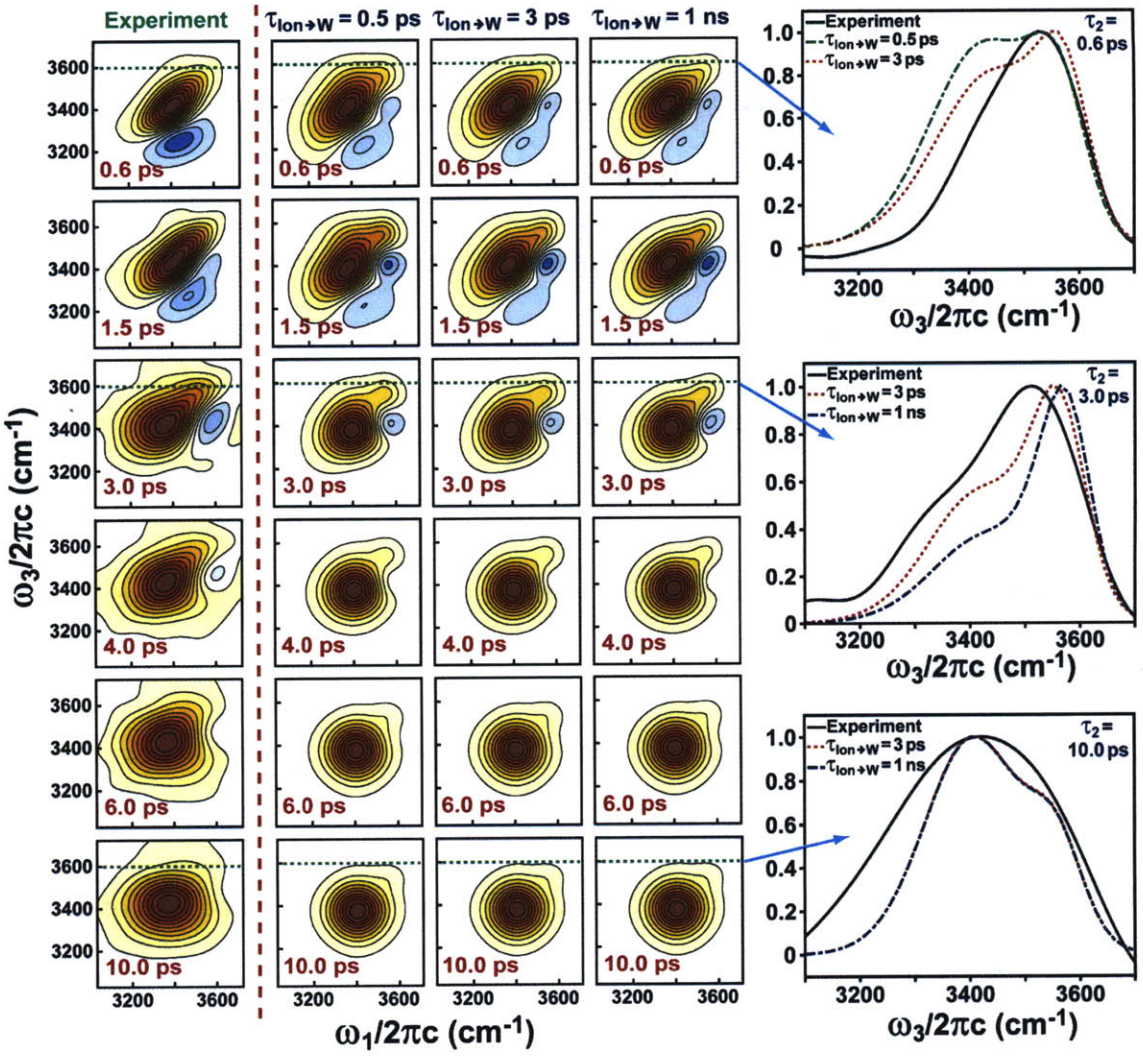


Figure 6-18: Comparison of spectra calculated from our spectral model using three different values of $\tau_{Ion\to W}$. While the best agreement with experiment is found for $\tau_{Ion\to W}$ = 3 ps, interference effects due to solvent induced heating lead us to the conclusion that this value should be interpreted as a lower limit for $\tau_{Ion\to W}$. To the right of the pictured 2D spectra, are horizontal slices of the experimental and calculated spectra taken along ω_3 = 3600 cm^{-1} for three different waiting times, 0.6 ps, 3.0 ps, and 10.0 ps.

peak. This shows that we can at least rule out exchange time scales that are smaller than 3 ps.

Increasing the waiting time to 3 ps, we find that the experimental 2D data now appears broadened above the diagonal axis, suggesting the conversion of molecules

initially excited at ω_W to ω_{Ion}. This is observed more prominently in the ω_1 slice shown to the right of the 2D data, which now shows a shoulder peaked near 3350 cm^{-1} that is indicative of the exchange of ω_W and ω_{Ion}. If we compare this experimental slice to that calculated from our model for $\tau_{Ion \to W}$ = 3 ps, we find that while the model calculation is peaked at too high a frequency, the intensity of the shoulder at lower frequency due to the exchange of ω_W and ω_{Ion} agrees well with experiment. Eliminating exchange from our model by increasing $\tau_{Ion \to W}$ = 1 ns, we find that the shoulder at 3400 cm^{-1} becomes suppressed, and suggests that some degree of chemical exchange is needed to model our data.

To determine the optimum value of $\tau_{Ion \to W}$, one would like to examine a comparison between experimental and calculated 2D IR spectra for waiting times at least two or three times longer than $\tau_{Ion \to W}$. However, the growth of thermal effects prevents us from measuring signatures of proton transfer that may occur past a waiting time of ~6 ps. 2D IR spectra calculated at this waiting time for different values of $\tau_{Ion \to W}$ are nearly indistinguishable since the thermal signal that arises from the relaxation of the O-H stretch dominates the nonlinear signal. By τ_2 = 10 ps, the calculated spectra lie on top of one another, as indicated by the ω_1 slices taken at this waiting time. Since the thermal response prevents a comparison between our calculations and experiment at longer waiting times, we view our optimal fit value of $\tau_{Ion \to W}$ = 3 ps as a *lower bound* for the solvation time scale of a newly formed OH^- ion upon proton transfer.

6.8.4. Implications of the Exchange Time Scale

While this result is somewhat disappointing since we cannot uniquely determine the time scale of hydroxide ion solvation following proton transfer, we can use our lower bound to gain some insight into the structural diffusion of the ion under the assumption that the actual transport time scale does not differ significantly from 3 ps. Much of the discussion in this chapter has been written in the language of a single proton transfer event between a water molecule and a hydroxide ion and the subsequent solvation of the products of this reaction. However, given that protons are believed to be able to rapidly transfer along hydrogen bonded chains, can concerted proton transfer reactions occur wherein the hydroxide ion charge defect hops from one water molecule to another? Halle and Karlström[84] investigated this prospect for the hydronium ion and concluded that under ambient conditions, it is unlikely that protons are transferred in a concerted manner. However, it is unclear if this is the case for the OH^- ion.

The diffusion constant for a three dimensional random walk is given by $D = \langle \ell^2 \rangle / 6\Delta t$, where ℓ denotes the hopping distance and Δt is the time between hops.[85] The diffusion constant of the deuteroxide ion determined from mobility measurements is 0.32 $Å^2$/ps.[84] Using this value of the diffusion constant and our estimate of the exchange time scale of 3 ps, we estimate a value of 2.4 Å for ℓ. This distance nearly matches the experimentally determined value of 2.3 Å for the separation of the oxygen atoms of the hydroxide ion and the water molecules in its first solvation shell from neutron scattering data.[24] This result implies that the correlation length for the transport of the hydroxide ion does not extend past its first solvation shell. Correlated proton hopping events on average do not occur in aqueous hydroxide.

We can also ask questions regarding the solvation process that leads to the formation of a cross peak. Given that the frequency of an O-H bond is largely determined by the hydrogen bonding configuration at the proton, the observed time scale for the growth of the cross peak must be related to how long it takes an OH^- ion to form a new hydrogen bond once it has accepted a deuteron from a neighboring water molecule to form HOD. The 3 ps exchange time scale that we observe is related to the reincorporation of the OH^- charge defect into water's hydrogen bonding network upon proton transfer. In Chapter 5, we found that the fluctuations that drive the structural rearrangement of water's hydrogen bonding network occur over a time scale of ~1.4 ps. Our observed lower limit of 3 ps for charge migration is ~2 times longer than this. This result is not unexpected since the transport of a proton requires not only the solvation of the new OH^- ion, but also that of the newly formed water molecule. This requires the loosely correlated motion of water molecules at least as far away as the second solvation shell of the new ion. In the course of our modeling, we also found evidence for the existence of a slow relaxation process that scales with the increase in the solution viscosity. It is plausible that the observed increase in solvent viscosity is at least in part due to the increasing contribution of the 3 ps solvation time associated with the formation of an OH^- charge defect upon proton transfer.

6.9. Conclusions

Through the use of a systematic series of ultrafast, nonlinear infrared measurements performed on the O-H stretching transition of a dilute solution of HOD in $NaOD/D_2O$, we have demonstrated the existence of at least two unique time scales associated with the structural diffusion of deuteroxide ions. At very early delay times, we

observe a feature that rapidly decays on a 110 fs time scale that we attribute to protons that are shared in Zundel-like configurations. Protons that we excite in such configurations are near the barrier for proton transfer, and the rapid disappearance of their spectral signature indicates the time needed for these protons to commit to the formation of a new, stable covalent bond. At longer time scales, we find evidence for a slow relaxation process that leads to an increase of the photon echo peak shift in the 0.2 – 2 ps waiting time regime. While we cannot resolve the value of this decay feature, we have found that its amplitude appears to scale linearly with the increase in solvent viscosity.

2D IR spectra show the appearance of spectral features that are consistent with a cross peak between the spectral range indicative of the O-H stretch of HOD molecules that participate in hydrogen bonds with D_2O and the non-hydrogen bonded OH^- stretching transition that appears at high frequency. The growth of these features is best reproduced by our spectral model when a time constant of 3 ps is used for the exchange rate between a OH^- like stretch and a HOD molecule hydrogen bonded to D_2O, and suggests that this corresponds to the time it takes the bath to solvate a newly formed HOD molecule. However, due to interference effects that arise from a thermal signal generated by the bath, the time scale we determine for this process should be viewed as a lower limit of its potential value. The increasing contribution of this slow solvation process to the dynamics of the system with increasing concentration of NaOD may in part explain the large increase of solution viscosity upon the addition of NaOD.

At present, our interpretation of our experimentally observed time scales is largely based on a combination of intuition and conjecture. In the next and final Chapter of this thesis, we will attempt to place our interpretation on a solid theoretical framework by

using a recently developed MS-EVB simulation model[34] to make a mechanistic connection between the spectra that we observe experimentally and the underlying dynamics of the system. We will show that the relaxation of a proton equally shared in a Zundel-like configuration is a highly collective process, involving dielectric fluctuations of the surrounding solvent. These fluctuations are largely complete by ~1 ps and prevent the back transfer of the proton. However, the solvent shells of the newly formed hydroxide ion and water molecule continue to evolve on longer time scales. Most notably, we find that the formation of a hydrogen bond to the newly formed HOD molecule occurs on a 7.4 ps time scale and leads to the cross peak observed in our 2D IR spectra. This presents a picture wherein a hierarchy of processes that range from tens of femtoseconds to picoseconds make important contributions to the transport of the hydroxide ion.

Acknowledgements

I would like to acknowledge Poul Petersen and Krupa Ramasesha for aid in acquiring the data presented in this chapter and for many useful conversations regarding its interpretation. I would also like to thank Aritra Mandal for aid in measuring the FT-IR spectra plotted in Fig. 6-14.

References

(1) P. Atkins, *Physical Chemistry*, 6th, (Oxford University Press, Oxford, U.K., 1997).

(2) R. Pomes and B. Roux, "Molecular mechanism of H^+ conduction in the single-file water chain of the gramicidin channel," Biophys. J 82, 2304 (2002).

(3) F. Garczarek and K. Gerwert, "Functional waters in intraprotein proton transfer monitored by FTIR difference spectroscopy," Nature 439, 109 (2006).

(4) S. A. Hassan, G. Hummer and Y.-S. Lee, "Effects of electric fields on proton transport through water chains," J. Chem. Phys. 124, 204510 (2006).

(5) P. Ball, "Water as an active constituent in cell biology," Chem. Rev. 108, 74 (2008).

(6) M. Eigen, "Proton transfer, acid-base catalysis, and enzymatic hydrolysis," Angew. Chem. Internat. Edit. 3, 1 (1964).

(7) G. Zundel, "Hydrogen bonds with large proton polarizability and proton transfer processes in electrochemistry and biology," Adv. Chem. Phys. 111, 1 (2000).

(8) D. Marx, M. E. Tuckerman, J. Hutter and M. Parrinello, "The nature of the hydrated excess proton in water," Nature 397, 601 (1999).

(9) O. Markovitch, H. Chen, S. Izvekov, F. Paesani, G. A. Voth and N. Agmon, "Special pair dance and partner selection: Elementary steps in proton transport in liquid water," J. Phys. Chem. B 112, 9456 (2008).

(10) N. Agmon, "The Grotthuss mechanism," Chem. Phys. Lett. 244, 456 (1995).

(11) M. K. Petersen, A. J. Hatt and G. A. Voth, "Orientational dynamics of water in the nafion polymer electrolyte membrane and its relationship to proton transport," J. Phys. Chem. B 112, 7754 (2008).

(12) G. Zundel, in *The Hydrogen Bond: Recent Developments in Theory and Experiment, Vol. II*, edited by P. Schuster, G. Zundel and C. Sandorfy, (North Holland, Amsterdam, 1976).

(13) H. Lapid, N. Agmon, M. K. Petersen and G. A. Voth, "A bond-order analysis of the mechanism for hydrated proton mobility in liquid water," J. Chem. Phys. 122, 014506 (2005).

(14) N. Agmon, "Mechanism of hydroxide mobility," Chem. Phys. Lett. 319, 247 (2000).

(15) D. Asthagiri, L. R. Pratt, J. D. Kress and M. A. Gomez, "Hydration and mobility of HO^-(aq)," Proc. Nat. Acad. Sci. 101, 7229 (2004).

(16) M. E. Tuckerman, D. Marx and M. Parrinello, "The nature and transport mechanism of hydrated hydroxide ions in aqueous solution," Nature 417, 925 (2002).

(17) B. Chen, I. Ivanov, J. M. Park, M. Parrinello and M. L. Klein, "Solvation structure and mobility mechanism of OH^-: A Car-Parrinello molecular dynamics investigation of alkaline solutions," J. Phys. Chem. B 106, 12006 (2002).

(18) B. Chen, J. M. Park, I. Ivanov, G. Tabacchi, M. L. Klein and M. Parrinello, "First-principles study of aqueous hydroxide solutions," J. Am. Chem. Soc. 124, 8534 (2002).

(19) M. E. Tuckerman, A. Chandra and D. Marx, "Structure and dynamics of OH^- (aq)," Acc. Chem. Res. 39, 151 (2006).

(20) A. Chandra, M. E. Tuckerman and D. Marx, "Connecting solvation shell structure to proton transport kinetics in hydrogen-bonded networks via population correlation functions," Phys. Rev. Lett. 99, 145901 (2007).

(21) M. Meot-Ner and C. V. Speller, "Filling of solvent shells about ions. 1. Thermochemical criteria and the effects of isomeric clusters," J. Phys. Chem. 90, 6616 (1986).

(22) W. H. Robertson, E. G. Diken, E. A. Price, J.-W. Shin and M. A. Johnson, "Spectroscopic determination of the OH^- solvation shell in the $OH^-(H_2O)_n$ clusters," Science 299, 1367 (2003).

(23) A. Botti, F. Bruni, S. Imberti and M. A. Ricci, "Solvation of hydroxyl ions in water," J. Chem. Phys. 119, 5001 (2003).

(24) A. Botti, F. Bruni, S. Imberti, M. A. Ricci and A. K. Soper, "Ions in water: The microscopic structure of concentrated NaOH solutions," J. Chem. Phys. 120, 10154 (2004).

(25) T. Megyes, S. Bálint, T. Grósz, T. Radnai, I. Bakó and P. Sipos, "The structure of aqueous sodium hydroxide solutions: A combined solution x-ray diffraction and simulation study," J. Chem. Phys. 128, 044501 (2008).

(26) M. Śmiechowski and J. Stangret, "Hydroxide ion hydration in aqueous solutions," J. Phys. Chem. A 111, 2889 (2007).

(27) G. E. Walrafen and R. T. W. Douglas, "Raman spectra from very concentrated aqueous NaOH and from wet and dry, solid, and anhydrous molten, LiOH, NaOH, and KOH," J. Chem. Phys. 124, 114504 (2006).

(28) T. Corridoni, A. Sodo, F. Bruni, M. A. Ricci and M. Nardone, "Probing water dynamics with OH^-," Chem. Phys. 336, 183 (2007).

(29) E. F. Aziz, N. Ottosson, M. Faubel, I. V. Hertel and B. Winter, "Interaction between liquid water and hydroxide revealed by core-hold de-excitation," Nature 455, 89 (2008).

(30) H.-K. Nienhuys, A. J. Lock, R. A. v. Santen and H. J. Bakker, "Dynamics of water molecules in an alkaline environment," J. Chem. Phys. 117, 8021 (2002).

(31) J. Thøgersen, S. K. Jensen, C. Petersen and S. R. Keiding, "Reorientation of hydroxide ions in water," Chem. Phys. Lett. 466, 1 (2008).

(32) S. T. Roberts, P. B. Petersen, K. Ramasesha, A. Tokmakoff, I. S. Ufimtsev and T. J. Martinez, "Observation of a Zundel-like transition state during proton transfer in aqueous hydroxide solutions," Proc. Natl. Acad. Sci. U.S.A. 106, 15154 (2009).

(33) I. S. Ufimtsev, A. G. Kalinichev, T. J. Martinez and R. J. Kirkpatrick, "A charged ring model for classical OH^-(aq) simulations," Chem. Phys. Lett. 442, 128 (2007).

(34) I. S. Ufimtsev, A. G. Kalinichev, T. J. Martinez and R. J. Kirkpatrick, "A multistate empirical valence bond model for solvation and transport simulations of OH^- in aqueous solutions," Phys. Chem. Chem. Phys. 11, 9420 (2009).

(35) A. Tokmakoff, "Orientational correlation functions and polarization selectivity for nonlinear spectroscopy of isotropic media. I. Third order," J. Chem. Phys. 105, 1 (1996).

(36) D. Schiöberg and G. Zundel, "Very polarizable hydrogen bonds in solutions of bases having infra-red absorption continua," J. Chem. Soc., Faraday Trans. 2 69, 771 (1973).

(37) P. A. Giguère and S. Turrell, "H_3O^+ ion in aqueous acid solutions. The infrared spectra revisited," Can. J. Chem. 54, 3477 (1976).

(38) J. Kim, U. Schmitt, J. Greutzmacher, G. A. Voth and N. E. Scherer, "The vibrational spectrum of the hydrated proton: Comparison of experiment, simulation, and normal mode analysis," J. Chem. Phys. 116, 737 (2002).

(39) C. C. M. Samson and W. Klopper, "*Ab initio* claculation of proton barrier and binding energy of the $(H_2O)OH^-$ complex," J. Mol. Struct. THEOCHEM 586, 201 (2002).

(40) E. G. Diken, J. M. Headrick, J. R. Roscioli, J. C. Bopp, M. A. Johnson and A. B. McCoy, "Fundamental excitations of the shared proton in the $H_3O_2^-$ and $H_5O_2^+$ complexes," J. Phys. Chem. A 109, 1487 (2005).

(41) M. Moskovits and K. H. Michaelian, "Alkali hydroxide ion paris. A Raman study," J. Am. Chem. Soc. 102, 2209 (1980).

(42) N. B. Librovich and V. D. Maiorov, "Vibrational spectra of $H_3O_2^-$ and $D_3O_2^-$ ions in aqueous and deuterated aqueous solutions of potassium and sodium hydroxides," Russ. J. Phys. Chem. 56, 624 (1982).

(43) J. J. Loparo, C. J. Fecko, J. D. Eaves, S. T. Roberts and A. Tokmakoff, "Reorientational and configurational fluctuations in water observed on molecular length scales," Phys. Rev. B 70, 180201 (2004).

(44) C. J. Fecko, J. J. Loparo, S. T. Roberts and A. Tokmakoff, "Local hydrogen bonding dynamics and collective reorganization in water: Ultrafast IR spectroscopy of HOD/D_2O," J. Chem. Phys. 122, 054506 (2005).

(45) G. M. Gale, G. Gallot, F. Hache, N. Lascoux, S. Bratos and J.-C. Leicknam, "Femtosecond dynamics of hydrogen bonds in liquid water: A real time study," Phys. Rev. Lett. 1068 (1999).

(46) H. K. Nienhuys, S. Woutersen, R. A. v. Santen and H. J. Bakker, "Mechanism for vibrational relaxation in water investigated by femtosecond infrared spectroscopy," J. Chem. Phys. 111, 1494 (1999).

(47) H. J. Bakker, "Structural dynamics of aqueous salt solutions," Chem. Rev. 108, 1456 (2008).

(48) M. F. Kropman and H. J. Bakker, "Effect of ions on the vibrational relaxation of liquid water," J. Am. Chem. Soc. 126, 9135 (2004).

(49) "Concentrative properties of aqueous solutions: Density, refractive index, freezing point depression, and viscosity," in *CRC Handbook of Chemistry and Physics*, edited by D. R. Lide, 89th, (CRC Press/Taylor and Francis, Boca Raton, FL, 2009).

(50) J. Stenger, D. Madsen, P. Hamm, E. T. J. Nibbering and T. Elsaesser, "A photon echo peak shift study of liquid water," J. Phys. Chem. A 106, 2341 (2002).

(51) T. Steinel, J. B. Asbury, J. Zheng and M. D. Fayer, "Watching hydrogen bonds break: A transient absorption study," J. Phys. Chem. A 108, 10957 (2004).

(52) S. Yeremenko, M. S. Pshenichnikov and D. A. Wiersma, "Interference effects in IR photon echo spectroscopy of liquid water," Phys. Rev. A 73, 021804 (2006).

(53) S. Yeremenko, *Water dynamics explored by femotsecond infrared spectroscopy*, Ph.D Thesis, University of Groningen, Dept. of Physical Chemistry, 2004.

(54) M. D. Fayer, "Dynamics of liquids, molecules, and proteins measured with ultrafast vibrational echo chemical exchange spectroscopy," Annu. Rev. Phys. Chem. 60, 21 (2008).

(55) M. Khalil, N. Demirdoven and A. Tokmakoff, "Coherent 2D IR spectroscopy: Molecular structure and dynamics in solution," J. Phys. Chem. A 107, 5258 (2003).

(56) A. B. McCoy, E. G. Diken and M. A. Johnson, "Generating spectra from ground-state wave functions: Unraveling anharmonic effects in the OH^-H_2O vibrational predissociation spectrum," J. Phys. Chem. A 113, 7346 (2009).

(57) S. A. Corcelli and J. L. Skinner, "Infrared and Raman line shapes of dilute HOD in liquid H_2O and D_2O from 10 to 90 ^oC," J. Chem. Phys. 109, 6154 (2005).

(58) J. R. Schmidt, S. A. Corcelli and J. L. Skinner, "Pronounced non-Condon effects in the ultrafast infrared spectroscopy of water," J. Chem. Phys. 123, 044513 (2005).

(59) J. J. Loparo, S. T. Roberts and A. Tokmakoff, "Multidimensonal infrared spectroscopy of water. I. Vibrational dynamics in 2D lineshapes," J. Chem. Phys. 125, 194521 (2006).

(60) R. Rey and J. T. Hynes, "Vibrational energy relaxation of HOD in liquid D2O," J. Chem. Phys. 104, 2356 (1996).

(61) C. P. Lawrence and J. L. Skinner, "Vibrational spectroscopy of HOD in liquid D_2O. I. Vibrational energy relaxation," J. Chem. Phys. 117, 5827 (2002).

(62) P. Hamm, M. Lim and R. M. Hochstrasser, "Vibrational energy relaxation of the cyanide ion in water," J. Chem. Phys. 107, 10523 (1997).

(63) J. Zheng, K. Kwak, J. Xie and M. D. Fayer, "Ultrafast carbon-carbon single-bond rotational isomerization in room-temperature solution," Science 313, 1951 (2006).

(64) S. Park, M. Odelius and K. J. Gaffney, "Ultrafast dyanmics of hydrogen bond exchange in aqueous ionic solutions," J. Phys. Chem. B 113, 7825 (2009).

(65) J. R. Zheng, K. Kwak, J. Asbury, X. Chen, I. R. Piletic and M. D. Fayer, "Ultrafast dynamics of solute-solvent complexation observed at thermal equilibrium in real time," Science 309, 1338 (2005).

(66) D. E. Moilanen, D. Wong, D. E. Rosenfeld, E. E. Fenn and M. D. Fayer, "Ion-water hydrogen-bond switching observed with 2D IR vibrational echo chemical exchange spectroscopy," Proc. Natl. Acad. Sci. U.S.A. 106, 375 (2009).

(67) K. Kwak, J. Zheng, H. Cang and M. D. Fayer, "Ultrafast two-dimensional infrared vibrational echo chemical exchange experiments and theory," J. Phys. Chem. B 110, 19998 (2006).

(68) K. Kwac, H. Lee and M. Cho, "Non-Gaussian statistics of amide I mode frequency fluctuation of N-methylacetamide in methanol solution: Linear and nonlinear vibrational spectra," J. Chem. Phys. 120, 1477 (2004).

(69) O. Golonzka and A. Tokmakoff, "Polarization-selective third-order spectroscopy of coupled vibronic states," J. Chem. Phys. 115, 297 (2001).

(70) D. Laage and J. T. Hynes, "On the molecular mechanism of water reorientation," J. Phys. Chem. B 112, 14230 (2008).

(71) C. J. Fecko, *Spectroscopic investigations of hydrogen bond dynamics in liquid water*, Ph.D Thesis, Massachusetts Institute of Technology, Dept. of Chemistry, 2004.

(72) D. Laage and J. T. Hynes, "Reorientational dynamics of water molecules in anionic hydration shells," Proc. Natl. Acad. Sci. U.S.A. 104, 11167 (2007).

(73) D. W. Oxtoby and S. A. Rice, "On vibrational relaxation in liquids," Chem. Phys. Lett. 42, 1 (1976).

(74) J. T. Fourkas, H. Kawashima and K. A. Nelson, "Theory of nonlinear optical experiments with harmonic oscillators," J. Chem. Phys 103, 4393 (1995).

(75) M. Khalil and A. Tokmakoff, "Signatures of vibrational interactions in coherent two-dimensional infrared spectroscopy," Chem. Phys. 266, 213 (2001).

(76) R. A. Goldbeck, Y. G. Thomas, E. Chen, R. M. Esquerra and D. S. Kliger, "Multiple pathways on a protein-folding energy landscape: kinetic evidence," Proc. Natl. Acad. Sci. USA 96, 2782 (1999).

(77) Y. L. A. Rezus and H. J. Bakker, "Oreintational dynamics of isotopically diluted H_2O and D_2O," J. Chem. Phys. 125, 144512 (2006).

(78) L. Piatkowski, K. B. Eisenthal and H. J. Bakker, "Ultrafast intermolecular energy transfer in heavy water," Phys. Chem. Chem. Phys. 11, 9033 (2009).

(79) C. J. Fecko, J. D. Eaves, J. J. Loparo, A. Tokmakoff and P. L. Geissler, "Ultrafast hydrogen bond dynamics in the infrared spectroscopy of water," Science 301, 1698 (2003).

(80) S. Park and M. D. Fayer, "Hydrogen bond dynamics in aqueous NaBr solutions," Proc. Natl. Acad. Sci. U.S.A. 104, 16731 (2007).

(81) A. W. Omta, M. F. Kropman, S. Woutersen and H. J. Bakker, "Negligible effect of ions on the hydrogen-bond structure in liquid water," Science 301, 347 (2003).

(82) B. Nigro, S. Re, D. Laage, R. Rey and J. T. Hynes, "On the ultrafast infrared spectroscopy of anion hydration shell hydrogen bond dynamics," J. Phys. Chem. A 110, 11237 (2006).

(83) Y.-S. Lin, B. M. Auer and J. L. Skinner, "Water structure, dyanamics, and vibrational spectroscopy in sodium bromide solutions," J. Chem. Phys. 131, 144511 (2009).

(84) B. Halle and G. Karlström, "Prototropic charge migration in water. Part 2. Interpertation of nuclear magnetic resonance and conductivity data in terms of model mechanisms," Journal of the Chemical Society, Faraday Transactions 2 79, 1047 (1983).

(85) R. A. Robinson and R. H. Stokes, *Electrolyte Solutions*, 2nd Revised Ed., (Dover, Mineola, N.Y., 1959).

6.A. Appendix. Calculation of Linear Absorption Spectra

The linear absorption spectra are that appear in Fig. 6-14 were calculated by adding the effects of population relaxation to Eq. 2-33 of Chapter 2 which describes the free induction decay of a vibrational transition within the second Cumulant and Condon approximations. This gives the following result for the free induction decay of ω_{Ion}:

$$S_{FID}^{Ion}(t) = \left|\boldsymbol{\mu}_{10}^{Ion}\right|^2 \exp\left[-i\left\langle \omega_{10}^{Ion}\right\rangle t - t/T_1^{Ion} - h_{10}^{Ion*}(t_1)\right]. \qquad (6\text{-A1})$$

Similar expressions can be written for ω_W and ω_{Sol}. The absorption lineshape is simply the Fourier transform of the sum of the free induction decays of ω_W, ω_{Ion}, and ω_{Sol}.

6.B. Appendix. Fit Parameters used for the Spectral Model

In Tables 6-B1 and 6-B2 we provide the best fit parameters for our spectral model. Table 6-B1 contains parameters that are independent of the sodium deuteroxide concentration whereas the values in Table 6-B2 are allowed to vary with concentration. In the course of modeling the hot ground state response, we found that the inclusion of a thermal heating contribution due to ω_{Sol} led to a long lived offset in the peak shift decay that is not observed experimentally. Thus, we have excluded any thermal contribution that arises from ω_{Sol} from our model. The shape of the hot ground state absorption is dictated by the two parameters $\left|\Delta\boldsymbol{\mu}_{10}\right|$ and $\Delta\omega_3$ which are initially set to match the form of the dispersed pump-probe at a waiting time of 10 ps. Although the value of $\left|\Delta\boldsymbol{\mu}_{10}\right|$ is found to vary with NaOD concentration, possibly due to the change in the thermal conductivity of the solvent upon the addition of NaOD, it was found that adequate agreement with our experimental data could be reached by using the same values of $\left|\Delta\boldsymbol{\mu}_{10}\right|$ and $\Delta\omega_3$ for ω_W and ω_{Ion} at each concentration of NaOD. Also, as others have

noted,[52,53] the intensity of the observed thermal response will be dependent on the number of O-H oscillators in the system. For each sample, the concentration of added NaOD was well controlled, however the amount of water that was added to each sample was adjusted on a day to day basis to provide an optical density below 0.4, leading to a slight variation in the amount of HOD present in each sample. We suspect that the lack of a visible trend in the best fit values for K_{Therm}^{W}, K_{Therm}^{Ion}, and K_{D_2O} is the result of this slight variation in the O-H concentration of each sample.

In Tables 6-B3 and 6-B4 we list parameters used to construct the frequency-frequency correlation function, $C(t)$, which describes the spectral diffusion of ω_W, ω_{Ion}, and ω_{Sol}. The functional form used for $C(t)$ is given by Eq. 6-12 of the main text.

$\langle\omega_{10}^{W}\rangle$	$\langle\omega_{21}^{W}\rangle$	$\langle\omega_{10}^{Ion}\rangle$	$\langle\omega_{21}^{Ion}\rangle$	$\langle\omega_{10}^{Zundel}\rangle$	$\lvert\mu_{10}^{W}\rvert$	$\lvert\mu_{21}^{W}\rvert$
3402 cm^{-1}	3178 cm^{-1}	3578 cm^{-1}	3413 cm^{-1}	3402 cm^{-1}	1.0	1.394
$\lvert\mu_{10}^{Ion}\rvert$	$\lvert\mu_{21}^{Ion}\rvert$	$\lvert\mu_{10}^{Sol}\rvert$	$\lvert\mu_{21}^{Sol}\rvert$	T_1^{W}	T_1^{Ion}	T_1^{Sol}
0.90	1.255	1.565	2.195	0.71 ps	1.30 ps	0.71 ps
T_1^{Zundel}	T_1^{Int}	$T_1^{D_2O}$	$\Delta\omega_3$	$\tau_{Ion\rightarrow W}$	τ_C^{Zundel}	
0.11 ps	2.0 ps	0.40 ps	0.3285 cm^{-1}	3.0 ps	35.0 fs	

Table 6-B1: Best fit parameters obtained from the model described in the text for terms that do not vary as a function of deuteroxide concentration.

[NaOD] (M)	$\langle\omega_{10}^{Sol}\rangle$ (cm^{-1})	$\langle\omega_{21}^{Sol}\rangle$ (cm^{-1})	K_{Zundel}	$\lvert\Delta\mu_{10}\rvert$	K_{Therm}^{W}	K_{Therm}^{Ion}	K_{D_2O}
0	NA	NA	NA	0.9986	60.0	NA	226.0
1.1	3208	3193	0.103	0.9984	47.0	37.6	75.9
2.6	3193	2823	0.266	0.9981	63.7	25.5	127.4
5.3	3167	2781	0.592	0.9977	35.0	43.7	46.8
7.9	3142	2741	0.740	0.9972	27.4	21.9	63.0
10.6	3116	2701	1.281	0.9968	19.9	9.95	106.4
15.1	3073	2635	1.324	0.9948	38.0	15.2	232.5

Table 6-B2: Best fit parameters obtained from the model for terms that are sensitive to the amount of deuteroxide present in solution.

$C^{W}(0)$	$C^{Ion}(0)$	$C^{Sol}(0)$	$C^{Zundel}(0)$
5.83×10^{-4} fs^{-2}	1.46×10^{-4} fs^{-2}	1.28×10^{-3} fs^{-2}	1.17×10^{-3} fs^{-2}
τ_{fast}	τ_{slow}	τ_{osc}	ω_{osc}
107 fs	1410 fs	104 fs	160 cm^{-1}

Table 6-B3: The time scales of components and initial values of the frequency-frequency correlation functions used to model the presented experimental data.

[NaOD] (M)	0	1.1	2.6	5.3	7.9	10.6	15.1
A_{fast}	0.4255	0.4712	0.5055	0.5209	0.3593	0.369	0.2547
A_{slow}	0.2018	0.147	0.1168	0.1108	0.0857	0.0083	0
A_{osc}	0.3727	0.351	0.3467	0.3018	0.3549	0.2982	0.2725
Δ_{static}	0	0.0308	0.031	0.0665	0.2001	0.3245	0.4728

Table 6-B4: Amplitudes of the four components that comprise $C(t)$ as a function of NaOD concentration.

Chapter 7

An Examination of Reaction Coordinates for Proton Transfer in Liquid Water using an Empirical Valence Bond Model of Aqueous NaOH

7.1. Introduction

Building a mechanistic description for a chemical reaction that takes place in liquid water is often a complex undertaking. Over small length scales, water's hydrogen bonding network imposes a high degree of structure that is not normally found in simple liquids. Changes in the structure of a reactant due to the formation or breakage of individual hydrogen bonds between the reactant and water can alter the barrier for a chemical reaction. For example, in the folding of small peptides, hydrogen bonds between the protein backbone and water must often be broken to allow native contacts to form between the protein residues.[1] Over length scales that span a few solvation shells in size, water's well defined structure is gradually lost. Nevertheless, the behavior of water molecules over these large length scales can be equally important in the description of a chemical reaction. Although difficult to describe in terms of the motion of individual molecules, the collective behavior of the liquid over long distances can give rise to both density and dielectric fluctuations that play important roles in chemical reactions. Collective coordinates of this type are at the heart of many theories for liquid phase

chemical reactions, such as Marcus theory which uses the collective reorganization of the solvent as a reaction coordinate for electron transfer.[2,3]

In aqueous proton transfer reactions, the formulation of a specific reaction coordinate is often difficult because both local and collective processes play important roles in guiding the motion of individual protons. In an extensive body of work, Zundel[4,5] has sought to explain the broad mid-infrared absorption continua observed in strong acids and bases as the result of polarization fluctuations of the solvent, and has proposed that such fluctuations guide the motion of the proton. Ando and Hynes[6,7] examined the dissociation of HCl in aqueous solution, and demonstrated that the initial transfer of the proton to a water molecule is driven by changes of the solvent polarization. However, the breakage of a hydrogen bond between a water molecule and the oxygen atom of the newly formed H_3O^+ ion was also found to stabilize the ion, highlighting the importance of both local hydrogen bond rearrangements and the collective fluctuations of the liquid. Likewise, a multistate empirical valence bond molecular dynamics simulation (MS-EVB) study of the aqueous H_3O^+ ion[8] identified a number of hydrogen bond creation and breakage events that can act to promote the transfer of a proton from the ion to a hydrogen bonded partner. It was also found that the time scale for the ion's diffusion mapped closely onto to that for hydrogen bond fluctuations of the liquid,[9] which have been shown to be related to fluctuations of the collective electric field of the solvent.[10]

In the case of autoionization, a Car-Parrinello molecular dynamics (CPMD) study[11] found that upon the dissociation of a water molecule into a hydroxide and hydronium ion, these two species rapidly travel along hydrogen bonded water "wires," which allows the newly formed ions to separate a distance of three or more water

molecules. While the breakage of the hydrogen bonded chain was found to be a principle means of preventing the recombination of these ions, the length of the chain itself could not provide a unique determination of the reaction's transition state. A second, collective coordinate based on the solvent electric field was found to provide the driving force for the reaction.

In studies of the structural diffusion of the hydroxide ion, researchers have largely emphasized how changes in the local hydrogen bonding structure surrounding the ion allows it to accept a proton from one of its hydrogen bonding partners. Recent CPMD simulations[12-15] have suggested that the most stable form of the aqueous hydroxide ion is a "hypercoordinated" configuration, wherein the ion's oxygen atom accepts four hydrogen bonds, but found that the number of hydrogen bonds accepted by the ion decreases to three during proton transfer events. This led to the suggestion that the rate limiting step for proton transfer is the breakage of a hydrogen bond to the ion. Such a mechanism can be rationalized by recognizing that the transfer of a proton to a hypercoordinated hydroxide ion results in a water molecule that accepts three hydrogen bonds, and is energetically unfavorable. The breakage of a hydrogen bond allows the ion to adopt a structure that can readily be reincorporated into water's hydrogen bonding network upon proton transfer. Tuckerman, Chandra, and Marx[14] named this process "presolvation" since the solvent must adopt a configuration that preferentially solvates the products of the proton transfer reaction before it can occur.

While this conduction mechanism has not gone without scrutiny, much of the published criticism has focused not on the validity of the presolvation concept, but instead questioned the relative stability of the three- and four-coordinate configurations

found in the CPMD work.[16] The role that collective coordinates play in the structural diffusion of the hydroxide ion remains unaddressed by the presolvation mechanism. While a hypercoordinated structure may represent a large barrier to proton transfer, once this barrier has been lowered by conversion of the ion to a three-coordinate state, the driving force that then leads to the transfer of a proton to the three-coordinate ion is not obvious. Also unclear is the mechanism by which molecules exchange into and out of the solvation shell of the ion. In bulk water, the rearrangement of hydrogen bonds is a highly collective process, involving the loosely correlated motion of many water molecules.[17,18] The results of recent molecular dynamics simulations[19-21] and our own experimental work[22-24] suggest that hydrogen bond exchange is a concerted process involving a large amplitude rotation of the exchanging molecule that occurs as a second solvation shell water inserts itself across a first solvation shell hydrogen bond (See Fig. 5-16). Given that the solvation shell structure of the ion can be quite different from that of bulk water, it is unclear over what length and time scales the correlated motions of the liquid act to accommodate a newly formed hydroxide ion into water's tetrahedral hydrogen bonding network. Questions are also raised by the observation that the viscosity of aqueous solutions is known to increase strongly upon the addition of sodium hydroxide.[25] While this implies a slowing of the overall system dynamics, whether this change is simply a slowing of the characteristic motions of the solvent due to the presence of charged particles or instead due to the introduction of new solvation processes specifically associated with the migration of the hydroxide charge defect is uncertain.

To address these issues, we have carried out a series of ultrafast, nonlinear infrared experiments that probe the O-H stretching transition of a dilute solution of HOD dissolved in $NaOD/D_2O$. We chose to employ the O-H stretch as a vibrational probe because its frequency, ω_{OH}, is related to the strength of the hydrogen bond formed by the proton. Changes in the local solvent environment about a HOD molecule due to the formation of a hydrogen bond to OD^-, the breakage of a hydrogen bond, or the formation of a delocalized shared proton state, $DO\cdot\cdot H\cdot\cdot OD^-$, each induce detectable changes in ω_{OH} that can be used to infer the system dynamics that promote the structural diffusion of the hydroxide ion. In the preceding chapter, we demonstrated that our experimental results show the existence of at least two new time scales that appear upon the addition of sodium deuteroxide to HOD/D_2O. At short time delays, a spectrally broad feature that decays with a time constant of 110 fs was observed in pump-probe and 2D IR experiments. In the 1-10 ps waiting time range, 2D IR spectra demonstrated features consistent with the growth of cross peaks indicating exchange between the high frequency OH^- stretch and the main HOD/D_2O band. The appearance of these exchange features describes the time scale for the solvation of a newly formed OH^- ion upon proton transfer. While heating effects complicated the extraction of a time scale for the growth of this feature, our data enabled us to determine a lower limit of 3 ps for this solvation process.

While our experiments allow us to measure time scales associated with the structural diffusion of the hydroxide ion, it is difficult to build a mechanistic interpretation of these time scales based solely on our experimental results. In recent years, the interpretation of nonlinear infrared experiments has greatly benefited from the

development of semiempirical methods that allow the calculation of nonlinear signals from both classical[10,26-30] and *ab initio* based molecular dynamics simulations.[31,32] These techniques allow a direct connection to be made between the signals that are measured in nonlinear experiments and the underlying dynamics of the system that give rise to these signals. The calculation of spectroscopic observables also provides a new means of validating classical simulation models. Simulation models are often optimized to reproduce bulk thermodynamic properties, calling into question their ability to reproduce microscopic dynamics. Comparison between experimental and simulated nonlinear signals allows us to test the validity of the employed simulation model and the semiemprical method used for the calculation of nonlinear signals[33,34] while gaining microscopic insight into the origin of the dynamics observed in experiments.

In this chapter, we provide a mechanistic interpretation of our experimentally measured nonlinear spectra through the use of a newly developed MS-EVB simulation model of aqueous hydroxide.[35,36] To make a direct comparison between our spectroscopic results and the dynamics found in the MS-EVB simulation, we have devised a methodology for the calculation of nonlinear signals from this classical simulation model that is able to reproduce the trends observed in linear infrared spectra of HOD/D_2O upon the addition of NaOD. Calculated 2D IR spectra indicate that the transient feature observed at short waiting times is associated with excitation pathways that involve the direct excitation of vibrational overtone transitions of Zundel-like $DO{\cdot\cdot}H{\cdot\cdot}OD^-$ states, wherein a proton is significantly shared between a HOD molecule and a deuteroxide ion. When individual proton transfer events are examined, evidence in support of the presolvation mechanism proposed on the basis of CPMD simulations is

found, but we are unable to identify a unique transition state solely on the basis of a decrease in hydroxide ion's coordination number. Instead, we find that the collective electric field along the proton transfer direction is better suited to describe the creation and relaxation of Zundel-like transition states. The relaxation of this coordinate largely mimics that found for structural relaxation of the surrounding water bath, suggesting that equilibrium fluctuations of the liquid provide the driving force for the proton transfer reaction. While electric field fluctuations largely direct the motion of the shared proton, we also observe an additional slow time scale of 7.4 ps associated with the breakage of a hydrogen bond to the hydrogen atom of a newly formed hydroxide ion. This process manifests itself through the growth of a cross peak in the calculated 2D IR spectra over picosecond waiting times. The slow time scale associated with the process is believed to be the result of the water molecules forming an asymmetric solvation shell around a newly formed hydroxide ion upon proton transfer.

7.2. MS-EVB Simulation Model of Aqueous Sodium Hydroxide

The multistate, empirical valence bond method provides a convenient means of simulating the breakage and formation of chemical bonds within the confines of a classical molecular dynamics simulation.[37,38] In this approach, for each simulated atomic configuration, a set of limiting states are identified that correspond to different possible chemical bonding connectivities. These bonding configurations serve as a set of basis states used to construct an EVB Hamiltonian wherein the energy of each state and the coupling between them are determined on the basis of either quantum calculations or an empirical parameterization based on a set of experimental observables. Once the EVB Hamiltonian has been computed, it is subsequently diagonalized and the lowest energy

eigenstate and its corresponding eigenvector denote the ground state potential energy and the chemical bonding configuration of the system.

While MS-EVB simulation models have been employed for nearly a decade to study the transport of the excess proton,[39-42] it is only within the course of the past year that this methodology has been used to examine the transport of the hydroxide ion.[43] The model used for this study was developed by our collaborators at the University of Illinois at Urbana-Champaign.[36] In this model, the offdiagonal elements of the EVB Hamiltonian are parameterized to reproduce the results of *ab initio* electronic structure calculations (MP2/aug-cc-pVDZ) of various configurations of the $H_3O_2^-$ ion, while the diagonal elements are based on a classical empirical simulation potential of aqueous NaOH that does not allow for proton transfer.[35] This empirical potential describes water molecules using a flexible SPC/E model[44] and treats the sodium cation as a Lennard-Jones particle with a positive charge of 1.0 *e*.

The electron density of the hydroxide ion is treated in a unique manner in the classical potential. Previous attempts to model the hydroxide ion using simple point charges placed on the atom centers often result in the appearance of overcoordinated structures, wherein the ion accepts 5 to 7 hydrogen bonds[45] and donates a strong hydrogen bond through its hydrogen atom. These results are inconsistent with neutron scattering experiments, which suggest that on average the ion can only donate a weak hydrogen bond and possesses a coordination number of 3.9.[46,47] To correct this problem, the empirical potential that we employ distributes the negative charge of the ion onto a massless, charged ring instead of a point centered on its oxygen atom (Fig. 7-1). This choice is motivated by the results of CPMD simulations that show that the negative

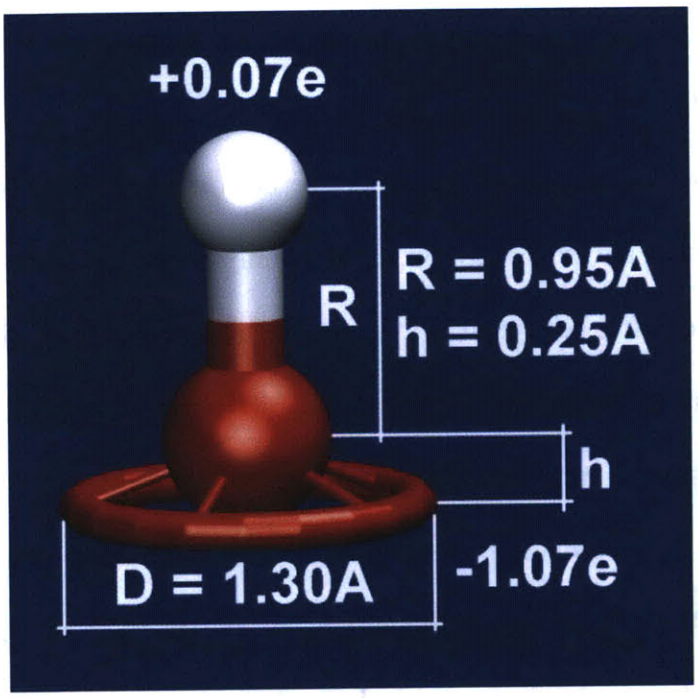


Figure 7-1: Empirical charged ring model employed for the OH^- ion. From Ref. 36. Instead of placing the charge of the oxygen atom at the atomic center, it is spread uniformly along twenty massless positions along a ring perpendicular to the OH^- bond axis.

charge of the ion is often distributed in space somewhat evenly about its oxygen atom.[12] MS-EVB Simulations carried out employing this potential give an average coordination number* of 3.7 for the ion and radial distribution functions similar to those found in the CPMD simulations.[36] The model gives a diffusion constant of 0.31 $Å^2$/ps for the hydroxide ion, which is within a factor of two of the experimental value of the diffusion constant, 0.53 $Å^2$/ps, determined on the basis of mobility measurements.[48]

The results presented in this chapter were derived using a pair of MS-EVB simulation trajectories consisting of a single NaOH ion pair solvated by 214 H_2O

* One of the most commonly used hydrogen bonding definitions in water is one based on geometric criteria, $R_{OO} \leq 3.5$ Å and a HOO angle less than 30° (See Fig. 5-1 of Chapter 5). We adopt this definition when discussing hydrogen bonding, but drop the angular constraint when determining the coordination number of the ion. Small changes in the cutoff values used in this definition were found to make only minor changes to the results presented in this chapter.

molecules in a cubic box with periodic boundary conditions (density = 1.01 g/cm^3). The system was equilibrated for 100 ps by using velocity rescaling (T = 303.8 K) before making a production run 900 ps in length in the NVE ensemble using the Velocity-Verlet integrator.[49] For one trajectory, a 0.5 fs time step was used while a 1.0 fs step size was employed for the other, but no discernable differences in the dynamics were detected. Ewald summation was used to account for long-range electrostatic forces. The kinetic energy was rescaled every 10 ps to compensate for minor energy drift. This energy rescaling has been demonstrated to not affect the diffusion constant of the ion,[36] leading us to conclude that it does not disturb the dynamics of the system over the time scales of interest.

7.3. Methodology for the Calculation of Vibrational Frequencies

Comparison between simulation and experiment can provide us with a means of interpreting our experimental results in mechanistic detail. In Chapter 5, we employed a method based on second order perturbation theory to calculate vibrational frequencies from a classical water simulation model. However, given that the stretching potential of a Zundel-like $H_3O_2^+$ state is expected to resemble a double well, we anticipate that the method used for the calculation of vibrational frequencies in Chapter 5,[10] which describes changes to the O-H stretching frequency through weak perturbations applied to a Morse potential, will be unable to properly describe the spectral signatures associated with proton transfer events. This has forced us to develop a new methodology[50] for the calculation of both vibrational frequencies and transition dipoles that is derived from semiempirical cluster-based mapping methods used in simulations of isotopically dilute water.[27,32,51-54]

Our methodology employs a Hamiltonian similar to that used in Chapter 5 to describe the spectroscopy of dilute HOD in D_2O:

$$H = H_S + H_B + H_{SB}. \tag{7-1}$$

H_S denotes the quantum mechanical degree of freedom probed by our experiments, the O-H stretch of the HOD molecule, while H_B describes the remaining intra- and intermolecular degrees of freedom of the system. In writing Eq. 7-1, we have made an adiabatic separation between the O-H stretch and the modes of the bath. For liquid configurations wherein the proton is localized on the HOD molecule, this assumption holds well sine the motions of the bath are much slower than the O-H bonds vibrational period. However, as a proton becomes shared between a HOD molecule and an OD^- ion, its vibrational frequency is expected to decrease significantly. Infrared spectra of concentrated bases display a broad absorption continuum that spans values from a few hundred wavenumbers up to the low frequency side of the O-H stretch peaked at 3400 cm^{-1}.[55] Gas phase measurements of the $H_3O_2^-$ ion have shown that the shared proton stretch can reach values as low as 697 cm^{-1}.[56] Thus, as the frequency of the O-H stretch decreases during proton transfer, it can come into resonance with both the bending transition of the HOD molecule as well as combination bands involving intermolecular motions such as librations. In this case, our assumption of a lack of coupling between the O-H stretch and the other modes of the system is not expected to hold. Despite this shortcoming, as we shall see in the discussion that follows, we can still gain insight into our experimental results through the use of this model. In the sections below, we will note instances where this inadequacy of our model manifests itself in our results.

To determine the shift in the energy of each of the system eigenstates due to the coupling between the system and bath degrees of freedom, H_{SB}, we use a map generated from electronic structure calculations that links the shift in the energy of each eigenstate to a collective coordinate that can be computed from the MS-EVB simulation at each time step. To generate this map, we output a series of instantaneous atomic configurations from the simulation. For each configuration, we select a hydrogen atom and then form a cluster containing any water molecules whose oxygen atoms are within 9.286 Å, half the simulation box size, of the selected hydrogen. We also include both the Na^+ and OH^- ions present in the simulation if they fall within this distance criterion. Although the simulation dynamics are propagated with an entirely protonated sample, in constructing the cluster we assume that the selected hydrogen atom is that of a HOD molecule and that all other hydrogens in the cluster are deuterons.[†] We then stretch the O-H bond using DFT calculations (Gaussian 98: B3LYP 6-311+G(d,p)) in which all molecules within 5 Å of the selected hydrogen (16-18 molecules) are treated explicitly and the remaining molecules in the cluster (~100) are treated as point charges and calculate the vibrational potential in 0.1 Å steps (Fig. 7-2). The calculated potentials are then fit to an 8th order polynomial and the vibrational frequencies and transition dipole moments for transitions involving v = 0-3 are obtained from the 1D O-H stretching potential through the discrete variable representation method using a basis set of 75

[†] From this point forward we will describe the simulation as if it consists of an isotopically dilute mixture even though it consists of a fully hydrogenated system. When referring to multiple water molecules, the designation of a given molecule as HOD or as an OH^- ion will indicate that we are examining the vibrational frequencies of that molecule. Molecules referred to as D_2O or OD^- may influence the behavior of molecules whose frequencies we examine, but are assumed to be spectroscopically inactive. It should also be kept in mind that each of the time scales that we determine from the simulation correspond to that of a hydrogenated bath. Experimentally, we examined a dilute solution of HOD in $NaOD/D_2O$. While the comparison of experimental and simulated time scales for motions involving the shared proton stretch are appropriate, we expect simulated time scales for the motions of the bath to be faster than those inferred from our experiments.

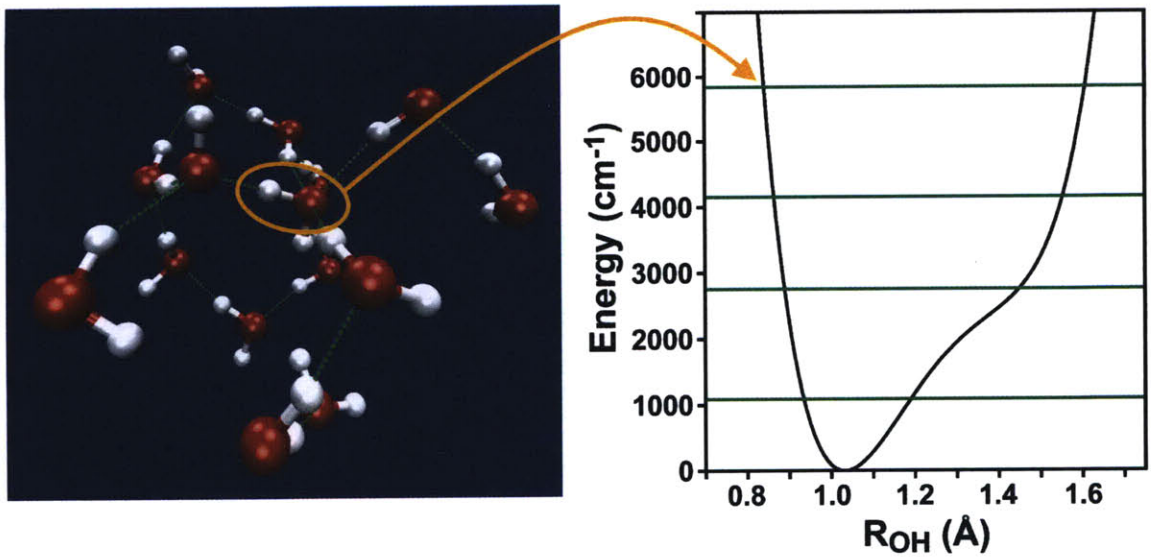


Figure 7-2: Illustration of our procedure for the calculation of vibrational frequencies. Clusters extracted from the MS-EVB simulation serve as an input to DFT electronic structure calculations that are used to stretch an O-H bond in the middle of the cluster. This yields a 1D potential energy surface from which the vibrational eigenstates and transition dipole moments can be calculated. The set of calculated frequencies and transition dipoles are then mapped onto a coordinate that can be easily calculated from the simulation at each time step.

harmonic oscillator states and the reduced mass of the HOD molecule (0.954426 amu). 1205 separate clusters were analyzed to generate the frequency map. In 19% of these clusters, the nearest neighbor to the HOD molecule is another water molecule, while 44% of the clusters correspond to a HOD molecule that is hydrogen bonded to the hydroxide ion. In the remaining clusters we stretch the O-H bond of the hydroxide ion itself. To ensure a proper sampling of proton transfer events, ~60% of the clusters where the HOD molecule is in the solvation shell of the hydroxide ion were sampled at evenly spaced intervals over 24 separate proton exchange events.

Once the frequencies and transition dipoles of each cluster have been determined, a suitable mapping variable that can be calculated from the simulation at each time step at low computational cost must be selected. Previous simulation studies of HOD/D_2O have

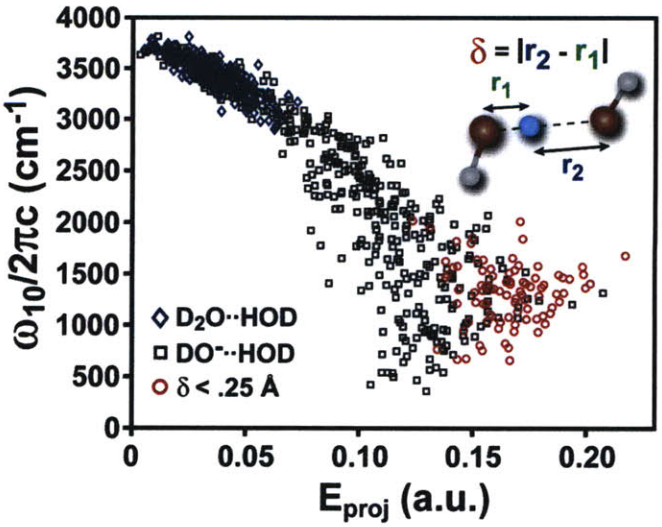


Figure 7-3: Correlation between the projection of the collective electric field onto the O-H bond at the position of the proton, E_{proj}, and ω_{10} calculated from clusters taken from the MS-EVB simulation. For a given DOH··OD$^-$ configuration, $\delta = |r_{HO}-r_{OH}-l|$. An equally shared proton corresponds to $\delta = 0$.

noted a strong correlation between ω_{OH} and the component of the electric field projected along the O-H bond at the position of the proton.[32,51,57] This represents a logical coordinate to choose for the mapping of ω_{OH} since the first order perturbative correction to the O-H frequency resembles a Stark shift Hamiltonian.[10] In Fig. 7-3 we plot a comparison between the frequency of the $v = 1 \leftarrow 0$ transition (ω_{10}) determined from our cluster calculations and the collective electric field projected along the O-H bond. To calculate the collective field, we have only included field contributions due to molecules contained within each cluster, and assumed that the negative charge of the hydroxide ion is localized on its oxygen atom. Calculations of the collective field including all molecules in the simulation box as well as Ewald sums make only minor changes in the calculated values of the field.[10,32] For values of the field below 0.06 a.u. (1 atomic unit = 51.442 V/Å), a range indicative of HOD molecules hydrogen bonded to D_2O, we find that the correlation between ω_{10} and E_{proj} is approximately linear, similar to the results

presented in Fig. 5-1 of Chapter 5. However, this linear correlation observed for weak to strong hydrogen bonds is observed to break down for DO··H··OD$^-$ structures when the difference in O-H distances, δ, becomes small (δ < 0.25 Å). At a value of E_{proj} = 0.15 a.u., the calculated values of ω_{10} span a range between 600 cm^{-1} and 2000 cm^{-1}, indicating that a variable better correlated with ω_{10} is needed for the mapping of vibrational frequencies.

Recent simulations of a model parameterized to describe proton transfer in a phenol-amine complex dissolved in chloromethane found a 1:1 mapping between the difference in energy of the reactant and product wells of the O-H stretching potential and its vibrational frequencies.[58] In Fig. 7-4B we plot the correlation between the frequency of the v = 1←0 transition, ω_{10}, and the solvent coordinate, ΔE_{sol}, calculated from the 1D potentials derived from the electronic structure calculations. ΔE_{sol} is defined as the difference in energy of the O-H stretching potential evaluated at two distances, 1.0 and 1.5 Å, which approximate the positions of the two minima of the potential for a proton that is strongly shared between two oxygen atoms (Fig. 7-4A).[‡] For a proton localized on a HOD molecule, we expect ΔE_{sol} to adopt a large value. As the proton becomes more delocalized between two oxygen atoms, ΔE_{sol} will decrease and eventually reach a value of zero for a proton that is equally shared in a Zundel-like configuration. This is exactly the behavior observed in Fig. 7-4B. HOD molecules that donate hydrogen bonds to D_2O display values of ΔE_{sol} in the range of 10000 – 23000 cm^{-1}, while configurations in which

[‡] This is not meant to mean that these two distances actually correspond to the minima of the potential for an isolated $H_3O_2^-$ ion. While physically motivated, these values were selected after computing ΔE_{sol} using different positions for the calculation of the potential energy of the system. The values 1.0 Å and 1.5 Å were found to give the largest change in ΔE_{sol} with ω_{10}.

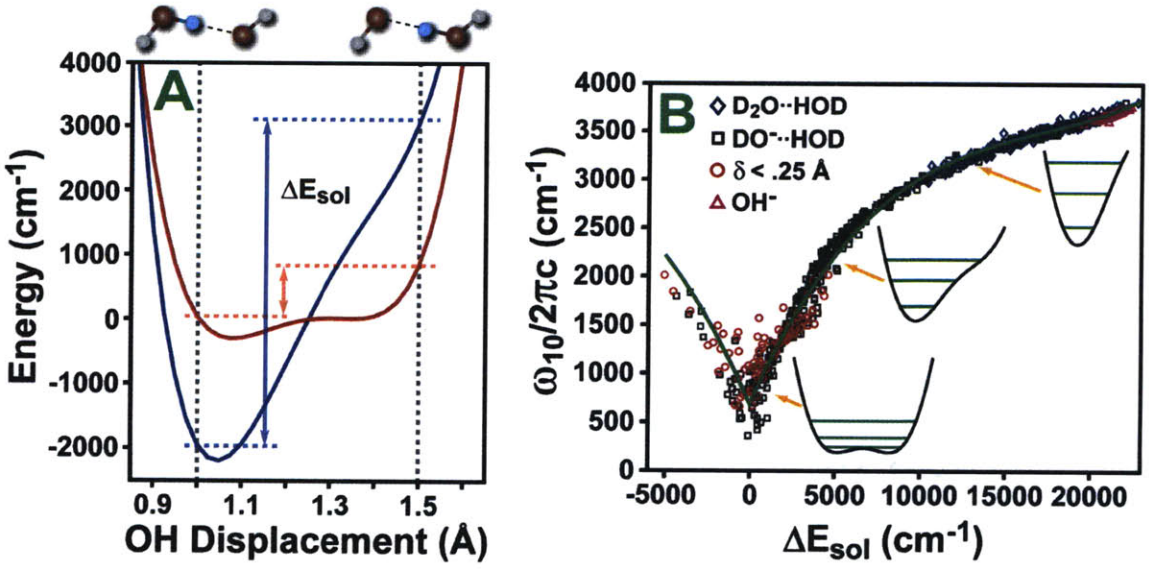


Figure 7-4: (A) Schematic illustration of the solvation coordinate, ΔE_{sol}, used as a mapping variable for the calculation of vibrational frequencies. This parameter corresponds to the difference in energy of the potential evaluated at two points close to the minima of the double well potential for a proton shared between two oxygen atoms. As the proton becomes equally shared, this parameter approaches zero. (B) Mapping between ΔE_{sol} and ω_{10} calculated from DFT calculations performed on clusters extracted from the MS-EVB simulation. As in Fig. 7-3, δ is defined as $\delta = |r_{HO}-r_{OH}|$ for a given $DOH\cdot\cdot OD^-$ configuration.

the proton is nearly equally shared ($\delta < 0.25$ Å) are clustered about $\Delta E_{sol} = 0$. Likewise, the stretching transition of the OH^- ion is found to adopt frequencies in the range of 3500 – 3700 cm^{-1}, consistent with the appearance of a peak on the high frequency side of the O-H stretching transition in Raman spectra of concentrated aqueous alkali solutions.[59-62] Although the mapping between ΔE_{sol} and ω_{10} is nonlinear, it is single valued and has a high correlation coefficient, $\rho = 0.955$. Thus, ΔE_{sol} can be used for the calculation of vibrational frequencies. Interestingly, no discontinuity is observed between points calculated by stretching the bonds of HOD molecules and OH^- ions despite the fact that these are two distinct chemical species. This suggests that a general relationship between ΔE_{sol} and ω_{10} may exist for many different types of O-H bonds.

Unfortunately, the calculation of ΔE_{sol} using DFT at each simulation time step is too computationally expensive to be practical. As an approximation of the solvent coordinate determined on the basis of DFT, at each time step we stretch the O-H bond and calculate ΔE_{sol} using the EVB potential. Tracing out the full O-H stretching potential in this fashion is inaccurate because the empirical model used for water parameterizes the Lennard-Jones force solely in terms of the oxygen atom positions. Nonetheless, our calculations suggest that although the computation of ΔE_{sol} in this manner is a poor approximation to that derived from DFT, comparison of the two quantities shows that they are linearly correlated ($\rho = 0.95$, See Appendix 7.A). Thus, as an initial step, we map the solvation coordinate calculated using the empirical EVB potential, ΔE_{EVB}, onto that estimated on the basis of DFT calculations, ΔE_{DFT}, using this linear correlation. The mapping shown in Fig. 7-4B is then subsequently used to calculate ω_{10}.

The green trace in Fig. 7-4B represents a 4th order polynomial fit to the calculated data. In a subset of the calculated points, ΔE_{sol} is found to adopt a negative value, indicating a preference for these configurations to engage in proton transfer. However, the mapping between ΔE_{sol} and ω_{10} appears to behave symmetrically about $\Delta E_{sol} = 0$, so we have reflected our polynomial fit to the data about this point. Values of ω_{10} calculated using this fit give a rms error of 54.8 cm^{-1} for HOD molecules hydrogen bonded to D_2O. This is a comparable level of error to that obtained for a recent electric field-based frequency map for HOD/D_2O.[53] In Appendix 7.A, we give tables of the fit parameters used to calculate the remaining vibrational frequencies of the potential and provide a description of our methodology for the calculation of the transition dipole moments that link the vibrational eigenstates of the potential.

7.4. Correlations Between Frequency and Structure

With a methodology in place to calculate vibrational frequencies, we can now directly test how changes in the hydrogen bonding configuration of the HOD molecule are reflected by shifts in the vibrational frequencies of the O-H stretching potential. In Fig. 7-5A we plot the correlation between ω_{10} and δ, the difference between the O-H bond length and the distance of the proton to its hydrogen bonding partner. The yellow/red contours plotted in the figure correspond to HOD molecules hydrogen bonded to D_2O (hereafter referred to as HOD/D_2O), while the blue contours denote water molecules in the solvation shell of the OD^- ion. At frequencies below 3400 cm^{-1}, the correlation between ω_{10} and δ for molecules hydrogen bonded to D_2O is relatively narrow and approximately linear. At higher frequencies, the correlation widens due to the large distribution of strained or broken hydrogen bonding geometries present in the liquid. The calculated correlation between δ and ω_{10} for HOD/D_2O appears similar to that which has been calculated between ω_{10} and other geometric parameters such as the oxygen-oxygen separation between the HOD molecule and its hydrogen bonding partner,[26,31,57,63] and lends support to the validity of our frequency calculation methodology.

Examining the correlation for the first solvation shell of the OD^- ion, we find that the range of frequencies spanned by molecules in the ion's solvation shell is quite broad, extending from values as low as ~700 cm^{-1} up to 3500 cm^{-1}. While the range of possible values of δ for a given value of ω_{10} is quite broad compared to that found for HOD/D_2O, we do find an approximately linear correlation between δ and ω_{10} below ω_{10} = 3000 cm^{-1}. This indicates that we can interpret spectral shifts in ω_{10} in terms of changes in the strength of the hydrogen bond formed to the ion. At higher frequencies, we find that the

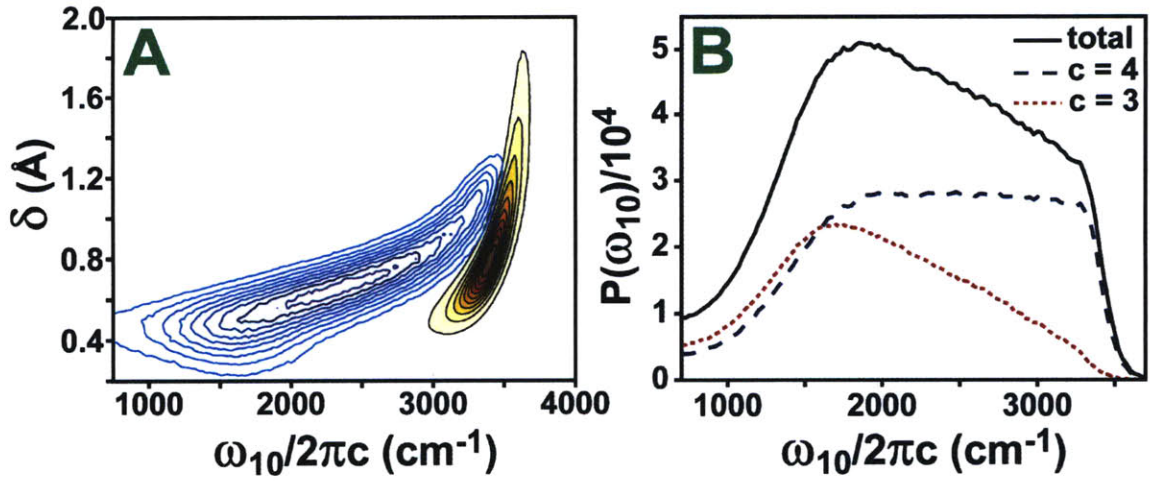


Figure 7-5: (A) Correlation between ω_{10} and δ for HOD molecules whose nearest neighbor is D_2O (yellow/red contours) and molecules within the first solvation shell of the OD^- ion (blue/purple contours). (B) Static frequency distribution for HOD molecules in the solvation shell of the OD^- ion (black). This distribution is subdivided into contributions due to three- (red dotted) and four-coordinate (blue dashed) OD^- ions.

correlation plots calculated for the solvation shell of the OD^- ion and for HOD/D_2O do not lie on top of each other. For an identical set of geometries, a hydrogen bond formed to OD^- will more strongly perturb the HOD molecule's O-H stretching potential than one formed to D_2O due to the ion's negative charge, resulting in a larger red shift of ω_{10}.

In the MS-EVB model, we find that in 60% of the realized simulation configurations, the OD^- ion has four nearest neighbors while in 38% of the configurations it only has three neighboring waters. In a study of the hydroxide ion in gas phase clusters, Li, Teige, and Iyengar[64] suggested that three- and four-coordinated hydroxide ions can be differentiated on the basis of their vibrational spectra. In Fig. 7-5B we test our ability to differentiate these two different types of ion configurations on the basis of ω_{10}. In black we plot the total static frequency distribution for molecules in the ion's first solvation shell, while in red and blue we plot the contributions to this distribution due to configurations in which the ion's solvation shell consists of three or four water molecules,

respectively. While we do find that molecules in three-coordinate configurations tend to preferentially absorb at lower frequency, the frequency distributions of three- and four-coordinate configurations are quite broad and overlapping. While gas phase spectra of these two types of configurations may allow them to be differentiated,[64] in the condensed phase we conclude that it will be difficult to identify spectral signatures that can be used to uniquely identify three- or four-coordinate hydroxide ions.

7.5. Signatures of Proton Transport in 1D Lineshapes

Before we can use our DFT-based frequency calculation methodology to compute nonlinear vibrational signals, we must first verify that it can reproduce the salient features of the linear absorption spectrum of dilute HOD in $NaOD/D_2O$. In the absence of lifetime effects, the absorption lineshape is proportional to the Fourier transform of the linear response function, $\mathbf{R}^{(1)}(\tau)$:[65-67]

$$\mathbf{R}^{(1)}(\tau) = \left\langle \left|\boldsymbol{\mu}_{10}(\tau)\right|\left|\boldsymbol{\mu}_{10}(0)\right| \exp\left[-i\int_0^{\tau}\omega_{10}(t)\,dt\right]\right\rangle \tag{7-2}$$

In writing Eq. 7-2, we explicitly take into account the variation of the O-H transition dipole with frequency (non-Condon effects) by allowing μ_{10} to vary in time. The variation of the O-H transition dipole has been demonstrated to play a strong role in the vibrational spectroscopy of water[52,68] and other hydrogen bonding systems.[69] We will show that this variation plays an extremely important role in vibrational spectra associated with the structural diffusion of the hydroxide ion.

To identify the spectral signatures associated with a HOD molecule simply interacting with the D_2O bath, we have calculated the 1D lineshape for a HOD molecule

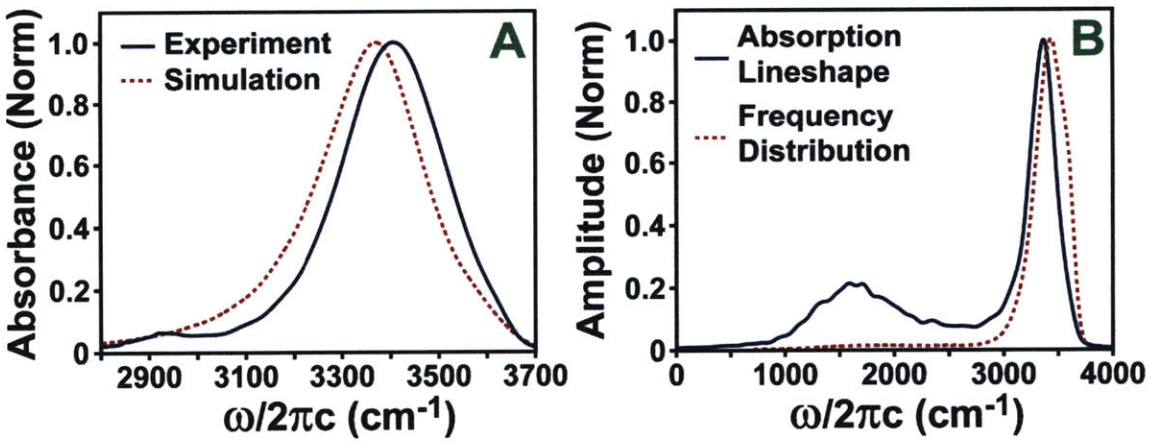


Figure 7-6: (A) Comparison between the experimental absorption spectrum of 1% HOD in D_2O and that calculated for a HOD molecule that does not enter the solvation shell of the OD^- ion. Although the calculated lineshape is red shifted by 36 cm^{-1} relative to experiment, its linewidth is quite comparable, validating to our simulation model. (B) Static frequency distribution and absorption lineshape calculated for a HOD molecule that spends 7.4% of the simulation trajectory in the solvation shell of the OD^- ion. The large increase in intensity at low frequency is due to a strong non-linear variation of the O-H transition dipole with ω_{10}.

that remains outside the solvation shell of the OD^- ion throughout the simulation run. In Fig. 7-6A, we plot a comparison between the calculated lineshape and the linear absorption spectrum of a solution of ~1% HOD dissolved in D_2O. While the calculated lineshape appears to be shifted to lower frequency by 36 cm^{-1} (ω_{max} = 3370 cm^{-1}), its linewidth of 252 cm^{-1} matches well with that found experimentally (260 cm^{-1} FWHM). The overall good agreement between the calculated and experimental lineshapes suggests that our simulation model may be able to reproduce the salient features that appear in the experimentally measured nonlinear signals described in Chapter 6.

In Fig. 7-6B, we extend our lineshape calculation to molecules in the solvation shell of the OD^- ion. The red trace shows the static frequency distribution for a HOD molecule that remains in the ion's solvation shell for 7.4% of the total simulation run. Examining this frequency distribution, we find that the HOD molecule maintains a

frequency centered near 3435 cm^{-1} when hydrogen bonded to D_2O. However, the frequency distribution also contains a long tail that extends to values as low as ~700 cm^{-1} due to interactions between it and the OD^- ion. In blue we plot the calculated absorption lineshape for this trajectory. While at high frequency we observe a red shift of ~65 cm^{-1} and narrowing of the absorption spectrum relative to the static frequency distribution due to non-Condon effects, the most striking feature seen in the absorption spectrum is the large increase in intensity in the frequency region below 3000 cm^{-1}, which corresponds to the frequency range wherein the HOD molecule forms a hydrogen bond to the OD^- ion. Even though the HOD molecule adopts a frequency below 2950 cm^{-1} for only 7% of the total simulation run, this spectral range contributes 43.5% of the total integrated absorption lineshape.

In Fig. 7-7A we plot the transition dipole of the $v = 1 \leftarrow 0$ transition determined from our cluster calculations as a function of its corresponding vibrational frequency, ω_{10}. As ω_{10} decreases, we find that μ_{10} increases sharply. Previous work that examined non-Condon effects in dilute HOD in D_2O concluded that μ_{10} varied by as much as a factor of 1.45 across the O-H lineshape at 20 °C.[70] Our results show that this observed increase in μ_{10} with decreasing frequency continues into the low frequency region indicative of protons shared in a $DO\cdot\cdot H\cdot\cdot OD^-$ configuration. At a frequency of 1000 cm^{-1}, μ_{10} is roughly five times as intense as its value at 3406 cm^{-1}, the peak of the experimental O-H stretch absorption lineshape of 1% HOD in D_2O. This large increase in the transition dipole moment allows us to rationalize the large increase in intensity at low frequency in the calculated linear absorption spectrum.

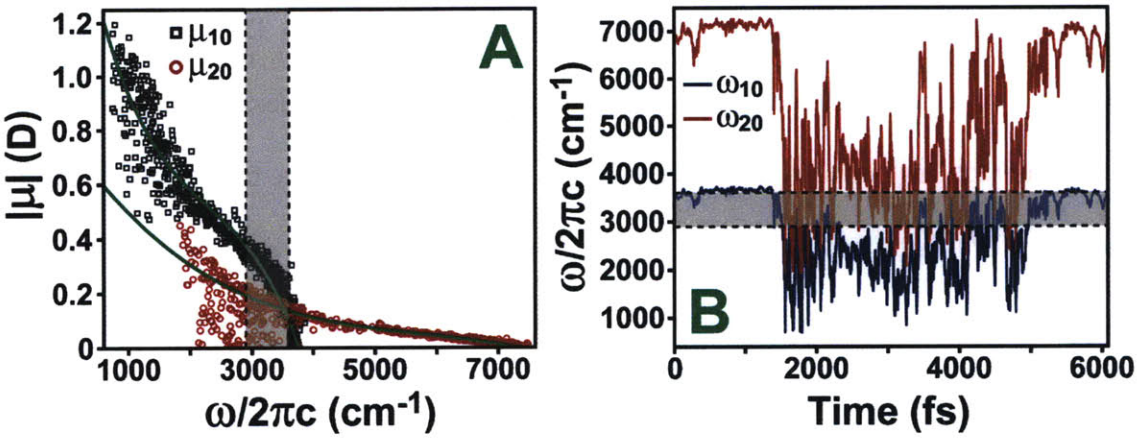


Figure 7-7: (A) Dipole matrix elements for the v = 1←0 and v = 2←0 transitions plotted vs. their respective frequencies, ω_{10} and ω_{20}. The green lines plotted on top of the data represent cubic fits that are used to calculate μ_{10} and μ_{20} from ω_{10} and ω_{20}. The shaded region represents the frequency range probed in the experiments described in Chapter 6. When ω_{20} enters this range, its transition dipole is ~2/3 that of ω_{10}. (B) A ~6 ps section of a frequency trajectory during which the observed proton partially transfers to the hydroxide ion. During each of the attempted transfer events, the ω_{20} transition moves within the experimentally probed frequency region (grey).

This very strong dependence of μ_{10} on frequency is not unexpected. Zundel originally proposed that the continuous absorption observed in strong acids and bases results from the presence of highly polarizable $H_5O_2^+$ or $H_3O_2^-$ ions, respectively.[4,5,55] The excess charge placed upon these species allows them to rapidly alter their structure in response to dielectric fluctuations of the surrounding liquid environment, thereby inducing large, rapid perturbations to the O-H stretching potential that can sweep its vibrational frequency across the entire mid-infrared range. Of course, the converse of this argument is also true. As the proton in the complex moves, the excess charge of the complex can rapidly redistribute itself to minimize its associated energy, thereby leading to a large variation in the dipole of the complex with the position of the proton. This hypothesis can also explain why such a strong absorption is seen from shared protons relative to the water stretching transition in strong acids and bases even though shared

proton configurations states are present in much smaller quantities. In 10.6 M NaOH solution, the molarity of H_2O is 50.85 M (calculated using density data in Ref. 25), which gives a water O-H bond concentration of 101.7 M. Even if every hydroxide ion in solution participated in a strong $H_3O_2^-$ ion, the concentration of these species would only be 10.6 M, roughly 10% of that of water. However, the continuum absorption that extends from the O-H stretch of HOD in 10.6 M NaOD to lower frequency is ~65% as intense as the peak of the O-H stretch (See Fig. 6-1), and implies that the O-H transition dipole must increase with decreasing frequency.

Simulations of a simple one dimensional model $A{\cdot\cdot}H{\cdot\cdot}A^+$ complex showed that modulations to the O-H stretching potential are capable of inducing large continuous absorption spectra with strong transition dipole moments,[71] lending support to Zundel's proposal. More recent simulations using an MS-EVB simulation model of the excess proton in water have shown that the bond lengths of the H_3O^+ ion are quite dynamic and respond rapidly to changes in the structure of its first solvation shell.[72] In the case of a partially deuterated HOD_2^+ ion, these dynamic bond length changes will induce large changes in the O-H stretching frequency of the ion as well as its associated transition dipole. In the case of the OH^- ion, CPMD simulations find that the three lone pair electrons of the complex can effectively blend together forming a delocalized ring around the ion's oxygen atom, but that as the ion begins to form a $H_3O_2^-$ ion, this ring of charge becomes polarized toward the shared hydrogen atom.[12] This change in the electronic structure of the ion suggests that small changes in the position of the shared proton can induce large changes in the overall dipole moment associated with the ion.

An important corollary to these observations is that since the large increase in the transition dipole of shared proton configurations is the result of a rapid redistribution of the ion's charge as the shared proton moves and not due to the matrix element of the position operator linking the v = 0 and 1 eigenstates, we expect not only a large increase in μ_{10} as the proton becomes more delocalized but a large increase in each of the transition dipole matrix elements of the potential (See Appendix 7.A for a description of the calculation of transition dipole matrix elements). In Fig. 7-7A, in addition to μ_{10}, we have also plotted the transition dipole for the first vibrational overtone transition determined from the cluster calculations, μ_{20}, against its corresponding vibrational frequency, ω_{20}. Similar to the behavior of the fundamental transition, μ_{20} shows a strong increase in intensity as ω_{20} decreases. While for any given configuration μ_{20} is at least an order of magnitude smaller than μ_{10}, a striking observation is made when we examine the 3 μm frequency region that we have probed experimentally in Chapter 6. Within this range of frequencies (2900 cm^{-1} – 3600 cm^{-1}, grey shaded region), we find that μ_{20} adopts values that are ~2/3 of that of μ_{10}. If the vibrational potential of the HOD molecule becomes distorted enough during proton transfer events that ω_{20} can shift to low enough frequency that it enters the bandwidth of our excitation pulses, it can generate a spectral signature that will be strong enough to observe experimentally!

In Fig. 7-7B we plot an example frequency trajectory wherein the examined HOD molecule undergoes multiple attempted proton transfer events with a neighboring OD^- ion. During these events, ω_{10} undergoes an extremely strong and rapid red shift as the O-H stretching potential broadens. However, as ω_{10} decreases in value, so too do the higher transitions within the vibrational potential. As in Fig. 7-7A, the shaded region in Fig. 7-

7B represents the frequency range probed in our nonlinear infrared experiments. During proton transfer events, ω_{20} moves into this range when the proton becomes shared between the HOD molecule and the OD^- ion. Given the large amplitude of μ_{20} when ω_{20} falls into this frequency range, these observed rapid modulations of the O-H vibrational potential suggest that excitation pathways exist wherein the first pulse can interact with the $v = 2 \leftarrow 0$ transition of a transferring proton in a Zundel-like state, but because of shifts in the shape of the vibrational potential as the proton localizes, subsequent pulses probe the fundamental transition of the now localized O-H stretch.

Before we can consider the implications these results have for the interpretation of our nonlinear infrared experiments, we must first verify that the linear absorption spectra predicted by our model is consistent with experiment. Unfortunately, making a proper comparison is complicated by the fact that the MS-EVB simulation model that we have employed has not yet been parameterized to include interactions between identical ions (i.e. OH^-/OH^- or Na^+/Na^+ mutual repulsion), limiting us to simulations containing only a single Na^+/OH^- ion pair. Given the number of water molecules we have chosen to simulate (214), our simulation box corresponds to a 0.26 M NaOH solution, a concentration that is much smaller than that which we investigate experimentally. Moreover, the simulation is run for a finite length of time that is much smaller than that needed to allow each water molecule in the simulation to properly sample all possible configurations available to it. Thus, each water in the simulation spends a different amount of time in the solvation shell of the OD^- ion. This complicates a proper determination of the quantitative scaling of intensities between the peak of the ω_{OH}

absorption spectrum near 3370 cm^{-1} and the continuum absorption band at lower frequency.

As a means of estimating how the absorption spectra of the MS-EVB model will change with increasing NaOD concentration, we make the assumption that we can decompose the linear absorption spectrum shown in Fig. 7-6B into two contributions, the peak centered near 3370 cm^{-1} due to HOD/D_2O and the broad absorption centered near 1600 cm^{-1} due to HOD molecules hydrogen bonded to OD^-. We then select different O-H frequency trajectories from the simulation wherein the selected HOD molecule spends differing amounts of time in the OD^- ion's solvation shell. Examining spectra for these selected HOD molecules, we find that the intensity of the two spectral features appears to change linearly as a function of residence time in the OD^- solvation shell. Based on the known concentration dependence of the density of aqueous NaOH[25] and estimates from neutron scattering[46] of how the coordination number of the OH^- ion changes with NaOH concentration, we can relate the percentage of the simulation time that each molecule spends in the OD^- solvation shell to an effective NaOH concentration by assuming that hydrogen bonds are statistically distributed between water and OD^- ions (See Table 6-2).[§] If we make the further assumption that the two broad spectral features that we identify do not change with NaOD concentration, we can extrapolate their intensities to higher deuteroxide concentration.

[§] In performing this calculation, we have assumed that we have assumed that the spatial composition of a NaOD solution is identical to that of a NaOH solution of equivalent concentration. As mentioned in the previous chapter, the molarities of pure D_2O and H_2O only vary by ~0.5%, so we feel that this assumption is valid. It is worth noting that the neutron scattering results described in the text[46,47] also require this assumption since isotopic dilution experiments are used to separately determine the oxygen-oxygen, oxygen-hydrogen, and hydrogen-hydrogen radial distribution functions.

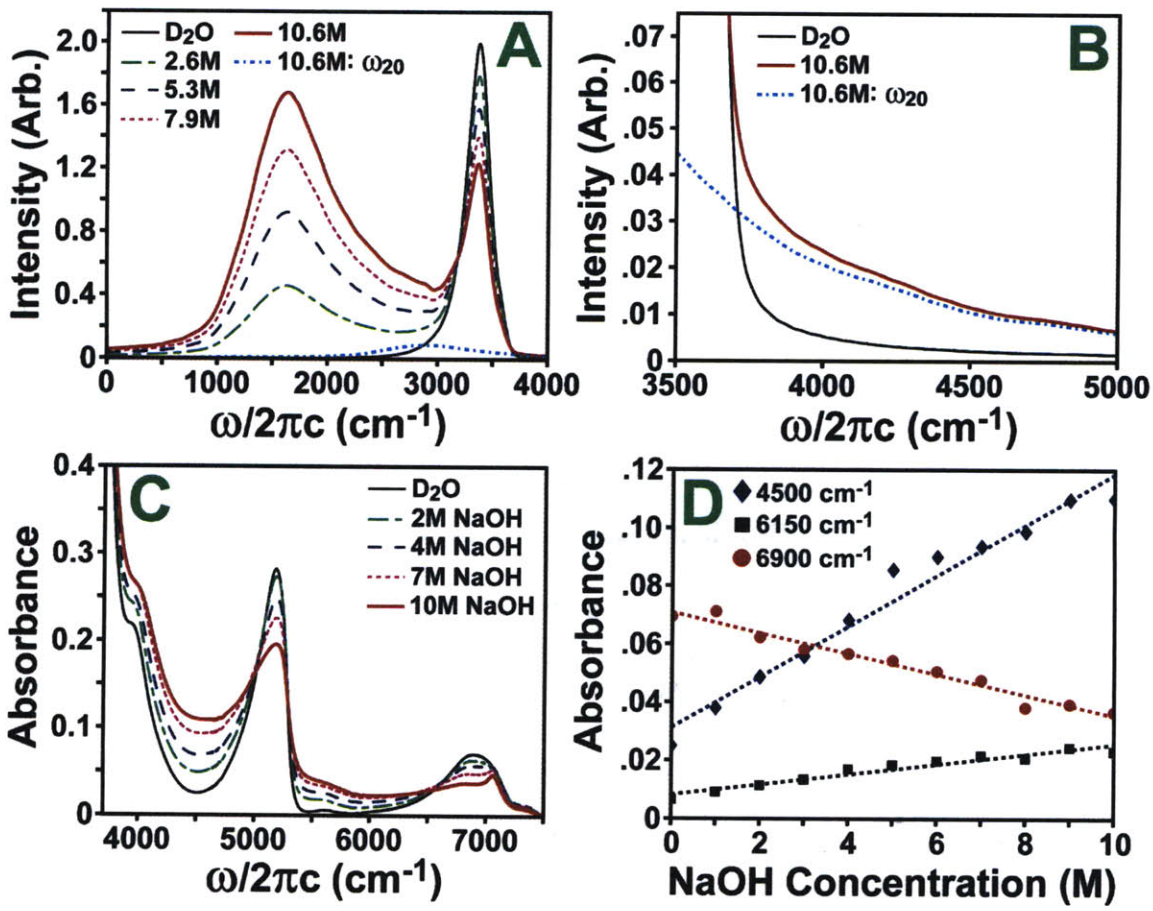


Figure 7-8: (A) Linear absorption spectra calculated from the MS-EVB simulation assuming that the spectrum can be decomposed into two separate features. Also plotted is the contribution to the 10.6 M spectrum from ω_{20} (dash dotted cyan), which forms a non-negligible contribution to the overall absorption profile. (B) Close up of the high frequency region above the peak of the ω_{10} contribution to the spectrum. In the case of 10.6 M NaOD, we find that the increase in absorption in this region is almost completely due to ω_{20}. (C) Experimental NIR spectra of the overtone and stretch-bend combination band of the O-H stretch of aqueous NaOH solutions. (D) As the NaOH concentration increases, the peak of the O-H stretch overtone at 6900 cm^{-1} decreases linearly, while the continuum absorption below the stretch increases. The intensity of the continuum appears to increase with decreasing frequency.

In Fig. 7-8A we plot the results of this extrapolation. The basis function used for the scaling of the HOD/D_2O like response was taken from the calculated lineshape for HOD molecules that do not enter the OD^- ion's solvation shell while the basis function for the solvation shell response was determined by performing a singular value decomposition analysis[73] on a series of lineshapes calculated for HOD molecules with

different residence times in the OD^- solvation shell. Contributions to the lineshape from both the $v = 1 \leftarrow 0$ and $v = 2 \leftarrow 0$ transitions are included in the analysis. From the figure, we see that the qualitative features observed in spectra of concentrated bases[55] are reproduced. As the NaOD concentration increases, the peak of the HOD/D_2O stretch is found to decrease while intensity grows in at lower frequency. In our model, instead of observing a largely featureless continuum absorption similar to that found in spectra of concentrated acids and bases,[4,5] we instead find a broad peak centered near 1600 cm^{-1}. One likely explanation for this discrepancy is our assumption that a single coordinate, ΔE_{sol}, can be used to uniquely map the vibrational frequencies and transition dipoles of the O-H stretching potential is not valid. While the correlation between ω_{10} and ΔE_{sol} displayed in Fig. 7-4B is quite good for large values of ΔE_{sol}, as this quantity approaches zero the correlation is observed to decrease. A recent study of the gas phase $F^-(H_2O)$ and $F^-(D_2O)$ complexes found that the frequencies and intensities of the vibrational transitions of the bridging hydrogen stretch could not be adequately reproduced unless the heavy atom O-F^- stretching coordinate was considered in addition to the O-H stretch.[74] We suspect that future versions of our frequency calculation methodology that takes into account the oxygen-oxygen stretch of Zundel-like shared proton configurations may give better agreement with experimental absorption spectra. Nevertheless, the qualitative agreement between experiment and our simulation model suggests that we can use this model as a means of interpreting our nonlinear experiments.

Fig. 7-7 shows that during proton transfer events, overtones of the O-H stretching potential may move into the frequency range normally associated with hydride stretches that are localized on a single HOD molecule. To determine the contribution of these

transient excursions involving the v = 2←0 overtone, in Fig. 7-8A we also plot the contribution to the 10.6 M spectra due to this transition. Over the 2900 – 3600 cm^{-1} frequency range, the v = 2←0 transition contributes 9.5% of the total integrated area of the calculated 10.6 M NaOD absorption spectrum, a small but non-negligible amount. Moreover, the contribution of this overtone in the frequency range normally associated with the O-H stretch fundamental makes a direct prediction about the spectra of hydroxide solutions at higher frequency. If we examine the high frequency side of our calculated lineshape, we find that there is an increase in absorption to the blue of the peak of fundamental O-H stretch that is entirely due to the overtone of HOD molecules that form strong hydrogen bonds to OD^- (Fig. 7-8B).

To determine if this prediction from our model matches experiment, we recorded spectra of NaOH solutions in the NIR frequency range between 3000 and 7200 cm^{-1} (Fig. 7-8C). In this range we find the presence of two peaks, the stretch bend combination band at 5200 cm^{-1} and the overtone of the O-H stretch broadly centered at 6900 cm^{-1}. As the NaOH concentration is increased, we observe both of these bands to decrease concurrent with the appearance of a continuous absorption over the entire examined frequency range (Fig. 7-8D). Moreover, the intensity of the continuum absorption is observed to increase with decreasing frequency, which is consistent with the variation of μ_{20} with ω_{20} predicted by our frequency model. NIR spectra measured for the frequency range corresponding to the third overtone (v = 3←0) of the O-H stretch in NaOH and KOH solutions show similar evidence for the appearance of a continuum absorption that extends from the peak of the third overtone to the high frequency side of the ω_{20} absorption lineshape.[75] Interestingly, at a NaOH concentration of 7 M, in Fig. 7-8C we

observe the appearance of the overtone of the OH^- stretch on the high frequency side of the O-H stretch overtone transition. The separation between these two overtone features is much greater than that observed for their fundamental transition (See Fig. 6-1), and may afford a clearer means of measuring spectral features due to the exchange of these two types of hydride stretches.

7.6. Calculation of the Third-order Response Including Forbidden Transitions

In Chapter 2, we described much of the theoretical framework that is commonly used for the calculation of nonlinear infrared signals and applied this in Chapter 5 to calculate 2D IR spectra of isotopically dilute HOD in D_2O. In this system, the O-H stretch of the HOD molecule is weakly anharmonic, and only transitions that obey the typical dipole selection rules associated with vibrational spectroscopy ($\Delta v = \pm 1$) needed to be considered. However, due to the large frequency shifts that occur during proton transfer events and the strong increase in the O-H transition dipole that accompanies these shifts, to properly calculate 2D spectra of dilute HOD in $NaOD/D_2O$ we must consider interaction pathways wherein overtone transitions of the HOD molecule can be directly excited.

In Fig. 7-9 we plot each of the Feynman pathways that are possible when overtone transitions involving a change in vibrational quantum number of ± 2 are allowed. In addition to the six Feynman diagrams normally considered for an isolated vibrational system (Fig. 7-9A), we find a similar set of excitation pathways involving only $\Delta v = \pm 2$ transitions (Fig. 7-9B) as well as pathways involving mixed excitation of $\Delta v = \pm 1$ and ± 2 transitions (Fig. 7-9C). Half of this set of mixed excitation pathways describes processes wherein the first pair of excitation pulses excites the $v = 2 \leftarrow 0$ transition of a proton

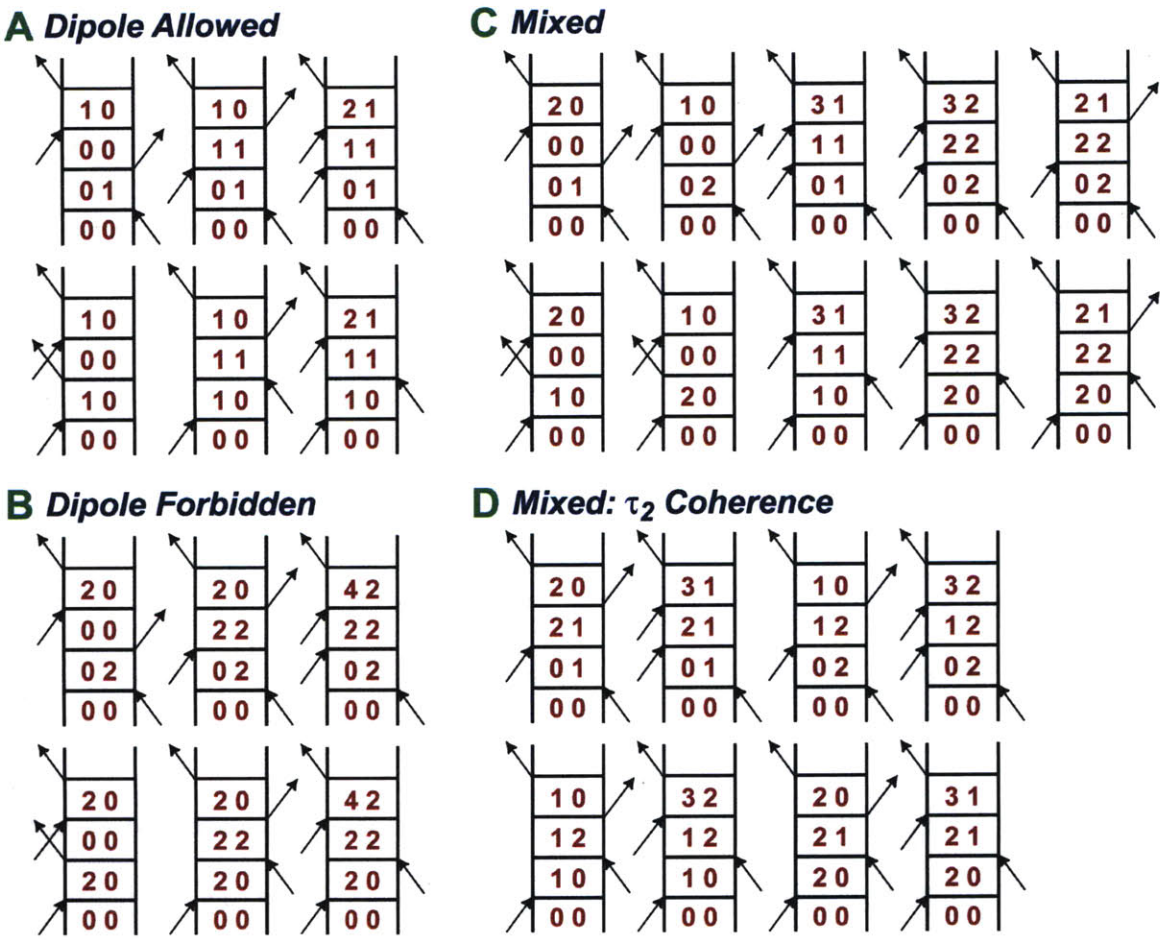


Figure 7-9: Feynman pathways that allow for vibrational transitions involving a change in quantum number of ±2 in addition to the normally allowed $\Delta v = \pm 1$ transitions. (A) Feynman diagrams for transitions with $\Delta v = \pm 1$ only. (B) Diagrams for transitions only involving $\Delta v = \pm 2$. (C) Diagrams involving both $\Delta v = \pm 1$ and $\Delta v = \pm 2$ transitions that form a population state during τ_2. (D) Feynman pathways containing both $\Delta v = \pm 1$ and $\Delta v = \pm 2$ excitations that form a vibrational coherence during the waiting time.

shared between a HOD molecule and an OD^- ion and due to shifts in the proton potential as the proton localized on either oxygen atom of the complex, the third excitation pulse interacts with either the newly formed molecule's $v = 1 \leftarrow 0$ transition or other $\Delta v = \pm 1$ transitions that fall within the bandwidth of the excitation pulse. Likewise, the other half of this set of pathways describes instances where the ω_{10} transition of a localized proton of a HOD molecule is excited, but subsequent pulses excite vibrational overtones due to

the formation of a Zundel-like configuration. A last subset of Feynman pathways wherein a coherence between the v = 1 and v = 2 eigenstates of the system oscillates during the waiting time is also possible (Fig. 7-9D). For this pathway to contribute to the measured experimental data, the O-H potential must fluctuate rapidly, so that both ω_{10} and ω_{20} fall into resonance with the excitation pulses during the τ_1 coherence period. Provided that the fluctuations of the vibrational potential are fast enough, these diagrams may contribute strongly to vibrational echo experiments like the photon echo peak shift and 2D IR spectroscopy, but will not contribute strongly to pump-probe spectra since τ_1 is limited to the excitation pulse length in these experiments.

With this set of Feynman diagrams in hand, we can write out expressions for the third-order response of the system using the methodology outlined in Section 2.4.1 of Chapter 2. More specifically, we can use the semiclassical result given by Eq. 2-22 to write out the following expression for the response in the limit of delta function pulses:

$$S_{\pm}(\tau_3,\tau_2,\tau_1) = \sum_{abcdefij} \left\langle \boldsymbol{\mu}_{ij}(\tau_1+\tau_2+\tau_3)\boldsymbol{\mu}_{ef}(\tau_1+\tau_2)\boldsymbol{\mu}_{cd}(\tau_1)\boldsymbol{\mu}_{ab}(0)\phi_{\pm}(\tau_3,\tau_2,\tau_1)\right\rangle$$

$$\phi_{\pm}(\tau_3,\tau_2,\tau_1) = \exp\left[\pm i\int_0^{\tau_1}\omega_{ab}(t)dt \mp i\int_{\tau_1}^{\tau_1+\tau_2}\left(\omega_{cd}(t)-\omega_{ab}(t)\right)dt \right. \qquad (7\text{-}3)$$

$$\left. +i\int_{\tau_1+\tau_2}^{\tau_1+\tau_2+\tau_3}\left(\omega_{ef}(t)-\omega_{cd}(t)+\omega_{ab}(t)\right)dt\right]$$

where S_- and S_+ represent the rephasing and nonrephasing responses respectively. Eq. 7-3 is written in a form applicable to the Feynman pathways that appear in Fig. 7-9, and is not generally true otherwise. To calculate the full third-order response, we must evaluate Eq 7-3 for each of the Feynman pathways that appear in Fig. 7-9, replacing the pairs of indices *ab*, *cd*, *ef*, and *ij* with the pair of eigenstates that are linked by each excitation pulse, keeping in mind the sign associated with each diagram. Diagrams that return to

the ground state after τ_3 denote either photo bleaching of the ground state or stimulated emission and are positively signed since they add to the signal field. Conversely, excitation pathways that result in the formation of an excited population state correspond to photo induced absorption, which detracts from the signal field and is negatively signed. In writing Eq. 7-3, we have written each of the transition dipole matrix elements as vectors for completeness. However, each 2D spectrum that we present in this chapter has been calculated without taking into account the orientation of the excited molecule.

In calculating 2D IR spectra, we wish to uniquely identify the spectral signatures associated with proton transfer events. However, since these events are somewhat rare, the calculation of 2D spectra from a frequency trajectory of a single HOD molecule will be biased towards the bulk water response. To isolate the spectral features of hydrogen atoms in the course of proton exchange we locate each proton transfer event in the simulation and calculate the third-order response windowed in time about this point. To identify transfer events, we find each instance in the simulation trajectory where the proton of a water molecule in the OD^- solvation shell becomes equidistant from its own oxygen atom and the OD^- oxygen ($\delta = 0$). Based on this criterion, 5609 proton transfer events are found. By using a geometric definition to identify proton transfer events, a number of events are found that do not result in the stable transfer of the proton (i.e. a shared proton rattling back and forth multiple times in a Zundel-like configuration before forming a stable chemical bond). We select against these back transfer events by only counting a proton transfer as successful if the next subsequent proton transfer event involves a different hydrogen atom. By applying this secondary criterion, only 892 (15.9%) of the identified proton transfer events are found to lead to the successful

structural diffusion of the OH^- ion. 2D IR spectra of the exchanging proton during these successful transfer events are then calculated using Eq. 7-3 and a time origin that precedes the transfer event by 250 fs. The time origin is then stepped up to a point 250 fs after the transfer and the 2D spectra calculated for each time origin are summed and averaged over each proton transfer event to determine the vibrational response of Zundel-like configurations. Mathematically, we can write this time windowed response as:

$$S_{PT\pm}(\tau_3,\tau_2,\tau_3) = \sum_{abcdefij} \Big\langle \boldsymbol{\mu}_{ij}(\tau_1+\tau_2+\tau_3)\boldsymbol{\mu}_{ef}(\tau_1+\tau_2)\boldsymbol{\mu}_{cd}(\tau_1)\boldsymbol{\mu}_{ab}(0)\phi_{\pm}(\tau_3,\tau_2,\tau_1) \times \Theta(0)\,E(\tau_1+\tau_2+\tau_3)E(\tau_1+\tau_2)E(\tau_1)E(0)\Big\rangle \tag{7-4}$$

where $\Theta(0)=1$ if a stable proton transfer event occurs within ±250 fs after τ_1 = 0. Otherwise, $\Theta(0)=0$. The size of this chosen time window does somewhat affect the quantitative values for the intensities of different contributions to the third-order response, but does not change the qualitative picture that we present on the basis of the calculated spectra. We have also included in Eq. 7-4 the spectral windowing effects of real pulses by multiplying the calculated response by the amplitude of the experimental pulse spectrum[**] at the frequency of each interaction. This is not formally equivalent to a true real pulse convolution since we still assume that each interaction occurs at the peak of each pulse, but it does allow us to determine which interaction pathways can contribute to the measured 2D signal given the finite bandwidth of our excitation pulses. As with Eq. 7-3, Eq. 7-4 is written explicitly for the Feynman pathways that appear in Fig. 7-9, and is not applicable to a system with an arbitrary level structure.

[**] To perform this convolution, the experimental pulse spectrum was fit using a Gaussian lineshape that was used to calculate the windowed 2D response. The Gaussian fit to the data was centered at 3345.9 cm^{-1} and had a FWHM of 408.6 cm^{-1}.

7.7. 2D IR Spectra of Proton Transfer Events

In Fig. 7-10 we plot a comparison between 2D IR spectra calculated during proton transfer events and spectra calculated for water molecules hydrogen bonded to D_2O. The spectra representing HOD/D_2O are similar to that calculated from other classical simulation models that take into account non-Condon effects,[34,53] such as the one presented in Chapter 5 of this thesis (See Fig. 5-8A as an example).[24] In sharp contrast, the spectra of HOD molecules undergoing proton transfer are quite broad, with positive intensity peaked at 3300 cm^{-1}, but covering the entire spectral range spanned by our excitation pulses. Moreover, the proton transfer peak is observed to rapidly decay, and has nearly disappeared within 200 fs. In Chapter 6, we suggested that the decay of intensity in the region above the diagonal axis was largely due to large spectral shifts of the $v = 2 \leftarrow 0$ transition associated with proton transfer events. To test this hypothesis, in Fig. 7-11A we plot the integrated intensity of the offdiagonal region (green shaded boxes in Fig. 7-10) of the calculated 2D spectra. As τ_2 increases, the spectra calculated for HOD/D_2O displays a small growth of intensity in this region as the spectra broaden and rotate due to hydrogen bond rearrangements and exchange. The displayed fit to the data corresponds to a rising exponential function with a time constant of 500 fs, which well describes the behavior of the data up to a waiting time of 18 ps. The behavior observed for molecules engaging in proton transfer is quite different. Instead of an initial rise, we find that the offdiagonal region of the spectra relaxes rapidly. Although oscillations appear in the spectra, notably at 180 fs, and may possibly be due to modulations of the O-H potential by low frequency modes such as the oxygen-oxygen stretch of the Zundel-like state, we can broadly describe the behavior of the spectra up to $\tau_2 = 500$ fs using a

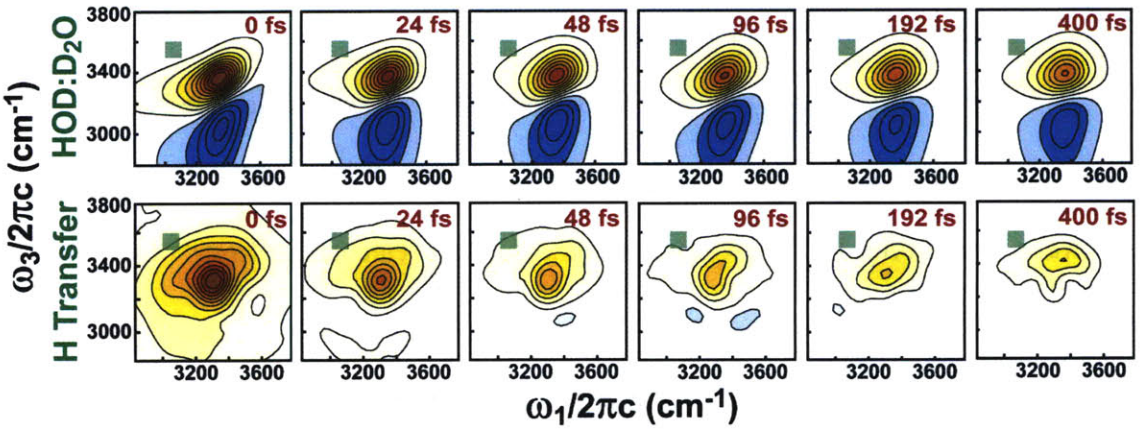


Figure 7-10: 2D IR spectra for HOD molecules that do not encounter the OD^- ion (Upper) and for HOD molecules engaging in proton transfer (Lower). Contours are plotted relative to the maximum positive signal at $\tau_2 = 0$. The shaded region represents the spectral range that was integrated to yield the data presented in Fig. 7-10.

single exponential decay with a time constant of 40 fs. This observation is qualitatively consistent with the rapid 110 fs decay time scale observed in our experimental pump-probe spectra and the rapid loss of offdiagonal intensity in measured 2D IR spectra presented in Chapter 6.

To further understand the origin of the observed decay, in Fig. 7-11B we plot the contributions to the decay of the offdiagonal intensity due to each of the four sets of Feynman pathways displayed in Fig. 7-9. The dominant contribution to the decay (~55%) comes from the excitation pathways in Fig. 7-9B, wherein the v = 2←0 transition is directly excited. Since our simulation model does not include effects due to vibrational population relaxation or the reorientation of excited molecules out of the plane of the excitation pulses, the calculated decrease in intensity of these Feynman pathways must be the result of ultrafast spectral sweeping. The first set of excitation pulses interacts with the v = 2←0 transition of the shared proton, but as the proton localizes on either oxygen

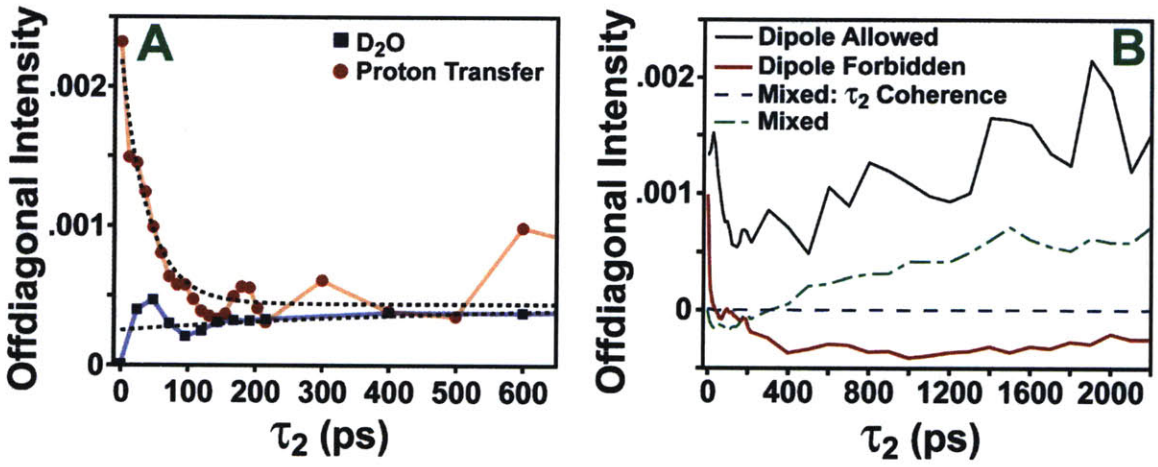


Figure 7-11: The integrated area $\omega_1 = 3000 - 3100$ cm^{-1} and $\omega_3 = 3500 - 3600$ cm^{-1} of the 2D IR spectra displayed in Fig. 7-10 for HOD molecules either hydrogen bonded to D_2O or engaging in proton transfer. Each spectrum was normalized to the integrated absolute value spectrum calculated at $\tau_2 = 0$ before calculating the displayed integrated intensity. (B) Contributions to the offdiagonal intensity of the proton transfer spectra from each of the four sets of Feynman pathways displayed in Fig. 7-9. The majority of the amplitude of the decay at early waiting times (~55%) is due to dipole forbidden pathways involving direct excitation of the $v = 2 \leftarrow 0$ vibrational transition.

atom of the Zundel-like complex during τ_2, the frequency of the $v = 2 \leftarrow 0$ transition moves out of the frequency region probed by our experiments.

We also find a strong contribution to the decay of the offdiagonal region (~37%) simply due to pathways involving the fundamental $v = 1 \leftarrow 0$ transition (Fig. 7-9A). In the case of these diagrams, a decrease in intensity is observed when a molecule is labeled before the proton exchange occurs. At a waiting time near 600 fs, we begin to see an increase in the intensity of the offdiagonal contribution due to these diagrams. This increase indicates the completion of the proton transfer event and the appearance of a more bulk like HOD/D_2O response. This growth of intensity also appears in the contribution to the offdiagonal intensity from diagrams involving an initial excitation of the first overtone and subsequent probing of the fundamental transition, indicating the completion of the proton transfer event. While this predicted growth of intensity is

interesting, we do not find experimental evidence for this recurrence. One potential explanation for the absence of this phenomena from the experimental data is that as the frequencies associated with Zundel-like configurations undergo rapid spectral sweeping, these frequencies will eventually come into resonance with the HOD bending transition or one of its associated overtones that can serve as a sink for the transfer of vibrational energy. Nonetheless, in the sub-ps regime, our results lend support to our initial hypothesis that the spectral sweeping of vibrational overtone transitions of the O-H potential can strongly contribute to the rapid decrease of intensity found in our experimental pump-probe and 2D IR data.

Interestingly, we find that the contribution to the 2D spectra from excitation pathways wherein a coherence is prepared that oscillates during τ_2 is quite small. For these diagrams to contribute to the third-order response, the O-H potential must oscillate rapidly enough that during the τ_1 coherence period (~100 fs) interactions at ω_{10} and ω_{20} both occur. While the fluctuations of the potential can be quite large and rapid as evidenced by the frequency trajectories in Fig. 7-7B, they are on average not large enough to generate a significant signal from the oscillatory Feynman pathways in Fig. 7-9D when the finite bandwidth of the excitation pulses is properly accounted for. In a previous report,[50] we presented 2D IR spectra calculated from the MS-EVB simulation model that did not explicitly account for the limited bandwidth of the excitation pulses, which caused the calculated spectra to show a strong contribution from these excitation pathways. Since the subset of these oscillatory Feynman pathways that appear along the diagonal axis correspond to nonrephasing processes, the calculated spectra in this report[50] had an overall dispersive character. While we no longer believe that these processes

contribute strongly to our experimental data, if the spectral bandwidth of the excitation pulses could be greatly increased, perhaps through the extension of continuum generation methods commonly used to generate terahertz pulses to the mid-infrared,[76] unique spectral signatures due to these processes may possibly be observed.

Our conclusion that the decay observed in the 2D spectrum is due to spectral sweeping of the overtone transition of the O-H stretch suggests that a portion of our measured nonlinear signal may in fact be due to the D_2O bath. As Zundel-like $D_3O_2^-$ ions are formed, the first overtone of the O-D stretch is expected to sweep through the 3 μm frequency region probed by our experiments. A calculation of the relative contribution of the D_2O response to the 2D spectra on the basis of the MS-EVB simulation is currently beyond the scope of our work as it would require the calculation of maps that relate the vibrational frequencies and transition dipoles of the O-D stretch to ΔE_{sol}. However, we did find that the use of a procedure similar to that used to construct the concentration dependent absorption spectra shown in Fig. 7-8A, when applied to the calculation of 2D data, was able to give spectra in which the intensity of the offdiagonal region qualitatively matched that observed experimentally. A measurement of the nonlinear signal simply due to the fully deuterated liquid was not possible since the stock solutions used for the preparation of experimental samples were not isotopically pure. However, the intensity of the measured signal does increase with the amount of added H_2O, suggesting that the measured response is due to the O-H stretch. While we cannot entirely rule out the contribution of $D_3O_2^-$ ions to our measured spectra, we note that even if they do make a strong contribution to the spectra, our explanation that the observed decay is due to spectral sweeping of Zundel-like configurations is unchanged. Simply

more ions would contribute to the decay observed at early waiting times than would be assumed given the isotopic concentration of the sample.

7.8. Linear and Nonlinear Spectra of the Free OH^- Ion Stretch

In addition to the rapid decay time scale discussed in the previous section, the experimental 2D IR spectra presented in Chapter 6 displayed the growth of new spectral features that are consistent with the appearance of a cross peak signifying the exchange of population between the OH^- stretch centered near 3600 cm^{-1} and the main O-H stretching band at 3400 cm^{-1}. Modeling of the experimental data placed a lower limit of 3 ps as the time scale for this exchange process, whose origin was attributed to the solvation of the newly formed water/ion pair upon proton transfer. To determine if the results of the MS-EVB simulation support this interpretation of the experimental results, we have used our methodology for the calculation of vibrational transitions to investigate how the frequency of the OH^- stretch changes during proton transfer events.

In Fig. 7-12, we present both the static frequency distribution and corresponding absorption spectrum calculated from frequency trajectories in which the monitored hydrogen atom exists for at least 500 fs as an OH^- ion. To emphasize the spectral features of the ion, each frequency trajectory was windowed so that it only contained the 20 ps range preceding the formation of a hydroxide ion containing the selected hydrogen and the 10 ps following this ion's conversion to a HOD molecule. Examining the static frequency distribution (blue) we find the presence of a sharp, narrow feature peaked at 3692 cm^{-1} due to the free OH^- stretch. This frequency distribution bears a qualitative resemblance to Raman spectra of concentrated alkali hydroxide solutions,[59-62] which show a strong, narrow peak associated with the OH^- stretch in the 3610 cm^{-1} – 3640 cm^{-1}

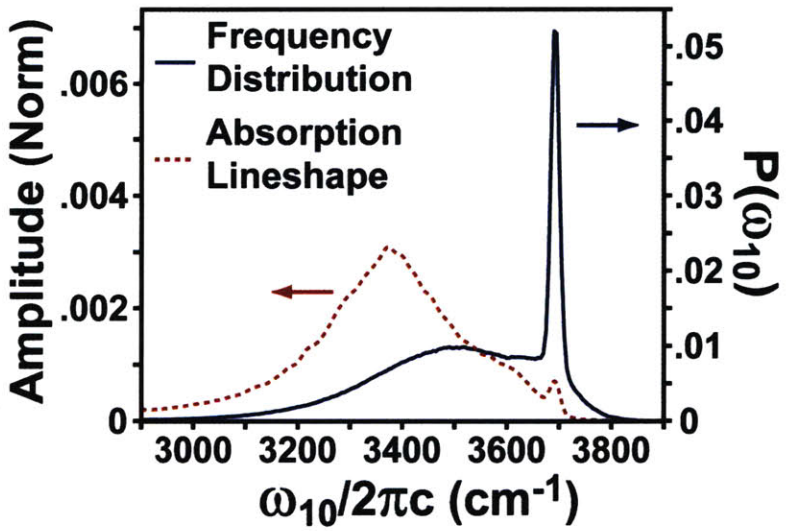


Figure 7-12: Comparison between the static frequency distribution and absorption spectra calculated for frequency trajectories wherein the investigated hydrogen atom exists as an OH^- ion for a minimum of 500 fs. The appearance of the sharp OH^- peak in the static frequency distribution agrees well with Raman spectra of alkali hydroxide solutions, while the decrease of this feature in the absorption spectrum is consistent with our measured FT-IR spectra of HOD in $NaOD/D_2O$.

spectral range. According to a standard geometric definition of a hydrogen bond ($R_{OO} \leq$ 3.5 Å & HOO angle $\leq 30°$) we find that the ion only donates a hydrogen bond for 1.6% of the total simulation run. The narrowness of this feature as well as its high frequency relative to HOD/D_2O reflects this lack of a hydrogen bonding partner. In the calculated linear absorption spectrum (red dashed), we find that the sharp OH^- feature present in the static frequency distribution has undergone a drastic decrease in intensity relative to the peak of the main O-H stretching transition due to non-Condon effects. This result is consistent with our measured spectra of HOD in $NaOD/D_2O$ solution (Fig. 6-1), wherein the strong OH^- peak found in Raman spectra of alkali hydroxide solutions is only visible as a shoulder on the high frequency side of the O-H stretch.

In Fig. 7-13A we plot a comparison between 2D IR spectra of the OH^- ion frequency trajectories (labeled "exchange") and corresponding spectra calculated for

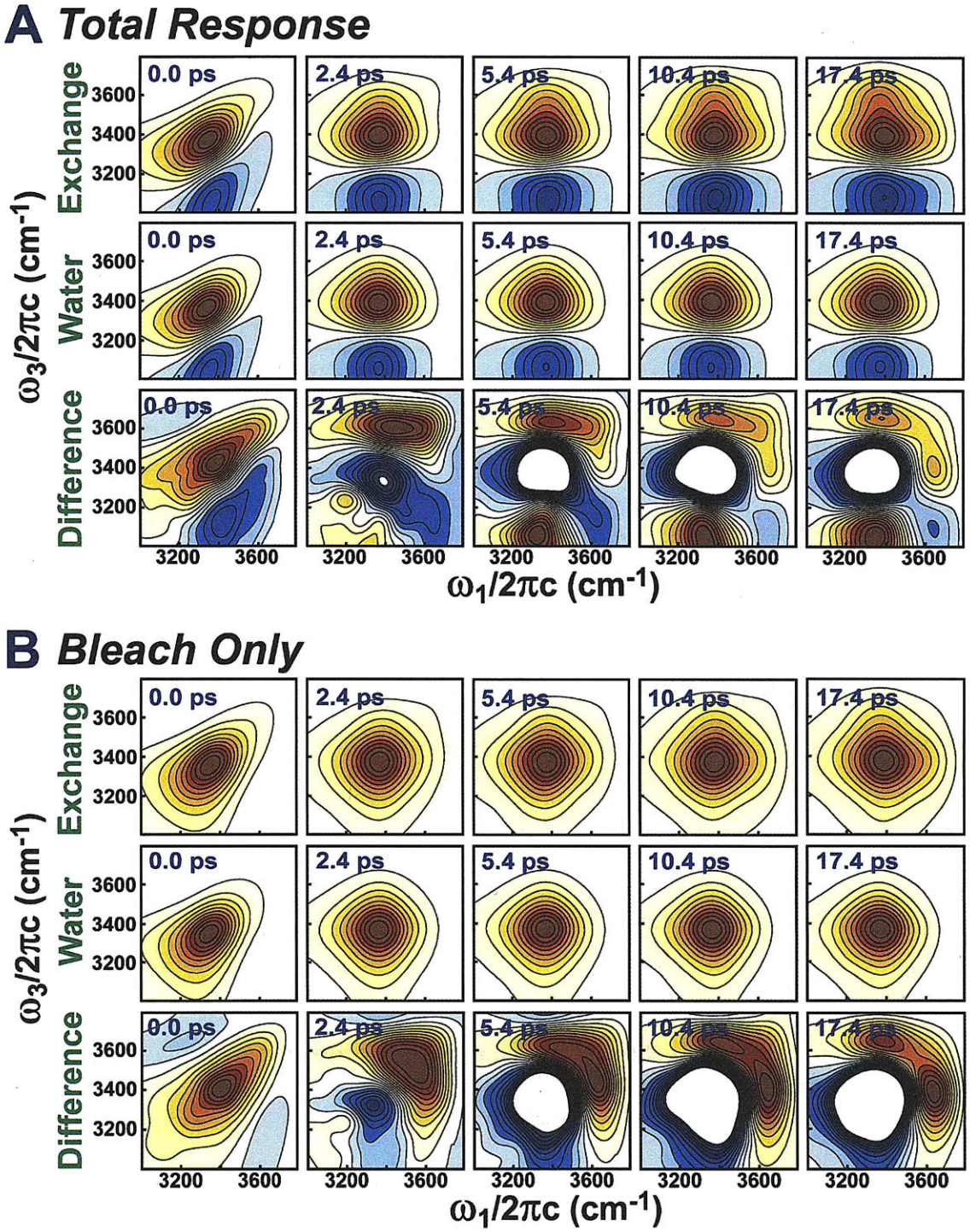


Figure 7-13: 2D IR spectra calculated for HOD/D_2O and for frequency trajectories wherein the monitored hydrogen atom spends a set amount of time as the OH^- ion. To emphasize spectral features associated with the proton transfer reaction, this latter set of frequency trajectories have been windowed about proton transfer events as described in the text. In (A) we plot the full response while in (B) we remove the contribution of the negative $v = 2 \leftarrow 1$ transition to highlight the growth of cross peaks signaling exchange between OH^- and HOD.

HOD/D_2O. Examining the HOD/D_2O spectra, we find that by the second waiting time pictured, 2.4 ps, the spectra appear completely homogeneous, as indicated by the round shape and decrease in the vertical tilt of the nodal line separating the positive $v = 1 \leftarrow 0$ peak from the negative $v = 2 \leftarrow 1$ peak, signaling that spectral diffusion is complete. Beyond this waiting time, the calculated HOD/D_2O spectra are not observed to change. The spectra calculated for the OH^- frequency trajectories reflect these features of the HOD/D_2O lineshape, but in addition show distinct features due to the OH^- ion stretch. At $\tau_2 = 0$, we see that the OH^- spectra appear elongated along the diagonal axis with respect to the HOD/D_2O spectra due to the appearance of the OH^- stretch near 3650 cm^{-1}. As τ_2 increases, we observe the growth of positive intensity to the left and below the OH^- peak due to the appearance of cross peaks indicating the return of the OH^- stretch to the main HOD absorption band. The growth of these cross peaks is highlighted by the difference spectra included in Fig. 7-13A.[††] Along the diagonal axis we see a large negative feature due to the loss of signal from HOD/D_2O, but in the offdiagonal regions between the OH^- stretch and the peak of the HOD/D_2O response, we find the appearance of positive intensity indicating exchange between these two transitions. Due to the small frequency separation between the OH^- stretch and the peak of the HOD/D_2O absorbance, we do not observe isolated cross peaks in the offdiagonal region but instead find a smearing of positive intensity. Additionally, interference between these exchange features and the negative $v = 2 \leftarrow 1$ transition causes the exchange spectral features to appear asymmetric about the diagonal axis. We can eliminate this latter effect by removing the contribution

[††] The procedure for the calculation of the difference spectra is identical to that used for the calculation of the experimental difference spectra in Fig. 6-10. Briefly, we construct the dispersed pump-probe from each calculated 2D spectrum, and then normalize one 2D data set to the other by matching the tails of the calculated pump-probe signals.

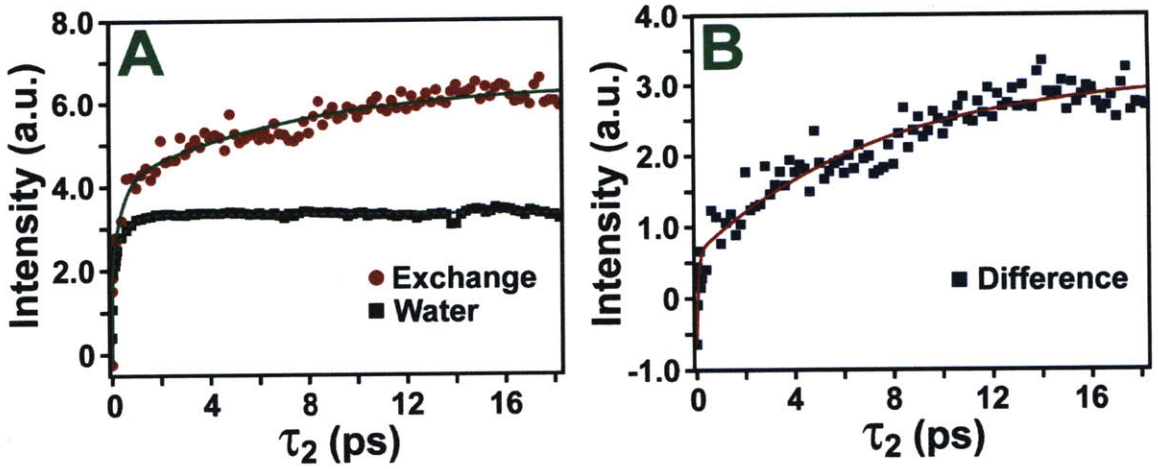


Figure 7-14: (A) Integrated intensity of the bleach only spectra of Fig. 7-13B within the spectral range ω_1 = 3300 cm^{-1} – 3400 cm^{-1} and ω_3 = 3600 cm^{-1} – 3700 cm^{-1}. The green lines represent biexponential and triexponential fits to the observed growth of intensity in this spectral range for the HOD/D_2O and exchange 2D spectra, respectively. (B) Integrated difference between the 2D exchange and HOD/D_2O spectra within the spectral range integrated in (A). The red line represents a biexponential fit to the data with time constants of 75 fs and 7.7 ps, which approximately match the short and long time scales of the growth of the exchange spectra in (A).

to the 2D spectra from the v = 2←1 transition (Fig. 7-13B), which allows us to clearly see the appearance of two separate peaks above and below the diagonal axis as τ_2 increases. A slight asymmetry in the intensity of the two cross peaks remains due to our choice for the time window applied to each frequency trajectory to bias the calculated spectra about proton transfer events, but the time scales for the appearance of both exchange peaks are identical.

In Fig. 7-14A, we plot the integrated intensity of the cross peak that appears above the diagonal axis in the absence of contributions from the v = 2←1 transition. In the case of HOD/D_2O, the growth of intensity in this spectral range is well described by a biexponential rise towards an asymptotic limit with time constants of 30 and 465 fs. This latter time constant is nearly the same as that observed for the growth of intensity in the offdiagonal region integrated in Fig. 7-11A and we attribute it to changes in the HOD

lineshape associated with the loss of frequency correlation. Examining the cross peak region of the exchange spectra, we observe a slow growth of intensity due to the transformation of HOD molecules to OH^- ions. This feature can be fit well using a triexponential function, giving time scales of 18 fs, 395 fs, and 7.4 ps. The first two time scales approximately map onto that observed for the HOD/D_2O response while the latter time scale we hypothesize to correspond to the solvation of the newly formed D_2O/OH^- molecular pair upon proton transfer. Qualitatively, this time scale is consistent with our estimate of a lower bound of 3 ps for this process based on our experimental data.

7.9. Reaction Coordinates for the Structural Diffusion of the OH^- Ion

Given the agreement between our experimental and simulated 2D data, we can now use the simulation to test different possible reaction coordinates for the structural diffusion of the hydroxide ion. In CPMD simulations employing the BLYP density functional, two principle time scales associated with the proton transfer reaction have been identified, a 180 fs time scale corresponding to "proton rattling" events wherein a proton within a Zundel-like configuration preferentially associates with either oxygen of the ion multiple times and a slower 1.7 ps process that acts to gate the formation of a Zundel-like configuration.[15] Given that these simulations use a fully deuterated bath whereas our experiments examine the transfer of a hydrogen atom, we feel that the time scale for proton rattling agrees well with our experimental value of 110 fs and qualitatively agrees with the rapid 40 fs decay observed in calculated 2D spectra from our MS-EVB simulation model. To determine the identity of the slower 1.7 ps process, the authors of Ref. 15 noted that this slow time scale matched well the lifetime of hypercoordinated hydroxide ion configurations, and suggested that the breakage of a

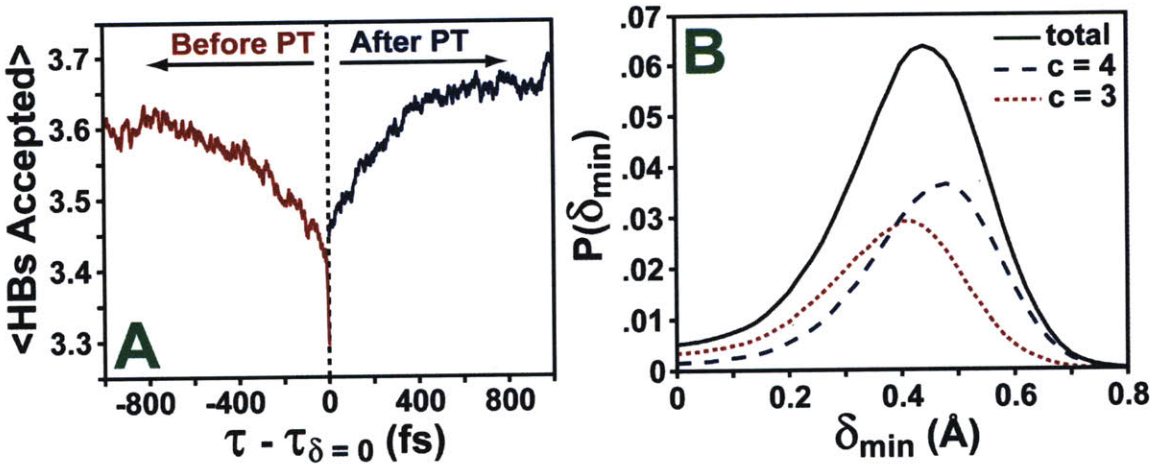


Figure 7-15: (A) Average number of hydrogen bonds donated to the OD^- ion during proton transfer events. $\tau = 0$ is defined as the point where $\delta = 0$. At this point, the average number of hydrogen bonds accepted by the ion is 3.27, suggesting that an additional coordinate is needed to describe the transport of the ion. (B) Distribution of the values of δ found for three- and four-coordinate OD^- ions. For each ion configuration, we identity the smallest value of δ among the hydrogen bonds donated to the complex and only use these values to construct the plotted histograms.

hydrogen bond donated to the ion acts to gate the proton transfer event.

In Fig. 7-15A we plot the average number of hydrogen bonds accepted by the hydroxide ion before and after proton transfer events. As with the 2D data shown in Fig. 7-10, we exclude back transfer events that do not result in the structural diffusion of the ion from this average. During proton transfer events, we indeed find that the number of hydrogen bonds donated to the ion decreases from 3.66 to 3.27, supporting the general picture determined from analysis of the CPMD simulations. However, the observation that the size of the ion's solvation shell does not decrease uniformly to 3 reflects the fact that ~27% of the proton transfer events in the MS-EVB simulation occur from four-coordinate configurations. This point is emphasized by Fig. 7-15B, which plots the distribution of δ values found for both three and four coordinate configurations. While three-coordinate configurations generally have smaller values of δ than hypercoordinated

ones, the distributions are quite broad and overlapping. At $\delta = 0$, a three-coordinate configuration is only 2.3x as likely when proton rattling is taken into account. These observations show that although the coordination number of the ion is certainly correlated with proton transfer events, it cannot provide a unique identification of the proton transfer transition state.

Because the vibrational spectroscopy of the proton is inseparable from the proton transfer coordinate, a meaningful variable should be able to describe both the motion of the proton and the accompanying frequency shifts of its vibrational potential. The time scale over which the frequencies of the vibrational potential return to their equilibrium values should be reflected in the behavior of an appropriate reaction coordinate. In Fig. 7-16 we plot the average values of the frequencies and transition dipoles of the transferring proton during proton transfer events. Echoing the observations made on the basis of the calculated 2D lineshapes presented in Fig. 7-10, we find that ω_{20} indeed enters the spectral range that we have investigated experimentally during the formation of a Zundel-like state. Likewise, at $\delta = 0$, μ_{20} adopts a value similar to that of μ_{10} for a water molecule whose fundamental frequency is equal to the peak of the HOD/D_2O frequency distribution (3370 cm^{-1}). About $\tau = 0$, we see strong oscillations in each of the calculated frequencies and transition dipoles that are reminiscent of the rapid spectra sweeping inferred from the 2D data. These oscillations have a period of ~90 fs (370 cm^{-1}), and may correspond to the oxygen-oxygen stretch of a strongly hydrogen bound Zundel-like configuration, the compression and expansion of which can rapidly induce changes in the associated O-H stretching frequencies of the potential.

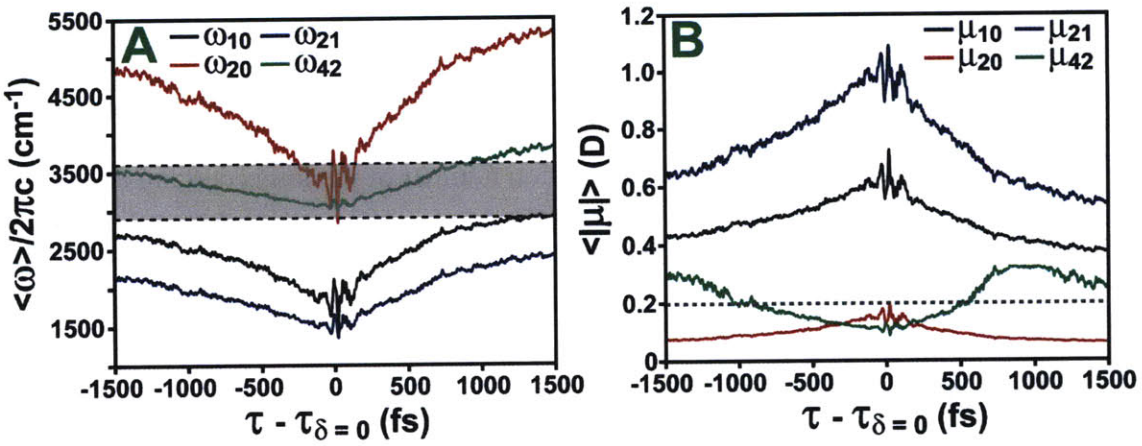


Figure 7-16: Average frequencies (A) and transition dipoles (B) of protons transfering to an OD^- ion. In (A) the shaded region denotes the spectral range viewed by our experiments while the dashed grey line in (B) corresponds to the value of μ_{10} for a HOD molecule with a vibrational frequency of $\omega_{10} = 3370\ cm^{-1}$.

Beyond τ = 200 fs, we find that the relaxation of each of the vibrational transitions back to values resembling HOD/D_2O is somewhat slow. This slow return qualitatively explains the lack of contributions to the calculated 2D spectra from the mixed excitation pathways that oscillate during the waiting time given in Fig. 7-9. While the perturbations to the O-H stretching potential are quite large during proton transfer events, on average the rate of change in the shape of the potential is not fast enough to drive transitions involving both ω_{10} and ω_{20} within a few tens of femtoseconds. In the case of ω_{10}, the return to its equilibrium values can be well fit using a biexponential function with time constants of 460 fs and 4.6 ps (Fig. 7-17A). These time constants are similar to the intermediate and slow decay time scales observed for the growth of cross peaks in the 2D exchange spectra in Fig. 7-14A. The intermediate time scale was also found in spectra calculated for HOD/D_2O leading us to hypothesize that it is related to the relaxation of the water bath. In Fig. 7-17B we present two time correlation functions calculated for isolated water molecules that do not encounter the OD^- ion: the frequency-

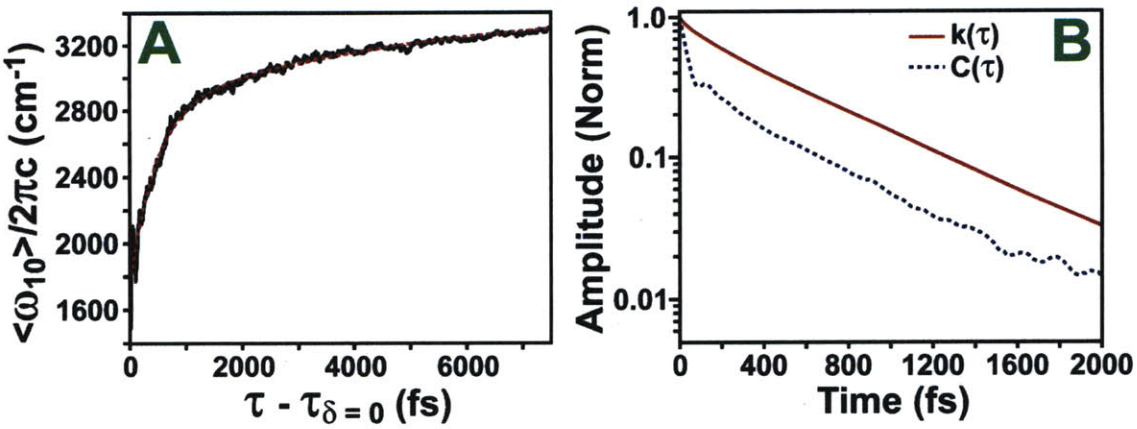


Figure 7-17: (A) $<\omega_{10}>$ following a proton transfer event at τ = 0 (black) and a corresponding biexponential fit (red) with time constants of 460 fs and 4.6 ps. (B) Frequency-frequency, $C(\tau)$, and hydrogen bonding, $k(\tau)$, time correlation functions for HOD/D_2O. The long time decay time scale of both of these functions falls within the range of 500 fs – 600 fs, which allows us to ascribe this as the characteristic time scale for fluctuations of the bath.

frequency time correlation function, $C(\tau) = \langle \omega_{10}(\tau)\omega_{10}(0)\rangle - \langle \omega_{10}\rangle^2$, and the hydrogen bonding time correlation function,[77] $k(\tau) = \langle h(\tau)h(0)\rangle$, where $h(\tau)$ is equal to 1 if at time τ the examined O-H bond participates in a hydrogen bond and is 0 otherwise. Other than a difference in the amplitude of the decay in the sub-100 fs regime, both correlation functions appear to decay at the same rate. Biexponential fits to both correlation functions give decay time scales of 535 fs and 610 fs for $C(\tau)$ and $k(\tau)$, respectively, which both are similar to the 460 fs rise of ω_{10} following proton transfer events. This suggests that the same motions of the liquid that act to drive hydrogen bond fluctuations and rearrangements act to stabilize the newly formed HOD molecule following proton transfer. A more appropriate reaction coordinate for the proton transfer reaction is not necessarily one that is dependent on the positions and momenta of a specific set of atoms, but one which describes the collective behavior of the liquid, similar to that commonly used in Marcus theory[2,3] to describe electron transfer.

Simulations of autoionization in water have found that this process is driven by strong transient electric fields[11] that arise due to the collective fluctuations of the liquid. Zundel has also proposed that the motion of a proton between a donor and acceptor molecule responds adiabatically to fluctuations of the electric field generated by the surrounding solvent.[5] Our spectral calculations show that the frequency of the O-H stretching transition is well correlated with proton exchange events and previous molecular dynamics simulations[10,57] have shown a strong correlation between ω_{10} and the projection of the collective electric field of the surrounding solvent onto the O-H bond at the proton position (See Fig. 5-1). These observations argue that the collective electric field serves to describe both the vibrational spectroscopy of the O-H stretch and the proton transfer reaction.

Motivated by these observations, we have examined the behavior of the collective electric field during proton transfer events. In performing these calculations, we have assumed that the charge of the OD^- ion is localized on the atomic centers. Since the charge of $H_3O_2^-$ is expected to be symmetrically distributed about the ion when $\delta = 0$, the calculation of the electric field in the manner caused some spurious results near the point of transfer due to the assumption of an instantaneous jump of charge from one oxygen atom of the complex to the other. To correct discontinuities in the calculated fields, we have assumed that the charge placed on the oxygen and hydrogen atoms of the water molecule hydrogen bound to the OD^- ion are identical to those used in the parameterization of the ion. While this assumption no longer allows us to properly account for the correct charge of the system, no spurious dynamics are observed in our values for the calculated field.

In Fig. 7-18A, we plot a histogram of values calculated for the projection of the collective electric field due to all other atoms in the simulation box along the line connecting the nearest neighbor proton to the oxygen atom of the OD^- ion, $E_{Acceptor}$.[‡‡] In general, the field projected along this direction adopts a positive value, indicating that the collective field due to the surrounding solvent acts to stabilize the HOD bond. Also plotted in Fig. 7-18A is a histogram of the field along this direction calculated at points where the proton is equally shared between the HOD molecule and the OD^- ion ($\delta = 0$). At these proton transfer points, we find $E_{Acceptor}$ has decreased to zero, indicating that the solvent no longer electrostatically opposes the breakage of the O-H bond. In Fig. 7-18B we plot both the time dependence of $E_{Acceptor}$ as well as the projection onto the O-H bond axis of the HOD molecule at the position of the proton, E_{Donor}. Leading up to the proton transfer, we find that E_{Donor} is nearly equal and opposite to $E_{Acceptor}$, which reflects the fact that the hydrogen bond formed to the OD^- ion is nearly linear. The proton transfer event itself results in a rapid, sharp inversion in the signs of both E_{Donor} and $E_{Acceptor}$, implying that the solvent is rearranging in such a way as to destabilize the donor bond in favor of the acceptor bond.

A crude measure of the length scale over which charge fluctuations are important can be obtained by excluding different sets of atoms from the field calculation. In Fig. 7-18C we plot the behavior of $E_{Acceptor}$ and E_{Donor} calculated by excluding the field contributions of the donor and acceptor atoms themselves. In this case, the asymptotic

[‡‡] In much of the recent literature (For example, Ref. 10, 53, and 54) that has examined the connection between electric field fluctuations in water the vibrational frequencies of the HOD molecule, the projection of the electric field along the O-H bond does not include the intramolecular contribution due to the HOD molecule's oxygen and deuterium atoms. For an inflexible water molecule, the field contribution due to these atoms simply constitutes a large, constant offset. However, in the case examined here, the imbalance of the field contributions between the OD^- ion and the atoms of the HOD molecule plays a strong role in determining the behavior of the shared proton, so they are included in the calculations presented in Fig. 7-18A and 7-18B as described in the text.

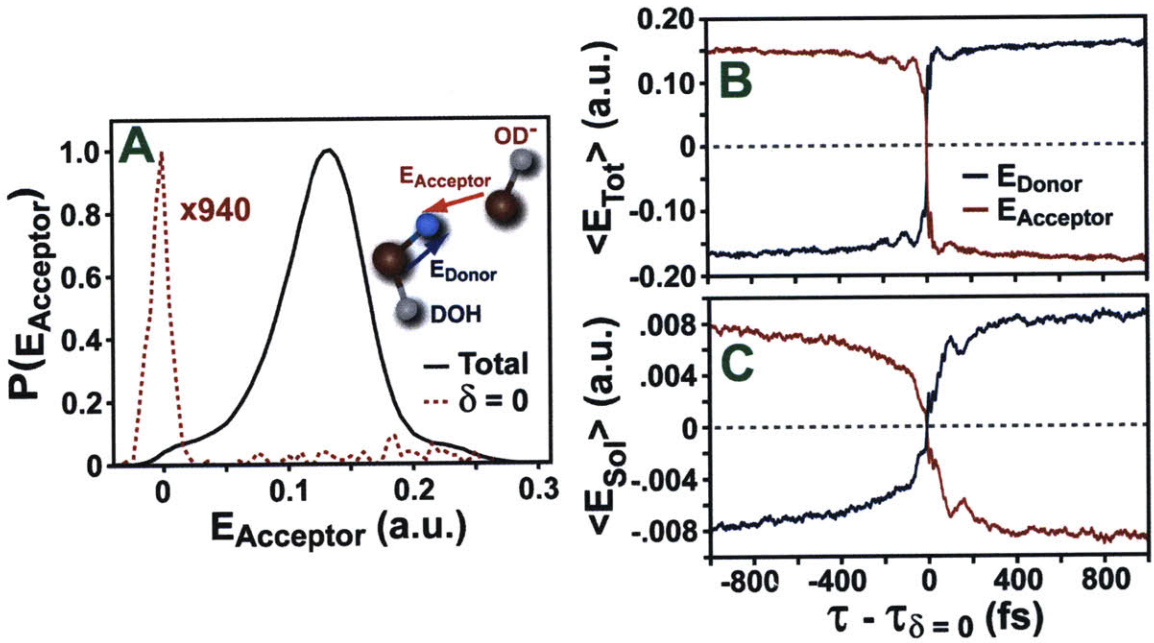


Figure 7-18: (A) Histograms of the collective electric field due to all atoms in the simulation projected along the $E_{Acceptor}$ direction for each simulation time step (black) and for shared proton configurations only ($\delta = 0$, dashed red). (B) Projection of the total electric field along the donor bond that is broken and the acceptor bond that is formed during proton transfer. (C) Same as in (B), but excluding the field contributions due to the five atoms pictured in the inset to (A).

limits of the field appear to have decreased by roughly an order of magnitude, which is to be expected given the $1/r^2$ scaling of the electric field strength with distance.[32] Nonetheless, the observed behavior is qualitatively identical to that displayed in Fig. 7-18B. $E_{Acceptor}$ and E_{Donor} exchange about the point of proton transfer, showing that the motion of water molecules outside of the first solvation shell is correlated with the proton transfer event.

In this model, the fluctuating electric field is a better predictor of proton transfer events than four- to three-coordinate switching. However, these processes are not mutually exclusive because the first solvation shell of the hydroxide ion and the proton donor necessarily make the largest contributions to the electric field. Although the data in both Fig. 7-18B displays some oscillations due to underdamped intermolecular modes

such as the oxygen-oxygen stretch that modulates the data in Fig. 7-16, a crude exponential fit to E_{Donor} beginning at 200 fs gives a decay time scale of 415 fs. This decay rate is similar to the ~500 fs time scale for the fluctuations of water's hydrogen bonding network found in this simulation model, suggesting that water dynamics form the heart of the field fluctuations that drive the motion of the proton.

7.10. Solvation of the DOD··OH^- Ion Following Proton Transfer

While we now have a description of the proton transfer reaction in the sub-ps regime, we still have yet to build an explanation for the longer 7.4 ps rise of the calculated cross peak between the OH^- ion stretch and the main HOD absorption band. Examining our calculated frequency map in Fig. 7-4B, we find that the set of frequencies calculated for OH^- ions lies on top of the points calculated for HOD molecules when the HOD stretch falls within the frequency range spanned by the OH^- stretch. This implies that the shift of the OH^- stretch to high frequency with respect to a hydrogen bonded HOD molecule is not due to the extra electron of the ion directly influencing the O-H stretching potential, but instead reflects the lack of a strong hydrogen bond to the ion. This suggests that the decrease in the stretching frequency of the OH^- ion upon its conversion to a HOD molecule will be highly correlated with the formation of a hydrogen bond to the O-H group.

Fig. 7-19A plots the average frequency of the OH^- stretch following a proton transfer event that converts the ion to a HOD molecule. The decay of the average frequency is surprisingly slow, fitting to a single exponential decay of 7.8 ps within the calculated signal-to-noise, and matches well the slow rise of the cross peak in the calculated 2D data. This long time scale is reflected in the behavior of the hydrogen

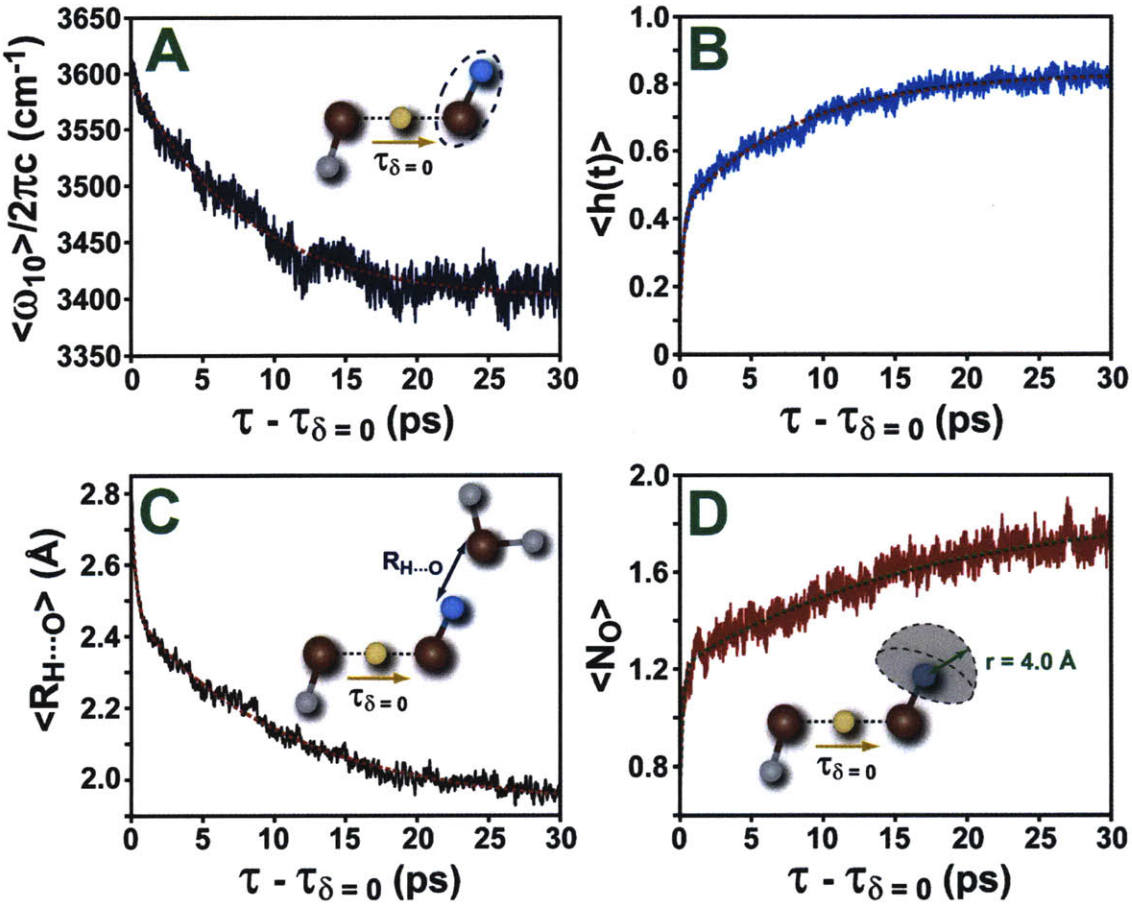


Figure 7-19: Average behavior of structural parameters associated with the O-H stretch of a newly formed HOD molecule following proton transfer (light blue hydrogen identified in the cartoon): (A) ω_{10}, (B) h(t), (C) $R_{H\cdots O}$, and (D) N_O.

bonding function, $h(\tau)$, following the proton transfer event. At $\tau = \tau_{\delta=0}$, $h(\tau)$ on average has a value of 0.11, which reflects the hydroxide ion's predisposition against the formation of a hydrogen bond to its proton. Following the conversion of the OH^- ion to a HOD molecule, $h(\tau)$ displays an initial fast increase (225 fs) followed by a slow rise (8.4 ps) towards the asymptotic limit of 0.9 calculated for HOD/D_2O, indicating the slow formation of a hydrogen bond. The slow time scale observed for the formation of this bond is consistent with the slow growth of the exchange peak in our calculated 2D IR spectra.

Of course, given that the rearrangements of the water bath occurs on a time scale that is roughly an order of magnitude faster than the hydrogen bond formation implied by Fig. 7-19A and 7-19B, it is not necessarily clear as to why this latter process is so slow. Fig. 7-19C plots the average distance between the hydrogen of the newly formed HOD molecule and the nearest neighboring oxygen atom, $R_{H\cdots O}$, which displays a biexponential decay that reflects the rise of $h(\tau)$. The initial decay of $R_{H\cdots O}$ suggests that the decrease in the charge of the newly formed HOD molecule following proton transfer allows waters arrayed about the HOD's hydrogen atom that were initially repulsed by the negative charge of the ion to fill some of the empty space above the molecule. To test this hypothesis, in Fig. 7-19D we have plotted the average value of the number of oxygen atoms within a hemisphere with a radius of 4.0 Å centered on the hydrogen atom of the new HOD molecule, $\langle N_O \rangle$. This distance corresponds to the minimum following the second peak in the water Hydrogen/Oxygen radial distribution function, $g_{HO}(r)$, calculated for this simulation model. Thus, the growth of $\langle N_O \rangle$ following proton transfer describes how long it takes the liquid surrounding the HOD molecule to adopt a structure resembling bulk water.

At $\tau = \tau_{\delta=0}$, we find that N_O on average adopts a value of 0.65, well below the limiting value of 2.1 calculated on the basis of $g_{HO}(r)$ for a water molecule well separated from the hydroxide ion.[35] This value is indicative of the asymmetric solvation shell of an OH^- ion. While the ion forms a number of strong hydrogen bonds to its oxygen atom, in our simulation model the density of water molecules about the ion's hydrogen atom is smaller than in bulk water since the formation of a hydrogen bond to

the ion's weakly positive hydrogen atom is not strong enough to overcome the electrostatic repulsion due to the ion's negative charge. As τ increases, $\langle N_O \rangle$ displays a biexponential rise similar to $h(\tau)$, consistent with the formation of a hydrogen bond to the new HOD molecule. However, the slower of the two time scales associated with $\langle N_O \rangle$ is 17.1 ps, which is approximately twice as long as the 7.4 ps time scale that we observe for the rise of the cross peaks in the 2D IR spectra (Fig. 7-14). This implies that a hierarchy of time scales exists for the solvation of the newly formed HOD molecule. While the growth of the exchange cross peak in the calculated 2D IR spectra is indicative of the formation of a hydrogen bond to the new HOD molecule, this molecule's solvation shell continues to evolve beyond the 7.4 ps time scale observed for the formation of a hydrogen bond to the HOD molecule, and gradually approaches that of water on a much longer time scale. The formation of this hydrogen bond is a part of a larger process that involves an increase in the density of water molecules around the newly formed HOD molecule. Given that water molecules near the ion's hydrogen atom are initially repulsed by the ion, these molecules perhaps form a hydrogen bonded cage about the ion as a means of incorporating the OH^- charge defect into water's hydrogen bonding network with minimal energetic cost. Upon the transfer of a proton to the ion, the hydrogen bonding contacts between these water molecules must break to allow them to properly solvate the newly formed HOD molecule. The breakage of these hydrogen bonds may explain why the collapse of density around this molecule following proton transfer is slower than the hydrogen bond fluctuations of bulk water.

Of course, microscopic reversibility dictates that a similar process occurs in the solvation of the newly formed OD^- ion, only in reverse. As more OD^- ions are added to

solution, the relative contribution to the overall dynamics of the system from the slow solvation of the OD^- charge defect following proton transfer will increase. This may provide a partial explanation for the large increase in the viscosity of alkali hydroxide solutions with increasing ion concentration.

7.11. Summary and Conclusions

Our investigations of the structural diffusion of the hydroxide ion in dilute aqueous NaOH solution have shown that this process is highly collective, requiring the loosely correlated motion of multiple water molecules. Through the use of the MS-EVB simulation, we have identified three principle time scales associated with this process. (1) A 40 fs time scale associated with "proton rattling" events wherein a shared proton is quickly transferred back and forth between the oxygen atoms of a Zundel-like $H_3O_2^-$ ion that represents the transition state for the proton transfer reaction. As the proton's motion is rapidly modulated by the fluctuations of the surrounding solvent, the vibrational frequencies associated with the shared proton undergo large, rapid changes, causing a decay in the intensity of 2D IR spectra calculated about proton transfer events. (2) The motion of the system away from the transition state is largely guided by electrostatic fluctuations of the surrounding environment occur with a characteristic time scale of ~500 fs. The range over which these fluctuations are important decreases with distance, and changes in the size of the solvation shell of the ion can play an important role since molecules in this solvation shell will make the largest contributions to the collective electric field that guides the motion of the transferring proton. (3) As a final step, we observe a 7.4 ps time scale that corresponds to the solvation of the water molecule formed by the proton transfer event. This process corresponds to the formation of a

hydrogen bond to the new water molecule and is part of a larger process by which the density of waters surrounding the new water molecule increases following the proton transfer reaction. Each of these time scales qualitatively map onto the experimental data that we presented in the preceding chapter, which found that proton rattling occurs on a time scale of 110 fs and the solvation of the newly formed water molecule and hydroxide ion following a proton transfer event occurs with a lower bound of 3 ps.

These results show that a proper description of the structural diffusion of the hydroxide ion requires the usage of a mixture of local hydrogen bonding coordinates that describe the solvation of the products of the reaction and a collective coordinate that represents the electric field fluctuations of the surrounding solvent that guide the motion of shared protons in Zundel-like configurations. This latter coordinate is the same that is largely responsible for hydrogen bond rearrangements in liquid water,[10] and shows that the same types of fluctuations that act to drive the evolution of water's hydrogen bonding network are those responsible for the transport of the OH^- charge defect.

Acknowledgements

I would like to acknowledge Ivan S. Ufimtsev and Todd J. Martinez for the donation of the MS-EVB simulation trajectories and for insightful discussions. I would also to thank Aritra Mandal for his aid in the measurement and computation of the data presented in Fig. 7-8.

References

(1) G. D. Rose and R. Wolfenden, "Hydrogen bonding, hydrophobicity, packing, and protein folding," Annu. Rev. Biophys. Biomol. Struct. 22, 381 (1993).

(2) R. A. Marcus, "On the theory of oxidation-reduction reactions involving electron transfer. I," J. Chem. Phys. 24, 966 (1956).

(3) R. A. Marcus and N. Sutin, "Electron transfers in chemistry and biology," Biochim. Biophys. Acta 811, 265 (1985).

(4) G. Zundel, in *The Hydrogen Bond: Recent Developments in Theory and Experiment, Vol. II*, edited by P. Schuster, G. Zundel and C. Sandorfy, (North Holland, Amsterdam, 1976).

(5) G. Zundel, "Hydrogen bonds with large proton polarizability and proton transfer processes in electrochemistry and biology," Adv. Chem. Phys. 111, 1 (2000).

(6) K. Ando and J. T. Hynes, "HCl acid ionization in water: A theoretical molecular modeling," Journal of Molecular Liquids 64, 25 (1995).

(7) K. Ando and J. T. Hynes, "Molecular mechanism of HCl acid ionization in water: *Ab initio* potential energy surfaces and Monte Carlo simulations," J. Phys. Chem. B 101, 10464 (1997).

(8) H. Lapid, N. Agmon, M. K. Petersen and G. A. Voth, "A bond-order analysis of the mechanism for hydrated proton mobility in liquid water," J. Chem. Phys. 122, 014506 (2005).

(9) M. K. Petersen, A. J. Hatt and G. A. Voth, "Orientational dynamics of water in the nafion polymer electrolyte membrane and its relationship to proton transport," J. Phys. Chem. B 112, 7754 (2008).

(10) J. D. Eaves, A. Tokmakoff and P. Geissler, "Electric field fluctuations drive vibrational dephasing in water," J. Phys. Chem. A 109, 9424 (2005).

(11) P. L. Geissler, C. Dellago, D. Chandler, J. Hutter and M. Parrinello, "Autoionization in liquid water," Science 291, 2121 (2001).

(12) M. E. Tuckerman, D. Marx and M. Parrinello, "The nature and transport mechanism of hydrated hydroxide ions in aqueous solution," Nature 417, 925 (2002).

(13) B. Chen, I. Ivanov, J. M. Park, M. Parrinello and M. L. Klein, "Solvation structure and mobility mechanism of OH^-: A Car-Parrinello molecular dynamics investigation of alkaline solutions," J. Phys. Chem. B 106, 12006 (2002).

(14) M. E. Tuckerman, A. Chandra and D. Marx, "Structure and dynamics of OH^- (aq)," Acc. Chem. Res. 39, 151 (2006).

(15) A. Chandra, M. E. Tuckerman and D. Marx, "Connecting solvation shell structure to proton transport kinetics in hydrogen-bonded networks via population correlation functions," Phys. Rev. Lett. 99, 145901 (2007).

(16) D. Asthagiri, L. R. Pratt, J. D. Kress and M. A. Gomez, "Hydration and mobility of HO^-(aq)," Proc. Nat. Acad. Sci. 101, 7229 (2004).

(17) I. Ohmine and S. Saito, "Water dynamics: fluctuation, relaxation, and chemical reactions in hydrogen bond network rearrangement," Acc. Chem. Res. 32, 741 (1999).

(18) I. Ohmine, "Liquid water dynamics: Collective motions, fluctuation, and relaxation," J. Phys. Chem. 99, 6767 (1995).

(19) D. Laage and J. T. Hynes, "A molecular jump mechanism of water reorientation," Science 311, 833 (2006).

(20) D. Laage and J. T. Hynes, "Do more strongly hydrogen-bonded water molecules reorient more slowly?," Chem. Phys. Lett. 433, 80 (2006).

(21) D. Laage and J. T. Hynes, "On the molecular mechanism of water reorientation," J. Phys. Chem. B 112, 14230 (2008).

(22) J. D. Eaves, J. J. Loparo, C. J. Fecko, S. T. Roberts, A. Tokmakoff and P. L. Geissler, "Hydrogen bonds in liquid water are broken only fleetingly," Proc. Natl. Acad. Sci. U.S.A. 102, 13019 (2005).

(23) J. J. Loparo, S. T. Roberts and A. Tokmakoff, "Multidimensonal infrared spectroscopy of water. II. Hydrogen bond switching dynamics," J. Chem. Phys. 125, 194522 (2006).

(24) S. T. Roberts, K. Ramasesha and A. Tokmakoff, "Structural rearrangements in water viewed through two-dimensional infrared spectroscopy," Acc. Chem. Res. 42, 1239 (2009).

(25) "Concentrative properties of aqueous solutions: Density, refractive index, freezing point depression, and viscosity," in *CRC Handbook of Chemistry and Physics*, edited by D. R. Lide, 89th, (CRC Press/Taylor and Francis, Boca Raton, FL, 2009).

(26) R. Rey, K. B. Møller and J. T. Hynes, "Hydrogen bond dynamics in water and ultrafast infrared spectroscopy," J. Phys. Chem. A 106, 11993 (2002).

(27) T. Hayashi, T. l. C. Jansen, W. Zhuang and S. Mukamel, "Collective solvent coordinates for the infrared spectrum of HOD in D_2O based on an *ab initio* electrostatic map," J. Phys. Chem. A 109, 64 (2005).

(28) S. Mukamel and D. Abramavicius, "Many-Body approaches for simulating coherent nonlinear spectorscopy of electronic and vibrational excitons," Chem. Rev. 104, 2073 (2004).

(29) S. Li, J. R. Schmidt, S. A. Corcelli, C. P. Lawrence and J. L. Skinner, "Approaches for the calculation of vibrational frequencies in liquids: Comparison to benchmarks for azide/water clusters," J. Chem. Phys. 124, 204110 (2006).

(30) M. Cho, "Coherent two-dimensional optical spectroscopy," Chem. Rev. 108, 1331 (2008).

(31) B. S. Mallik, A. Semparithi and A. Chandra, "Vibrational spectral diffusion and hydrogen bond dynamics in heavy water from first principles," J. Phys. Chem. A 112, 5104 (2008).

(32) F. Paesani, S. S. Xantheas and G. A. Voth, "Infrared spectroscopy and hydrogen-bond dynamics of liquid water from centroid molecular dynamics with an *ab initio*-based force field," J. Phys. Chem. B 113, 13118 (2009).

(33) E. Harder, J. D. Eaves, A. Tokmakoff and B. J. Berne, "Polarizable models in the vibrational spectroscopy of water," Proc. Nat. Acad. Sci. 102, 11611 (2005).

(34) J. R. Schmidt, S. T. Roberts, J. J. Loparo, A. Tokmakoff, M. D. Fayer and J.L.Skinner, "Are water simulation models consistent with steady-state and ultrafast vibrational spectroscopy experiments?," Chem. Phys. 341, 143 (2007).

(35) I. S. Ufimtsev, A. G. Kalinichev, T. J. Martinez and R. J. Kirkpatrick, "A charged ring model for classical OH^-(aq) simulations," Chem. Phys. Lett. 442, 128 (2007).

(36) I. S. Ufimtsev, A. G. Kalinichev, T. J. Martinez and R. J. Kirkpatrick, "A multistate empirical valence bond model for solvation and transport simulations of OH^- in aqueous solutions," Phys. Chem. Chem. Phys. 11, 9420 (2009).

(37) A. Warshel and R. M. Weiss, "An empirical valence bond approach for comparing reactions in solutions and in enzymes," J. Am. Chem. Soc. 102, 6218 (1980).

(38) J.-K. Hwang, G. King, S. Creighton and A. Warshel, "Simulation of free energy relationships and dynamics of S_N2 reactions in aqueous solution," J. Am. Chem. Soc. 110, 5297 (1988).

(39) U. W. Schmitt and G. A. Voth, "The computer simulation of proton transport in water," J. Chem. Phys. 111, 9361 (1999).

(40) T. J. F. Day, A. V. Soudackov, M. Cuma, U. W. Schmitt and G. A. Voth, "A second generation multistate empirical valence bond model for proton transport in aqueous systems," J. Chem. Phys. 117, 5839 (2002).

(41) Y. Wu, H. Chen, F. Wang, F. Paesani and G. A. Voth, "An improved multistate empirical valence bond model for aqueous proton solvation and transport," J. Phys. Chem. B 112, 467 (2008).

(42) G. A. Voth, "Computer simulation of proton solvation and transport in aqueous and biomolecular systems," Acc. Chem. Res. 39, 143 (2006).

(43) C. D. Wick and L. X. Dang, "Investigating hydroxide anion interfacial activity by classical and multistate empirical valence bond molecular dyanmics simulations," J. Phys. Chem. A 113, 6356 (2009).

(44) L. X. Dang and B. M. Pettitt, "Simple intramolecular model potentials for water," J. Phys. Chem. 91, 3349 (1987).

(45) P. B. Balbuena, K. P. Johnston and P. J. Rossky, "Molecular dynamics simulation of electrolyte solutions in ambient and supercritical water. 1. Ion solvation," J. Phys. Chem. 100, 2706 (1996).

(46) A. Botti, F. Bruni, S. Imberti, M. A. Ricci and A. K. Soper, "Ions in water: The microscopic structure of concentrated NaOH solutions," J. Chem. Phys. 120, 10154 (2004).

(47) A. Botti, F. Bruni, S. Imberti and M. A. Ricci, "Solvation of hydroxyl ions in water," J. Chem. Phys. 119, 5001 (2003).

(48) B. Halle and G. Karlström, "Prototropic charge migration in water. Part 2. Interpertation of nuclear magnetic resonance and conductivity data in terms of

model mechanisms," Journal of the Chemical Society, Faraday Transactions 2 79, 1047 (1983).

(49) M. P. Allen and D. J. Tildesley, *Computer Simulation of Liquids*, (Oxford University Press, New York, 1989).

(50) S. T. Roberts, P. B. Petersen, K. Ramasesha, A. Tokmakoff, I. S. Ufimtsev and T. J. Martinez, "Observation of a Zundel-like transition state during proton transfer in aqueous hydroxide solutions," Proc. Natl. Acad. Sci. U.S.A. 106, 15154 (2009).

(51) S. A. Corcelli, C. P. Lawrence and J. L. Skinner, "Combined electronic structure/molecular dynamics approach for ultrafast infrared spectroscopy of dilute HOD in liquid H_2O and D_2O," J. Chem. Phys. 120, 8107 (2004).

(52) S. A. Corcelli and J. L. Skinner, "Infrared and Raman line shapes of dilute HOD in liquid H_2O and D_2O from 10 to 90 ^{o}C," J. Chem. Phys. 109, 6154 (2005).

(53) B. Auer, R. Kumar, J. R. Schmidt and J. L. Skinner, "Hydrogen bonding and Raman, IR, and 2D-IR spectroscopy of dilute HOD in D_2O," Proc. Natl. Acad. Sci. U.S.A. 104, 14215 (2007).

(54) T. l. C. Jansen, T. Hayashi, W. Zhuang and S. Mukamel, "Stochastic Liouville equations for hydrogen-bonding fluctuations and their signatures in the two-dimensional vibrational spectroscopy of water," J. Chem. Phys. 123, 114504 (2005).

(55) D. Schiöberg and G. Zundel, "Very polarizable hydrogen bonds in solutions of bases having infra-red absorption continua," J. Chem. Soc., Faraday Trans. 2 69, 771 (1973).

(56) E. G. Diken, J. M. Headrick, J. R. Roscioli, J. C. Bopp, M. A. Johnson and A. B. McCoy, "Fundamental excitations of the shared proton in the $H_3O_2^-$ and $H_5O_2^+$ complexes," J. Phys. Chem. A 109, 1487 (2005).

(57) C. J. Fecko, J. D. Eaves, J. J. Loparo, A. Tokmakoff and P. L. Geissler, "Ultrafast hydrogen bond dynamics in the infrared spectroscopy of water," Science 301, 1698 (2003).

(58) K. R. Mitchell-Koch and W. H. Thompson, "Infrared spectra of a model phenol-amine proton transfer complex in nanoconfined CH_3Cl," J. Phys. Chem. B 112, 7448 (2008).

(59) M. Moskovits and K. H. Michaelian, "Alkali hydroxide ion paris. A Raman study," J. Am. Chem. Soc. 102, 2209 (1980).

(60) N. B. Librovich and V. D. Maiorov, "Vibrational spectra of $H_3O_2^-$ and $D_3O_2^-$ ions in aqueous and deuterated aqueous solutions of potassium and sodium hydroxides," Russ. J. Phys. Chem. 56, 624 (1982).

(61) G. E. Walrafen and R. T. W. Douglas, "Raman spectra from very concentrated aqueous NaOH and from wet and dry, solid, and anhydrous molten, LiOH, NaOH, and KOH," J. Chem. Phys. 124, 114504 (2006).

(62) T. Corridoni, A. Sodo, F. Bruni, M. A. Ricci and M. Nardone, "Probing water dynamics with OH^-," Chem. Phys. 336, 183 (2007).

(63) C. P. Lawrence and J. L. Skinner, "Vibrational spectroscopy of HOD in D_2O. III. Spectral diffusion, and hydrogen-bonding and rotational dynamics," J. Chem. Phys. 118, 264 (2003).

(64) X. Li, V. E. Teige and S. S. Iyengar, "Can the four-coordinated, penta-valent oxygen in hydorxide water clusters be detected through experimental vibrational spectroscopy," J. Phys. Chem. A 111, 4815 (2007).

(65) S. Mukamel, *Principles of Nonlinear Optical Spectroscopy*, (Oxford University Press, New York, 1995).

(66) J. G. Saven and J. L. Skinner, "A molecular theory of the line shape: Inhomogeneous and homogeneous electronic spectra of dilute chromophores in nonpolar fluids," J. Chem. Phys. 99, 4391 (1993).

(67) A. M. Walsh and R. F. Loring, "Time resolved stimulated light scattering from a solvated chromophore: A molecular dynamics study," J. Chem. Phys. 94, 7575 (1991).

(68) J. R. Schmidt, S. A. Corcelli and J. L. Skinner, "Pronounced non-Condon effects in the ultrafast infrared spectroscopy of water," J. Chem. Phys. 123, 044513 (2005).

(69) G. Hanna and E. Geva, "Computational study of the one and two dimensional infrared spectra of a vibrational mode strongly coupled to its environment: Beyond the Cumulant and Condon approximations," J. Phys. Chem. B 114, 12991 (2008).

(70) J. J. Loparo, S. T. Roberts, R. A. Nicodemus and A. Tokmakoff, "Variation of the transition dipole moment across the stretching band of water," Chem. Phys. 341, 218 (2007).

(71) D. Borgis, G. Tarjus and H. Azzouz, "An adiabatic dynamical simulation study of the Zundel polarization of H-bonded complexes in solution," J. Chem. Phys. 97, 1390 (1992).

(72) O. Markovitch, H. Chen, S. Izvekov, F. Paesani, G. A. Voth and N. Agmon, "Special pair dance and partner selection: Elementary steps in proton transport in liquid water," J. Phys. Chem. B 112, 9456 (2008).

(73) W. H. Press, S. A. Teukolsky, W. T. Vetterling and B. P. Flannery, *Numerical Recipes in C++*, (Cambridge University Press, Cambridge, 2002).

(74) S. Horvath, A. B. McCoy, J. R. Roscioli and M. A. Johnson, "Vibrationally induced proton transfer in $F^-(H_2O)$ and $F^-(D_2O)$," J. Phys. Chem. A 112, 12337 (2008).

(75) A. Heiman and S. Licht, "Fundamental baseline variations in aqueous near-infrared analysis," Anal. Chim. Acta 394, 135 (1999).

(76) P. B. Petersen and A. Tokmakoff, Opt. Lett. In Preparation (2009).

(77) A. Luzar and D. Chandler, "Hydrogen bond kinetics in liquid water," Nature 379, 55 (1996).

(78) L. S. Rothman, C. P. Rinsland, A. Goldman, S. T. Massie, D. P. Edwards, J.-M. Flaud, A. Perrin, C. Camy-peyret, V. Dana, J.-Y. Mandin, J. Schroeder, A. McCann, R. R. Gamache, R. B. Wattson, K. Yoshino, K. V. Chance, K. W. Jucks, L. R. Brown, V. Nemtchinov and P. Varanasi, "The HITRAN molecular spectroscopic database and hawks (HITRAN atmospheric workstation): 1996 edition," J. Quant. Spectrosc. Radiat. Transfer 60, 665 (1998).

7.A. Appendix. Calculation of Frequencies and Transition Dipole Moments

As described in the main text of the chapter, we calculate vibrational frequencies by making use of a map generated from DFT that relates the instantaneous vibrational frequencies of the HOD molecule to the solvation coordinate, ΔE_{sol}. To calculate frequencies at each simulation time step, we make use of the linear correlation between ΔE_{sol} calculated using DFT, ΔE_{DFT}, and that estimated by stretching the O-H bond using the empirical simulation force field, ΔE_{EVB}. This latter quantity can be readily computed at each simulation time step with little cost. Fig. 7-A1A shows the correlation between ΔE_{DFT} and ΔE_{EVB}. Although the spread of points is somewhat large, the two quantities are linearly related with a correlation coefficient of $\rho = 0.95$. In Fig. 7-4B of the main text we display the frequency map connecting ΔE_{DFT} and ω_{10}. Fig. 7-A1 plots the remaining frequency maps for ω_{20}, ω_{30}, and ω_{40}, as well as 4th order polynomial fits to each map (See Table 7-A2 for a list of fit coefficients). As the proton becomes shared between two oxygen atoms (i.e. as $\Delta E_{DFT} \rightarrow 0$), each of the calculated vibrational frequencies are found to decrease. In particular, ω_{20} undergoes a strong red shift, bringing it into the experimentally probed frequency range.

The calculation of transition dipole moments is performed in a manner similar to that of Corcelli and Skinner.[52] The dipole matrix element for the transition between vibrational states *n* and *m* is defined as:

$$\boldsymbol{\mu}_{nm} = \langle n | \boldsymbol{\mu} | m \rangle . \tag{7-A1}$$

We expand $\boldsymbol{\mu}$ to first order in the O-H stretching coordinate, r_{OH}, about the minimum of the potential:

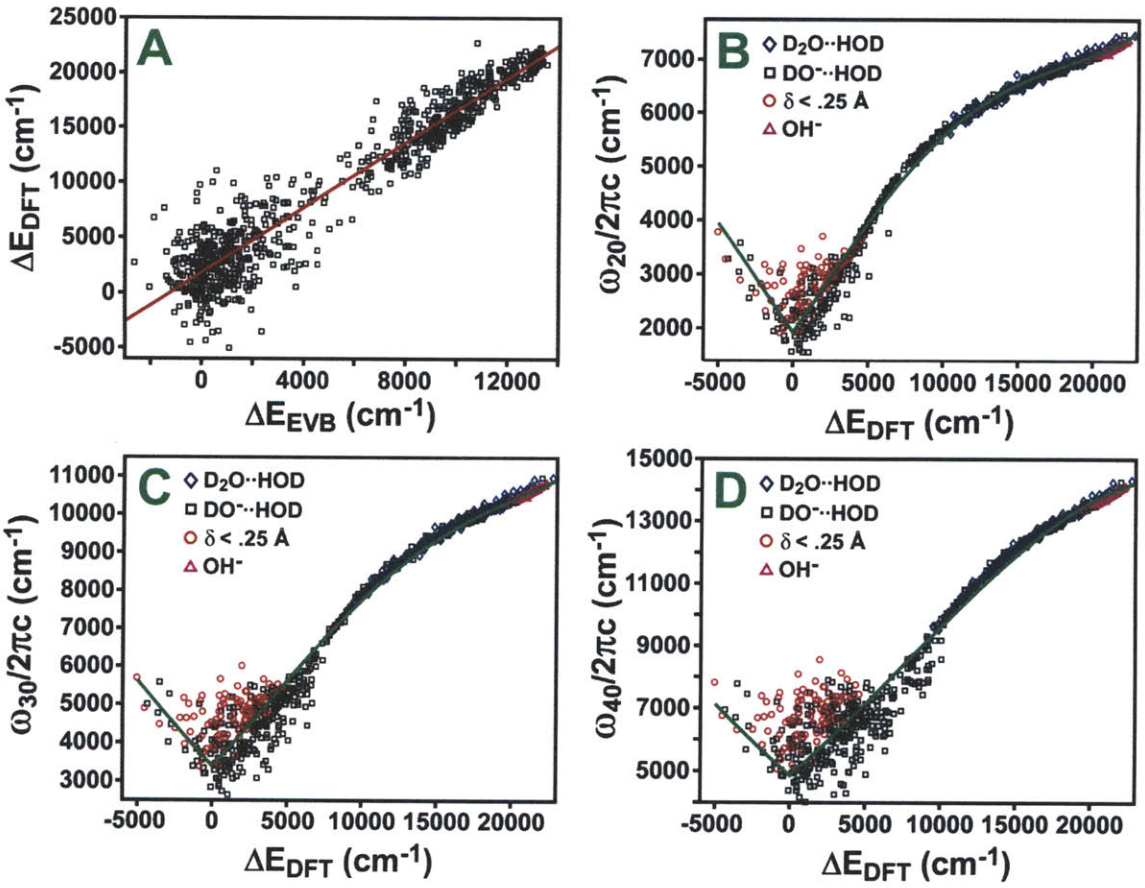


Figure 7-A1: (A) Mapping between the solvation coordinate calculated from the cluster calculations, ΔE_{DFT}, and that calculated using the simulation force field, ΔE_{EVB}. (B - D) Empirical maps linking ω_{20}, ω_{30}, and ω_{40} to ΔE_{DFT}. As with Fig. 7-4B, we separately label points calculated for clusters wherein the stretched O-H bond corresponds to a HOD molecule hydrogen bonded to D_2O, hydrogen bonded to OD^-, or an OH^- ion.

$$\boldsymbol{\mu}_{nm} \approx \langle n | \boldsymbol{\mu}_o + r_{OH} \left(d\boldsymbol{\mu}/dr_{OH} \right)_{r_{OH}=r_{eq}} | m \rangle = \mu' r_{nm} \hat{\mathbf{u}} \qquad (7\text{-A2})$$

where $r_{nm} = \langle n | r_{OH} | m \rangle$, $\mu' = \left| \left(d\boldsymbol{\mu}/dr_{OH} \right)_{r_{OH}=r_{eq}} \right|$, and $\hat{\mathbf{u}}$ is the orientation of the O-H transition dipole which we take to be the O-H bond vector. We obtain the matrix elements, r_{nm}, from the eigenstates of the DVR calculation used to determine the vibrational frequencies.

Typically, μ' is independent of the vibrational coordinate for weakly anharmonic systems, but this has been shown to break down in the case of hydrogen bonding systems

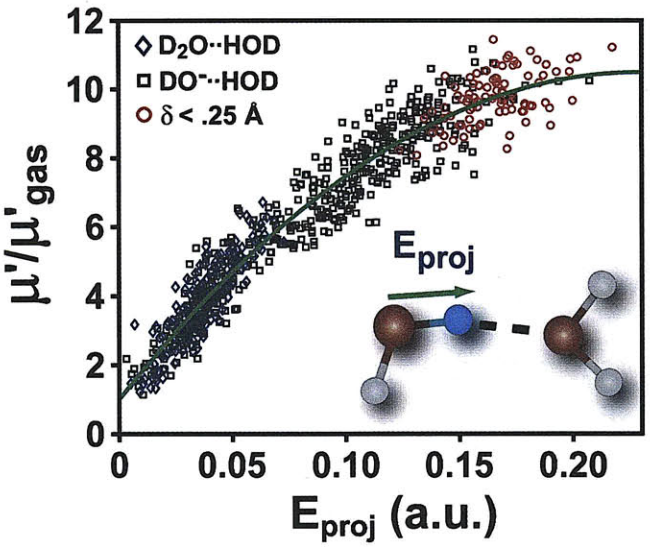


Figure 7-A2: Correlation between the projection of the collective electric field of the solvent along the O-H bond at the position of the proton, E_{proj}, and the magnitude of the derivative of the electric dipole moment, μ'. E_{proj} is calculated in a manner identical to that used to construct Fig. 7-3.

such as water where μ' is found to strongly vary with the magnitude of the electric field projected along the O-H bond.[52,68] For each of the examined clusters, we determine μ' by calculating the static dipole moment at five points about the minimum of the potential, project each onto the O-H bond axis, and then numerically differentiate the projection. We indeed find that μ' varies strongly with the magnitude of the electric field projected along the O-H bond at the position of the proton, E_{proj} (Fig. 7-A2). Over the range of field strengths indicative of a hydrogen bond between HOD and D_2O, the correlation between E_{proj} and μ' appears to be linear, consistent with previous simulations of HOD in D_2O/H_2O.[52,53,68] As E_{proj} increases beyond this range, we observe a deviation from linearity. The green line in Fig. 7-A2 represents a quadratic fit to μ':

$$\mu'/\mu'_{gas} = -180.6625\ E_{proj}^2/(\text{a.u.})^2 + 82.820\ E_{proj}/\text{a.u.} + 1, \qquad (7\text{-A3})$$

where E_{proj} is in atomic units and μ'_{gas} represents the value of μ' calculated at the gas phase value of ω_{10}, 3707 cm^{-1}.[78]

The frequency dependence of the transition dipole for a given vibrational transition is dictated by the product of μ' and the matrix element, r_{nm}, for the transition. Fig. 7-7A of the main text plots $\mu_{10} = \mu' r_{10}$ and $\mu_{20} = \mu' r_{20}$ against their respective vibrational frequencies, ω_{10} and ω_{20}. The green lines plotted on top of the data represent cubic fits to μ_{10} and μ_{20}, which are used to calculate these quantities from their respective frequencies. Although the correlation between ω_{nm} and μ_{nm} beaks down somewhat at low frequency, it is clear that as both ω_{10} and ω_{20} decrease, a strong increase in μ_{10} and μ_{20} is observed. In Fig. 7-A3, we plot corresponding transition dipole maps for other transitions of the O-H vibrational potential that are pertinent to the experiments described in this thesis, namely the two dipole allowed transitions, μ_{21} and μ_{32}, and the dipole forbidden transitions, μ_{31} and μ_{42}. Each of the pictured transition dipole moments are plotted against μ_{10}, which was the parameter found to have the highest degree of correlation to each dipole. At small values of μ_{10}, the correlation between this parameter and the other transition dipoles of the potential appears approximately linear, but as μ_{10} approaches a value of 0.4, a sharp increase followed by a decrease of each transition dipole is observed. We do not seek to put forth an explanation for this observed behavior, and have simply chosen to fit each of the plotted transition dipole maps using a functional form that can adequately reproduce the behavior of each dipole when its corresponding frequency falls into our experimentally accessible frequency range. In the case of μ_{21}

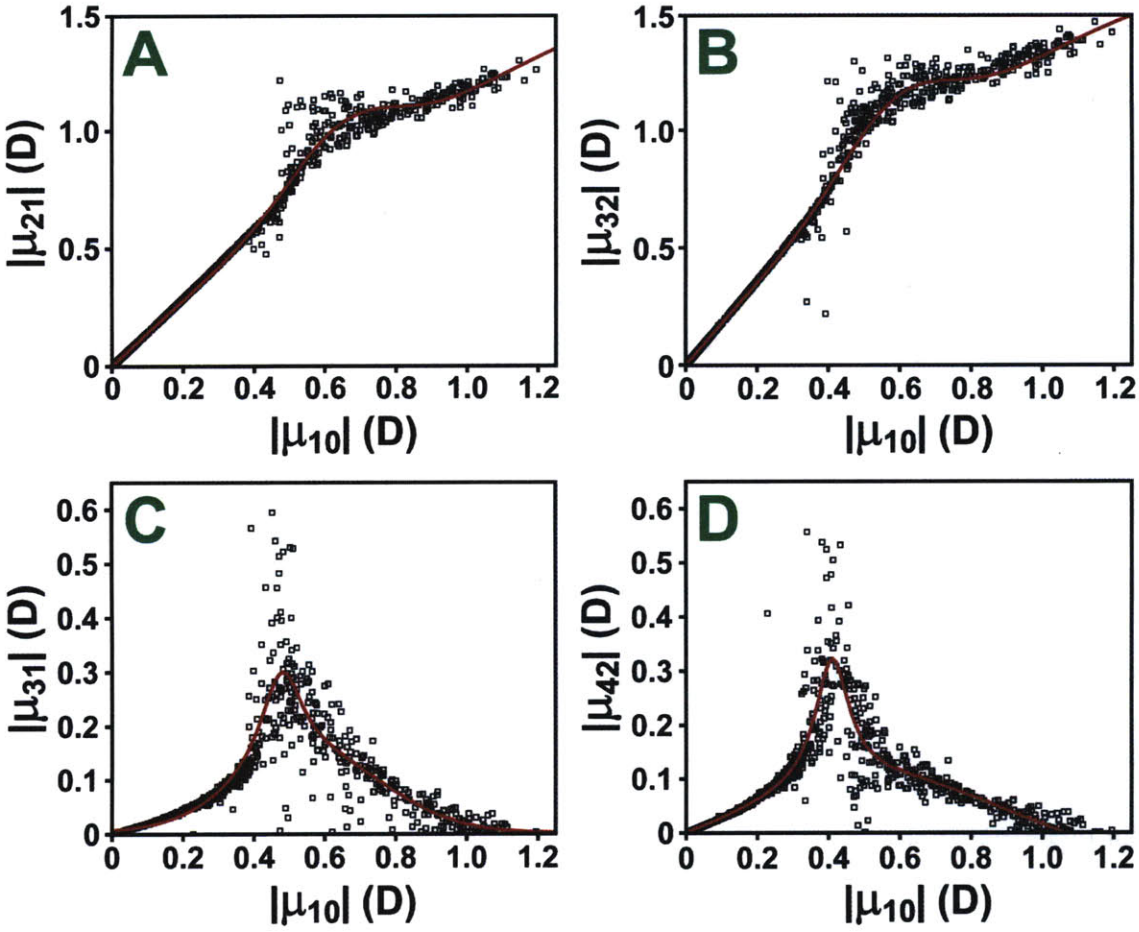


Figure 7-A3: Empirical maps used for the determination of μ_{21}, μ_{32}, μ_{31}, and μ_{42} on the basis of μ_{10}. Each transition dipole is fit using a function that can reproduce the dipole's variation with changes in the O-H stretching potential. We do not ascribe any specific meaning to the choice of functional form, having chosen ones solely based on their ability to reproduce the calculated data.

and μ_{32}, a quadratic function added to a Gaussian lineshape gives good agreement with the calculated dipole maps. For μ_{31} and μ_{42}, a sum of Gaussian and Lorentzian lineshapes is used to fit the transition dipoles. Tables 7-A3 and 7-A4 list the set of parameters that describe the fits pictured in Fig. 7-7A and 7-A3.

Empirical Relationship	Correlation Coefficient
$\Delta E_{DFT} = 1.4769 \Delta E_{EVB} + 1819\ cm^{-1}$	0.949

Table 7-A1: Empirical relationship between ΔE_{DFT} and ΔE_{EVB}. ΔE_{EVB} is in units of cm^{-1}.

Transition Frequency	a/cm^{-1}	b	c/cm	d/cm^2	e/cm^3
ω_{10}	688.3	0.39699	-2.00×10^{-5}	3.5214×10^{-10}	1.1361×10^{-15}
ω_{20}	1919.9	0.400	7.3306×10^{-6}	-1.4227×10^{-9}	3.5112×10^{-14}
ω_{30}	3395.7	0.400	1.5750×10^{-5}	-1.5255×10^{-9}	3.0520×10^{-14}
ω_{40}	4868.1	0.40876	1.1375×10^{-5}	-4.9785×10^{-10}	0

Table 7-A2: Empirical relationships between ΔE_{DFT} and the transition frequencies: $\omega_{nm} = a + b|\Delta E_{DFT}| + c|\Delta E_{DFT}|^2 + d|\Delta E_{DFT}|^3 + e|\Delta E_{DFT}|^4$. ΔE_{DFT} is in units of cm^{-1}

matrix element	a/D	b/D•cm	c/ D•cm^2	d/ D•cm^3
μ_{10}	1.8336	-1.2973×10^{-3}	4.7136×10^{-7}	-6.8016×10^{-11}
μ_{20}	0.77529	-3.2758×10^{-4}	5.2584×10^{-8}	-3.0474×10^{-12}

Table 7-A3: Empirical relationships between μ_{nm} and their respective frequencies: $\mu_{nm} = a + b\omega_{nm} + c\omega_{nm}^2 + d\omega_{nm}^3$. ω_{nm} is in units of cm^{-1}.

Fit Parameter	μ_{21}	μ_{32}	μ_{31}	μ_{42}
a/D	-8.56×10^{-4}	-1.372×10^{-3}	0.0	-6.013×10^{-2}
b	1.4429	1.7933	--	--
c/D^{-1}	-0.285	-0.475	--	--
A_g/D	0.22	0.25	0.12472	0.15808
x_g/D	0.65	0.59	0.57474	0.53661
σ/D	0.15	0.15	0.20513	0.37703
A_l/D^2	--	--	1.4274×10^{-2}	1.3649×10^{-2}
x_l/D	--	--	0.47734	0.40965
Γ/D	--	--	0.15178	0.11723

Table 7-A4: Empirical relationships between μ_{nm} and μ_{10}. μ_{nm} is described by: $\mu_{nm} = a + b\mu_{10} + c\mu_{10}^2 + A_g \exp[-(\mu_{10} - x_g)^2/2\sigma^2] + A_l(\Gamma/2)/\left((\mu_{10} - x_l)^2 - (\Gamma/2)^2\right)$, where μ_{10} is in units of Debye.

Sean T. Roberts

116 Sycamore St. #25 ▪ Somerville MA, 02145
Office: (617) 253-7372 ▪ seanr@mit.edu

Education

Massachusetts Institute of Technology (Cambridge, MA)
Ph.D. in Physical Chemistry, Expected December 2009 (g.p.a. 5.0/5.0)
Thesis: Hydrogen Bond Rearrangements and the Motion of Charge Defects in Water Viewed using Multidimensional Ultrafast Infrared Spectroscopy.
Advisor: Andrei Tokmakoff

University of California Los Angeles (Los Angeles, CA)
B.S. in Chemistry, Physical Chemistry Concentration, 2003,
g.p.a. 3.962/4.0, Highest Departmental Honors, Summa Cum Laude
Advisor: Benjamin J. Schwartz

Research

Doctoral Research (2003 – present)
Massachusetts Institute of Technology Department of Chemistry
Advisor: Andrei Tokmakoff

- Performed time-resolved infrared spectroscopy on water and on concentrated acids and bases to monitor transient changes to water's hydrogen bonding structure and how these changes influence the transport of excess protons and proton holes in water.
- Developed methods for the calculation of experimental observables from classical molecular dynamics simulations.
- Developed simple metrics which can be used to track the loss of frequency correlation in two-dimensional infrared spectra.
- Aided in the development of a novel method of acquiring two-dimensional infrared spectra without the use of expensive infrared array detectors.
- Wrote extensive C^{++} and matlab code to model experimental data.

Undergraduate Research (2001 – 2003)
University of California Los Angeles Department of Chemistry
Advisor: Benjamin J. Schwartz

- Performed fluorescence quenching measurements of novel functionalized organic conjugated polymers in the presence of inorganic salts and fullerene molecules to correlate the performance of devices made from such materials to their solution phase conformations
- Maintained a VAC dry nitrogen glovebox and worked extensively with a JY-Horiba Fluorolog-3 time resolved fluorimeter.

Teaching

Teaching Assistant (Fall 2003, Spring 2005)
Massachusetts Institute of Technology Department of Chemistry
- Recitation leader in undergraduate quantum mechanics class.
- Substitute lecturer and grader in graduate quantum mechanics class.

Honors/Awards

American Compositeness in Chemistry Graduate Fellowship (ACC-F) (2009)
- Postdoctoral research fellowship awarded by the National Science Foundation to involve beginning scientists in efforts to broaden participation in chemistry.

Coblentz Society Student Award (2009)
- Awarded to a student that has demonstrated excellence in research in the field of vibrational spectroscopy.

FACSS Student Poster Award (2009)
- Award given at the 2009 Federation of Analytical Chemistry and Spectroscopy Societies meeting in Louisville, KY.

Morse Travel Grant (2008)
- Competitive travel award for students in the MIT chemistry department.

Massachusetts Institute of Technology Presidential Fellowship (2003-04)
- Highly competitive award given to a subset of incoming MIT graduate students across a wide array of disciplines.

Phi Beta Kappa Graduate Fellowship (2003):
- Awarded to a new member of the UCLA Phi Beta Kappa chapter pursuing graduate education.

Ramsey Award (2003)
- Departmental Award at UCLA given to a graduating student for excellence in physical chemistry.

Arnold O. Beckman Undergraduate Research Fellowship (2002-03)
- Highly competitive award given to ~100 undergraduate researchers at schools across the United States.

University of California Los Angeles Summer Research Scholarship (2002)

Publications

1. **S. T. Roberts**, P. B. Petersen, K. Ramasesha, A. Tokmakoff, I. S. Ufimtsev, and T. J. Martinez "Observation of a Zundel-like transition state during proton transfer in aqueous hydroxide" Proc. Natl. Acc. Sci. U.S.A. 106(36), 15154, (2009).
2. **S. T. Roberts**, K. Ramasesha, and A. Tokmakoff, "Structural rearrangements in water viewed through two-dimensional infrared spectroscopy" Acc. Chem. Resh. 42(9), 1239, (2009).

3. P. B. Petersen, **S. T. Roberts**, K. Ramasesha, D. G. Nocera, and A. Tokmakoff, "Ultrafast N-H vibrational dynamics of cyclic doubly hydrogen-bonded homo- and heterodimers" J. Chem. Phys. B. 112, 13167, (2008).
4. J. J. Loparo, **S. T. Roberts**, R. A. Nicodemus, and A. Tokmakoff, "Variation of the transition dipole moment across the OH stretching band of water" Chem. Phys. 341(1-3), 218 (2007).
5. J. R. Schmidt, **S. T. Roberts**, J. J. Loparo, A. Tokmakoff, M. D. Fayer, and J. L. Skinner, "Are water simulation models consistent with steady-state and ultrafast vibrational spectroscopy experiments?" Chem. Phys. 341(1-3), 143, (2007).
6. **S. T. Roberts**, J. J. Loparo, and A. Tokmakoff, "Characterization of spectral diffusion from two-dimensional line shapes" J. Chem. Phys. 125, 084502 (2006).
7. J. J. Loparo, **S. T. Roberts**, and A. Tokmakoff, "Multidimensional infrared spectroscopy of water. I. Vibrational dynamics in two-dimensional IR line shapes" J. Chem. Phys. 125, 194521, (2006).
8. J. J. Loparo, **S. T. Roberts**, and A. Tokmakoff, "Multidimensional infrared spectroscopy of water. II. Hydrogen bond switching dynamics" J. Chem. Phys. 125, 194522, (2006).
9. J. D. Eaves, J. J. Loparo, C. J. Fecko, **S. T. Roberts**, A. Tokmakoff, and P. L. Geissler, "Hydrogen bonds in liquid water are broken only fleetingly" Proc. Natl. Acc. Sci. U.S.A. 102(37) 13019. (2005).
10. C. J. Fecko, J. J. Loparo, **S. T. Roberts**, and A. Tokmakoff, "Local hydrogen bonding dynamics and collective reorganization in water: Ultrafast infrared spectroscopy of HOD/D_2O" J. Chem. Phys. 122, 054506 (2005).
11. J. J. Loparo, C. J. Fecko, J. D. Eaves, **S. T. Roberts**, and A. Tokmakoff, "Reorientational and configurational fluctuations in water observed on molecular length scales" Phys. Rev. B. 70, 180201(R), (2004).
12. A. D. Smith, C. K.-F. Shen, **S. T. Roberts**, R. Helgeson, and B. J. Schwartz, "Ionic strength and solvent control over the physical structure, electronic properties and superquenching of conjugated polyelectrolytes" Res. Chem. Intermed. 33(1-2), 125, (2007).

Conference Proceedings

1. **S. T. Roberts**, P. B. Petersen, K. Ramasesha and A. Tokmakoff, "The dynamics of aqueous hydroxide ion transport probed via ultrafast vibrational echo experiments," in *Ultrafast Phenomena XVI*, edited by P. Corkum, S. De Silvestri, K. A. Nelson, E. Riedle and R. W. Schoenlein, (Springer-Verlag, Berlin, 2008).
2. J. J. Loparo, **S. T. Roberts**, and A. Tokmakoff, "2D IR spectroscopy of hydrogen bond switching in liquid water," in *Ultrafast Phenomena XV*, edited by P. Corkum, D. Jonas, D. Miller, and A. M. Weiner, (Springer-Verlag, Berlin, 2006).

Presentations

1. **S. T. Roberts**, P. B. Petersen, K. Ramasesha, and A. Tokmakoff, "Aqueous Hydroxide Ion Transport Viewed Using Ultrafast 2D IR Spectroscopy" Presented at

the 14th International Conference on Time-Resolved Vibrational Spectroscopy, Meredith, New Hampshire. May 2009.

2. **S. T. Roberts**, "Transport of the Aqueous Hydroxide Ion Measured Using Nonlinear Infrared Spectroscopy" Special Physical Chemistry Seminar, Kobe University. Japan. September 2008.
3. **S. T. Roberts**, P. B. Petersen, K. Ramasesha, and A. Tokmakoff, "Transport of the Aqueous Hydroxide Ion Probed Through Ultrafast Two-Dimensional Infrared Spectroscopy" Presented at the 4th Coherent Multidimensional Spectroscopy Conference, Kyoto, Japan. August 2008.
4. **S. T. Roberts**, P. B. Petersen, K. Ramasesha, and A. Tokmakoff, "Aqueous Charge Transfer Dynamics Probed Via Ultrafast Nonlinear Infrared Spectroscopy" Presented at the 236th American Chemical Society National Meeting, Philadelphia, PA. August 2008.

Professional Memberships

Phi Beta Kappa (inducted 2003)
American Chemical Society (since 2003)